Tampere University

JARI RÄMÖ

Experimental Studies and Numerical Modeling of Strain Rate and Temperature Dependent Material Behavior in Dynamic Processes

Tampere University Dissertations 167

Tampere University Dissertations 167

JARI RÄMÖ

Experimental Studies and Numerical Modeling of Strain Rate and Temperature Dependent Material Behavior in Dynamic Processes

ACADEMIC DISSERTATION
To be presented, with the permission of
the Faculty of Engineering and Natural Sciences
of Tampere University,
for public discussion in the Auditorium K1703
of Konetalo Building, Korkeakoulunkatu 6, 33720 Tampere,
on the 22nd of November 2019, at 12 o'clock noon.

ACADEMIC DISSERTATION

Tampere University, Faculty of Engineering and Natural Sciences
Finland

Responsible supervisor and Custos	Prof. Veli-Tapani Kuokkala Tampere University Finland	
Supervisor	Asst. Prof. (tenure track) Mikko Hokka Tampere University Finland	
Pre-examiners	Assoc. Prof. Adinel Gavrus INSA Rennes France	Ph.D. Bo Song Sandia National Laboratories USA
Opponents	Prof. Ezio Cadoni University of Applied Sciences and Arts of Southern Switzerland Switzerland	Ph.D. Hervé Couque Nexter Munitions France

The originality of this thesis has been checked using the Turnitin OriginalityCheck service.

Cover design: Roihu Inc.

ISBN 978-952-03-1336-4 (print)
ISBN 978-952-03-1337-1 (pdf)
ISSN 2489-9860 (print)
ISSN 2490-0028 (pdf)
http://urn.fi/URN:ISBN:978-952-03-1337-1

PunaMusta Oy – Yliopistopaino
Tampere 2019

Abstract

The rate of loading plays an increasingly important role in many technological processes and applications, and even in many everyday events. In all these cases, it would be important to know in advance how the material will react to the loading conditions where the strain rate can exceed what is generally considered 'normal' or 'conventional'. In this thesis, the main objective was to examine technological processes and events involving time and temperature dependent material behavior and to develop modeling concepts based on experimental materials research for simulation purposes. As a rule of thumb, the instantaneous strength of virtually all materials increases with increasing strain rate and decreasing temperature, which can have both positive and negative implications, depending on the case. In the crusher pressure sensor case, the consequence of increasing strain rate is that the obtained pressure values start to increasingly deviate from the correct values, when the gun pressure increases. From the materials science point of view, this problem can be easily solved by proper calibration that accounts also for the strain rate effect, but there are still issues related to knowing the actual strain rate, as will be shown in the thesis. Cold heading, in turn, is a process where metal wire is deformed to the desired shape in a die. With increasing production rates, also in this application the strain rate can reach levels where it must be accounted for. In this work, the properties of the cold heading steel were determined at wide ranges of strain rate and temperature using both hydraulic materials testing machines and the Hopkinson Split Bar testing techniques. Based on the experimental results, an 'ad-hoc' material model was developed and implemented in finite element software to be used in numerical simulations. To validate the simulation results, a relatively simple case that could be carried out both numerically and experimentally was chosen. The results show that the agreement between the experimental and simulated results is much better with the developed model that takes into account the strain rate and temperature effects than with the Johnson-Cook model based on the same data, or with the 'ad-hoc' model based on the quasi-static data only. There were, however, still some minor differences observed between the experimental and simulated results, which could be attributed mostly to the nonhomogeneous properties of the cold heading steel and the deviations of the steel wire shape and size from the 'ideal' ones used in the simulations. The other applications studied in this thesis deal with the optimization of paper machine roll covers with finite element modeling, the effects of microstructure on the dynamic strain aging (DSA) of carbon steels, and the high temperature high strain rate testing of a titanium alloy with the tensile Hopkinson Split Bar

technique. In the first case, comparison of the experimental and simulated data shows that a hyperelastic model of the cover material is more suitable for the prediction of the contact conditions between the rolls than an elastic model. The main result of the DSA studies is that under certain strain rate and temperature conditions, the DSA effect can be rather strong and should be taken into account especially when modeling the behavior of this type of materials at elevated temperatures. Finally, the round-robin type high temperature testing with tensile Hopkinson bar devices underlines the importance of the specimen fixing method on the quality of the test results, especially at higher temperatures, as well as the effect of heating time on the usability of different methods, in particular adhesive bonding of the specimen to the stress bars.

Preface

During the past 10+ years, I have had an opportunity to conduct a lot of research work, of which only a small part has actually materialized as this thesis. Luckily, I have had Veli-Tapani Kuokkala as my professor and supervisor. He has finally pushed the work in the right direction. Veli-Tapani's pressure and guidance were absolutely necessary to get this dissertation completed. Also, Mikko Hokka's contribution was important in the final stages of finalizing the manuscript.

Naturally, the co-authors of the articles, for example Ph.D. Taina Vuoristo and Ph.D. Heli Nyberg – to mention but a few – deserve to be recognized for their excellent work.

I want to thank all my colleagues, current and former, for their help and companionship, which I consider essential for good results. There are so many persons I could mention by name that the space here would not be enough, so I must thank them all collectively.

One of the important aspects in research work is the financial support – nothing could be done without it. Some of the partners who have provided funding for this research are Tekes (now Business Finland) and Matine, as well as CSC, which provided the data processing capacity needed in the simulations. There has also been a lot of fruitful collaboration with several companies. As a researcher, for me the work where scientific viewpoint is combined with practical importance, or at least a possibility for that, is the most satisfying. I am grateful that there have been companies facilitating that.

My wife, Sirpa, has supported me in numerous ways. One of those has been the delicious content of the daily lunch box. I am thankful for her support.

People are social living creatures and they need a proper social network around them. I am lucky to have that in my family, relatives, and friends.

Tampere, November 2019

Jari Rämö

Contents

Symbols and abbreviations

A, B, C, n, m	constants in the Johnson-Cook equation (Eqn. 5)
A, B	fitting parameters (Eqn. 12)
A_b	cross-sectional area of the pressure bars
A_s	cross-sectional area of the sample
a, b, c	fitting parameters (Eqn. 11)
a_i, b_j, c_k, . . h	fitting parameters or material constants (Eqns. 9 and 10)
BCC	body centered cubic
C_0	speed of sound
CCT	Cold Contact Time
CG	coarse-grain(ed)
CKHL	constant in the Khan-Huang-Liang model (Eqn. 6)
C_p	specific heat
DMA	dynamic mechanical analyzer
DMTA	dynamic mechanical thermal analyzer
DSA	dynamic strain aging
E	elastic modulus, Young's modulus
EH+GF	electric heating and mechanical clamping
F	force
FCC	face centered cubic
FH+GF	furnace heating and mechanical clamping
FH+MC	furnace heating and adhesive (glue) fixing
GP	globular pearlite
HSB	Hopkinson Split Bar
HT/LT	high temperature/low temperature
K	Kelvin degree
k	spring constant (in Fig. 5)
KHL	Khan-Huang-Liang model
L_s	length of the sample
MTS	Mechanical Threshold Stress model
OFHC	oxygen-free high conductivity
P_{cr}	crusher pressure
P_h	piezoelectric peak pressure
R	universal gas constant, or reference microstructure
RT	room temperature, or available thermal energy
SG	strain gage
SHPB	Split Hopkinson Pressure Bar
t	time
T_0	Temperature (Figs. 1 and 2)

T_g	glass transition temperature
T-HSB	tensile Hopkinson Split Bar
v	activation volume
WB	banded structure
ΔH	height of the potential barrier
R_{eH}	yield stress
ε	strain
$\dot{\varepsilon}$	strain rate
ε_t	strain in the transmitted bar
ε_i	strain in the incident bar
ε_r	strain in the incident bar (reflected wave)
η	temperature sensitivity factor (Eqn. 14), viscosity (in Fig. 5)
λ	Taylor-Quinney coefficient
μ	elastic modulus (in Fig. 5)
δ	phase (lag) angle
ρ	density
σ	stress

List of Publications

I. V-T. Kuokkala, J. Rämö and T. Vuoristo: ”Calibration of crusher pressure gauges by high strain rate testing”, SEM X International Congress & Exposition on Experimental and Applied Mechanics, Costa Mesa, California, U.S.A., June 7-10, 2004.

II. J. Rämö, T. Vuoristo, V-T. Kuokkala, G. Simbierowicz and R. Vanninen: "Influence of rubber parameters on the calculation of nip pressure profile in paper coating", Proc. ECCMR 2005 - Fourth European Conference on Constitutive Models for Rubber, The Royal Institute of Technology, Stockholm, Sweden, June 27-29th, 2005, pp. 415-420, 2005.

III. T. Vuoristo, V-T. Kuokkala, J. Rämö, J. Partinen and J. Kolsi: "Strain rate dependent deformation behavior of cold heading steels", Proc. Asia Steel International Conference 2006 (Asia Steel ’06), Fukuoka, Japan, 9-11.5.2006, pp. 902-907.

IV. H. Nyberg, V.-T. Kuokkala, J. Rämö, A. Järviniemi: “A Dynamic Calibration Method for Crusher Gauges Based on Material Testing”, Propellants, Explosives, Pyrotechnics, 32, No. 1, 61-67, 2007.

V. J. Rämö, V-T. Kuokkala and T. Vuoristo: "Influence of Strain Rate and Adiabatic Heating on the Deformation Behavior of Cold Heading Steels", Journal of Materials Processing Technology, pp. 5186-5194, 2009.

VI. Hueto, F., Hokka, M., Sancho, R., Rämö, J., Östman, K., Galvez, F., & Kuokkala, V-T. (2017): “High Temperature Dynamic Tension Behavior of Titanium Tested with Two Different Methods”, Procedia Engineering, 197, 130-139, 2017.

VII. M. Hokka, J. Rämö, A. Mardoukhi, T. Vuoristo, A. Roth and V.-T. Kuokkala: “Effects of microstructure on the dynamic strain aging in ferritic-pearlitic steels”, Journal of Dynamic behavior of materials (2018). https://doi.org/10.1007/s40870-018-0169-z.

Author's Contribution

In Publications I and IV, Jari Rämö conducted most of the experimental and numerical work and analysis of the results. He also acted as a co-author in both publications. Publication IV was used also as a part of Heli Nyberg's doctoral thesis in 2011 [1].

In Publication II, Jari Rämö was the main researcher and author, planning and executing the experimental testing and numerical simulations and conducting the analysis of the results.

In Publications III and V, Jari Rämö was the principal researcher, conducting all the experimental and numerical work as well as the development of the testing techniques needed in the validation experiments of the modeling and simulation results. In Publication V, he was the main author and in Publication III a co-author.

In Publication VI, Jari Rämö was part of the team developing the high temperature tension Hopkinson Split Bar facility at TUT and conducting the round-robin testing with it. He acted also as a co-author in the publication. The testing at the Polytechnic University of Madrid were conducted by M.Sc. Francisco Hueto.

In Publication VII, Jari Rämö conducted the experimental testing and primary analysis of the results at the TUT SHPB laboratory and acted as a co-author in the publication.

In the publications, as indicated by the respective author lists, and in the writing of the summary (compendium) part of the thesis manuscript, Professor Veli-Tapani Kuokkala and Assistant Professor Mikko Hokka helped by commenting and correcting the manuscripts.

1 Introduction

A characteristic feature for the testing of almost any material's strength properties is that with increasing strain rate the material's instantaneous resistance to deformation, i.e., its momentary flow stress, also increases [2]. The words 'instantaneous' and 'momentary' refer to the fact that in most of the cases the changes in the material's microstructure, i.e., in its strain hardening behavior, are not, at least markedly, affected by the used strain rate (there is, however, a slight difference for example in the strain rate dependent work hardening behavior between body centered and face centered metals, as will be discussed later on in this thesis). The same phenomenon is, naturally, observed in many industrial processes, such as machining, cold heading, forging, and so forth, as well as in many dynamic events, such as impacts, collisions and explosions. Depending on the case, the strain rate sensitivity of the strength properties can be either beneficial and/or desired, or totally unwanted and even detrimental, as also the cases considered in this thesis will demonstrate. Another important effect related to the deformation taking place at higher strain rates is the deformation-induced heating of the test piece or an actual component [3]. This is because typically a large part of the mechanical work (energy) imparted to the work piece during deformation is converted to heat, which may not be able to dissipate fast enough but rises the deformed object's internal temperature. This can have several possible consequences, such as (at least partly) canceling out the flow stress increase caused by the increased strain rate, affecting the transformation mechanisms such as twinning or martensite formation in the material [4, 5, 6], or increasing the diffusion rate of interstitial atoms and thus affecting for example the dynamic strain aging effect in the material [7].

To determine the material's strain rate sensitivity, several different testing methods are typically employed in different strain rate regimes. At low (or 'quasi-static') strain rates, ordinary mechanical or servo-hydraulic materials testing machines up to the strain rate of ca. 1 s^{-1} can be used. At a little bit higher strain rates, up to some tens per second, special 'high-speed' hydraulic testing systems are sometimes used, but they are often plagued by the problems related to the use of load cells in the measurement of load. The most common method used to measure the material's stress-strain response at high strain rates, typically in the range from a few hundred per second up to ca.

10,000 s^{-1} (or even higher), is the Hopkinson Split Bar technique, also known as the Kolsky Bar technique [8, 9]. There are several different versions and practical implementations of this technique, but basically, they all rely on the generation and detection of elastic stress waves in the so-called stress bars, to which the sample is somehow attached. The Hopkinson Split Bar experiments can also be conducted at different temperatures, ranging from very low (cryogenic) temperatures up to ca. 1000 °C and even above. A detailed description of these techniques will be given in Chapter 4.

One of the challenges in the numerical simulation of technological processes, such as cold heading or nip compression in the paper machine, is that very seldom the stress and strain state of the workpiece, as well as its temperature or rate of deformation, are uniform or constant across the entire volume of the material(s). In fact, the same is true even in the simple samples used in the ordinary laboratory tensile tests, especially if they are conducted at higher speeds. These variations in the local conditions necessitate that for example for the simulations of the processes mentioned above to be meaningful, the properties of the used materials must be known in wide ranges and complex combinations of external (and internal) conditions, which all obviously cannot be experimentally determined. Therefore, the correct numerical modeling of the properties and behavior of materials has turned out to be a crucial factor for example in the finite element modeling and simulation of component or process behavior, as will also be shown in this thesis.

2 Aims of research

The main aim of this study is to develop and utilize enhanced material models for the computation and prediction of strain rate (time) and temperature dependent material behavior in selected applications and processes. For example, in the cold heading application, the results of this thesis are hoped to expedite the FE designing of the forming processes, lead to more precise tool designs, and so forth. In the crusher pressure gauge application, in turn, the aim is to enhance the safety of trial firings by improving the accuracy of pressure measurements. The developed material models are based on the experimental results obtained from the tests conducted at different strain rates and temperatures using various testing techniques and test setups. The material models are applied to finite element modeling and simulation of the selected applications, and their validity is assessed by conducting identical tests both experimentally and numerically. The studied practical applications include the calibration of a crusher type pressure sensor (Publications I and

IV), the behavior of a carbon steel in the cold heading process (Publications III and V), and the viscoelastic behavior of a polymeric coating in the paper machine nip conditions (Publication II). In addition, the dynamic stress-strain response of ferritic-pearlitic steels in dynamic strain aging conditions is studied and modeled (Publication VII), and the dynamic response of titanium as a function of temperature is explored with two different testing methods (Publication VI).

The research question of this thesis can be formulated as follows:

1. how the deteriorating accuracy of the crusher pressure sensor method at increasing gun pressures can be corrected using a materials scientific approach?

2. how the increasing deformation rates and the associated internal heating effects can be best accounted for in the cold heading processes?

3. how to account for the strain rate and temperature dependent mechanical behavior of elastomeric (rubber) materials in paper machine roll coating designing?

4. what kind of effects the dynamic strain aging phenomenon brings about to the high strain rate high temperature response of carbon steels?

To answer these questions, this study uses novel experimental research techniques to facilitate the formulation of proper material models to be used in the numerical simulations of the studied applications or processes, and to validate the obtained results by comparing the experimental (physical) and numerical (simulated) test outcomes. The answers to the research questions, as well as the main scientific contributions of this work, will be presented in Chapter 10, *Summary and research questions revisited.*

3 Time and temperature dependence of material behavior

In crystalline materials, such as metals, plastic deformation is mainly produced by the movement of dislocations (glide, slip), the "easiness" of which manifests itself as the macroscopic strength of the material [2,10]. Movement of dislocations happens by coordinated jumps of individual atoms from one low energy position to the next one. For this, the atoms need energy, which they can get from their own thermal vibrations or from an externally acting mechanical force (in practice a shear stress). The magnitude of the energy of the thermal vibrations depends on temperature, and the distribution of the individual atom's vibration can be described by the Boltzmann's distribution. At a low strain rate, the dislocation, or more specifically the atoms constituting it, have a high probability to possess enough thermal vibration energy to move the atom to the next location with no or minimal external mechanical energy. At higher strain rates, however, the probability for the atom to obtain enough thermal energy decreases as the waiting time for the high enough atomic vibration becomes shorter, which then must be compensated by the increasing use of external mechanical energy. Decreasing temperature has a similar effect on the macroscopic flow stress of the material as increasing strain rate, but now the effect comes from the decreased magnitude of thermal vibrations instead of the decreased waiting time of the atom in front of the glide obstacle, such as the Peierls stress or a sessile dislocation. Figure 1 shows the amount of external (stress) energy at different temperatures needed to surmount the obstacle (slant-shaded areas), i.e., at T_0 (basically 0 K), no thermal energy is available, while at T_3, all the energy needed for surmounting the obstacle is obtained from the thermal vibration energy of the atom.

In addition to the fully thermally surmountable obstacles, such as that described in Fig. 1, some of the obstacles are too 'strong' ('long range') to be affected by the thermal vibration energy, and therefore they are usually called 'athermal'. As seen in Fig. 2, the strength of athermal obstacles is not much affected by the temperature, except through the temperature dependence of the shear modulus, which slightly decreases with increasing temperature. The strength of the thermal ('short range') obstacles, instead, decreases with increasing temperature and increases with increasing strain rate for the reasons explained above. At temperatures T_1 through T_3 in Figs. 1 and 2, all thermal

obstacles can be overcome purely by the thermal energy when the strain rate is low enough. However, with increasing strain rate, the allowed waiting time for the dislocations in front of the obstacles becomes too short, and extra energy is need from the mechanical work, i.e., the observed flow stress of the material increases.

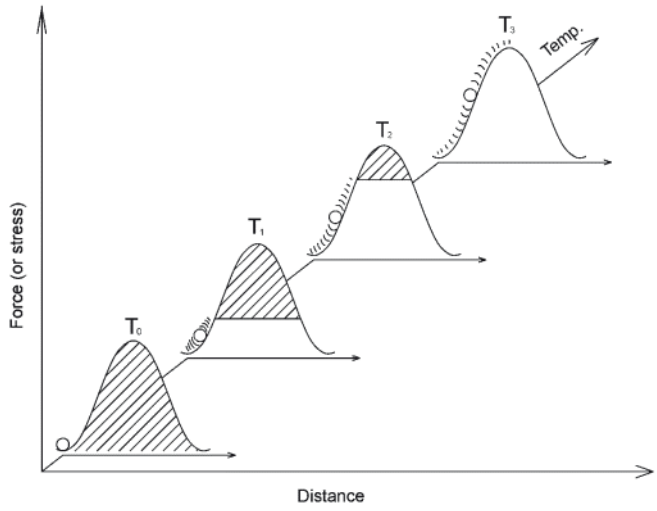

Figure 1. Mechanical and thermal energy used to overcome a thermally activated obstacle at different temperatures. The slant-shaded area represents the mechanical (external) energy and the unshaded area the energy of the thermal vibration of the atom (Publication V).

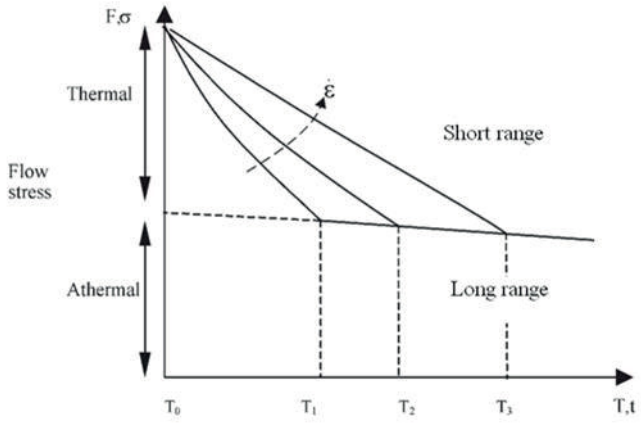

Figure 2. Division of the flow stress to thermally activated and athermal components at different temperatures and strain rates (modified from [10]).

In most cases, plastic deformation is carried out by moving (gliding) dislocations, but sometimes also twinning plays an important role in the deformation and strain hardening behavior of crystalline materials. Internal or external conditions favoring twinning include, for example, shortage of dislocations, high strain rates, low temperatures, bcc crystal structure, and large grain size [11, 12]. Normally, however, twinning may not account for more than ca. 3% of the total plastic deformation of a material or work piece, but it can be a major facilitator of strain hardening, as for example in the case of so-called twinning induced plasticity (TWIP) steels [13].

As already mentioned in the *Introduction*, the strain rate and temperature dependence of the stress-strain response (curves) is somewhat different for the body centered and face centered metals [14]. In addition, compared with the fcc metals, the bcc metals show a large temperature dependence of the yield strength but a small temperature dependence of the rate of strain hardening. For pure bcc metals, the shape of the stress-strain curves obtained at different temperatures and/or different strain rates is practically the same, and the changing strain rate or temperature manifest themselves only as a change in the overall level of the flow stress, as demonstrated in Fig. 3a. The reason for this behavior is that the thermal component of the flow stress is mainly due to the 'lattice friction', commonly referred to as the Peierls stress, which essentially does not depend on the amount of plastic deformation of the material. In the fcc metals, instead, the thermal component of flow stress is primarily due to the interaction of the gliding dislocations with sessile

dislocations on the same or intersecting lattice planes, often referred to as the 'forest' dislocations, the density of which increases with increasing plastic strain [15].

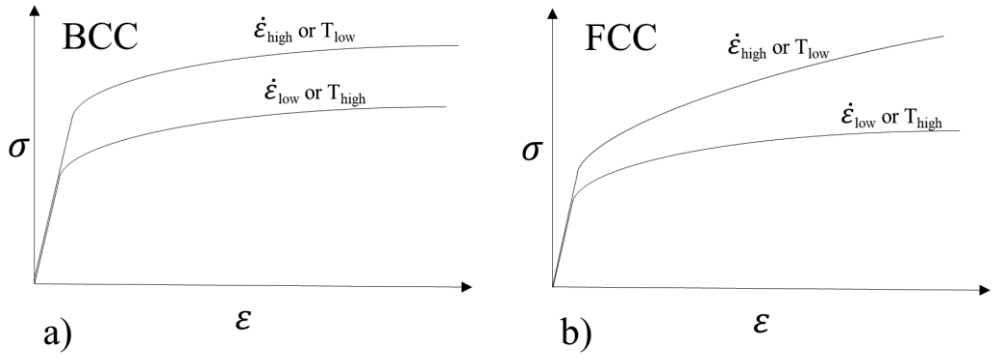

Figure 3. Effects of strain rate and temperature on the stress-strain curves of a) bcc metals and b) fcc metals.

If the strain rate is increased during a tensile test, also the flow stress jumps up, as depicted in Fig. 4 [10]. Correspondingly, if the strain rate is decreased, the flow stress would decrease. Another important aspect that Fig. 4a visualizes is the history effect, i.e., the flow stress at a certain strain rate at a certain amount of plastic strain may depend on the strain rate history, i.e., at which strain rate(s) the material had been deformed to this strain. As we can see, at strain ε_1 the flow stress at the strain rate $\dot{\varepsilon}_2$ is either σ_2 or σ_3, depending at which stage of deformation the strain rate was increased. Again, the fcc and bcc metals show a little bit different type of behavior, as Fig. 4b illustrates: for the bcc metals, the history effect is typically small or even negligible, while the fcc metals in most of the cases exhibit a clear strain rate history dependent behavior.

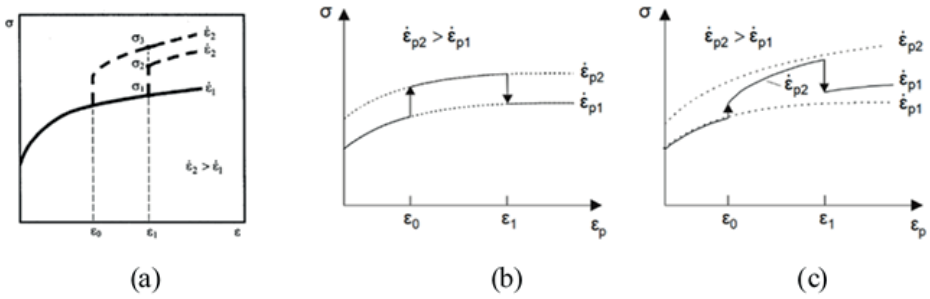

Figure 4. a) effect of strain rate jump on the flow stress, including the 'history effect' (basically in bcc metals) [10], and comparison of the history effects in b) fcc and c) bcc metals [4].

For bcc metals containing also other alloying or impurity elements, such as steels with small carbon atoms residing in the interstitial sites of iron, the increase in the diffusional movement of these alloy atoms may cause a sudden increase in the flow stress at certain strain rate – temperature combinations. In addition, at low strain rates, so-called jerky or serrated flow can be observed, where intermittent load drops 'decorate' the stress-strain curve of the material. Although there are several physical processes that can lead to serrations in the material flow curve, probably the most common and most important of them is the dynamic strain aging (DSA) or the Portevin–Le Chatelier effect [16]. In the DSA effect, small alloy atoms, such as carbon and nitrogen, diffuse into the dislocation cores and minimize the lattice strain energy, temporarily stopping and locking the dislocations in their place. For the dislocation to continue its glide on the slip plane, additional energy is needed to release it from the cloud of the alloy atoms. At higher strain rates, the dynamic strain aging appears at higher temperatures as an increase of strength without evident serrations, and it has been observed for a wide variety of metals and alloys, such as titanium [17], niobium [18], vanadium [19], molybdenum [20, 21], iron [22], and different types of steels [23, 24, 25, 26]. For example, Gilat and Wu [27], who studied the behavior of the 1020 steel at various strain rates in shear, discovered strong dynamic strain aging to occur in the temperature range of 150-550 °C, depending on the strain rate. Nemat-Nasser and Guo [23, 28], in turn, observed strong dynamic strain aging to take place at temperatures between 350 °C and 750 °C in the case of the DH-36 and HSLA-65 steels. In the works of both Gilat and Wu and Nemat-Nasser and Guo, the peak of the dynamic strain aging shifted towards higher temperatures when the strain rate was increased. A common observation related to the occurrence

of dynamic strain aging is also the decrease in the ductility of the steel, as shown for example by Shahriary et al. [24] for the 4340 steel. The decreased ductility in the temperature range of 250-400 °C is commonly known as blue brittleness, and it is generally attributed to the dynamic strain aging phenomenon.

In non-crystalline materials, such as many of the polymers, the time dependence of the mechanical response can be explained by the viscous nature of the deformation mechanisms. In the simplest forms, the viscoplastic and viscoelastic material behavior can be explained by various spring-dashpot models, of which some examples are presented in Fig. 5. In the Maxwell models a) and d), the deformation will be elastic-viscoplastic, i.e., the deformation of the dashpot(s) will not be recovered during unloading, while in the Voigt and Standard linear models, all deformation will be eventually recovered upon unloading [29, 30].

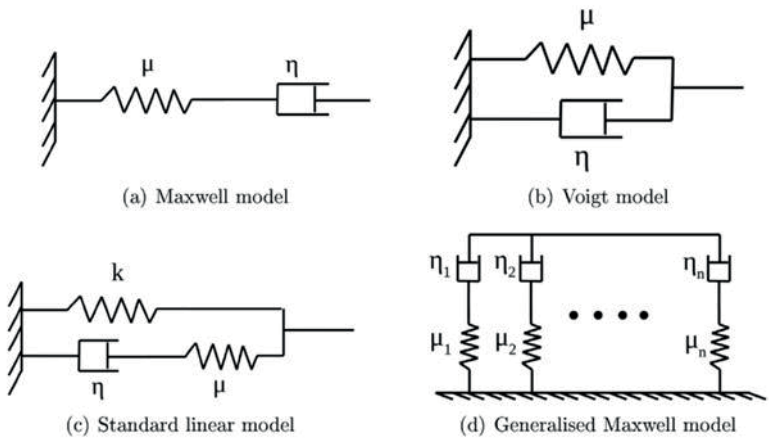

Figure 5. Spring and dashpot-based models of viscoelastic materials [30].

The main difference between elastic and viscoelastic deformation is that while elastic deformation is time independent, i.e., stress and strain are always in the same phase, in viscoelastic deformation there is a time and temperature dependent phase difference (angle) between stress and strain, as shown in Fig. 6. One of the main implications of this difference is that although elastic and viscoelastic deformations are both reversible, viscoelastic deformation dissipates energy while elastic deformation only stores it temporarily but releases all of it upon unloading. This is the main reason why components made of a viscoelastic material, such as rubber tires of vehicles, tend to warm

up during use. Another practical consequence of the time dependence of viscoelastic deformation is that for example during the periodic loading of rotating objects, such as vehicle tires or paper machine rolls, the compressed part of the component may not have time to fully recover before being loaded again. In paper machines, for example, this may lead to a phenomenon known as 'barring' [31].

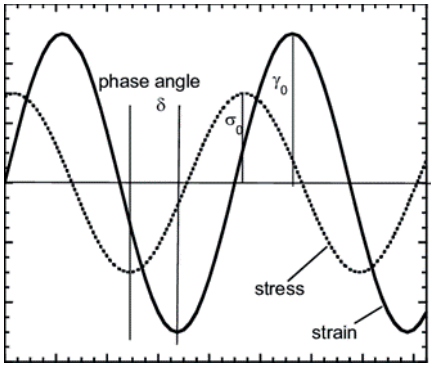

Figure 6. The phase lag occurring in the periodic (sinusoidal) loading of a viscoelastic material [32].

The basic viscoelastic response ('stiffness') of polymers can be described by a few rather simple parameters, i.e., the storage modulus, the loss modulus, and the loss factor [29], which all can be determined for example from a cyclic loading test such as that shown in Fig. 6. Increasing loss factor implies increasing viscoelastic behavior. From the Standard linear model depicted in Fig. 5c, we can deduce that the loss factor has its maximum at some intermediate frequency or time scale, because at very low frequencies or long times, the dashpot is able to deform (practically) at the same rate as the springs, i.e., there is no phase shift between the stress and the strain. At high frequencies or very short times, in turn, the time scale is such that the dashpot does not have time to react at all to the stress, i.e., only the springs are elastically strained in phase with the stress. From the stiffness point of view, this means that in the intermediate (viscoelastic) frequency/time regime the material becomes increasingly stiffer with increasing frequency or shortening time scale. Another important feature of viscoelastic materials is the time-temperature equivalence, also known as the time-temperature superposition [33], which relates the time (or strain rate) and temperature sensitivity of the viscoelastic material behavior. In its simplest form that means that the viscoelastic behavior exhibited by the material at one temperature can be

obtained at another temperature simply by changing the time scale, i.e., the frequency or strain rate.

4 Testing techniques for the determination of strain rate (time) dependent material behavior

Determination of the mechanical properties of materials can be performed with a wide variety of testing devices and testing techniques. In this work, the main division between them is done based on the required strain rate and temperature. For testing at quasi-static (low) strain rates, so-called universal mechanical and servo-hydraulic materials testing devices are used in the strain rate range from very low (10^{-6} s^{-1} or so) up to ca. 1 s^{-1}. At such strain rates, the measurement of load (or stress) can be done conveniently and accurately with commercially available load cells. The so-called high-speed servo-hydraulic testing machines can reach strain rates up to some tens per second, but their common problem is in the accurate determination of the load because of the interfering vibrations inside the load cells at such testing conditions. This problem, however, can be circumvented by combining a fast servo-hydraulic actuator with a long stress bar-type 'load cell', as done at the Dynamic Mechanics of Materials Laboratory of The Ohio State University [34]. For the actual high strain rate testing (starting from ca. 200 s^{-1}), the most commonly used device is the Hopkinson Split Bar (HSB) device, also known as the Split Hopkinson Pressure Bar (SHPB) or the Kolsky Bar. The viscoelastic properties, such as the storage and loss moduli as well as the loss factor of polymeric materials, in turn, can be determined, in addition to common servo-hydraulic materials testing machines, by the dynamic mechanical analyzer (DMA) and dynamic mechanical thermal analyzer (DMTA) devices.

4.1 Hopkinson Split Bar technique

The Hopkinson Split Bar (HSB) technique is used to measure the stress-strain response of materials at high strain rates, typically in the range of $2x10^2...10^4$ s^{-1}. The HSB method is based on the propagation of one-dimensional elastic pressure waves in solid slender bars. A schematic illustration of the compressive HSB technique, the data acquisition setup, and an example of the recorded signals is shown in Figure 7 [35].

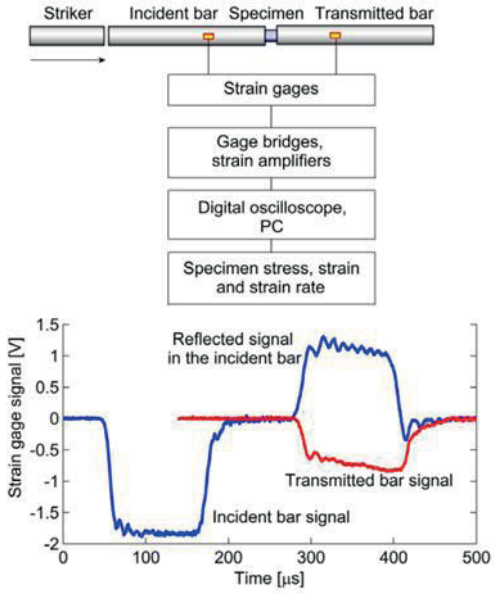

Figure 7. Construction of a compression Hopkinson Split Bar apparatus [35].

When the striker bar, accelerated to a velocity ranging from a few meters up to some tens of meters per second hits the front end of the incident bar, a compressive stress wave is generated and propagates in the bar at the velocity of sound (about 5100 m/s in steel) until it reaches the interface between the incident bar and the specimen. Due to the impedance mismatch at the interface, part of the stress wave is reflected back as a pulse of tension, while the remaining part of the incident pulse is transmitted through the specimen to the transmitted bar. The three generated stress pulses are recorded by strain gages bonded on the surfaces of the incident and transmitted stress bars (see Fig. 7). The average stress, strain, and strain rate in the specimen are calculated from the measured strain signals using Equations 1-3 (the so-called 1-wave solution) [9, 36].

Average engineering stress in the specimen: $\sigma(t) = \frac{A_b E \varepsilon_t(t)}{A_s}$ (1)

Average engineering strain in the specimen: $\varepsilon(t) = \frac{2C_0}{L_s}\int_0^t \varepsilon_r(t)\,dt$ (2)

Average engineering strain rate in the specimen: $\dot{\varepsilon} = \frac{2C_0\varepsilon_r(t)}{L_s}$ (3)

where A_b is the cross-sectional area of the bars and E and C_0 the Young's modulus and the elastic wave speed of the bar material, respectively. L_s and A_s are the length and the cross-sectional area of the specimen. $\varepsilon_r(t)$, and $\varepsilon_t(t)$ are the reflected and transmitted axial strains measured in the incident and transmitted bars as a function of time. In addition to Eqns. 1-3, it is possible to use equations that include also the incident stress pulse (the so-called 3-wave solution), which also enables the calculation of the stress at both end surfaces of the specimen and the assessment of the stress equilibrium in the specimen, which is an essential prerequisite for the correct use of the above equations.

Because the stress pulses are in practice composed of wave components of different frequencies, which travel in the bars at different velocities, the resulting dispersion of the stress pulses is usually corrected for, for example using the technique proposed by Gorham in 1983 [37]. In practice, the dispersion correction is performed by making use of the Fourier transform, i.e., by making the appropriate phase shifts in the frequency domain for each frequency component, and then getting back to the time domain with an inverse Fourier transform. The outcome of the dispersion correction procedure is that the stress pulses, which for practical reasons are measured some distance away from the specimen, will be 'virtually' moved to the bar-specimen interfaces. An example of the original and dispersion corrected incident and reflected signals is given in Fig. 8 [35], showing that a) the incident signal is moved forward in time (i.e., it was measured 'too early'), b) the reflected signal is moved backward in time (i.e., it was measured 'too late'), and c) the oscillations in the signals, caused primarily by the mechanics of the measurement technique, are after the correction more or less in phase with each other. It should be emphasized that the mechanical oscillations, such as those seen in Fig. 8, have nothing to do with the specimen, as they appear also in the incident signal, which is measured much before the pulse 'knows' that it is going to hit the specimen. From the stress-strain curve point of view, it is of course important that the dispersion correction is done also for the transmitted signal, from which alone the stress in the specimen is calculated in the 1-wave solution. Basically, when the mechanical oscillations appear in the reflected and transmitted signals in phase, the oscillation in the stress-strain curve takes place more along the curve than perpendicular to it, making the curve look much smoother than it would be without the dispersion corrections. The mathematical procedure of dispersion correction is explained in detail for example in [35].

Another (direct) way to reduce the oscillations in the stress pulses is to use a so-called shaper between the striker and the incident bar to smoothen the contact and to better control (decrease) the pulse rise time. The shaper is usually a thin disk made of a soft deformable material, such as annealed pure copper, although also other materials may be used depending on the required pulse shape and the actual construction of the testing device itself [38].

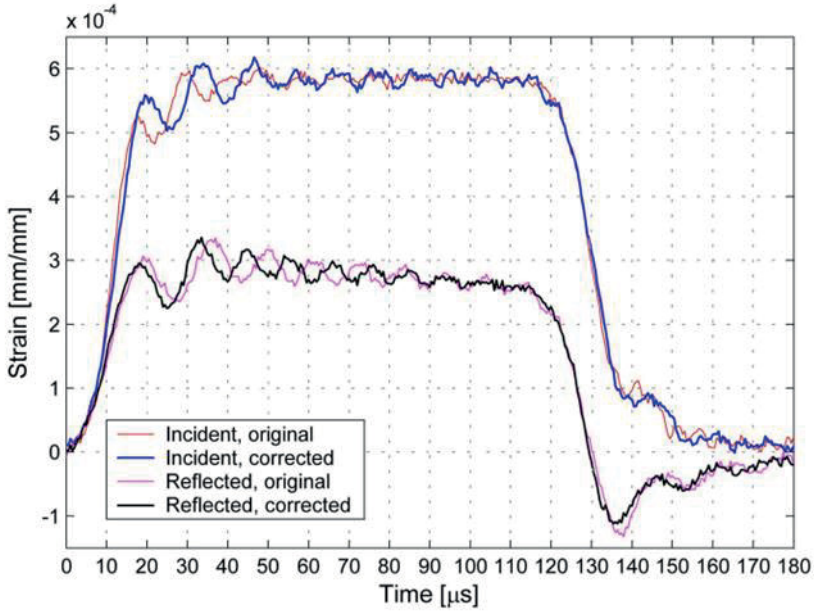

Figure 8. Effect of dispersion correction on the incident and reflected signals in an HSB test (sign of the incident pulse is reversed) [35].

What is said above applies to the compressive version of the Hopkinson Split Bar device, but also other versions, such as tensile and torsional Hopkinson bar devices, are used in many high strain rate research laboratories. The tensile Hopkinson bar device (T-HSB) differs from the compression device in two major respects: 1) the specimen must be permanently fixed to the bars prior to the impact (in the compression bar, the specimen normally stays between the bars simply by friction), and 2) the stress wave is produced by shooting a striker away from the specimen instead of towards the free end of the incident bar. Because of the first difference, the specimen cannot be manipulated anymore during or just before (in a very short time scale) the impact, which sets limitations for example for the high temperature testing with the T-HSB. The second difference means that we must apply some sort of a

preloading/clamping/release system on the incident bar to create the tensile stress pulse or use a tube striker placed around the incident bar with a flange at the far end to stop the striker. Otherwise, basically, the tensile Hopkinson Split Bar device works in the same manner as the compression bar, including the manipulation of the stress waves and calculation of the stress, strain, and strain rate in the sample. Fig. 9 shows schematically the construction of tensile Hopkinson bars using the incident bar preloading technique and the tube striker technique [39, 40].

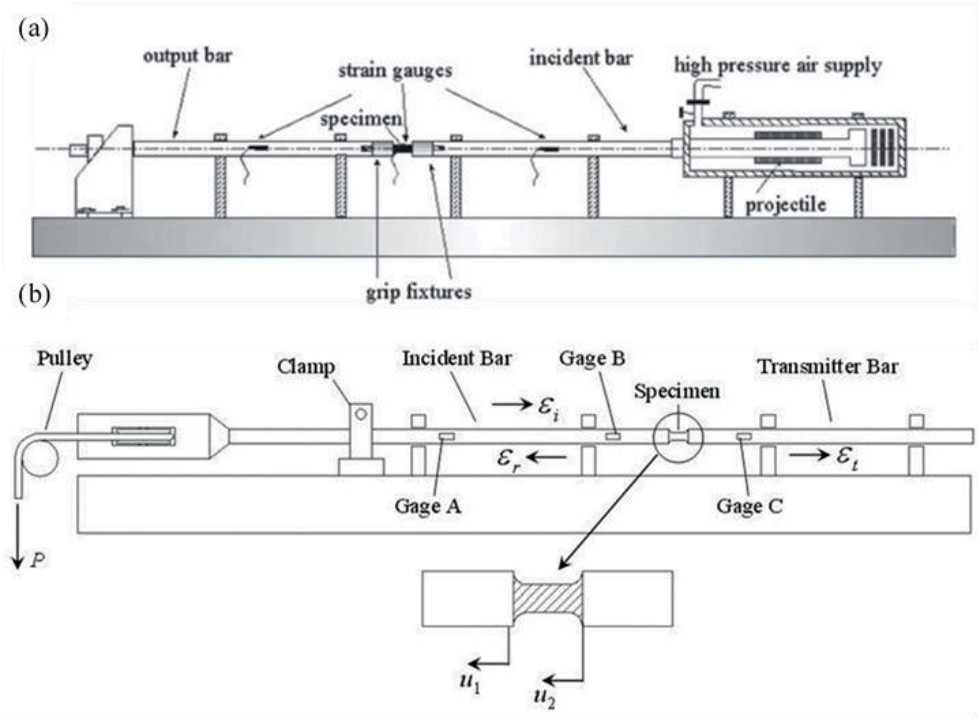

Figure 9. Tensile Hopkinson bar constructions, a) based on the use of a tube striker [40] and b) based on the preloading of the incident bar [39].

There are many ways to fix the specimen into the stress bars of the T-HSB device but, basically, they can be divided into two main categories: mechanical clamping and gluing (or a combination of them). In mechanical clamping, using for example a bolt going through the bar and the specimen grip section, or some kind of a threaded adaptor that is either glued or further mechanically fixed to the bar end, the main issue often is that the extra parts easily distort the propagating stress wave, which also shows in the final stress-

strain curve. On the other hand, use of an adhesive (glue) to fix the specimen to the loading bars does not always work well enough, as the strength of most adhesives is usually much less that the strength of the specimen to be tested. Therefore, for example, the glue sections of the specimen must be much larger than the load carrying cross section of the gage length, which is not always too convenient. Also, in non-ambient conditions (usually above RT but in some cases also below it), the strength of the organic adhesives drops significantly more than the strength properties of the specimen, and therefore the highest test temperature of glued specimens in usually limited to a few hundred degrees centigrade (at low temperatures, also the brittleness of the adhesive tends to become a problem) [41]. The issues related to the high/low temperature testing with tensile HSB will be discussed in more detail below.

4.2 Specimen recovery in Hopkinson Split Bar testing

One of the problems related to the Hopkinson bar testing is that unless something is done, the specimen tends to be loaded multiple times during the test due to the back-and-forth traveling waves reflecting from the free ends of the bars. From the stress-strain curve point of view, however, this is not a problem because the curve is determined from the first reflected and transmitted pulses (if we use the 1-wave equations), but if we wish to preserve the sample for example for microstructural examinations, we must have some kind of a system to protect the specimen from multiple loadings. In some cases, the amplitudes of the reflected waves are so low that they cannot anymore deform the specimen, in which case no other protective measures are needed. If, however, also the reflected waves are of high amplitude, there are several ways how we can 'save' the specimen [42]. In the compression test, the simplest way is to use a 'stopper ring' around the specimen to carry the load after the specimen has shortened to the length of the stopper ring, in which case the original length of the specimen and the stopper ring must be selected so that when the desired amount of specimen deformation is reached, it has the same length as the stopper ring (which, of course, must be built such that it does not deform under the test conditions).

Other specimen recovery techniques are usually much more complex than the stopper ring technique and based of somehow 'trapping' all stress waves following the initial incident, reflected and transmitted waves. There are many variations of these techniques, and they are usually also slightly different for the compressive and tensile Hopkinson Split Bar tests. Figure 10 shows schematically two examples of specimen recovery systems used in high strain

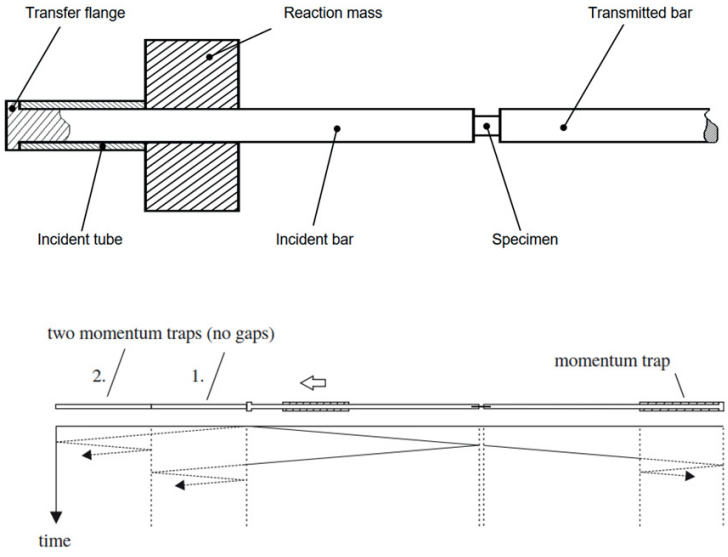

rate compression and tensile testing, respectively [43, 44].

Figure 10. Specimen recovery ('momentum trap') systems used with a) compressive and b) tensile HSB devices [43, 44].

4.3 Strain rate jump tests

The strain rate sensitivity of materials is usually studied by conducting mechanical material tests in compression or in tension and by plotting the flow stress as a function of the logarithmic strain rate at constant plastic strains. Another possibility is to conduct strain rate jump tests, i.e., to change the strain rate abruptly during the tensile or compression test. In the quasi-static regime this is usually a quite easy task, as the servo-hydraulic testing machines are capable of sudden piston speed increments or decrements. In the high strain rate region where the Hopkinson bar technique is the commonly used testing

technique, making a sudden strain rate change in the time scale of microseconds is, however, not so easy and requires special test arrangements. Also, the relative changes in the strain rate must usually be quite notable for observable differences in the flow stress to occur, which are not so easy to arrange with the Hopkinson bar setup [45].

Fig. 11 shows an example of a strain rate jump arrangement built into a conventional tensile Hopkinson bar setup. The basic difference between the setups in Figs. 10b and 11 is that while in the specimen recovery setup there is no gap between the incident bar and the first momentum trap bar, in the strain rate jump setup there is a small (typically of the order of 1 mm) gap between the incident bar end and the momentum trap bar [4]. The idea in the latter is that while the deformation in the specimen increases, the free end of the incident bar moves to the left in Figure 11 until it makes contact with the momentum trap bar. From that moment on, part of the compression stress (wave) enters the trap bar as shown schematically in Fig. 12 and the amplitude of the reflected tension wave drops, as shown in Fig. 13a. As seen in Fig.13b, in this test the strain rate drops from ca. 1000 s^{-1} to ca. 400 s^{-1} due to the use of the strain rate drop system in front of the Hopkinson bar setup.

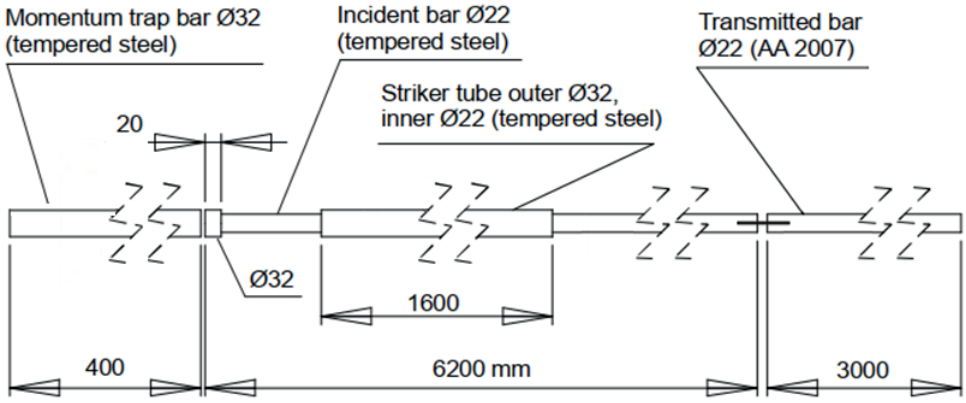

Figure 11. Realization of a strain rate jump test with a tensile Hopkinson bar system including a momentum trap bar placed in front of the far end of the incident bar at a preset distance (gap) [4].

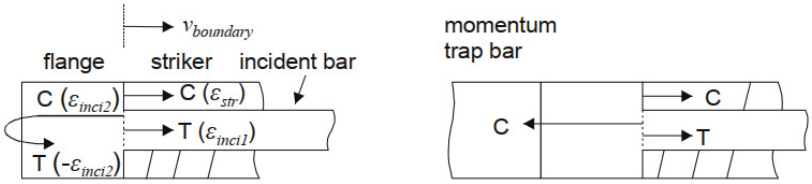

Figure 12. Wave propagation in and out of the flange without and with the momentum trap [4].

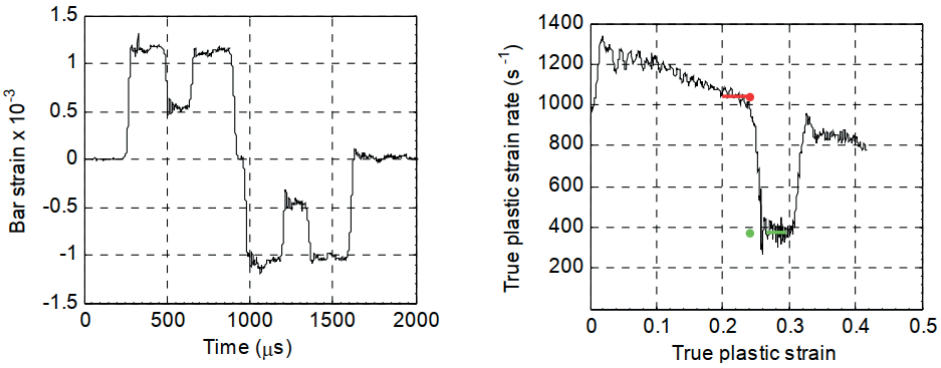

Figure 13. Changes in the incident stress pulse (a) and in the strain rate (b) during a strain rate jump test with a tensile Hopkinson bar device [4].

4.4 HSB testing at non-room temperatures

Split Hopkinson Bar devices can be used for testing of materials also at different temperatures. There are basically two different ways how a test can be carried out at a lowered or elevated temperature; 1) the specimen and short sections of the incident and transmitted bars are heated/cooled to the test temperature, or 2) only the specimen is heated/cooled and the bars are kept at or close to room temperature at all times [9]. Heating of the bars changes the elastic moduli and density of the bar material, leading to excess dispersion of the elastic stress waves. To compensate for the dispersion, one must either carry out complex numerical analysis of the system or mechanically compensate for the temperature gradients in the bars. The latter, however, requires a set of bars for each test temperature, and is therefore not a convenient method in practice.

In compression testing, the specimen is not physically fixed to the stress bars, and therefore the specimen and the bars can be manipulated before the test until the very moment of the impact. A commonly used method [46, 47] is to enclose the specimen in a furnace placed on the centerline of the bars. During heating of the specimen, the bars are kept outside the furnace to prevent them from heating up. Just before the impact by the striker, the stress bars are pushed into the furnace and the hot sample is pressed gently between the bars. Instead of using an enclosing furnace, the specimen can also be heated using, for example, infrared radiation or induction coil heating. Davoodi et al. [48], for example, used induction heating with a dog bone type sample, as shown in Fig 14a, facilitating relatively short heating-up times of the specimen and relatively long manipulation times for closing the bars without temperature decrease of the sample. The advantages of this method are that the microstructural changes in the specimen can be minimized and the bar manipulation does not necessarily require any additional 'contraptions'. On the other hand, the specimen preparation requires additional machining compared to the normally used simple cylindrical samples, and the stress-strain analysis of the specimen is not as straightforward as with the cylindrical samples. An alternative technique is to manipulate both the specimen and the

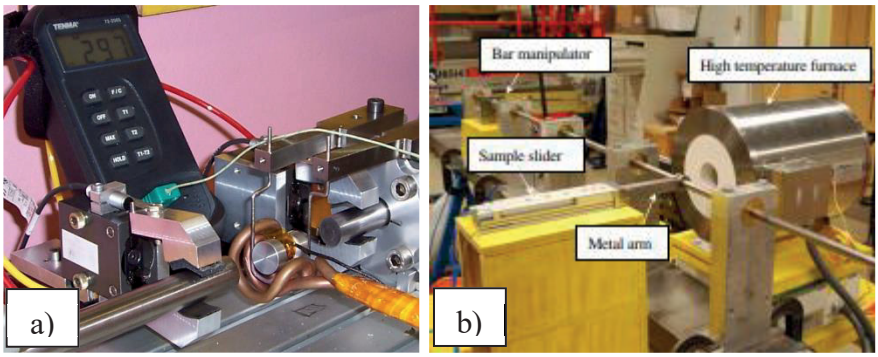

Figure 14. Examples of setups for high temperature HSB testing in compression, a) [48], b) [51].

bars [49, 50, 51]. In this method, the specimen is heated in a furnace located beside the bars. The sample is pushed into the furnace by a sample holder arm, and once the target temperature is reached, the same arm pulls the specimen rapidly to the centerline of the bars. At this point, the hot sample is not yet in contact with the cold bars. A second manipulator pushes the bars into contact with the specimen, again just a fraction of a second before the impact by the striker. Examples of both of the above-mentioned heating methods are presented in Figure 14.

All methods where the bars and the sample are manipulated aim to minimize the time that the hot sample is in contact with the cold bars, often referred to as the Cold Contact Time (CCT). Lennon and Rames [52] studied the effects of CCT on the reliability of the test using finite element methods. They suggested that CCT should be as low as 5 ms for the test to be valid. However, this conclusion has been challenged afterwards by several researchers. In their original work, Lennon and Ramesh did not consider the case where the specimen surfaces would be 'adiabatic', i.e., that the sample would be (at least partially) thermally isolated from its surroundings. Apostol [43, 49], instead, simulated the heat transfer in the case where the side surfaces of the specimen were protected by an isolating ceramic wool ring as part of the specimen holder, making the heat flow negligible from all but the actual contact (end) surfaces of the specimen with the bars. Their results showed that in 50-100 ms from the contact with the cold bars, the sample was cooled by just a few degrees and only in a very shallow layer of the contact surfaces. Seo et al. [53], in turn, measured the temperature change of a specimen by inserting thermocouples in the sample. According to their results, the sample actually cools down rather slowly and the test is valid even up to one second after the initial contact, which sounds like a very long time compared with the results presented by other researchers. However, the maximum allowable cold contact time depends on the temperature difference between the specimen and the bars, or the actual test temperature, the thermal conductivity and heat capacity of the specimen material, as well as the physical size of the specimen. Ideally, the cold contact time should be kept as short as possible, but technically it becomes increasingly more difficult to control the movements of the bars and the specimen, if the cold contact time is tried to be kept too short. For example, if the CCT is very short, the bars and the specimen might still be slightly moving or vibrating when the loading pulse arrives, which may appear as noise or oscillations in the measurement signals. Therefore, a practical minimum for the CCT is usually adopted, which is a compromise between the accuracy and constancy of temperature control and the repeatability and quality of the obtained stress pulses.

In tension testing with the Hopkinson Split Bar device, the sample must be physically attached to the bars, and no manipulation of the bars nor the specimen can be done after that. The specimen is typically attached to the stress bars using adhesive bonding or mechanical fixtures such as pins, wedges, or threads. The mechanical fixing allows heating of the specimen to high temperatures, but on the other hand, the mechanical fixtures can affect the quality of the measured stress pulses [Publication VI]. Gluing of the sample to the stress bars is slower, and either limits the temperature range to only 200-300 centigrade [54] or requires very fast heating rates [Publication VI]. If the sample is heated fast enough, the adhesive bonding may stay strong enough to carry the load during the high strain rate test. Fig. 15 shows a few heating methods used with the tensile Hopkinson Split Bar apparatuses.

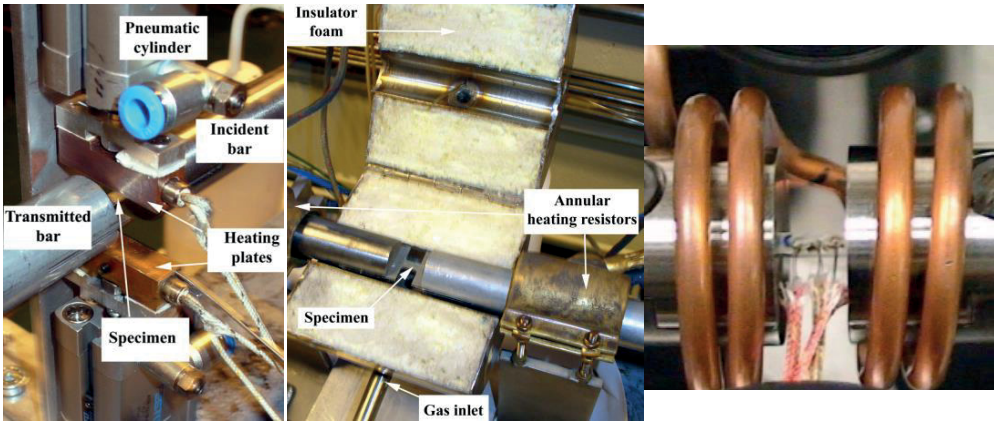

Figure 15. Examples of methods for heating/cooling of the specimen in tensile Hopkinson bar testing. a) [41], b) [50].

5 Modeling of time and temperature dependent material behavior

There are several reasons why modeling of material behavior has become an important and integral part of materials research. On one hand, experimental testing of material behavior at all conceivable regions or combinations of parameters may not be practical or possible at all, and therefore modeling can extend our data and/or understanding of the material behavior to such areas. On the other hand, simulation of material or process behavior by finite element methods has matured to such a level that in many cases the only limiting factor

in these activities is how to describe and implement the material behavior and properties in a correct manner.

When developing material models, one of the most important tasks is to first select the right variables for the model and then to describe their dependence on internal and external factors and conditions, as well as their possible interdependencies, in a correct manner. In other words, we need to select the correct state variables, state equations, and evolution equations [55]. For the plastic deformation of materials, for example, the commonly used state variables are true strain, true strain rate, and temperature. Then, the true flow stress of a material can be expressed as:

$$\sigma = f(\varepsilon, \dot{\varepsilon}, T) \tag{4}$$

However, as plastic deformation is a path dependent process, strain is not always a good choice for a state variable [56], since the microstructure at a certain strain can be quite different depending for example on the deformation temperature and strain rate under which the strain was achieved, as seen for example in Figs. 3 and 4. On the other hand, the use of plastic strain as a state variable is quite understandable, as it can be easily and reliably determined during the mechanical material testing, while the in-situ determination and quantification of the microstructure is very difficult or close to impossible in most of the cases (even unambiguous 'post mortem' determination and quantification of the microstructure is very difficult, even though there are many microscopic and other techniques available to attempt to do so).

What is expected from a good (mechanical) material model is that it should be able to describe the most important properties of the material and to reproduce its response to various external and internal variables, such as the mode, rate, and temperature of the loading, evolution of the microstructure, as well as to take account of the strain rate history and temperature dependence of the flow stress and strain hardening. However, to cover all those aspects accurately has in many cases turned out to be an impossible task, and therefore the material models contain practically always some simplifications or intentional omissions of factors that are considered insignificant or negligible for the task. Nevertheless, it can be safely stated that many of the current modeling and simulation exercises related to materials science, or use of materials in general, have provided a lot of new information and new possibilities that could not have been otherwise easily obtained. There are many approaches to the modeling of the mechanical behavior of materials, starting from *ab initio* or *'first principles'* and ending at the physical or numerical modeling of entire large structures. Depending on the modeling scheme, the parameters and

variables of the models are related to the real world to different degrees, i.e., some of them may have a clear physical meaning (such as the elastic constants, for example), while some others could be mere fitting parameters to make the modeled function fit the experimental data points. The quite widely used phenomenological material models often contain both kinds of variables and parameters, some of them having at least some kind of a physical background, but in general they usually are still closer to 'curve-fitting' type models. In the following, some examples of both phenomenological as well as (more) physically based models describing the strain rate and temperature dependence of material behavior are given.

Probably the most commonly used phenomenological model describing the strain rate and temperature dependent behavior of materials is the one presented originally by Johnson and Cook in 1983 [57]. The model presents the material's flow stress, σ, as a multiplication of three terms, the strain hardening term, the strain rate term, and the temperature term:

$$\sigma = (A + B\varepsilon^n)\left(1 + C_{JC} ln \frac{\dot{\varepsilon}}{\dot{\varepsilon}_{ref}}\right)\left(1 - \left[\frac{T - T_{ref}}{T_m - T_{ref}}\right]^m\right) \quad (5)$$

where ε is true plastic strain, A, B, n, and C are material constants, which are experimentally determined at the reference temperature T_{ref} and the reference true strain rate $\dot{\varepsilon}_{ref}$. T and T_m are the current and melting temperature of the material, and m is a constant describing the strength of thermal softening. For the determination of m, experiments must be conducted also at different temperatures. The first term in the parenthesis is the common parabolic strain hardening equation, also known as the Ludwik's equation, which describes the flow stress and the strain hardening behavior of the material as a function of plastic straining. Parameter A is the initial yield strength of the material, B is a material constant corresponding to the amount of strain hardening of the material at the strain of one, and n is the strain hardening coefficient of the material. The second term accounts for the strain rate dependence of the flow stress through a logarithmic relation, which has been observed for almost all materials and can also be derived from the theory of thermally activated dislocation motion in metals [2]. The last term describes the temperature dependence of the flow stress.

One of the strengths of the Johnson-Cook model is that since its introduction in 1983, its parameters have been experimentally determined and are freely available for a wide variety of materials. The model itself, however, has some clear drawbacks and limitations. For example, if the material exhibits positive

strain rate sensitivity, as most materials do, the model implies that also the material's strain hardening rate increases, which is not necessarily true [10]. Another common issue is that when the strain rate is increased to the region where thermally activated dislocation motion is not any more the rate controlling mechanism and the slope of the flow stress vs. logarithmic strain rate curve has a clear and often rather sharp upturn, the model predictions start to deviate significantly from the experimental data. Because of that, instead of one set of model parameters, two different sets may be needed to cover both the thermal activation as well as viscous drag controlled strain rate regimes. Also, the temperature term quite often does not work properly, partly because the exponent m is expected to be constant over the entire temperature and strain rate regions, which appears not to be true in many cases. Because of this, many modifications to the temperature term have been presented over the years to improve the accuracy of the model [58, 62].

There are also certain features in the material behavior that the JC model cannot capture at all, such as a sharp yield point, possibly followed by the so-called Lüder's strain, which are common features for many of the steels (Publication V). Also the effect of dynamic strain aging, which may lead to a notable increase in the flow stress with increasing temperature, cannot be described with the JC model (Publication V and VII). The general problem (or 'characteristic') of the JC model is that it consists of three multiplicative terms, accounting for the effects of strain, strain rate, and temperature, respectively. That leads to an inevitable interdependence between the effects of these main variables, which does not always lead to a correct end results when the model is utilized, as shown for example in Publication I.

Despite the limitations presented above, the Johnson-Cook model has proven quite useful especially in many practical applications, where only limited ranges of temperature and strain rate are of interest (Publication VI), and therefore it is included in many finite element codes by default. In addition to the original Johnson-Cook model, there are many 'modified Johnson-Cook models' presented in the literature with attempts to find remedies for the known general issues of the model, or to better account for certain specific features of certain materials or groups of materials [48, 59, 60, 61, 62, 63].

Another experimental model that quite much resembles the Johnson-Cook model, and can therefore also be classified as a 'modified Johnson-Cook model', was first proposed by Khan and Huang in 1992 [64] and later modified

by Khan and Liang [65], subsequently known as the Khan-Huang-Liang (KHL) model:

$$\sigma = \left[A + B\left(1 - \frac{ln\dot{\varepsilon}}{lnD_0^P}\right)^{n_1} \varepsilon^n\right]\left(\frac{\dot{\varepsilon}}{\dot{\varepsilon}_{ref}}\right)^{C_{KHL}} \left[\frac{T_m - \mathrm{T}}{T_m - T_{ref}}\right]^m \quad (6)$$

Where: n_1, n are constants, D_0^P is upper bound strain rate (e.g. 10^6 s $^{-1}$), others as in eq. (5). The basic difference between the Johnson-Cook and Khan-Huang-Liang models is that in the latter the strain hardening term contains also the strain rate, which means that an increase in the strain rate does not necessarily lead to an increase in the strain hardening rate. In addition, the increase in the flow stress due to the viscous drag effects can be estimated with the help of parameter C_{KHL} in the second term of the model. The temperature term also slightly differs from the original Johnson-Cook model but, in reality, it does not bring about much improvement compared with the Johnson-Cook model.

More physically based material models have been developed for example by Zerilli and Armstrong [66, 67], and by Kocks [68] and Kocks and Follansbee [69]. Both models are based on dislocation mechanics and thermal activation of dislocation glide. The Zerilli-Armstrong model is different for different crystal structures (fcc, bcc, and hcp), basically because the rate controlling mechanisms are different in each of the structures. The model of Kocks and Follansbee, commonly known as the Mechanical Threshold Stress (MTS) model, uses the mechanical threshold stress of the microstructure as a state variable. For this reason, the MTS model can predict the history effects better than most of the other models, but the downside of the MTS model is that it is quite complicated and requires mechanical testing also at subzero temperatures. Despite some added physical background, also the Zerilli-Armstrong and Mechanical Threshold Stress belong to the wide group of continuum-scale models, since even they do not include any true microstructural features in their formulations.

In addition to the above presented examples of general-purpose material models, also pure fitting of mathematical functions to the experimental data can in some cases lead to quite acceptable results. This is especially true when we are considering some specific and well-defined practical problems that we wish to handle numerically for example using finite element methods. There are currently plenty of easy-to-use curve fitting software available. For some of them, the fitting function must first be given (known), after which the software simply finds the optimal values for its coefficients. There is also

software available where the user does not have to know the fitted function in advance, but the software goes through thousands of functions and finds the optimal coefficients for all of them. One of such programs is TableCurve 2D®, the use of which will be demonstrated in one of the case studies presented in the experimental part of this work.

The viscoelastic behavior of polymers, which is caused by the stretching and relative movement of covalently bonded intertwined molecular chains in an amorphous or non-periodically ordered structure, is one of the key issues when modeling the mechanical response of polymeric materials. The exact structure of the polymer affects strongly the stiffness and overall viscoelastic behavior of the material. For example, enhanced cross-linking or copolymerization reduce the mobility of the polymer chains, increasing the stiffness of the material and affecting the time dependence of its mechanical response.

The time dependent behavior of polymers is typically studied with a dynamic mechanical analysis (DMA) or with creep and stress relaxation tests. In the DMA test, the loading amplitude of the sample is usually very small, and therefore also the strain rates remain at a rather low level, typically below 10 s^{-1}. When larger strains and higher strain rates are of interest, a Hopkinson bar device designed for low impedance materials is normally used.

When modeling the strain rate dependent behavior of polymers, the total strain is usually taken as the sum of the elastic, viscoplastic, and viscoelastic strains [29]. The elastic strain is fully recoverable and can be evaluated using the Hooke's law, while the viscoelastic strain is associated with the delayed movement of the polymer chains. The viscoelastic strain can be large especially at temperatures above the glass transition temperature T_g, i.e., in the rubbery region. The modeling of the viscoelastic stress-strain response of polymers is often carried out by making use of the mechanical models already introduced in Chapter 3, including the Kelvin-Voigt, Maxwell, and standard-linear-solid models.

As an example of the modeling schemes applied for the time and temperature dependence of the deformation of polymers, we can briefly examine the widely used model of Eyring [70], who assumed that the deformation of polymers can be expressed as a thermally activated process. For the rate of change of strain, we can write

$$\dot{\varepsilon} = \dot{\varepsilon}_0 exp\left(-\frac{\Delta H}{RT}\right) sinh\left(\frac{v\sigma}{RT}\right) \quad (7)$$

where ΔH is the height of the potential barrier to be surmounted, σ is the applied stress, RT is the available thermal energy, and v is the activation volume for the molecular event. Equation 7 defines an 'activated' viscosity, which is related to the dashpot of the standard linear solid model presented in Fig. 5 and represents the volume of the polymer segment that has to move as a whole for the plastic deformation to occur [29]. For the shear yield stress, further derivation leads to the formula

$$\frac{\sigma}{T} = \frac{R}{v}\left\{\frac{\Delta H}{RT} + ln\frac{2\dot{\varepsilon}}{\dot{\varepsilon}_0}\right\} \quad (8)$$

which plotted as σ/T vs. logarithm of strain rate at a constant temperature should form a straight line. Fig.16 shows the results of Bauwens-Crowet et al. [71] for polycarbonate, indicating that at least in this case the presented model fits the experimental results very well. For more practical work, virtually all finite element software contains linearly elastic, viscoelastic and hyperelastic material models built into the code. The hyperelastic models are sometimes classified into phenomenological models based purely on observed behavior, such as Mooney–Rivlin, Ogden, and Marlow models, and mechanistic models

that include also some structural features of the materials, such as Arruda–Boyce and neo-Hookean models [72].

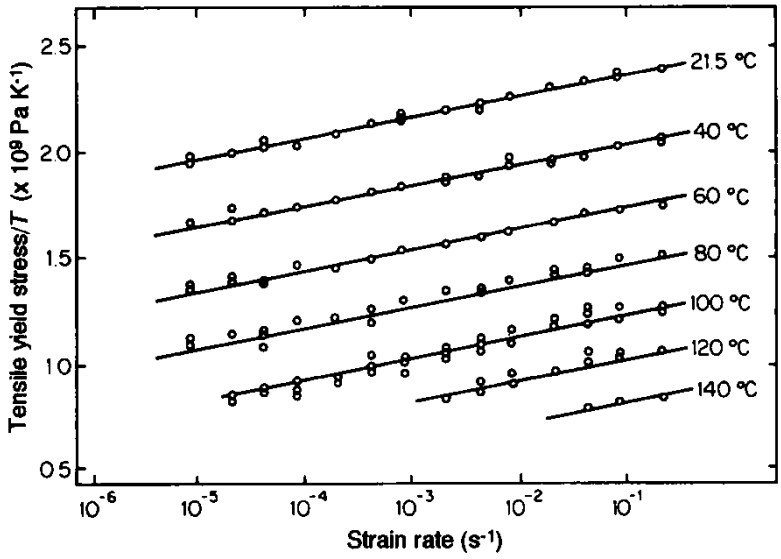

Figure 16. Fitting of experimental data for polycarbonate to the Eyring material model [70]

6 Experimental techniques and materials used in the current work

6.1 Compression Hopkinson Split Bar device

The construction and operation of the compression Hopkinson Split Bar device used in the studies included in this thesis conform to the general principles originally suggested by Bertram Hopkinson [8], i.e., it contains all the basic components described already in Fig. 7. However, as this device, like most of the similar devices used in the high strain rate research laboratories all over the world, has been built by the research group itself, it contains certain features that distinguish it from the other comparable devices. In particular, all the operations in the current device are computer controlled, including loading of the striker, pressurizing of the pressure accumulator, firing of the striker, measuring of the striker speed, etc. Fig. 17 shows schematically the construction and sequence of operations used in a typical compression test with the current device, and Fig. 18 is a photograph of the device, showing also the high temperature auxiliary unit attached to it. The

use of comprehensive computer control has several advantages: 1) it makes operation of the device simple and reliable, 2) it improves the accuracy and repeatability of the tests, and 3) it facilitates the incorporation of auxiliary components and units to the basic device, such as the (also) computer controlled high/low temperature system discussed in more details later on.

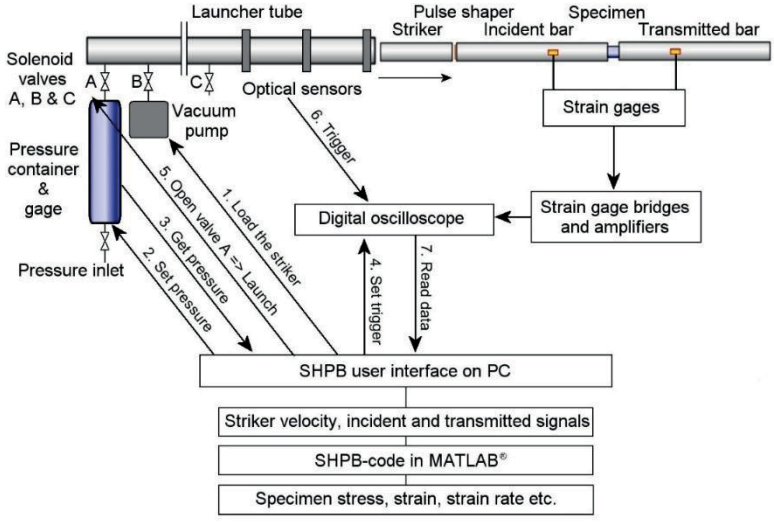

Figure 17. Construction and sequence of operations of the compression Hopkinson Split Bar device used in this work [35].

Figure 18. Photograph of the compressive split Hopkinson pressure bar equipment used in this work.

6.2 Modified Hopkinson Split Bar device

In the Hopkinson Split Bar technique, the strain and strain rate in the specimen are adjusted by varying the speed v_{str} and length L_{str} of the striker, and/or the length l_s of the specimen. When the speed of the striker is increased by increasing the launching pressure, the amplitude of the incident stress pulse (or strain pulse, as the Hooke's law applies) will increase in the same proportion, as $\varepsilon_{bar}=v_{str}/(2\cdot c_{bar})$, where c_{bar} is the speed of sound in the bar material. This, in turn, will lead to a larger extension of the incident bar's end in contact with the specimen, and thus to a larger strain in the specimen. The amount of specimen strain can be approximated as $\varepsilon_s=2\cdot v_{str}\cdot L_{str}/(l_s\cdot c_{bar})$. Because the physical length ($2L_{str}$) and duration ($2L_{str}/c_{bar}$) of the stress pulse created by a particular striker are independent of the striker speed, the strain rate will increase with increasing striker speed only, i.e., $\dot{\varepsilon}_s=v_{str}/l_s$. To summarize the above, the amount of strain depends linearly on both the striker speed and striker length, but the strain rate only on the striker speed. This means that if we, for example, wish to double the strain rate but obtain the same (maximum) amount of strain, we should double the striker's speed but halve its length (assuming that the length of the specimen is not changed). There are, however, practical limits for the striker length and striker speed,

which limits the free adjustment of strain and strain rate independent of each other. For example, as the physical length of the incident stress pulse is twice the length of the striker bar, the required length of the incident bar in the normal case increases accordingly, assuming that we wish to avoid overlapping of the incident and reflected pulses in the incident bar. In practice, the striker bar length should therefore be well under half of the length of the incident bar. A practical limitation for the use of extra-long stress bars often is the limited size of the laboratory space. Therefore, other solutions must usually be sought after if long pulses are needed. Another way to affect the strain and strain rate is to vary the length of the specimen, but as they both depend on the specimen length in a similar (inverse) manner, for example doubling the specimen length would halve both the strain and the strain rate, which may be unwanted.

In certain applications, such as that discussed in Publications I, III and V, extra-large deformations at relatively low strain rates are needed, which means that either the specimen or the stress pulse must be very long, the latter requiring long striker and incident bars. For that reason, in the cold heading studies, an incident bar 1800 mm long and a striker bar 1500 mm (in some tests 'only' 800 mm) long were used. Instead of the normal practice of gluing the strain gages in the midway of the bars, in this case they were glued at the both ends of bar, as shown in Figure 19. This configuration allows the direct measurement of the incident pulse (with SG1), but the reflected pulse will overlap with the incident pulse almost totally. The reflected pulse, however, can be calculated by subtracting the pulse measured at the end of the incident bar (SG2) from the incident pulse measured by the strain gage at the beginning of the bar (SG1). With this test arrangement, it is possible to obtain an adequate combination of a reasonably low strain rate of 500 1/s and a reasonably high strain of 30 %. The quality of the calculated reflected pulse may not be as good as if it was measured directly but, on the other hand, the general quality of longer pulses is usually better than that of short (or 'normal length') pulses, so the small loss of accuracy due to the calculated reflected pulse becomes at least partly compensated in that way.

Figure 19. Positions of the strain gages in the tests of cold heading materials with extra-long strikers (Publication V).

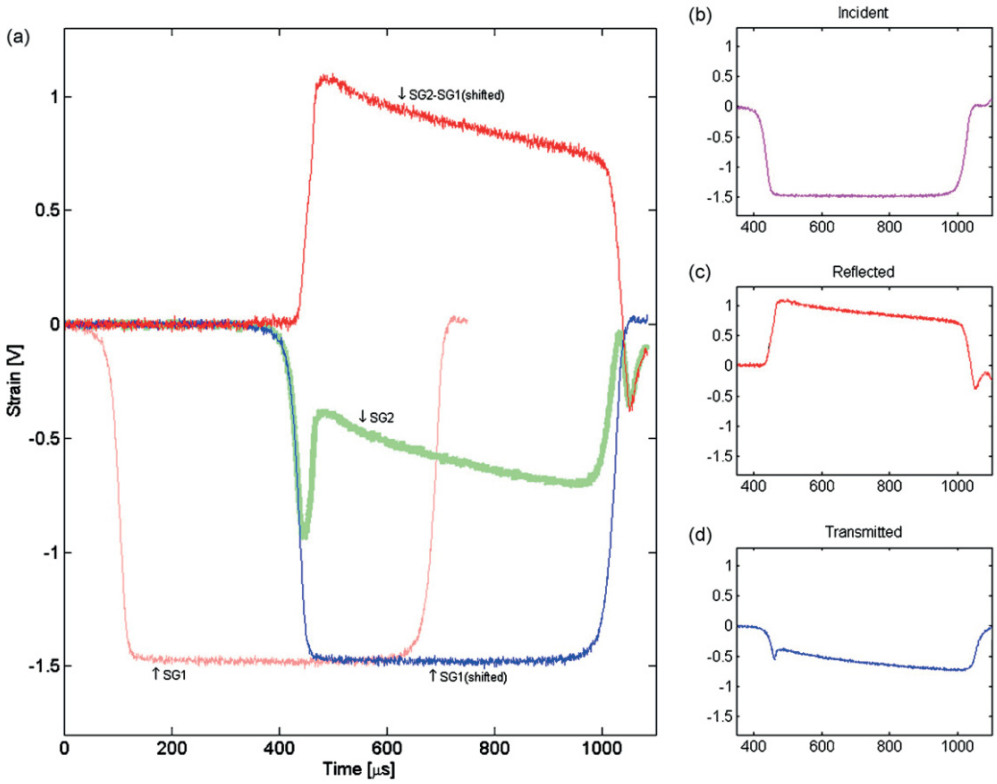

Figure 20. Waves from an HSB test with an extra-long striker bar: (a) incident bar waves recorded at positions SG1 and SG2, the incident bar wave measured at position SG1 and transferred to the same starting point with the wave measured at position SG2, and the reflected wave obtained by subtraction of the wave measured at position SG2 from the wave measured at position SG1, (b–d) the separated incident, transmitted and reflected waves used in further calculations of the specimen's stress–strain relations (Publication V).

In most of the tests discussed in this thesis, the diameter of the stress bars, as well as of the striker bars, was 22 mm. In the crusher pressure sensor studies (Publications I and IV), however, the initial strength of the fully annealed copper samples was so low that the transmitted signals were difficult to detect properly with 22 mm diameter stress bars. Therefore, in those tests, bars of 12 mm in diameter were used instead of the 22 mm bars to increase the transmitted signal output. Otherwise, there was no difference between the tests conducted with 12 mm or 22 mm bars.

6.3 Tension Hopkinson Split Bar device

As discussed earlier, the tensile version of the HSB equipment is based on the same principles as the compressive one. Of the two commonly used versions for generating the tensile stress pulse, in the current work the one with a tube striker, shown schematically in Figure 9a, was used. Fig. 21 shows schematically the construction of the T-HSB device used in this work, and Fig. 22 is a photograph of the actual device. The longest striker tube length used in the current system is 1600 mm, giving the maximum loading pulse duration of ca. 640 µs. Fixing of the (sheet) samples into the bars is done using a cyanoacrylate adhesive, which compared to somewhat stronger epoxies has the benefit of being dissolvable in acetone, which expedites the removal and remounting of the specimens considerably.

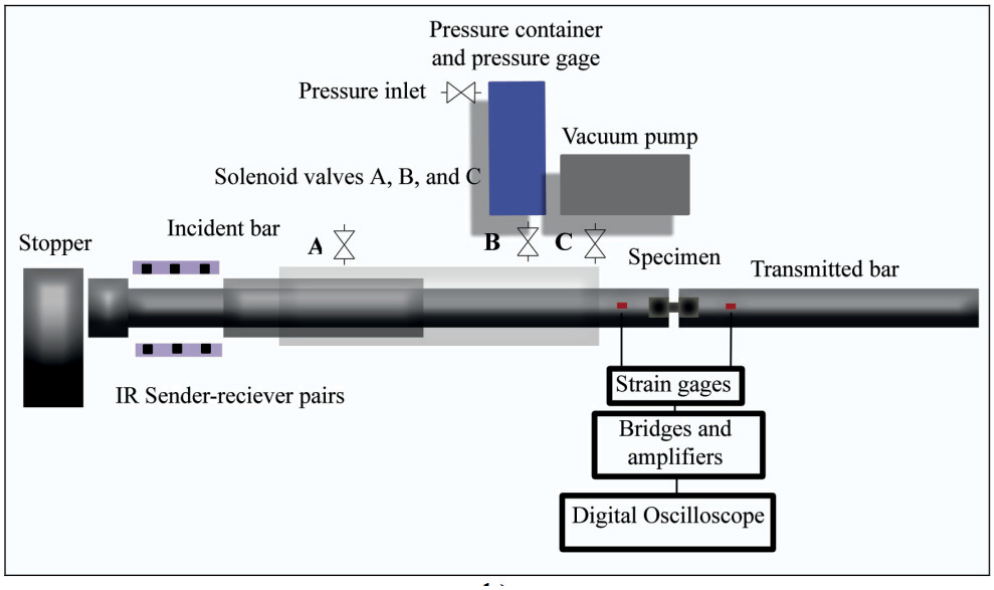

Figure 21. Construction and components of the tensile Hopkinson Split Bar device used in Publication VI.

Figure 22. Photograph of the tensile split Hopkinson pressure bar equipment used in this thesis.

6.4 Universal servo-hydraulic testing machine

All material tests at strain rates of 1 s^{-1} and lower were conducted with a servo-hydraulic Instron 8801 universal materials testing machine. In most of the cases, instead of using the rather heavy hydraulic general-purpose grips of the testing machine, simpler fixtures and hard metal compression platens attached directly to the piston and the load cell were used. Fig. 23 shows an example of such a setup with a furnace and a high temperature extensometer attached to the specimen.

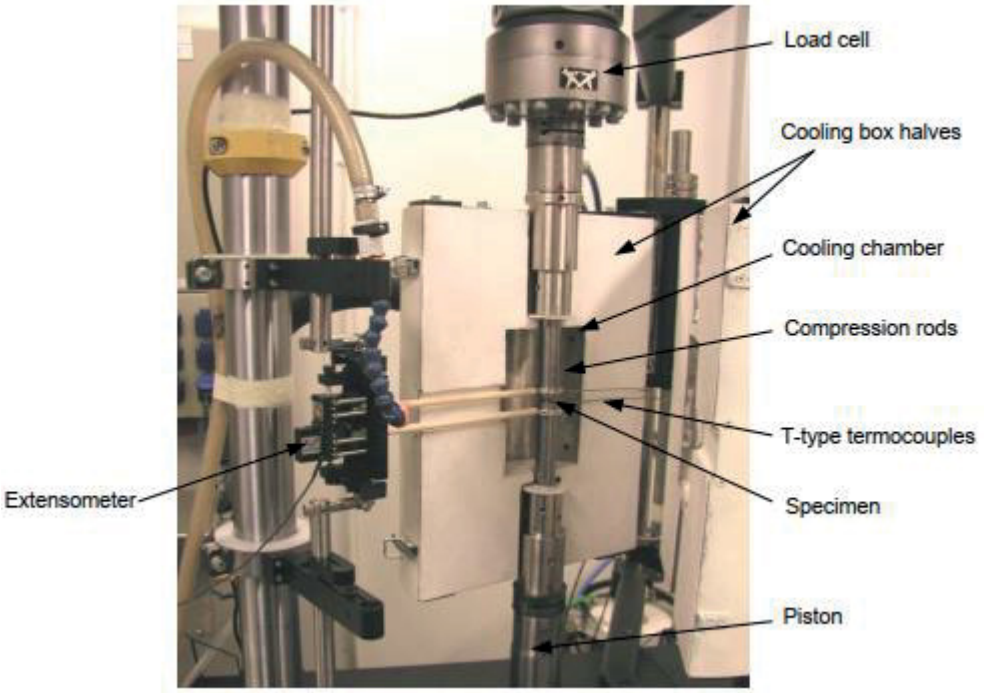

Figure 23. Compression test setup in an Instron 8801 materials testing machine with a furnace and a high temperature extensometer [43].

6.5 Heating systems

In the studies included in this thesis, three different heating systems were employed. In all high strain rate compression tests conducted at non-RT temperatures, the method based on the manipulation of both the specimen and the stress bars and a temperature conditioning unit (furnace or cooling chamber) located beside the bars was used. Figure 14b already showed a picture of the employed system, the components and operation of which are schematically shown in Fig. 24. For testing at temperatures below RT, only the furnace is replaced by a cooling chamber cooled with the controlled flow of cold nitrogen gas. More detailed descriptions of the employed HT/LT testing system can be found in Publication VII and in Ref. [43].

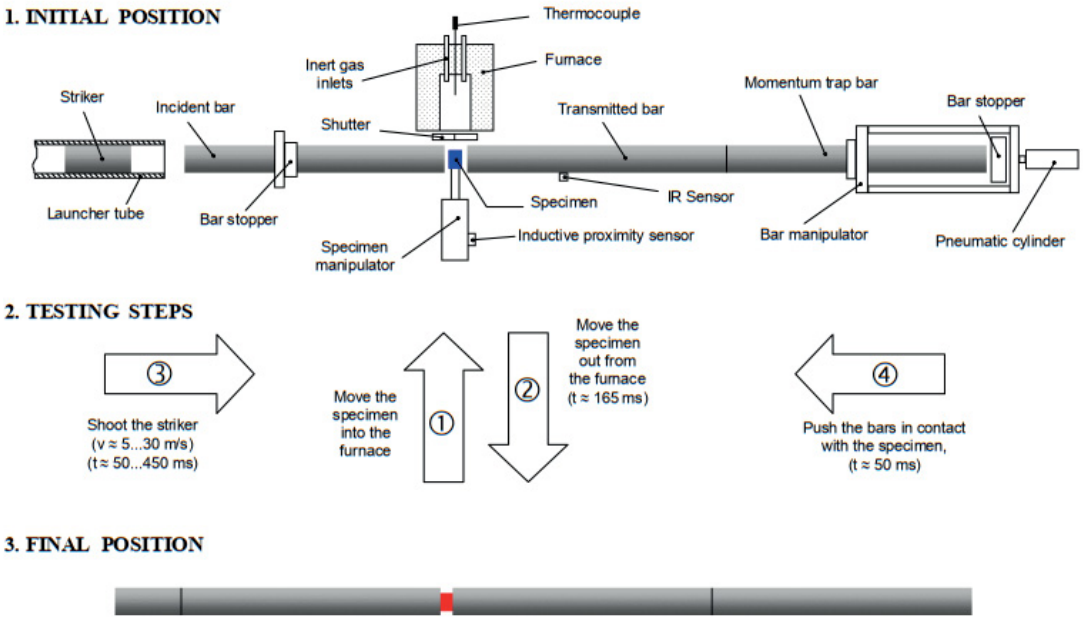

Figure 24. Schematic illustration of the high temperature testing setup incorporated in the compression Hopkinson Split Bar, showing also the testing steps during a test with the system [49].

For high temperature tensile tests, two different heating methods were used and compared with each other. The first method, used at UPM Madrid, is based on a small furnace, where the sample and short sections of the bars are enclosed. The furnace, shown in Figure 25, contains eight resistors, capable of bringing the specimen up to 900 ºC in a few minutes, and bar-size openings at both ends. After heating the sample to the desired temperature, the furnace can be moved to one side of the bars to provide a direct line of sight to the specimen for example for high speed camera recording. More details of the experimental setup and the heating system can be found in Publication VI.

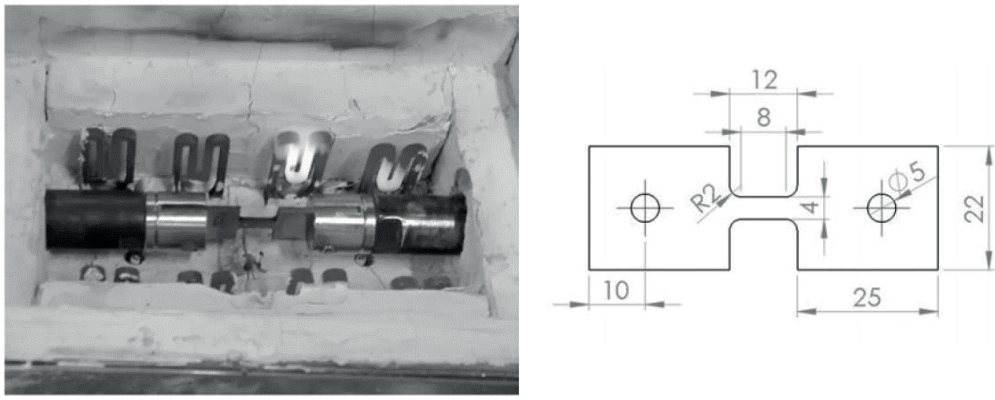

Figure 25. High temperature high strain rate testing of a sheet specimen at UPM Madrid, a) furnace for heating up the specimen and sections of the bars made of a nickel-base superalloy (Rene 41), b) specimen gage length and grip section dimensions (Publication VI)

The second heating system for the tension Hopkinson bar testing, used in the tests conducted for Publication VI at Tampere University (of Technology), is based on direct electric heating, as depicted in Figure 26a. In the method, four small copper electrode pins are moved by a pneumatic actuator in and out of contact with the 'fins' machined to the grip sections of the sample, as shown in Fig. 26b. The electric current is fed though the gage section of the specimen through the pin-fin contact points for rapid heating of the specimen. When the desired temperature has been reached, the pneumatic actuator retracts the electrodes far enough from the specimen (and the bars) to avoid damaging them during the subsequent high-speed test and to allow the use of high-speed imaging of the specimen for further digital image correlation analysis of the sample surface strains.

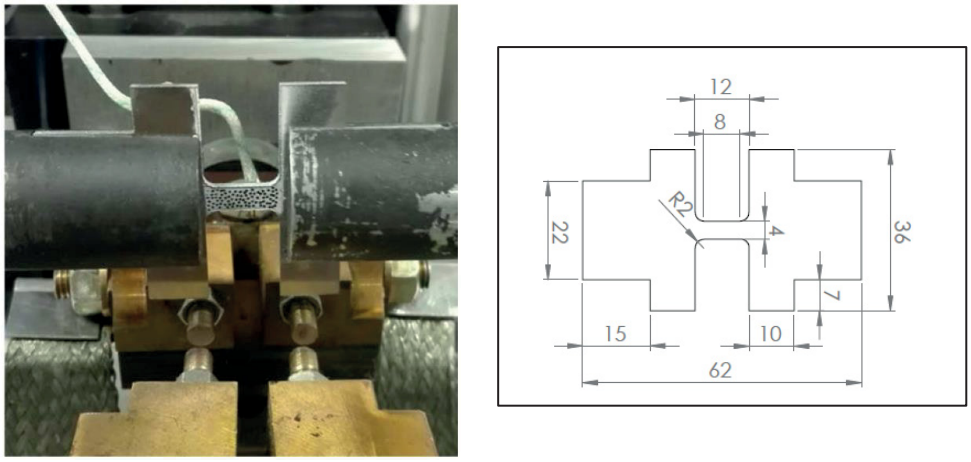

Figure 26. High temperature high strain rate testing of a sheet specimen at TUT Tampere, a) direct heating of the specimen, b) specimen gage length and grip section dimensions (Publication VI).

With direct electric heating, for example the temperature of 800 °C could be achieved in less than half a second, which is good also in regard of the adhesive bonding between the specimen and the stress bars. The downside of the method, however, is that there tends to be substantial deviations between the target temperature and the actual (reached) test temperature, mostly because the contact conditions between the electrodes and the specimen 'fins' may not be exactly the same every time. On the other hand, the true specimen temperature can be measured with a thermocouple spot welded on the specimen surface and/or with a high-speed thermal (infrared) camera, and therefore this is usually not a serious problem or limitation for the method.

7 Materials and tests

Table 1 gives an overview of the materials and mechanical tests conducted in the studies included in this thesis. As seen, most of the tests were conducted in compression, except for the tests on the titanium alloy (Publication VI).

Table 1. Overview of the tests included in this thesis.

Material	Loading	Test methods	Test-Temperatures	Heating/cooling method	Publication
Rubber	Compr.	Hopkinson Bar, Instron	RT, HT	Furnace	II
Copper	Compr.	Hopkinson Bar, Instron	RT only	•	I, IV
Ti6Al4V	Tension	Hopkinson Bar	RT...725 C	Direct electric heating, furnace	VI
C17C	Compr.	Hopkinson Bar, Instron	LT, RT, HT	Furnace, liquid nitrogen cooling	III, V
C45	Compr.	Hopkinson Bar	RT...680 C	Furnace	VII
27MnCr5	Compr.	Hopkinson Bar	RT...680 C	Furnace	VII

The samples used in Publications I and IV were manufactured from oxygen-free high conductivity (OFHC) copper of 99.998% purity. The exact compositions of the two different patches (from different manufacturers) used in the tests can be found in Publications I and IV. The samples were in a fully annealed condition with initial yield strength of ca. 30 MPa.

The material studied in Publication II was a heat, wear, and chemical resistant fully cross-linked rubber material containing also inorganic fillers. This material, with a brand name RayFlex 5000, is commonly used as a cover material in paper machine rolls.

The aim of Publication VII was to study the high temperature high strain rate behavior of two standard alloys, 27MnCr5 and C45, in different heat treatment conditions. The exact chemical compositions of the steels can be found in Table 1 in Publication VII. The studied heat treatment (microstructural)

conditions of both materials were the 'standard' or reference (R) microstructure obtained by austenization annealing followed by isothermal annealing below the austenization temperature, the globular pearlite (GP) structure obtained by adding an additional annealing cycle to the reference heat treatment, the coarse grain (CG) structure produced by increasing the austenization temperature of the steels, and the 'banded structure' (WB) containing pearlite bands that were allowed to grow during slow cooling from the austenization temperature to the subsequent isothermal annealing temperature. Details of the microstructures and their differences are given and discussed in Publication VII.

The cold heading quality steel studied in Publications III and V is used in lower strength grade bolts, screws, and other cold-formed fasteners. The steel is aluminum-killed (de-oxidized) and not intended for any heat treatments such as quenching. The EN 10263 standard designation of the steel is C17C, and its nominal composition and tensile strength values are given in Table 1 in Publications III and V. The microstructure of the steel is ferritic-pearlitic with an average ferrite grain size of about 10 μm.

The primary purpose of the research presented in Publication VI was to compare the test results obtained by two different testing methods, especially related to the heating of the tensile Hopkinson Split Bar specimen to high temperatures. In that sense, the research is not specifically related to the used test material, i.e., Ti6Al4V alloy. The choice of this alloy for the test material is, however, sensible as it retains its good strength properties also at elevated temperatures.

8 Results

As presented in the previous Chapters, the research contained in this thesis focuses on the strain rate dependent behavior of a wide variety of different materials, i.e., pure copper, several steels, a titanium alloy, and a rubber. They all have a different crystal structure and/or microstructure, ranging from the face centered cubic single-phase copper through the body centered crystal structure and varying phase structures of the steels and the hexagonal close packed crystal structure of the titanium alloy to the long-chain crosslinked polymer structure of rubber. The differences in the crystal structures and microstructures of the studied materials are reflected in their mechanical behavior, which has to be accounted for also in the development and use of the material models.

8.1 Cold heading steels (Publications III and V)

The effect of strain rate on the room temperature flow stress of C17C cold heading steel is shown in Figure 27a, where the compressive flow stress is plotted against the logarithmic strain rate at various constant plastic strains. Starting from the low (quasi-static) strain rate region, the strength of the material increases gradually and linearly up to about 500 s^{-1}, after which the rate sensitivity and strength of the material begin to increase at a faster rate. In addition to the tests conducted at room temperature, the compressive strength properties of the C17C steel were determined at the strain rate of 1100 s^{-1} also at temperatures ranging from −150 to 800 °C. The specimens at high and low temperatures could only be compressed to relatively low strains, approximately 20 % of plastic strain, due to the experimental constraints of the test setup. The resulting flow stresses at different temperatures are shown in Fig. 27b at selected constant plastic strains. As can be seen, the flow stresses first decrease in a quite normal manner with increasing temperature, until at higher temperatures the dynamic strain aging effect comes into play and the flow stresses start to increase again. At this strain rate, ca. 1100 s^{-1}, the maximum of the dynamic strain aging effect appears at about 600 °C, but as will be shown later on in this thesis, the temperature at which the peak appears depends also on the applied strain rate.

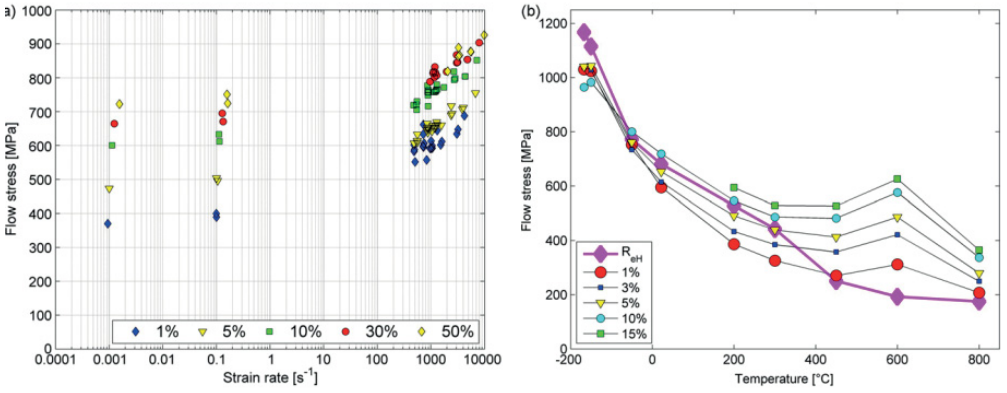

Figure 27. Results of compression tests on the C17C cold heading steel, (a) flow stresses at different constant plastic strains as a function of strain rate at RT, (b) flow stresses at different constant plastic strains as a function of temperature at the strain rate of 1100 s^{-1}. R_{eH} is the yield strength of the material (Publication V).

The experimentally determined mechanical behavior of C17C was also numerically modeled with the objective to simulate the steel's behavior in the cold heading process. The model needed to be simple and accurate enough, as well as easily implementable to the ABAQUS/Explicit FE-software. The selected modeling strategy was to describe the stress-strain response of the steel as precisely as possible, including also the sharp yield point, which is an important feature of the material in regard of the cold heading process. As it is practically impossible (or at least extremely difficult) to describe both the strain hardening behavior occurring at larger plastic strains with the same model (equation) as the sharp yield point, a choice was made to model the full stress-strain response of the material in two parts. Two sets of polynomial functions were chosen to describe the material response, one for the low strain region to describe the sharp yield point behavior, and another one for the high strain region to describe the strain hardening behavior of the material. As seen in Eqns. 9 and 10, both parts describe the flow stress of the material as a function of strain, strain rate, and temperature. The two polynomial models were fitted separately to the data of their respective regions of strain. As the example in Figure 28 shows, the correspondence between the measured and modeled data points is quite good, and therefore the presented equations appear to describe the behavior of the C17C steel well enough to be used in the FE simulations of the cold heading process.

Sharp yield point behavior (part 1):

$$\sigma(\varepsilon, \dot{\varepsilon}, T) = \sum_{i=1}^{3} a_i \varepsilon^i + b \ln(\dot{\varepsilon}) + \sum_{j=1}^{3} c_j T^j + d \tag{9}$$

Strain hardening behavior (part 2):

$$\sigma(\varepsilon, \dot{\varepsilon}, T) = \sum_{i=1}^{5} e_i \varepsilon^i + \sum_{j=1}^{5} f_j \dot{\varepsilon}^j + \sum_{k=1}^{4} g_k T^k + h \tag{10}$$

where σ is the true stress, ε the true strain, $\dot{\varepsilon}$ the true strain rate, T is the temperature, and a_i, b_j, c_k. . . h are fitting parameters or material constants. The parameter values, listed in Table 2 of Publication V, were determined using the Matlab function "fminsearch". It should be noted that even through the

applied equations are based on 'correct' variables, i.e., strain, strain rate, and temperature, the approach is basically only numerical 'curve fitting', and also other equations leading to a good match with experimental data could have been used instead. The fitting was carried out on the original measured data that was sampled so that both the yield point and the hardening parts of the stress–strain curves were represented by approximately 20–30 points. The initial temperature of the specimen before the loading was measured with a thermocouple. The adiabatic heating of the specimens in the tests with strain rate exceeding 100 s^{-1} was calculated by using 0.9 as the value of the Taylor-Quinney coefficient, i.e., by assuming that 90 % of the energy expended in the deformation is converted adiabatically to heat. All quasi-static tests were assumed to be fully isothermal.

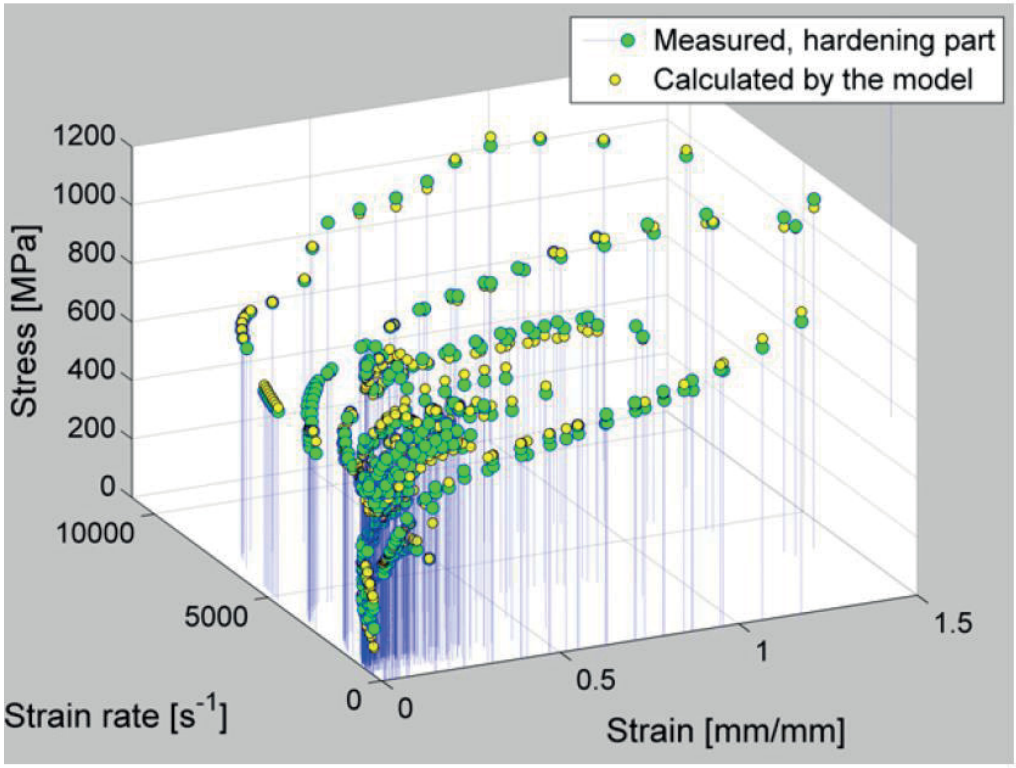

Figure 28. Comparison of the measured and modeled stress–strain data for the C17C steel at different strain rates (Publication V).

The developed material model was verified by comparing the results of finite element simulations with experimental results of a cold heading test carried out with a modified Hopkinson bar setup shown in Figure 29. The experiment was carried out simply by cold heading a small button (8.5 in diameter, 3.5 mm long) to the end of a steel specimen with an original diameter of 5.5 mm. The test was carried out by inserting the specimen, a piece of the steel wire, into the cold heading die and impacting the 1.5 m long striker bar at the speed of 14 m/s directly on the specimen. The impact upsets the impacted end of the specimen and forces the material to flow inside the die cavity in approximately 0.8 milliseconds.

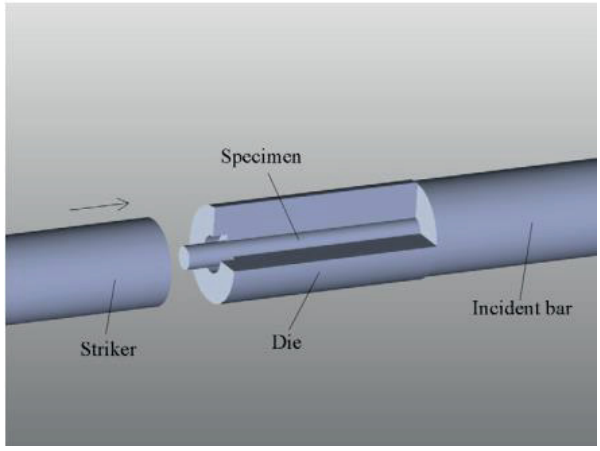

Figure 29. Experimental setup used for the model verification (Publication V).

The material model described above was used to represent the material behavior in the numerical cold heading experiment with ABAQUS/Explicit. A 2D axisymmetric model was used in the simulations with only half of the geometry, as all components of the setup comprising the die, the bar, and the specimen are axisymmetric. The steel wire specimen was meshed with approximately 260 four-node reduced integration axisymmetric quadrilateral continuum elements (CAX4R). High-quality mesh during the large deformation process was ensured by using adaptive meshing. A friction coefficient of 0.19 was used to describe the contact between the different components of the model, i.e., the wire, the striker bar, and the die. The friction value was adjusted to match the simulated button shape with the actual cold headed test piece. The effect of friction was studied by simulating the cold heading experiment also with friction values of 0.14 and 0.24, but 0.19

appeared to yield the best results. The same striker velocity (14 m/s) was used both in the simulations and the experiments. In the simulations, the deformation of the material was assumed adiabatic with the Taylor-Quinney coefficient value of 0.9. Figure 30 shows the mesh and the equivalent plastic strain distribution in the simulated button-head at the end of the cold heading operation. Input data of the material behavior was evaluated at different strains, strain rates, and temperatures, and the tabulated flow stress values calculated using Eqs. 9 and 10 were given to ABAQUS. The original experimental data extended to approximately 1.5 mm/mm, but in the simulations even higher local strains were observed. Therefore, the input data was extrapolated up to 2.0 mm/mm. Luckily the need for such high strains in the simulations was limited to very small regions and only at the very end of the simulation. Therefore, the possible errors caused by the extrapolations in the final simulation results are assumed to be quite small. The maximum simulated strains were observed around the inner corner (up to ~3 mm/mm). Similarly, the simulated temperatures and strain rates in those regions were very high (~ 1000 °C, 16,000 s^{-1}), but mostly the strains were less than 1.9 mm/mm, temperatures below 600 °C, and strain rates below 9000 s^{-1}.

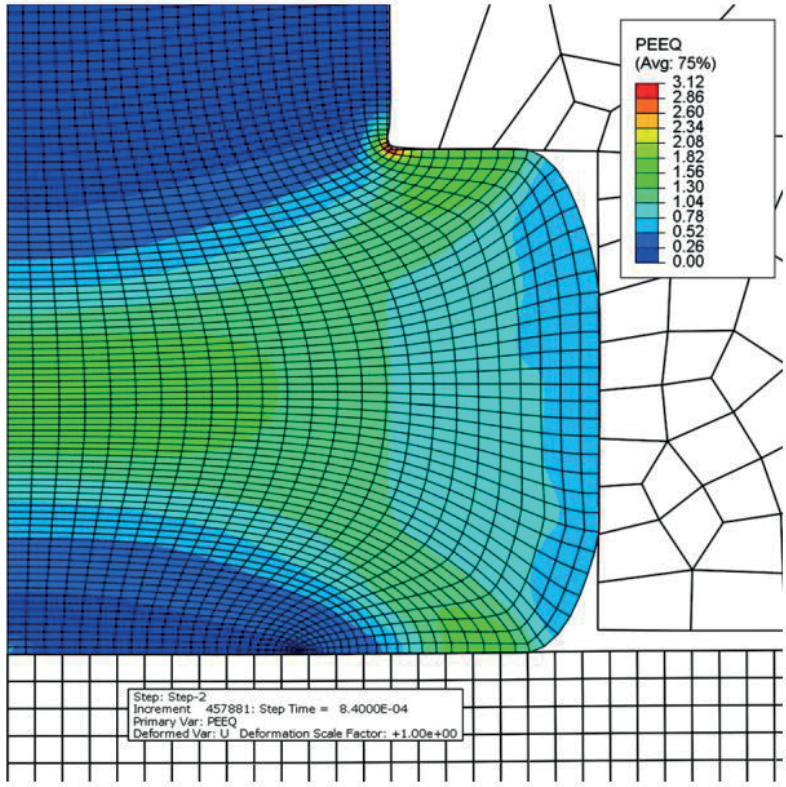

Figure 30. Element mesh and plastic strain distribution in the cold headed part (Publication V).

The strains on the stress bars were recorded during the cold heading experiment with strain gages bonded on the stress bar 50 mm from the cold heading die. The force acting on the interface between the stress bar and the cold heading die was calculated from the obtained strain pulses. The force on the same interface was also obtained from the simulations. The simulated and experimental forces shown in Figure 31 are in good agreement with each other. A slight detachment of the die from the incident stress bar causes a peak in the measured force values at around 300 ms. The simulated and experimental peaks appear at slightly different times, which most likely is due to the slightly non-circular shape of the hot rolled wire, leading to a slightly earlier contact of the wire with the die channel in the experiment. If the experiment is simulated with a large die with no interfaces, the force peak disappears and therefore confirms the source of the peak to be the interface between the die and the bar. Although the final dimensions of the experimental

and simulated buttons were the same, filling of the corners of the die was not quite perfect in the cold heading experiment.

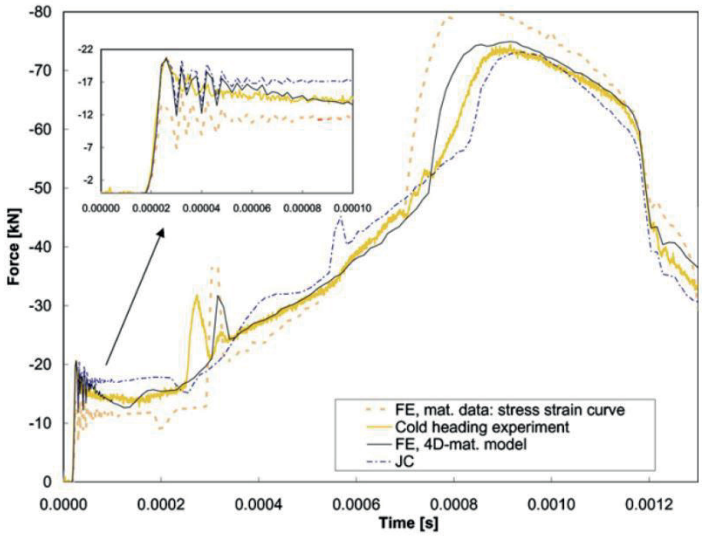

Figure 31. Force as a function of time obtained from the cold heading experiment and the numerical simulations with Abaqus (Publication V).

The microstructure of the studied cold-drawn C17C wire is 'banded', as shown in Fig.1 of Publication V, which in general is not a desired property for a microstructure. In this case, however, it opens up a possibility to follow the flow of material during the cold heading process and to compare it with the movement of so-called tracer particles in Abaqus simulations. If the flow of material is similar both in the simulation and the experiment, the tracer particles should form similar shapes as the material microstructure in the experiment. The comparison of the real microstructure and the simulated flow of material is shown in Figure 32, revealing that there is clear mismatch between the flow lines and the tracer particle arrays in some parts of the cold headed part. In general, this indicates that the material flow is not perfectly homogeneous. There are many possible reasons for this, including changes in the microstructure, geometrical imperfections such as non-straightness and ovality of the wire, as well as imperfect alignment of the striker and the specimen. In the simulations, the use of a simple friction model could also lead to differences between the simulated and observed flow of material.

For comparison, another modeling approach was also attempted by using a single quasi-static compression stress–strain curve as the material input data. This approach is, unfortunately, still quite common, as the high strain rate and temperature dependent material data is often not (yet) available. In addition to the measured force–time curve and the simulated curve obtained by using the model presented by Eqns. 9 and 10, Fig. 31 contains also the curve obtained by using the simple quasi-static stress–strain data in the simulation (dashed line). From Fig. 31 it is evident that if the material behavior is described by the quasi-static data only, the forces are underestimated in the beginning of the cold heading process and overestimated at the later stages. This can be explained by the stronger net effect of the strain rate at small plastic strains before the adiabatic heating sets in at larger strains and reduces the flow resistance of the material. Based on the results of this work, the simulation of the cold heading process cannot be done accurately enough with low strain rate quasi-static data only, but also information about the material behavior at higher strain rates and temperatures is needed. For another comparison, the Johnson–Cook model was calibrated with the available experimental data, and the model was used to simulate the same cold heading experiment as discussed above. As shown in Fig. 31, also the JC model overestimates the flow strength of the material and consequently also the simulated cold heading forces at low and intermediate strains. On the other hand, the JC model slightly underestimates the forces at high strains, which can be explained by the fact that the JC model assumes a linear dependence of the flow stress on the logarithmic strain rate. However, as discussed already in Chapter 3, at high strain rates the strength of basically all materials tends to increase much faster than predicted by the JC model, and therefore the (dynamic) strength of also the C17C steel exceeds the predicted values used in the simulations at high strain rates.

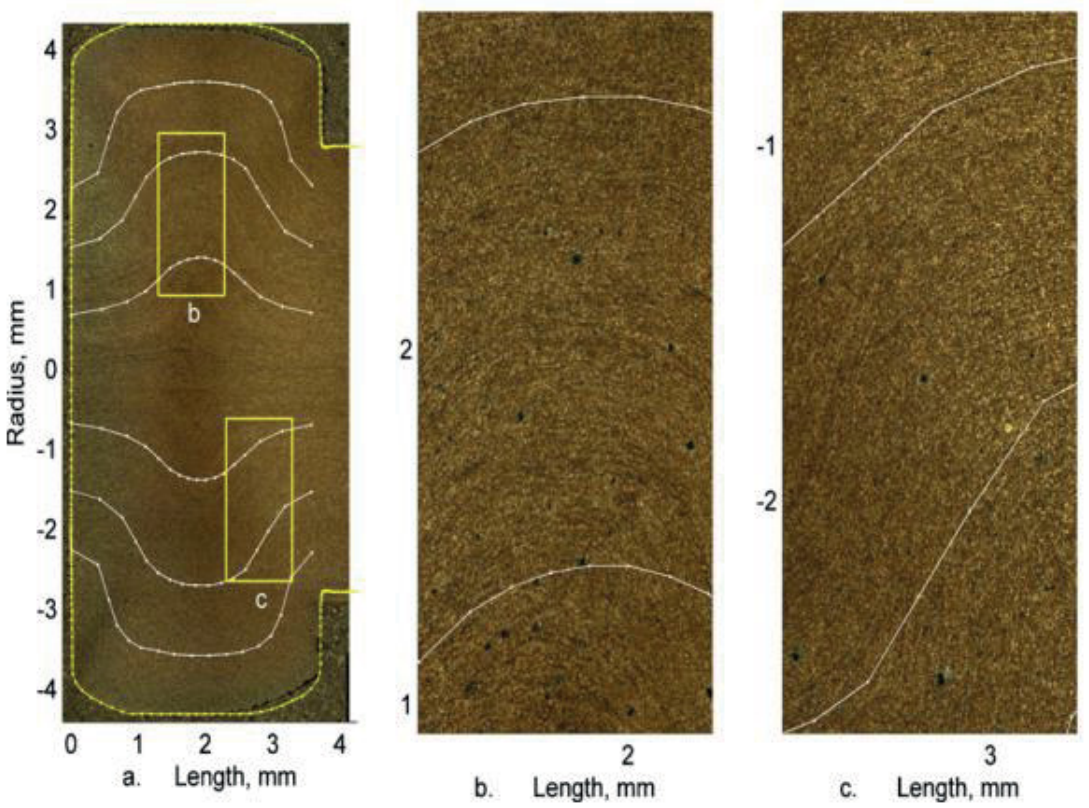

Figure 32. Comparison of the flow lines delineated by the banded structure of the C17 steel and the tracer particles in the Abaqus simulation (Publication V).

8.2 Crusher pressure gage (Publications I and IV)

The main reasons for the use of crusher pressure gages for example in the acceptance test firings of guns and ammunition are that they are inexpensive, easy to use, and do not require any electronic instrumentation or changes made in the gun construction. In contrast to this, the more sophisticated piezoelectric pressure transducers need both instrumentation and, especially, drilling of holes in the guns for mounting the transducer. In the test firings, it was observed that the pressure readings obtained by the crushers and by the piezoelectric pressure transducers could differ by as much as –10 to +20 % in the pressure range of ca. 90-500 MPa, which is not acceptable and poses a serious threat of gun failure.

From the materials science point of view, the principal reason behind the observed problem related to the use of crusher pressure gages was obvious from the very beginning of the study: increasing pressure increases the compression rate of the crusher element, which again increases the (instantaneous) strength of the (copper) element and, consequently, decreases the amount of deformation corresponding to a certain pressure. In other words, for the same amount of deformation, which is what is measured from the crusher element after firing of the gun, higher pressure is needed if the rate of deformation is higher. The only remaining question therefore is, how to take the observed strain rate effect into account in a simple but reliable manner.

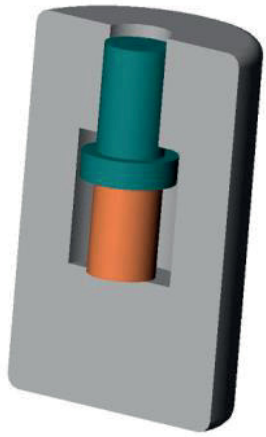

Figure 33. Schematic construction of the crusher pressure gage (Publication I).

Figure 33, which shows the simple construction of the crusher pressure gage, reveals also that the only information that is obtained with the use of this type of a pressure gage is the maximum pressure, determined from the permanent shortening of the copper element during the firing event. Therefore, the main task would be to find a model that can convert the change in the crusher element's length to maximum pressure. In principle, any of the existing material models could be applicable, but for example the common Johnson-Cook model turned out not to provide accurate enough results. As there is no need for the applied model (or equation) to be a so-called parametric constitutive model, any fitting function that describes accurately enough the dependence of the crusher element shortening on the maximum pressure under the given circumstances would suffice. As discussed already in Chapter 3, the easiest way for finding the best possible mathematical function that fits all the

determined stress-strain curves separately, i.e., each curve with its own fitting parameters, is a software that searches automatically through a large number of pre-programmed functions, such as TableCurve 2D®. When such a search was conducted, the best simple function turned out to be the rational function of type

$$\sigma = \frac{(a+c\varepsilon)}{(1+b\varepsilon)} \tag{11}$$

The coefficients for the true stress-strain curves determined at nine different strain rates are presented in Table 2, and Fig. 34 shows that Eqn. 11 with correct coefficients can reproduce each of the experimental stress-strain curves quite accurately. It should be noted that Eqn. 11 is used only to describe numerically and as well as possible the individual experimental stress-strain curves and to facilitate the final two steps of the model development.

Table 2. Fitting parameters of Eqn. 11 for the reproduction of the experimental true stress-strain curves at nine different strain rates (Publication I).

$\dot{\varepsilon}$ (s^{-1})	a	b	c
0.0014	23.28798	5.345203	2405.492
0.1126	23.42199	4.784474	2375.701
2.3963	24.84452	4.67641	2423.818
88.3	29.26381	4.315714	2287.817
306	20.64857	3.600842	2222.203
492	24.54853	3.460277	2167.054
519.8	18.22643	3.840796	2302.682
916	24.34579	3.335467	2156.783
928.2	26.66988	3.710483	2310.544

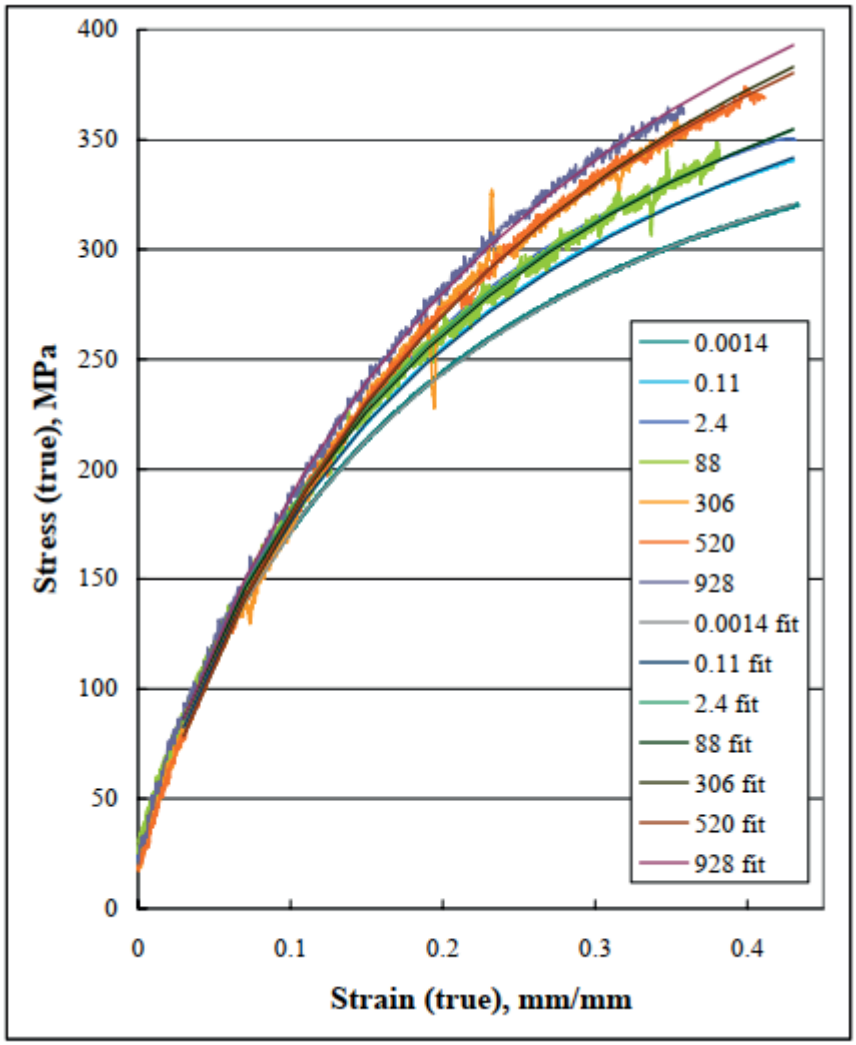

Figure 34. Experimental and fitted stress strain curves of copper at seven different strain rates (two of the strain rates included in Table 2 were left out for clarity). (Publication I)

So, at this point we have a set of coefficients (a, b, c) for every strain rate used in the tests, but this not yet very useful for our final aim. From experience, however, we know that when the dislocation motion is controlled by thermally activated obstacles, the flow stress has a logarithmic dependence on strain rate, i.e., $\sigma \propto \ln(\dot{\varepsilon})$. In the case of pure copper, these obstacles are in practice other

dislocations on the glide and intersecting crystallographic planes, and their amount and arrangement depends on the amount of preceding strain and the strain rate at which this strain was achieved. This means that the flow stress depends on strain both directly and through the strain dependent strain rate effect, i.e.,

$$\sigma(\varepsilon) = A(\varepsilon) + B(\varepsilon) ln(\dot{\varepsilon}) \quad (12)$$

Using the numerical representations of the experimental stress-strain curves, i.e., Eqn. 11, we can easily make constant plastic strain 'cuts' or 'sections' to the stress-strain curves to obtain flow stress vs. logarithmic strain rate data points at any constant plastic strain. When we plot the obtained new data points as in Fig. 35, we will observe that the points representing the same strains form straight lines, which also proves that Eqn. 12 is of correct form. From the straight-line fits also shown in Fig. 35, we will obtain the values for coefficients A and B as a function of plastic strain. The final step in this model development is to find again simple functions for the A vs. ε and B vs. ε data. It turns out that the same rational function used to describe the stress-strain curves works also very well for A(ε), while for B(ε), a second order polynomial function provides a good fit. This means that the final model, i.e., Eqn. 12, is based on altogether six fitting parameters, three for A(ε) and three for B(ε), as shown in Table 3. The entire procedure described above is presented in full details in Publication I.

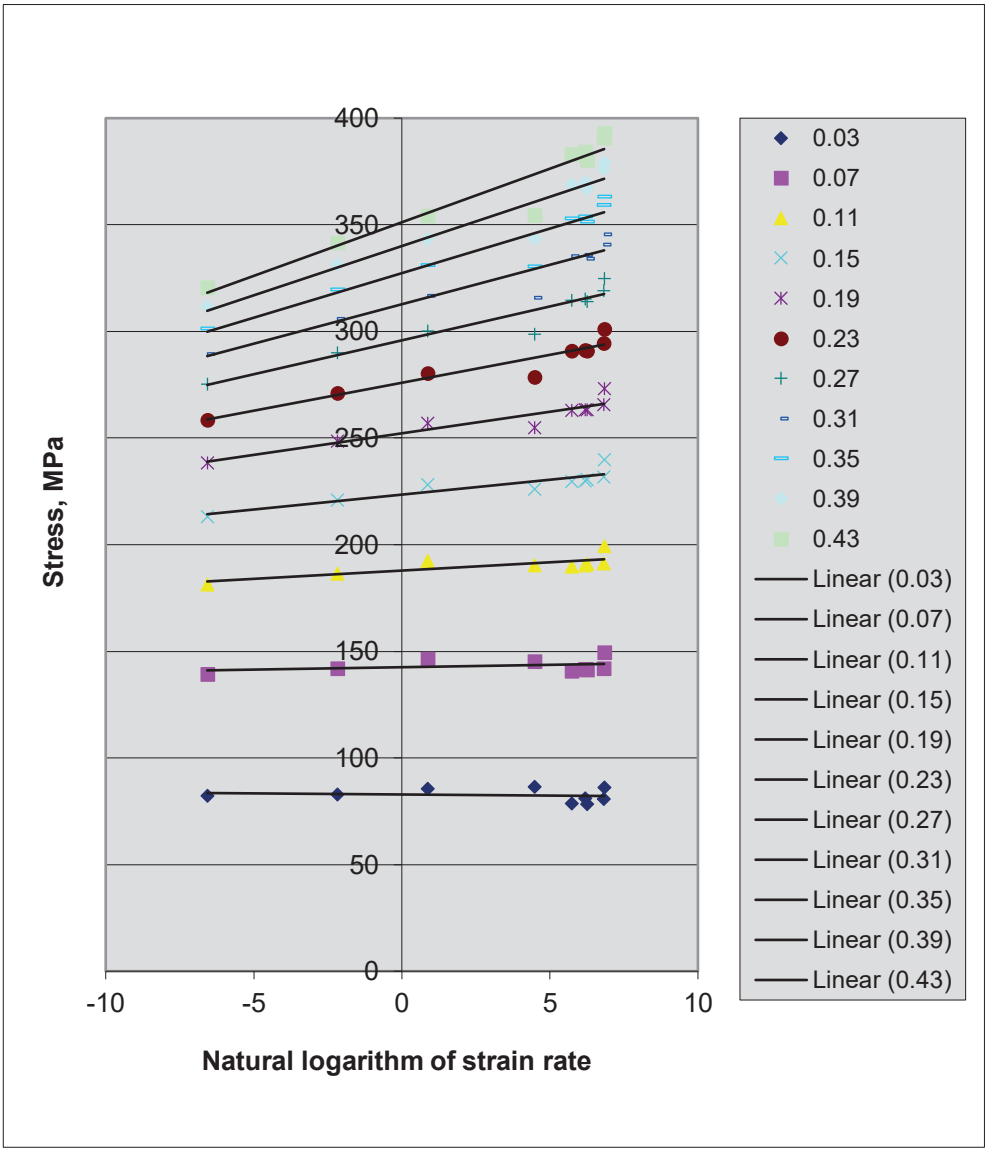

Figure 35. Plots of Eqn. 12 at various constant plastic strains (Publication I).

Table 3. Fitting functions A(ε) and B(ε) and the values of their parameters.

$A(\varepsilon) = \frac{(a + c\varepsilon)}{(1 + b\varepsilon)}$			$B(\varepsilon) = a_0 + a_1 x + a_2 x^2$		
a	b	c	a_0	a_1	a_2
24,35	4,446288	2321,055	- 0,7338	15,343	-4,1075

The crusher gage results with various calibrations were compared with the piezoelectric peak pressures obtained from test firings at different gun pressures. As Table 4 shows, the difference between the piezoelectric peak pressure P_h and the crusher pressure P_{cr} based on the quasi-static calibration increases from 3 MPa to 64 MPa with gun pressure increasing from 153 MPa to 414 MPa (relative error increases from 2 % to 15 %). With dynamic calibrations assuming the strain rates of 10, 35 and 80 s^{-1}, the errors at lower gun pressures become first slightly negative (ca. -2%), but for example at the highest gun pressure of 414 MPa, the errors are much smaller than with the quasi-static calibration. As seen in Table 4, the difference between the piezoelectric peak pressure and the dynamically calibrated crusher pressure decreases with the use an increasing strain rate in the calibration, being only 2 % at the gun pressure of 414 MPa with the 80 s^{-1} calibration. The biggest issue in the use of dynamically calibrated crusher elements is that we do not have any direct knowledge of the true strain rate in the crusher element during an individual firing. The measurements with piezoelectric pressure transducers have, however, revealed that the maxim pressure rise time in a certain gun type is almost constant independent of the amount of gunpowder, which makes it possible to calculate, or at least reasonably estimate, the strain rate in the crusher element and in that way facilitate use of Eqn. 12. A more thorough analysis of the above questions is presented in Publications I and IV and in Chapter 0 (*Discussion*).

Table 4. Comparison of the pressure differences between the piezoelectric peak pressure and the crusher pressure obtained with different calibrations (Publication IV).

P_h MPa	$P_h - P_{cr}$ MPa	$dP_{10\ 1/s}$ MPa	$dP_{35\ 1/s}$ MPa	$dP_{80\ 1/s}$ MPa
153	3	−3	−3	−4
207	7	−2	−4	−5
268	16	2	−1	−3
336	36	9	4	2
414	64	18	13	9

8.3 Testing of Ti6Al4V titanium alloy at high temperatures (Publication VI)

The tensile tests on the Ti6Al4V titanium alloy were carried out using two different Hopkinson Split Bar apparatuses and heating methods, as described in Chapter 6.5. The tests were first carried out at Tampere University (of Technology) using the direct electric current heating method at the strain rate of ca. 1300 s^{-1}. After that, (nominally) similar tests were carried out at the Polytechnic University of Madrid (UPM) at the same strain rate and temperature using the furnace heating method.

Figure 36 shows the stress-strain plots obtained from the tests conducted at 300 °C and 700 °C with both heating methods. In the tests performed with furnace heating, the stress-strain curves show large oscillations due to the mechanical fixing of the specimen to the bars (FH+MC). Gluing together with mechanical fixing with a pin going through the grip section of the specimen was also attempted (FH+GF), but because of the relatively long heating time needed to reach the test temperature, the glue could not bring any relief to the oscillation problem. Especially in the beginning of the tests, the stress-strain curves do not portray the material behavior correctly, and for example the yield strength of the material cannot be read (nor estimated) from the data. The electric heating method and, especially, the fixing of the sample to the stress bars with glue (EH+GF), provide a much better raw signal quality. Filtering of the data obtained from the tests with furnace heating (or rather with mechanical fixing of the specimen) with low pass and median filters improves the signal quality considerably, as shown in Fig. 36b: after filtering, the stress-strain curves obtained with the direct electric heating (EH+GF) and furnace heating (FH+MC) methods appear to be quite similar. In general, however, (excessive) filtering of the raw data should always be dealt with caution, as it may easily lead to distortion of the data and incorrect interpretation of the results.

The stress-strain behavior of the Ti6Al4V alloy was modeled by fitting the Johnson-Cook equation (Eqn. 5) to the obtained data. The constants of the model, shown in Table 5, were obtained by using the least-squares fitting method. Figure 37 shows the stress-strain curves reproduced by the Johnson-Cook model at three different temperatures together with the corresponding experimental data. As the Johnson-Cook model (in its original form) is incapable of accounting for the strain (or thermal) softening of the material, the modeled flow stress in Fig. 37 is presented only for the region of uniform deformation. As can be seen, at least under the given conditions, the Johnson-Cook model reproduces the experimental data very well and can therefore be

used to describe the dynamic behavior of the studied material for example in finite element simulations.

Table 5. Values of the Johnson-Cook model parameters for the studied titanium alloy (Publication VI). Tests were done only at one strain rate, 1300 s^{-1}, and therefore C was not determined.

A	B	n	T_{room}	T_{melt}	m
800 MPa	700 MPa	0.096	25ºC	1400ºC	0.65

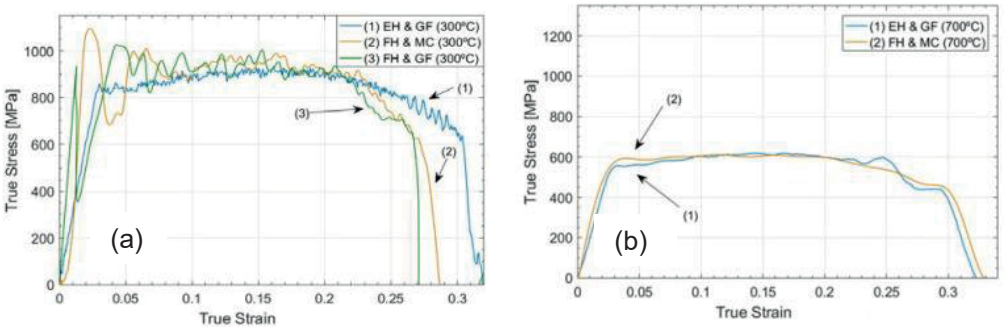

Figure 36. Comparison of the stress-strain curves obtained with the two different heating and specimen fixing methods a) raw data obtained at 300 °C with both heating methods, and b) raw data from a test with direct electric heating and filtered data from a test with furnace heating at 700 °C (Publication VI).

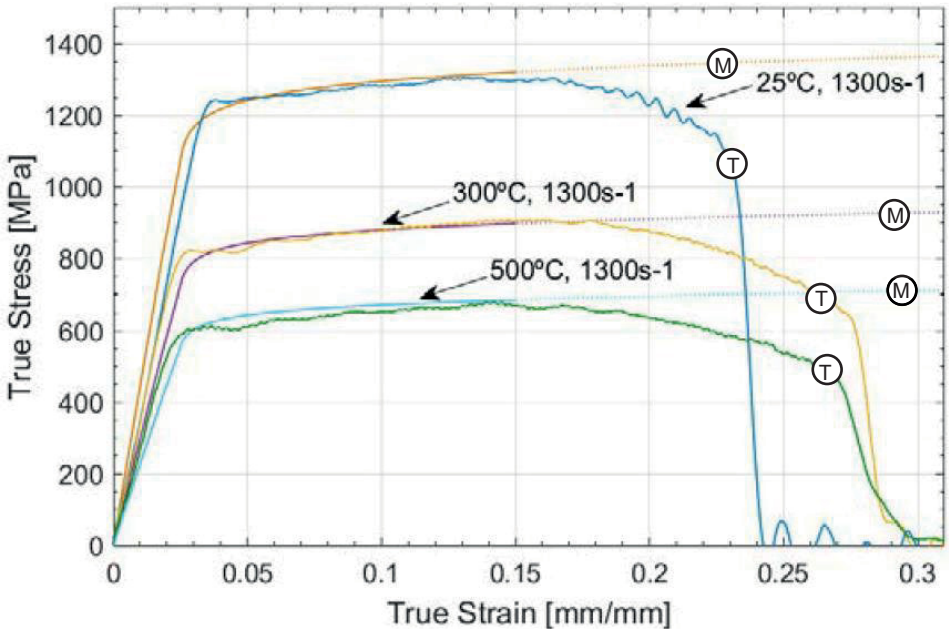

Figure 37. Experimental stress-strain curves and the corresponding data predicted by the Johnson-Cook model (Publication VI). T indicates the experimental data and M the model.

In a mechanical material test, usually quite large part of the work imparted to the material is converted to heat. Under certain conditions, especially in the tests at sufficiently high strain rates, there may not be enough time for the heat to be conducted away from the specimen, making its temperature increase. This kind of internal or 'adiabatic' heating can also be included in the Johnson-Cook model by allowing the test temperature to change with plastic strain. If one assumes that an increment of plastic work done on the specimen (dW), obtained from the increment of the area under the stress-strain curve, equals an increment of heat (dQ) in the material, one can easily calculate the amount of adiabatic heating (dT), if certain physical constants of the material are known (density ρ, specific heat C_p). In addition, the fraction of work converted to heat is usually less than unity, i.e., some amount of the energy is permanently stored in the defect structure of the material, such as dislocations. Consequently, this effect must be accounted for in the calculation of the temperature increase dT by including factor λ (or more commonly β) in Eqn. 13. One problem is that the precise value of lambda/beta is usually not known, and therefore the value of 0.9 is assumed unless better data is available. Depending on the thermal properties of the material, the strain rate above

which the conditions can be expected to become more or less (fully) adiabatic can be surprisingly low, for example for austenitic steels with low thermal conductivity only of the order of 10^{-1} s^{-1}. On the other hand, for example for copper with one of the best heat conductivities of metals, the thermal conditions become adiabatic only when the strain rate exceeds ca. 10 s^{-1} [73], [74]. To estimate the adiabatic heating using Eqn. 13, we assume that no loss of heat from the system takes place during the test. Equally, we assume that no heat generation takes place during the test for example through exothermic phase transformation(s).

$$\Delta T = \frac{\lambda}{\rho C_p} \int \sigma d\varepsilon \tag{13}$$

Where ΔT is heat rise caused by deformation, λ is factor telling portion of energy converting to heat (~0.9), ρ = density, C_p = specific heat, σ = stress and ε = strain.

The direct electric heating allows high speed imaging of the specimen during a high strain rate high temperature test. On the other hand, when the specimen is heated in a furnace, the painted contrast pattern dries up and becomes brittle, and despite the possibility to remove the furnace and to expose the specimen to the high-speed cameras just before the impact, the obtained images are not good enough to be used for digital image correlation. The images obtained from the high strain rate tests conducted on specimens heated with the direct electric heating method were processed with the Davis 8 software from LaVision. An example of the full field surface strain data from a specimen deformed at a high rate at the temperature of 700 °C is shown in Fig. 38a. From the full field data, one can produce for example so-called waterfall plots or line profiles of the strains by plotting the strain along the length of the gage section of the specimen. A waterfall plot is very useful in the visualization of the strain distribution along the gage section, and especially for studying the strain localization and necking during a tension test. Figure 38b shows an example of the waterfall plot of the specimen deformed at 700 °C. In the beginning of the test, the strain is uniform along the gage length of the specimen. At an average strain of approximately 10 %, two localizations form on the gage section, and further deformation focuses more in these regions. With continuing deformation, one of the localizations becomes the dominant neck, where the failure finally occurs.

Figure 38c shows the last determined profile of the samples tested at three different temperatures, revealing that the maximum strain in the gage section of the sample increases as the test temperature increases. At 60 °C, the maximum strain at the neck is close to 50 %, whereas at 300 °C the maximum failure strain is around 65 %. At 700 °C, the maximum strain is as high as 80 %.

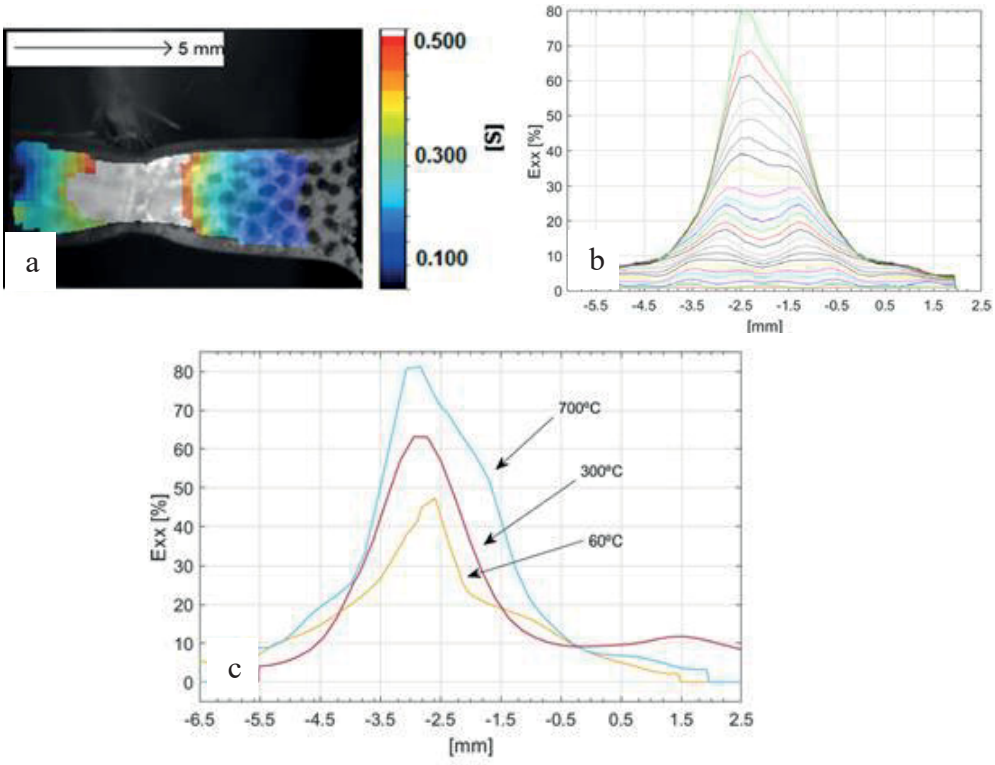

Figure 38. a) full-field strains obtained from the surface of the sample deformed at 700 °C, last frame before the fracture, S is the maximum normal strain, b) waterfall plots showing the axial strain along the gage length of the specimen, and c) last waterfall plots before the fracture at different temperatures (Publication VI).

8.4 Rubber coated paper machine rolls (Publication II)

The OptiSizer film coating method applies color or primers simultaneously on both sides of the paper web, as it passes between two polymer coated steel rolls, i.e., the 'nip'. If the nip pressure distribution is not even, the coating process does not perform in the intended manner and the paper will have

uncoated stripes or ‘wrinkles. To improve the contact conditions and to reduce undesired wrinkling, the rolls are designed to have in a slightly convex shape, or ‘crowning’. The optimal shape of the rolls is difficult to estimate by trial and error, and therefore the process needs to be simulated to evaluate the nip pressure distributions. In modern paper machines, however, the speeds at which the rolls are rotating increase the strain rate of the roll covers dramatically, and the strain rate effects must be taken into account in the modeling of the nip pressures. The aim of this study was to evaluate and quantify the rate effects in the paper machine roll cover materials, and to demonstrate how they can be accounted for in the accurate design of the roll geometry.

RayFlex 5000 is a heat and wear resistant fully cross-linked rubber roll cover material that also has excellent chemical resistance. The low strain rate behavior of the material was studied in compression using cylindrical specimens of 18 mm in diameter and 15 mm in length, while its high strain rate behavior was studied with the HSB method using shorter samples of 5 mm in length. The strain rate sensitivity of the material is almost linear (strain rate on log scale) up to the strain rate of 1 s^{-1}, and still at the strain rate of 1600 s^{-1}, no drastic increase in the material’s flow stress is observed, as Fig. 39 shows. Increasing amount of strain increases also the strain rate sensitivity of RayFlex 5000, as the steepening slope of the line fitted to the experimental data in Figure 39 reveals. Figure 40 depicts the stress-strain plots (‘hysteresis loops’) obtained at different temperatures at the strain rate of 1 s^{-1}, showing that the strength of the material decreases with increasing temperature. On the other hand, the moisture did not seem to have a strong effect on the strength of the material, as the material does not absorb large quantities of water.

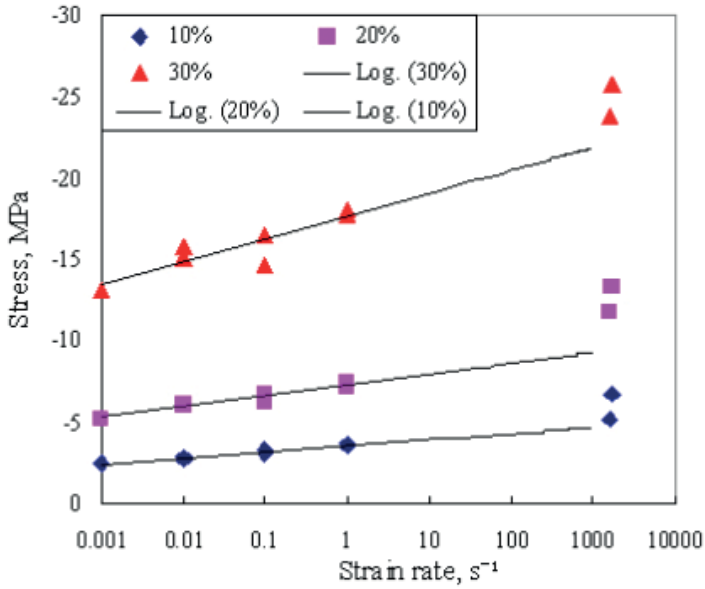

Figure 39. Flow stress of RayFlex 5000 at different plastic strains as a function of logarithmic strain rate. During the measurements, the relative humidity was 50 % (Publication II).

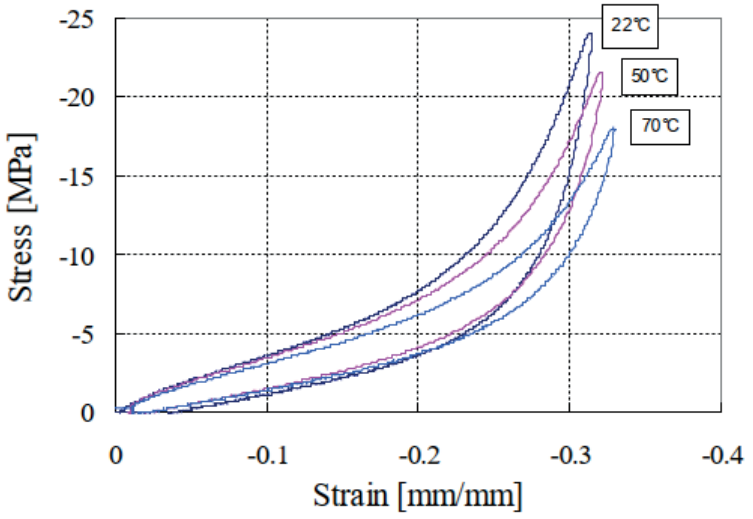

Figure 40. Stress-strain ('hysteresis') plots obtained at different temperatures at the strain rate of 1 s^{-1} (Publication II).

The behavior of the coater nip was simulated at two different loading conditions: 1) room temperature, strain rate of 1 s^{-1}, and ambient moisture, and 2) temperature of 60 °C, strain rate of 1600 s^{-1}, and saturated moisture in paper machine water at the test temperature. The experimental data needed in the modeling was obtained from the compression tests conducted at the temperatures of RT, 50 °C, and 70 °C. Before the actual compression tests from which the data was recorded, the samples were mechanically loaded twice at the same conditions to 33 % of strain to go past the Mullins effect [29]. An arithmetic average of the loading parts of the stress-strain curves of several tests at each temperature was used as the input data for the simulations in Abaqus. The 60 °C material data used in the simulations was obtained by averaging the experimental data of the 50 °C and 70 °C tests. The stress-strain curves used in the simulations are shown in Fig. 41.

For the hyperelastic models, the elastic behavior of materials can be described by strain energy functions [75]. The Marlow form of the strain energy potential can be used if material data is available only in one loading condition, e.g., only in compression or tension. This model assumes that the strain energy potential is independent of the second deviatoric invariant. The model can be implemented by providing test data that describes the deviatoric

behavior and, optionally, the volumetric behavior if compressibility must be included.

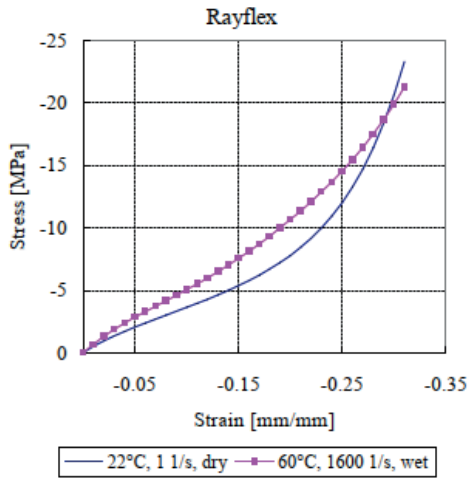

Figure 41. Material data for RayFlex 5000 used in the nip simulations (Publication II).

The contact between the rolls was modeled with Abaqus using a 3D nonlinear static analysis. The simulated pressures were first compared with the measured nip pressures to check the reliability of the simulations. The nip pressures were measured with Fuji color forming and developing films. Unfortunately, the method requires dry surfaces and a low rotation speed, and therefore the process must be slowed down for the measurement. Consequently, the measurements do not represent true dynamic conditions, and the obtained values may differ significantly from the true pressures during normal operation.

Figure 42 shows a comparison of the experimental and calculated pressures for a production size paper machine with a roll width of 11 m. At lower nip loads, the simulated and experimental nip pressures match fairly well when using the elastic model for the roll cover (i.e., constant Young's modulus and Poisson's ratio). The difference between the simulations and the experiments increases as the nip load increases. The shape of the rolls can be modified by changing the crowning profile to decrease the nip pressure gradient in production conditions. In this way, the width of the nip increases while the maximum pressure in the middle of the nip contact area decreases.

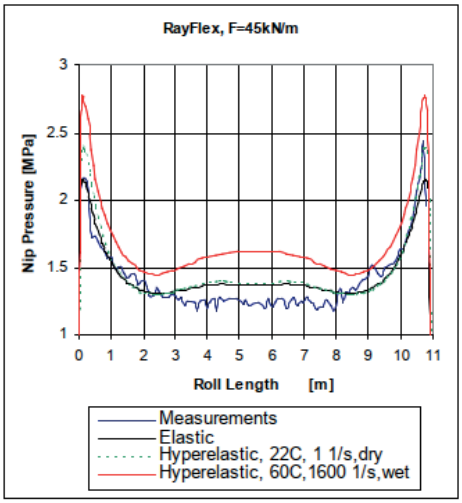

Figure 42. Comparison of the results given by different models with actual measurements (Publication II).

8.5 Dynamic strain aging (Publication VII)

In this study, stress-strain curves for two steels with four different heat treatments each were first determined at various strain rates and temperatures using a compressive Hopkinson Split Bar device. From the determined stress-strain curves, the flow stresses at 5 and 15 percent of plastic strain were extracted for further examination and evaluation of the effects of the microstructure. Figure 43 shows these flow stresses for the G45 steel as a function of test temperature at the strain rate of 4500 s^{-1}. Similar plots for the other tested steel, 27MnCr5, can be found in Fig. 6 of Publication VII. As the plots show, a strong dynamic strain aging (DSA) effect can be observed for both materials at elevated temperatures. For all microstructural variants, the strength first decreases significantly as the temperature is increased from room temperature to 400 °C. The minimum strength for all materials is observed at temperatures close to 500 °C. As the temperature is further increased, the flow stresses of both steels start to increase again due to the dynamic strain aging effect that activates with the increased diffusivity of free carbon atoms. For all variants of the 27MnCr5 steel, the flow stress increases steadily up to the highest test temperature of 680 °C. On the other hand, two of the variants of C45 (Ref and CG) show a maximum in the flow stress already at around 620 °C, and at 680 °C their flow stress is already decreasing. However, both in the case of the 27MnCr5 steel and the other two variants of G45, it is likely that

the peak in the flow stress still exists but at a slightly higher temperature, where tests in this work were not conducted. On the other hand, changes in the microstructure of the steels occurring at temperatures above 700 °C can change the situation, and therefore continuing the testing at higher temperatures may not be worthwhile, at least from the dynamic strain aging study point of view. When comparing the test results of the different variants of the 27MnCr5 steel, it seems that the differences in their microstructures do not have a strong effect on their mechanical properties and behavior (Figs. 4 and 6 in Publication VII). The response of the C45 steel, on the other hand, is significantly different for the different variants, i.e., microstructures, as comparison of the data presented in Fig. 5 of Publication VII and in Fig. 43 very well reveal.

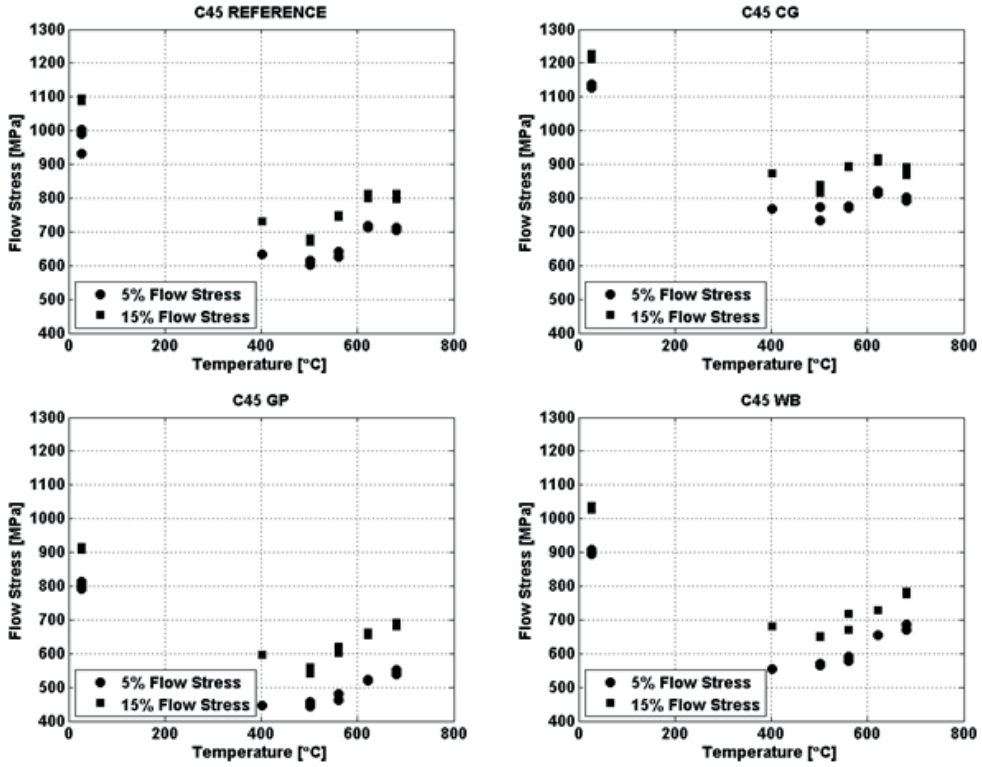

Figure 43. Flow stress of the G45 steel at 5% and 15% of plastic strain as a function of temperature at the strain rate of 4500 s^{-1} (Publication VII).

The temperature sensitivity factor η, defined in Eqn. 14, can be used to quantify the magnitude of the dynamic strain aging effect. In the equation,

$\sigma_{\varepsilon RT}$ and $\sigma_{\varepsilon T}$ are the flow stresses obtained at a constant plastic strain at room temperature (RT) and at a higher temperature.

$$\eta = 1 - \frac{\sigma_{\varepsilon,RT} - \sigma_{\varepsilon,T}}{\sigma_{\varepsilon,RT}} \tag{14}$$

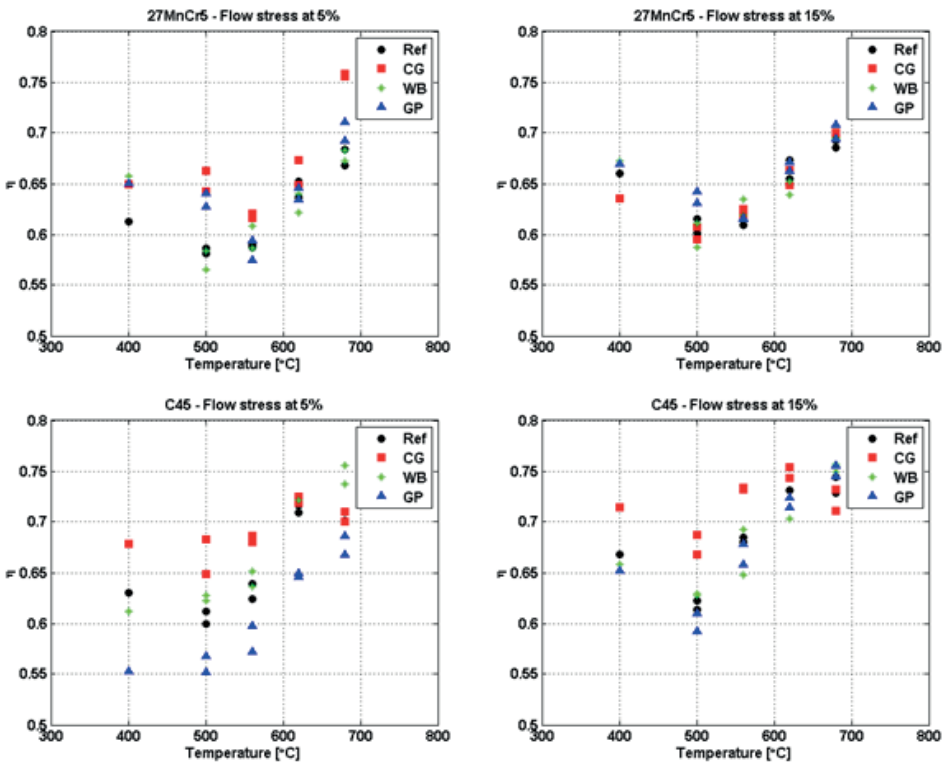

Figure 44. Temperature sensitivity factor η as a function of temperature for a) 27MnCr5 at 5 % of plastic strain, b) 27MnCr5 at 15 % of plastic strain, c) C45 at 5 % of plastic strain, and d) C45 at 15 % of plastic strain. The strain rate in the tests was 4500 s^{-1} (Publication VII).

At room temperature, the temperature sensitivity factor equals one, but at higher temperatures it decreases and shows values between zero and one. The rate of change of η can be used to assess the sensitivity of the microstructure to dynamic strain aging, while its absolute values describe the overall thermal softening relative to the room temperature strength (note that a *smaller* η

means *stronger* thermal softening). Figure 44 shows the temperature sensitivity factor as a function of the test temperature at the strain rate of 4500 s^{-1} for all studied steels. The coarse-grained variant of the 27MnCr5 steel shows the highest temperature sensitivity to DSA, i.e., the highest slope of the η vs. T data points, at temperatures above 560 °C. The other variants follow in a somewhat scattered order. A more thorough analysis of the results will be presented in Chapter 9 (*Discussion*)

9 Discussion

In the previous Chapter, where the main results obtained in the studies included in this thesis were presented and summarized, also some preliminary interpretations and discussion of the findings were already offered. In this Chapter, some additional observations and discussion will be presented with an attempt to give an overall picture of the common strain rate and temperature dependent phenomena taking place in the examined applications. More detailed comments and discussions dealing with the research findings are provided in the Discussion sections of the seven Publications this doctoral thesis is based on.

From the results of all individual studies and applications included in this thesis, it is evident that 1) practically all materials show strain rate dependence in their mechanical behavior, 2) except for a few exceptions, this dependence is positive in the sense that increasing strain rate increases the flow resistance of the material, 3) the strain rate dependence can have either a positive or a negative effect from the application point of view, 4) there are still many challenges in the experimental determination of the strain rate sensitivity of materials, and 5) strain rate dependence can be (and already is) included in many of the material models, but there are still many challenges that need to be addressed and solved.

When comparing the different materials studied in the framework of this thesis, many similarities but also differences in respect of the strain rate sensitivity can be observed. One division can be made based on the type and details of the deformation mechanism(s) controlling the flow of material during stressing. It is not too surprising that such differences exist between different material groups, such as (crystalline) metals and (non-crystalline) organic polymers, but there can be also rather big differences for example between the behaviors of metals with different atom arrangements (crystal structure) and/or microstructures in different scales. The latter becomes quite evident if we, for example, compare the stress-strain curves determined at

different strain rates and/or temperatures for pure copper with a face centered cubic crystal structure (the crusher application) with the results for the cold heading steels with a body centered crystal structure. Similarly, the effects of a particular microstructure on the strain rate and temperature dependent behavior of carbon steels, including dynamic strain aging, were brought up by the tests discussed in Publication VII.

A rather interesting observation is that when the flow stress vs. logarithmic strain rate curves of metals and polymers are compared with each other, in both cases a change in the slope of the curves is commonly found to occur around the strain rate of 10^3 s^{-1} (in the case of polymers, however, also different kind of behavior is observed, depending on the type of the polymer [76]. In the case of metals, a rather well-proven explanation based on the mechanisms of thermally activated dislocation motion and various drag mechanisms acting on the dislocations is nowadays generally accepted. In the case of polymers, especially when considering the wide range of polymers with different kinds of chain motion relaxation processes, it is quite unexpected that they would, not all but many, undergo a change in the strain rate sensitivity at around the more or less same strain rate. Because of this, many researchers have considered the possibility that the abruptly increasing strain rate sensitivity of polymers is not at all a material effect but rather a test related artifact, related for example to inertia or friction affecting the specimen's response, or to the different testing methods used in the different strain rate regimes (see for example the discussion in [77]). It seems, however, that the effect is real, but so far, no good and similarly 'simple' explanation as for the metals has been offered.

As mentioned above, usually the strain rate sensitivity of materials is positive, except for a few exceptions. One of the cases where increasing strain rate may lead to decreasing flow stress is with materials containing metastable austenite that at low strain rates can mechanically transform to martensite. At higher strain rates, however, the internal temperature of the material can increase by several tens of degrees due to the adiabatic heating effect, which can lead to the suppression of the martensite reaction and subsequently lower strength of the material. Another example of the possible occurrence of negative strain rate sensitivity is also related to adiabatic heating, but through the direct thermal softening effect, i.e., the amount of thermal softening exceeds the amount of the transient strain rate hardening. For example, for aluminum

alloys that in general exhibit quite low strain rate sensitivity, this kind of behavior is quite commonly observed at high degrees of plastic deformation, but also other materials, such as the cold heading steel studied in this work, may exhibit such behavior if the amount of deformation (and amount of internal heating) becomes extremely large. One more thing that a bit complicates the assessment of the strain rate sensitivity of materials is the common practice to plot the flow stress as a function of (logarithmic) strain rate at selected constant plastic strains. The possible problem here is that plastic strain is not the best possible 'state variable', because the same plastic strain can correspond to somewhat different microstructures depending on the conditions under which it was reached, including the applied strain rate.

Whether the transient strain rate hardening is a positive or a negative effect depends very much on the application and at which stage of the process it appears. For example, in the crusher application the strain rate effect is basically only negative, as 1) it necessitates the calibration of the crusher element material also at higher strain rates and, in particular, 2) it assumes that we know what the strain rate during the firing was. As we have seen, the first hurdle can be overcome as we have the means to do the calibration also at higher strain rates, although it requires some extra effort. The second one, however, is more problematic as we normally have no way of directly measuring the strain rate during the use of the crusher pressure gage, and we have to rely on secondary information that we have, for example, gathered from firing tests with guns equipped with piezoelectric pressure gages. Therefore, the conclusion in this case is that we would be much better off without the strain rate effect, but because it exists, we can only do our best to mitigate the problems that it is causing for the measurement accuracy.

In the cold heading application, in turn, the strain rate effect could be thought to have both negative and positive implications. In a similar manner as with the crusher application, accounting for the effect in any case requires extra effort, i.e., experimental determination of the behavior of the material at different strain rates and, in this case, also at different temperatures. Then, if we wish to simulate the cold heading process, the material behavior must be accurately implemented in the applied finite element code, such as Abaqus. From a more practical point of view, the strain rate effect increases the forces needed in the cold heading process, which may set new requirements for example for the used machinery and the cold heading dies. On the positive

side, however, is that during the final use of cold headed parts such as fasteners, higher strain rate for example in a car crash would make them stronger than at quasi-static conditions.

For the experimental determination of the strain rate (time) and temperature dependent material behavior, there is a wide variety of testing methods available. There are, however, still many practical issues that can affect the conduction of the tests and the results they produce. At quasi-static strain rates, the common servo-hydraulic materials testing machines equipped with up-to-date load and strain (or elongation) measurement capabilities can produce most of the data that we need, including results over wide ranges of temperature. One of the common deficiencies of these testing techniques, however, is that the conducted tests are mostly uniaxial, i.e., not accounting for the generally multi-axial stress states that often prevail in the real-world cases (or vice versa, we *think* that our test is (fully) uniaxial, even if it really is not). That can cause some problems or inaccuracies for example when designing complex components, especially if the design work is based on simulations relying on material models based on inaccurate or insufficient experimental data. At higher strain rates (above 1 s^{-1} or so), one of the common problems is that there are not too many (good) techniques available for accurate materials testing until the strain rate region covered by the Hopkinson bar –type testing devices. With Hopkinson bar type testing, one of the problems is that they are not usually calibrated against known loads or displacements (as can be easily done for ordinary load cells or extensometers), but they rely on the known properties of the bar material, i.e., the longitudinal wave speed and the Young's modulus. As Eqns. 1-3 show, any errors in these parameters affect the stress, strain, and strain rate values directly, and therefore they should be known as precisely as possible. In many cases, the wave speed is only calculated from the simple relationship $c = \sqrt{(E/\rho)}$, which requires that we know the values of E and ρ precisely. Especially the determination of the precise value of E is more difficult than generally understood, and the commonly applied technique of using the linear part of the tensile test stress-strain curve cannot be recommended. Probably the best (and simplest) technique to obtain E and c is to determine the wave speed directly from the Hopkinson bar by measuring the transit time of multiple wave reflections in the bar of known length by making use of the (already) glued strain gages and a digital oscilloscope. Determination of the density of the bar material is relatively easy and accurate with the Archimedes principle,

and from the determined values of c and ρ, we can calculate the value for E using the above equation.

Numerical modeling of the properties and behavior of materials has turned out to be a difficult task, largely because of the large number and complexity of the affecting factors and their interdependencies. As mentioned already several times, probably the most commonly used model for describing the strain rate and temperature dependent behavior of (primarily) metals is the Johnson-Cook model, which evidently has many shortcomings and even flaws. It seems to work 'somehow' for many materials in certain limited conditions, but even then, it is essentially only descriptive by nature without any real predictive or explanatory power. One of the problems with most of the current material models is that they treat the materials as a continuum, i.e., as if the properties of the materials were the same everywhere in the material and that the materials do not have any internal structure in the micro or nanoscale. A good example of this is the cold heading steel discussed in Chapter 8.1, whose microstructure is heavily banded and therefore its properties and behavior vary considerably by location and direction, being one big reason for the observed differences between the simulated and experimental results of the cold heading experiments. Because of the problems of the 'generic' models such as the Johnson-Cook model, in many cases it is wiser to settle for simple *ad-hoc* 'fitting models' that can describe the material behavior well enough in the examined case, but which may not have much wider use in other (even quite) similar applications, as done in the crusher and cold heading applications included in this thesis work.

As shown by the results presented in Chapter 8.1, Figs. 5 thru 7 in Publication III, and Figs. 4 and 5 in Publication V, the transient strain hardening effect in the cold heading steel is so strong that it must be accounted for when the manufacturing speeds and the resulting strain rates increase. The strain rate sensitivity factor $m=\log(\sigma)/\log(d\varepsilon/dt)$, i.e., the slope of the logarithmic flow stress - strain rate curve, depends on both the strain rate region and the amount of plastic strain, as depicted in Fig. 6b of Publication III. For both the quasi-static and high strain rate regions, the strain rate sensitivity decreases with increasing strain, but at higher strain rates the effect is much more pronounced. As Fig. 7a in Publication III shows, also the strain hardening parameter n of the Hollomon-Ludwik parabolic strain hardening equation decreases with increasing strain rate and increasing strain. Fig. 5 of Publication V, in turn,

shows that at the strain rate of 1100 s^{-1}, the strain hardening rate increases with increasing temperature and that at lower strains this effect is stronger. It is also interesting that at the lowest test temperature of -150 °C, the yield stress of the material is very high but after that the material shows only strain softening. For a large part, the above observations can be attributed to the adiabatic heating effect at higher strain rates and increasing strains, but also the 'normal' strain hardening effect, i.e., increase in the dislocation density with increasing plastic strain, has some contribution to the observed strain rate and temperature effects.

The discrepancies observed between the simulations and experimental verification tests of the cold heading process can be attributed to three main factors: 1) the material models do not describe the material properties and mechanical behavior well enough, 2) the material models do not take into account the microstructural details of the material (in the cold heading case, especially the banded structure), and 3) the simulations do not properly take into account the deviations of the experimental test setup from the 'ideal' situation, such as the dimensions and shape of the sample, contact conditions including friction, etc. In the recent years, researchers have started to include more and more of the microstructural features and mechanisms, such as texture, twinning, martensite transformation, etc., in their simulations [78], but the first attempts are still rather modest and include a lot of guesswork in the form of extra 'fitting coefficients'. So far, the same argument applies also to the possible inclusion of the 'imperfections' of the real-world cases in the numerical simulations. Therefore, one example of good validation strategy is to choose first only simple tests that with high certainty can be conducted similarly both numerically and experimentally, and then to proceed towards more complex cases and full processes or components [79].

In the comparison of the stress-strain curves for pure copper presented in Fig. 34 with the corresponding curves for the cold heading steel (Publications III and V) and the steels used in the dynamic strain aging studies (Publication VII), the influence of the crystal structure is clear and in line with the schematic presentation of Figure 3. In addition to the different crystal structures, the materials also differ with respect to the homogeneity of their microstructures: the copper samples used in the crusher tests are almost ideal in the sense that the material is a fully annealed high purity single element material with low initial dislocation density and rather uniform and non-

textured grain structure. This means that the bulk or continuum properties of the material describe the material's behavior accurately enough and make, for example, modeling of the material's behavior much simpler and more accurate.

In the tensile tests conducted on the titanium alloy, the original purpose was to compare the results obtained with two different heating methods, but in practice the study turned out to be also a comparison of specimen fixing methods to the bars, and of the combination of the above two. On a general level, the results support the common observation that mechanical fixing of the specimen to the stress bars is prone to cause problems in the wave propagation and subsequent calculation of the stress-strain curve. In addition, it seems that those problems tend to increase with increasing temperature, presumably because of the different thermal expansion of the components involved in the specimen fixing process (specimen itself, bars, pins/bolts, etc.). With proper design and selection of all involved materials, however, such problems might be reduced considerably, although that may also mean that different test materials and specimen designs require different solutions, making testing much more time consuming and requiring trial tests before the actual tests can be performed.

Digital Image Correlation (DIC) is a relatively new technique for the full-field determination of surface strains. At temperatures close to RT, the required speckle patterns can be easily produced by paints that stay on the surface to rather high strains. Also, the high-speed imaging technology (cameras) has made great advances in recent years, and therefore also high-rate events can be recorded at high resolutions. At high temperatures, however, maintaining a good speckle pattern long enough on the surface is still a clear problem, especially if the heating must be continued for extended periods of time. This was seen in the titanium tests, where only the samples heated rapidly with direct electric heating provided good enough images that the DIC software could interpret correctly.

The mechanical behavior of polymeric materials differs from that of metals (and ceramics) considerably because their recoverable (elastic) behavior is time dependent, i.e., viscoelastic, and because their (choice of) active deformation mechanism(s) also depends on the time scale of deformation. If we consider the polymer/elastomer coated paper machine rolls, the first feature could lead to the so-called barring effect, if the relaxation time of the

material is longer than the time of the roll rotation, as mentioned already in Chapter 8.4.

The thermomechanical behavior of steels has a strong dependence on the details of the microstructure. For example, if the microstructure contains free solute atoms, such as carbon or nitrogen, their diffusion before or even during deformation can increase the strength of the material at high temperatures. The latter, of course, refers to the dynamic strain aging phenomenon. It is also important to bear in mind that the chemical composition of materials, especially of steels, is not the only important factor affecting the strength, as the microstructure of most of the metal alloys can be varied by heat treatments. The heat treatment history of the material can also affect the material's strain rate and temperature sensitivities, which further complicates the modeling of the material behavior. In this work, the thermomechanical response of two standard steels with four different heat treatments was studied with special emphasis on the dynamic strain aging effect during high strain rate deformation. For both steels, at low strains the temperature sensitivity is rather low for the banded (WB) and reference microstructures. At higher amounts of plastic strain, the stress-strain response of different steel variants becomes more similar, especially at higher temperatures. The behavior amongst the C45 variants, however, shows more differences than that amongst the corresponding variants of 27MnCr5. This is easily explained by the results of the microscopic inspections, which reveal that in the case of 27MnCr5, the microstructures produced by the different heat treatments are quite similar as opposed to C45, where the microstructures clearly differ from each other. This highlights the effect of microstructure on the material behavior and emphasizes the importance of taking it into account also in the model development.

10 Summary and research questions revisited

The main purpose of this thesis was to examine various technological processes, where time and temperature dependent material behavior plays an important role, and to develop and utilize modeling concepts of material behavior for each of these cases. Three of the cases deal with metals, and one with an elastomer/polymer. An additional case deals with high strain rate high temperature research methods in the form of round-robin testing at two different laboratories. The main scientific contributions of this work, as well as answers to the research questions introduced in Chapter 2, will be presented in the following.

The starting point for the crusher pressure sensor study was the observation that with increasing gun pressures, the crusher sensor readings start to increasingly deviate from the piezoelectric pressure gage readings, which are assumed to represent the correct values. The main results and conclusions from this study can be summarized as follows: 1) the problem arises simply from the use of quasi-static calibration of the copper crusher sensor elements also at higher gun pressures and consequent higher strain rates, 2) with calibration curves that take into account also the strain rate, the observed errors in the pressure readings can be diminished to a reasonable level, and 3) the remaining uncertainty is mainly related to the uncertainty in the determination (or estimation) of the true strain rate during firing. In the modeling of the strain rate dependent stress-strain (or pressure-compression) behavior of the crusher element, the accuracy and applicability of the Johnson-Cook model was found to be insufficient, and therefore a more phenomenological method, comprising pure curve fitting as well as formulations based on known material behavior at high strain rates, was applied. One of the main reasons why the selected approach was successful is that high-purity soft-annealed copper is a 'well-behaving' material with straightforward strain hardening based on the multiplication and interactions of dislocations.

Cold heading is a process where (a piece of) metal wire is deformed to the desired shape in a die. With increasing production rates, also the deformation rates of the metal wire have in many cases increased to a level where the strain rate effects must be accounted for. In the first study (Publication III), the effects of strain rate on the cold headability of steel wires were experimentally investigated by compression and tensile tests conducted in the strain rate range from 10^{-4} to 10^{3} s^{-1} with servo-hydraulic materials testing machines and the Hopkinson Split Bar technique. The primary aim of this study was to develop experimental techniques for the determination of optimal loading amplitudes and loading rates to avoid the formation of cracks in the cold headed components. The main conclusions of this study can be summarized as follows: 1) even at relatively low strain rates in the quasi-static region, the rate of deformation affects the flow stress of steels and should therefore be accounted for in the cold heading processes, 2) at very high strain rates, the transient (strain rate) hardening effect becomes significant and can affect the cold heading process significantly, 3) strain hardening of the studied cold heading steel decreases and strain rate sensitivity increases with increasing strain rate, at least partly due the adiabatic heating of the material, and 4) a practical issue in the high strain rate deformation studies of cold heading steels are the conflicting requirements of large strains at relatively low strain rates

which, however, can be solved by proper modifications of the testing device, as shown in the second study of the cold heading process (Publication V).

Publication V adds four important aspects to the studies conducted in Publication III: 1) with the modified HSB technique, large strains at relatively low strain rates were achieved, 2) the tests were conducted also at elevated temperatures in order to account for the adiabatic heating of the work piece during the high-speed cold forming process, 3) the strain rate and temperature dependent behavior of the studied cold heading steel was numerically modeled and used in the FE simulations of the cold heading process, and 4) the simulation results were validated by an experiment conducted with the same parameter values as the simulation. The main scientific contribution of this study is that it demonstrates how also non-continuous stress-strain behavior of steels, such as the sharp yield point, can be modeled and implemented in finite element codes. It also shows how the microstructural features of steels, in this case a banded structure, can be utilized in the comparison of the simulation results with the experimental validation test results. The agreement between the simulated and experimental results of this study was very good, but also some discrepancies could be observed and attributed to the 'non-perfectnesses' of the experimental conditions compared with the more or less ideal conditions of the simulations.

In the optimization of paper machine roll covers, finite element modeling is a fast and inexpensive tool, provided that adequate material data is available and that it describes all the essential aspect of material behavior properly. In Publication II, the nip pressure was calculated using both linear elastic and hyperelastic models for the cover materials and compared with data measured from real rolls using Fuji color forming and developing films. At low nip loads, the agreement between the measured data and the results calculated using the elastic model for the cover material was reasonable, but the difference increased with increasing nip loads. For a production size paper machine, the measured behavior of the rolls was compared with the simulations done using the elastic model and the hyperelastic model at two different conditions (22 °C, 1 s^{-1}, dry, and 60 °C, 1600 s^{-1}, wet). According to the results, the hyperelastic model of the cover material works better than the elastic model, at least in static nip pressure conditions.

The studies conducted on two different carbon steels undergone four different heat treatments show that the microstructure has a strong effect on the steels' DSA sensitivity, especially at small plastic strains. However, when the amount of deformation increases, the differences between the different steel grades

and their variants decrease, i.e., the conditions for DSA seem to approach each other. In general, of the four variants of both studied steels, the coarse-grained microstructure with large pearlite grains was the most sensitive to dynamic strain aging. For the reference (or standard) and coarse-grained structures of the C45 steel, the maximum of DSA was observed at ca. 620 °C. The two other microstructural variants of C45 and all variants of 27MnCr5 did not yet reach their maximum DSA hardening in the studied temperature range, i.e., at temperatures extending to 680 °C.

The novel scientific contributions of this work can be summarized as follows:

1. Advanced experimental testing and numerical modeling approaches presented in this thesis help to understand the behavior of materials in dynamic industrial processes and facilitate the materials selection and optimization of the process parameters.

2. The results presented in this thesis show that the generic material models, such as the Johnson-Cook model, are useful in describing the material behavior on the general level, but do not usually provide the accuracy that many practical applications require. Therefore, in many cases the fitting-type 'ad hoc' models are more useful and safer to use, especially if they are at least to some extent based on real material phenomena or known type of behavior.

3. The agreement between the results of the cold heading simulations based on 'ad hoc' material models and the corresponding experimental validation tests was very good, except for certain minor differences that could be explained by the slightly 'non-perfect' experimental conditions compared with the simulated ones. In particular, the microstructural inhomogeneities, such as banded structures that result in severely oriented rather than continuum properties, as well as deviations of the work piece shape and size from the assumed ones, were shown to be at least partly responsible for the observed deviations. On the other hand, certain microstructural features, such as the above-mentioned banded structure, can be utilized in the comparison of the experimental and simulated results.

4. The studies related to the dynamic strain aging phenomenon at high strain rates show that the microstructure of materials, especially of steels, should be carefully accounted for when developing material models, and that certain phenomena occur only at some ranges of circumstances and their combinations.

5. The round-robin testing of the titanium alloy demonstrates the importance of the specimen fixing method in the tensile Hopkinson Split Bar testing, especially at elevated temperatures. The results also show that adhesive fixing of the T-HSB specimen is feasible also to quite high temperatures, provided that the specimen heating is very rapid as in the direct electric heating method described in this thesis.

In Chapter 2, four specific research questions were put forth. Many aspects related to these questions were already discussed above, but to finalize this work and to fulfill the formal requirements set for a doctoral dissertation, they are once more revisited to give a concise answer to each question based on the results obtained during the course of this work.

1. How the deteriorating accuracy of the crusher pressure sensor method at increasing gun pressures can be corrected using a materials scientific approach?

The operation of the crusher type pressure sensor is directly related to the response of the sensor element material (copper) to external loading (pressure). From the materials science point of view, the reason for the increasing measurement error with increasing pressure is self-evident: the strain rate in the element during firing of the gun increases and leads to a higher instantaneous strength and reduced deformation of the material. A straightforward remedy for the accuracy issue is to use calibrations that account also for the strain rate effect, as demonstrated in the present work. The remaining issue, however, is that the method as such does not give any direct information about the true strain rate in the element during firing. Luckily, it appears that good estimates for the effective strain rate for different round types can be obtained by analyzing large numbers of actual test firings, which enables achieving reasonably correct pressure readings with the calibrations including also the effect of strain rate.

2. How the increasing deformation rates and the associated internal heating effects can be best accounted for in the cold heading processes?

In technological processes involving large plastic deformations, increasing strain rates increase the demand of energy (force) and affect the flow of material due to local variations in the strain rate and the resulting flow stress. The basic requirement for accounting for the effect of strain rate is that we have reliable (experimental) flow stress data at different plastic strains and strain rates available. As shown in this work, and in a plethora of other publications for almost a century, obtaining stress-strain data over several decades of strain rate is not a problem, except for the range from a few tens to a few hundred per second. Luckily, in that range usually nothing exceptional happens, and the missing data can be quite safely interpolated from the servo-hydraulic testing machine data and the data obtained with the Hopkinson Split Bar technique. In addition, the data obtained at higher strain rates, where adiabatic heating comes into play, inherently contains also the possible effects of internal heating on the flow stress and plasticity of the material. So, based on the general material data determined at different strain rates, reasonable estimates for the required extra energy/force can be readily made. In the designing of the cold heading processes of parts and components, numerical (finite element) simulation is today an essential tool. For the simulation to be meaningful and accurate, the material behavior must be modeled appropriately, taking into account all essential and relevant details of the material behavior. In the case study presented in this thesis work, this means that in addition to the strain rate dependence of the stress-strain behavior of the steel, also its sharp yield behavior should be included in the model. This kind of 'discontinuous' behavior (in the sense of its mathematical formulation) is very difficult to model by any of the commonly used material models or their modifications, such as the Johnson-Cook model, and therefore an alternative approach of splitting the stress-strain curve into two separate parts and modeling each of them with the best available fitting function was taken. With this concept, the results of the experimental validation tests could be reproduced by simulation with reasonable accuracy. The deviations between the simulated and experimental results appear to stem from the "non-perfectness" of the experimental samples and the banded microstructure of the cold headed steel wire.

3. How to account for the strain rate and temperature dependent mechanical behavior of elastomeric (rubber) materials in paper machine roll coating designing?

Soft polymer or elastomer coatings are used in the paper machines for many different reasons. In practically all cases, modeling plays an important role as it both improves the technical performance of the roll systems as well as lowers the design expenses. For example, the rolls studied in this work are exceptionally long, up to 11 meters, and modeling is an excellent tool for determining the correct shape (crowning) of the rolls to ensure that the nip pressure is adequate and uniform. Finite element codes usually contain numerical models for linearly elastic, viscoelastic, and so-called hyperelastic materials. Basically, linearly elastic and hyperelastic materials, and consequently also their models, are strain rate independent. However, they can also be used to study the material behavior at different temperatures and strain rates, provided that they are properly calibrated at the same conditions where the simulations are to be performed. In this study, the calibration data was acquired by compression testing with a servo-hydraulic testing machine in the quasi-static strain rate region and with a Hopkinson Split Bar device at a high strain rate at predetermined temperature and moisture conditions. Comparison of the experimental data and the simulation results shows that the hyperelastic model of the cover material leads to a better agreement in the nip pressure than the elastic one. The simulations can be used to predict the mechanical contact conditions between the mating rolls and to explain the observed changes in the wrinkling amplitude and directions of the paper web.

4. What kind of effects the dynamic strain aging phenomenon brings about to the high strain rate high temperature response of carbon steels?

The strength of crystalline materials normally decreases with increasing temperature in a gradual and predictable manner, when the increasing thermal energy replaces part of the mechanical energy needed to move the dislocations on the glide planes. Above a certain strain rate dependent ‘critical’ temperature, however, the slope of the strength decline becomes very small, as the (still) increasing thermal energy cannot anymore help the dislocations move, i.e., the thermal component of flow stress approaches zero (cf. Figs. 1 and 2). The (dynamic) strength of certain low carbon steels, however, can again start to increase when the material temperature exceeds ca. 400 °C. This is due to the dynamic strain aging (DSA) effect, where the diffusional movement of small solute atoms is fast enough to keep up with the moving

dislocations, causing a drag force that impedes the dislocation motion. To maintain the imposed strain rate, more external force is required, which shows up as a higher flow strength of the material. The amount of hardening caused by the dynamic strain aging depends, at least, on the strain rate, temperature, density of mobile dislocations, concentration of free solute atoms, and the free glide distance of the dislocations. Several of these key factors are related to the microstructure of the material which, especially in the case of carbon steels, can be quite easily altered by thermomechanical treatments. This work focuses on the experimental characterization of the DSA effect in two commonly used steels, and on demonstrating the effects of the microstructure, grain size, and prior heat treatments on the overall dynamic thermomechanical response of the steels. The results reveal the strength of the DSA effect in altogether eight different variants of the two studied steel grades, as well as the circumstances (temperature and strain rate regimes) of their appearance. For a more precise quantification of the DSA effect in each studied case (i.e., steel composition and heat treatment/microstructure), determination of the free solute atom concentrations for example with the pendulum method would be necessary. In addition to the 27MnCr5 and C45 steels studied in Publication VII, also the cold heading steel C17C studied in Publications III and V showed a rather strong DSA effect with the maximum flow stress appearing at around 600 °C. The DSA effect was also included in the presented material model, but no separation between the 'ordinary' thermal softening and DSA hardening was attempted, primarily due to the fact that the temperatures where the DSA effect appears are rather high regarding the cold heading process. From a scientific point of view, however, separation of these two phenomena would be interesting, but that would require a different type of approach to modeling, based more on the underlying physics of thermal softening and dynamic strain aging, as well as the microstructural features of the examined materials.

11 References

1. Nyberg H. (2009) Evaluation of gun propelling charge by performance during the life cycle by statistical utilization of data collected in tests and troop gun firings. Doctoral dissertation, Aalto University.
2. Kettunen P.O. and Kuokkala V.-T. ”Plastic Deformation and Strain Hardening”, Materials Science Foundations, Vol 16-18, Trans Tech Publications, Uetikon-Zurich, 2003.
3. S. Osovski, D. Rittel, A. Venkert (2013), The respective influence of microstructural and thermal softening on adiabatic shear localization, Mechanics of Materials, Vol. 56, pp. 11-22.
4. Isakov M. (2012), Strain rate history effects in a metastable austenitic stainless steel. PhD thesis. Tampere University of Technology.
5. Curtze S. (2009), Characterization of the Dynamic Behavior and Microstructure Evolution of High Strength Sheet Steels. PhD thesis. Tampere University of Technology.
6. Hokka M. (2008), Effects of Strain Rate and Temperature on the Mechanical Behavior of Advanced High Strength Steels. PhD thesis. Tampere University of Technology.
7. Baird J (1971) Effects of strain aging due to interstitial solutes on the mechanical properties of metals. Metall Rew 149:1–18
8. Hopkinson B., A method of measuring the pressure produced in the detonation of high explosives or by the impact of bullets. Philosophical transactions of the Royal Society in London, A 213 (1914).
9. Gray George T. III “Classic Split-Hopkinson Pressure Bar Testing”, Mechanical Testing, Vol 8, ASM Handbook, American Society for Metals, 2002.
10. Meyers M. A., 1994. Dynamic Behavior of Materials, John Wiley & Sons, Inc., New York.
11 . Florando, Jeffrey N., El-Dasher, Bassem S., Chen, Changqiang, Swift, Damian C., Barton, Nathan R., McNaney, James M., Ramesh, K. T., Hemker, Kevin J., Kumar, Mukul. Effect of strain rate and dislocation density on the twinning behavior in tantalum. AIP Advances 6, 045120 (2016); https://doi.org/10.1063/1.4948528.
12 . Cronje, S., Kroon, R.E., ROOS, W.D. et al. Twinning in copper deformed at high strain rates. Bull. Mater. Sci., Vol. 36, No. 1, February 2013, pp. 157–162.

13 . S. Curtze, V.-T. Kuokkala Dependence of tensile deformation behavior of TWIP steels on stacking fault energy, temperature and strain rate/ Acta Materialia 58 (2010) 5129–5141.
14. Zerilli, F.J., Armstrong, R.W., 1987. Dislocation-mechanics-based constitutive relations for material dynamics calculations. J. Appl. Phys. 61, 1816–1825.
15. Rusinek A. Rodriguez-Martinez J., Arias A. A thermo-viscoplastic constitutive model for FCC metals with application to OFHC Copper. International Journal of mechanical sciences, 2010, vol. 52, n. 2, p. 120-135
16. Rodriquez P. (1984) Serrated Plastic Flow. Bull. Mater. Sci. Vol.6 pp. 653-663.
17. Chen J, Nemat-Nasser S (2000) A model for experimentally observed high strain rate dynamic strain aging in titanium. Acta Mat. 48:3131-3144.
18. Nemat-Nasser S (2000) Flow stress of commercially pure niobium over a broad range of temperatures and strain rates. Mat.Sci.Eng.A. 284:202-210.
19. Nemat-Nasser S, Guo W (2000) High Strain rate response of commercially pure vanadium. Mech.Mat. 32:243-260.
20. Cheng J, Nemat Nasser S, Guo W (2001) A unified constitutive model for strain rate and temperature dependent behavior of molybdenum. Mech.Mat. 33:603-616.
21. Nemat-Nasser S, Guo W, Liu M (1999) Experimentally based micromechanical modeling of dynamic response of molybdenum. Scripta Mat. 40:859-872.
22. Baird J, Jamieson A (1966) Effects of manganese and nitrogen on the tensile properties of iron in the range of 20-600 centigrades. J.Iron.Steel.Inst.
23. Nemat-Nasser S, Guo W (1997) Thermomechanical response of DH-36 structural steel over a wide range of strain rates and temperatures. Mech.Mat. 35:1023-1047.
24. Shahriary M, Koohbor B, Ahadi K, Akrami A, Khakian-qumi M (2012) The effect of dynamic strain aging on room temperature mechanical properties of high martensite dual phase steel. Mat.Sci.Eng.A. 550:325-332.
25. Forni D, Chiaia B, Cadoni E (2016) High strain rate response of S355 at high temperatures. Mat.design. 94:467-478.

26. Wang J, Guo W, Gau W, Su J (2015) The third type of strain aging and the constitutive modeling of a Q245B over a wide range of temperatures and strain rates. Int.J.Plasticity. 65:85-107.
27. Gilat A, Wu X (1997) Plastic deformation of 1020 steel over a wide range of strain rates and temperatures. Int.J.plast. 13:611-632.
28. Nemat-Nasser, S., Guo, W.-G., 2005. Thermomechanical response of HSLA-65 steel plates: experiments and modeling. Mech. Mater. 37, 379–405.
29. I. M. Ward, D. Hadley: An introduction to the mechanical properties of solid polymers, Wiley and sons, New York, 1997.
30. T. Mukhopadhyay, S. Adhikari, A. Batou, Frequency domain homogenization for the viscoelastic properties of spatially correlated quasi-periodic lattices, International Journal of Mechanical Sciences 150 (2019) 784–806
31. Vuoristo T., Kuokkala V-T., Creep, recovery and high strain rate response of soft roll cover materials, Mechanics of Materials 34 (2002) 493–504].
32 Vermonden, Tina. (2005). Supramolecular coordination polymers in water: rings, chains and networks. Doctoral dissertation, Wageningen University & Research, ISBN 90-8504-148-1.
33. Swallowe G.M. (1999) Time-Temperature Equivalence. In: Swallowe G.M. (eds) Mechanical Properties and Testing of Polymers. Polymer Science and Technology Series, vol 3. Springer, Dordrecht, https://doi.org/10.1007/978-94-015-9231-4_54
34. Gilat, A., Seidt, J.D., Matrka, T.A., Gardner, K.A., A New Device for Tensile and Compressive Testing at Intermediate Strain Rates, Experimental Mechanics 2019, Article in Press]
35. Vuoristo T. (2004), Effect of Strain Rate on the Deformation Behavior of Dual Phase Steels and Particle Reinforced Polymer Composites. PhD thesis. Tampere University of Technology.
36. Nemat-Nasser S., 2001. Introduction to high strain rate testing, In ASM Handbook Vol. 8: Mechanical Testing and Evaluation. Materials Park, Ohio.
37. Gorham, D.A., 1983. A numerical method for the correction of dispersion in pressure bar signals. J. Phys. E. 16, 477–479.
38. Frew, D.J., Forrestal, M.J., Chen, W., Pulse shaping techniques for testing brittle materials with a split Hopkinson pressure bar, Experimental Mechanics, Volume 42, Issue 1, March 2002, Pages 93-106.

39. Gilat A. Seidt J. Yang P. (2017) Incorporating DIC in high strain rate testing of fibrous composite with the split hopkinson Bar. International conference on Composite Materials, Xi'an, China.
40. Gomez-del Rio T., Barbero E., Zaera R., Navarro C., Dynamic tensile behavior at low temperatura of CFRP using a Split Hopkinson Pressure Bar. Composite Science and Tecnology, 2005, vol. 65, n. 1, p. 61-71
41. M. Hokka, S. Curtze, V.-T. Kuokkala: Tensile HSB testing of sheet steels at different temperatures. In the proceedings of SEM annual conference 2007, Springfield MA, USA.
42. Nemat-Nasser S., 2000. Recovery Hopkinson Bar Techniques, In ASM Handbook Vol. 8: Mechanical Testing and Evaluation. Materials Park, Ohio.
43. Apostol M. (2007) Strain rate and temperature dependence of the compression behavior of FCC and BCC metals. Development of experimental techniques and their application to material modeling. PhD thesis. Tampere University of Technology.
44. M. Isakov, S. Hiermaier, V.-T. Kuokkala (2014), Improved Specimen Recovery in Tensile Split Hopkinson Bar. Philosophical Transactions, A372.
45. Isakov M. Strain rate change tests with the Split Hopkinson Bar method, European Physical Journal: Special Topics. Volume 225, Issue 2, 1 April 2016, Pages 231-242.
46. Nemat-Nasser S, Guo W, Kihl D (2001) Thermomechanical response of AL-6XN stainless steel over a wide range of strain rates and temperatures. J. Mech.Phys.Sol. 49:1823-1846.
47. Zhang Chao, Suo Tao, Tan Weili, Zhang, Xinyue, Liu Jiejian, Wang Cunxian, Li Yulong. An experimental method for determination of dynamic mechanical behavior of materials at high temperatures. International journal of Impact Engineering. Vol. 102, April 2017.
48. B. Davoodi, A. Gavrus, E. Ragneau, 2005. A technique for measuring the dynamic behaviour of materials at elevated temperatures with a compressive SHPB, pp. 153-162, Computational Methods and Experiments in Materials Characterisation II, vol. 51, WIT Transactions on Eng. Sciences, C.A. Brebbia & A.A. Mammoli, (Eds.), Southampton, UK, 2005.
49. Apostol, M., Vuoristo, T., Kuokkala, V.-T., 2003. High temperature high strain rate testing with a compressive SHPB. J. Phys. IV 110, 459–464

50. B. Song K. Nelson R. Lipinski J. Bignell G. Ulrich E. P. George Dynamic High-temperature Testing of an Iridium Alloy in Compression at High-strain Rates. Strain, 2014, vol 50, pp 539-546.
51. X. Nie & W.W. Chen; Dynamic Equibiaxial Flexural Strength of Borosilicate Glass at High Temperatures. Experimental Mechanics (2012) 52, 135-143.
52. A.M.Lennon, K.T.Ramesh A technique for measuring the dynamic behavior of materials at high temperatures. International journal of plasticity, vol. 14, (1998), pp. 1279-1292.
53. Seo S, Min O, Yang H. Constitutive equation for Ti–6Al–4V at high temperatures measured using the SHPB technique. International Journal of Impact Engineering 2005; 31:735–54.
54. Loctite 480™, Technical Data sheet, (2006).
55. D. Raabe; Computational Materials Science, Wiley, New York 1998.
56. Hart, E.W., Constitutive relations for non-elastic deformation, Nuclear Engineering and Design Volume 46, Issue 1, March 1978, Pages 179-185.
57. Johnson G.R. and Cook W.H. "A constitutive model and data for metals subjected to large strains, high strain rates, and high temperatures", in "Proc. 7th Int. Symp. on Ballistics", publ. The Hague, The Netherlands, pp. 541-547, 1983.
58. A. Gavrus Formulation of a new constitutive equation available simultaneously for static and dynamic loadings DYMAT - International Conference on the Mechanical and Physical Behaviour of Materials under Dynamic Loading, 2 (2009) 1239-1244 DOI: https://doi.org/10.1051/dymat/2009174.
59. Ravindranadh Bobbili and VemuriMadhu, A modified Johnson-Cook model for FeCoNiCr high entropy alloy over a wide range of strain rates, Materials Letters Volume 218, 1 May 2018, Pages 103-105.
60. Sanxing Wang 1, Yuanchun Huang 1,2,*, Zhengbing Xiao 1,2 [OrcID] , Yu Liu 2 and Hui Liu 2, A Modified Johnson-Cook Model for Hot Deformation Behavior of 35CrMo Steel, Metals 2017, 7(9), 337; https://doi.org/10.3390/met7090337].
61. Leemet T, Hokka M, Shrot A, Baeker M, Kuokkala V-T (2012) Characterization and numerical modeling of the high strain rate mechanical behavior of Ti 15-3 alloy for machining simulations. Mat.Sci.Eng.A. 550:350-357.
62. Hokka M, Leemet T, Shrot A, Baeker M, Kuokkala V-T (2014) Dynamic behavior and high speed machining of ti-6246 and Alloy 625

superalloys: experimental and modeling approaches. Exp.Mech. 54:199:210.
63. Rule, W.K., Jones, S.E., 1998. A revised form for the Johnson–Cook strength model.Int. J. Impact Eng. 21, 609–624.
64. Khan A., Huang S., Experimental and theoretical study of mechanical behavior of 1100 aluminum in the strain rate range of 10-5 to 104 s-1. International Journal of Plasticity, 8 (1992).
65. Khan A., Liang R., Behaviors of three BCC metal over a wide range of strain rates and temperatures: experiments and modeling. International Journal of Plasticity, 15 (1999).
66. Zerilli, F.J., Armstrong, R.W., 1987. Dislocation-mechanics-based constitutive relations for material dynamics calculations. J. Appl. Phys. 61, 1816–1825.
67. Zerilli F., Armstrong R., Thermal activation based constitutive equations for polymers. Journal de Physique IV, 10 (2000).
68. Kocks U., Laws for work-hardening and low-temperature creep. Journal of Engineering Materials and Technology, 98 (1976).
69. Follansbee P, Kocks U (1988) A constitutive description of the deformation of copper based on the use of mechanical threshold stress as an internal state variable. Acta. Met. 36:81-93.
70. Eyring H., Viscosity, plasticity, and diffusion as examples of absolute reaction rates. Journal of Chemical Physics 4 (1936) 283-291.
71. Bauwens-Crowet, C., Bauwens, J.A. and Homes, G. (1969) Tensile yield-stress behavior of glassy polymers. J. Polym. Sci. A2, 7, 735.
72. Abaqus manuals. Version 6.5. 2004.
73. Isakov, M. Strain Rate History Effects in a Metastable Austenitic Stainless Steel, Doctoral thesis, Tampere University of Technology, 2012.
74. Kuokkala, V.-T., Isakov, M., Rämö, J., Curtze, S. and Hokka, M., Effects of adiabatic heating on the plasticity of steels at high strain rates, Proc. of the 15th International Symposium on Plasticity and its Current Applications, St. Thomas, US Virgin Islands, January 3.-8. 2009, pp. 154-156, 2009.
75. Austrell P.-E., 1997. Modeling of elasticity and damping for filled elastomers, Lund University, Sweden.
76. Walley S., Field J. Strain rate sensitivity of polymers in compression from low to high strain rates. Dymat Journal, Vol. 1. (1994) pp 211-227.

77. Siviour C. Jordan J. High Strain rate mechanics of polymers: A Review. Journal of Dynamic behavior of materials (2016), vol. 2, pp. 15-32.
78. M. Lindroos, A. Laukkanen, M. Isakov, T. Andersson and S. Forest, "Crystal plasticity modelling of transformation plasticity effects in metastable austenitic stainless steel microstructures," in International Conference of Plasticity, Damage & Fracture, Panama City, 2019.
79. Matti Lindroos, Maria Apostol, Veli-Tapani Kuokkala, Anssi Laukkanen, Kati Valtonen, Kenneth Holmberg, Olli Oja. Experimental study on the behavior of wear resistant steels under high velocity single particle impacts. International Journal of Impact Engineering, vol. 78, pp. 114-127. (2015).

PUBLICATION I

Calibration of crusher pressure gauges by high strain rate testing

V-T. Kuokkala, J. Rämö and T. Vuoristo

SEM X International Congress & Exposition on Experimental and Applied Mechanics, Costa Mesa, California, U.S.A., June 7-10, 2004

Calibration of crusher pressure gauges by high strain rate testing

Veli-Tapani Kuokkala, Jari Rämö and Taina Vuoristo
Tampere University of Technology, Institute of Materials Science
POB 589, FIN-33101 Tampere, Finland

ABSTRACT

Gun pressures can be measured by so-called crusher pressure gauges, which are based on the plastic deformation of cylindrical copper elements. Especially at high pressures the crusher pressure readings, however, may deviate from the corresponding values measured by piezoelectric pressure transducers by as much as 25 %. The basic reason for this difference is the strain rate dependence of the deformation behavior of copper. The purpose of this work was to improve the accuracy of crusher pressure measurement and to ensure that the readings are correct also at high pressures. For this aim, the plastic deformation of copper was studied at different strain rates by servo-hydraulic materials testing machines and the Hopkinson Split Bar (HSB) device. Based on experimental stress-strain curves, a mathematical model that converts the measured plastic deformation into maximum pressure was developed. The variables in the model are the amount of plastic deformation and the average strain rate in the crusher element during the application of pressure. The comparison of pressure values obtained form the manufacturers' calibration curves, piezoelectric pressure transducer measurements, and from the developed model shows that the new method improves significantly the accuracy of crusher gauge pressure measurements.

INTRODUCTION

In the acceptance test firings of guns and ammunition, gun pressures are routinely measured by so-called crusher pressure gauges, shown in Figure 1. The advantages of crusher gauges, compared with the newer piezoelectric pressure transducers, are that crusher gauges do not require any changes in the gun construction, they are inexpensive, easy to use, and do not require any electronic instrumentation. The problem, however, is the observation that the crusher pressure readings may deviate quite considerably from the corresponding values measured by piezoelectric pressure transducers. The pressure readings obtained by crushers from different manufacturers are not consistent, either. It has become clear that the crusher and piezoelectric pressure transducer readings differ, depending on the pressure range and the used gun type, by as much as –10 to +20 % in the pressure range of ca. 90-500 Mpa, and that the deviation normally increases with pressure. It is anticipated that the gun pressures in the future are still increasing, which means that the difference between pressure readings obtained by different measurement techniques is going to increase, too.

If the pressure measurement indicates a pressure that is much less than the true pressure, it is possible that the safety limits of the gun pressure are exceeded, resulting in a failure of the gun. Another practical problem is that the comparison of the pressures measured in different places (countries) is quite difficult, which complicates the acquisition and trade of guns and ammunition.

The starting point of this study is the assumption that the piezoelectric pressure transducer readings are reliable and that crusher readings contain errors that depend on the maximum pressure value during firing and the used gun type. The reliability of the piezoelectric pressure transducer readings was not separately analyzed.

The crusher method is based on the proportionality of the plastic deformation of the crusher element and gun pressure which, because of the strain hardening of copper, is non-linear not only with respect to stress (pressure) but also with respect to strain rate. Because the manufacturers of crusher elements usually give calibration tables (curves) determined for one or at most two different strain rates, the gun pressures calculated from these conversion tables cannot be accurate at all strain rates.

The aim of this study was to improve the accuracy of crusher pressure measurements and to make sure that the readings are reliable also at high gun pressures and high strain rates.

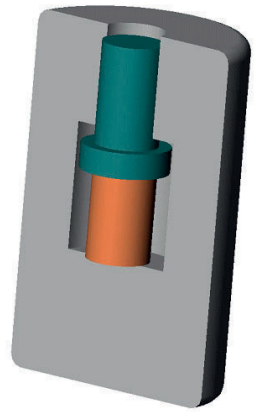

Figure 1. Crusher pressure gauge

The goal was to develop a mathematical model, which converts the measured plastic deformation of the crusher element to the maximum pressure taking into account the true deformation and strain hardening behavior of copper as a function of both stress (pressure) and strain rate. In order to achieve this goal, we need to know 1) the stress-strain response of the copper used in the crusher elements at different strain rates and 2) the strain rate in the element during firing.

The deformation behavior of crusher element materials at high strain rates can be studied with hydraulic testing machines of sufficient loading capacity and, especially, by the Hopkinson Split Bar (HSB) devices. By conducting compression tests at different strain rates, the entire pressure/strain rate range relevant to gun pressure measurements can be mapped. The variables in the mathematical model are the amount of plastic strain experienced by the copper element and the strain rate in it during firing. The amount of plastic deformation can be easily measured from the element after firing by a conventional micrometer, but the strain rate can be measured only *during* firing which, of course, is not possible in the crusher technique. It has turned out, however, that the time to reach the maximum pressure (and, consequently, maximum strain) depends more on the gun type than on the maximum pressure, and therefore quite reasonable estimates for the strain rate can be obtained indirectly by making use of piezoelectric pressure transducer time-pressure measurements on different gun types. Other possibilities for the measurement of strain rate are also discussed in this paper.

THEORETICAL BACKGROUND

Plastic deformation in metals takes place by the glide of dislocations. The force moving the dislocations is provided both by the external shear stress acting on the glide plane and by the thermal vibrations of atoms, so that the flow stress of the material (at a given strain and strain rate) can be written as $\tau = \tau_A + \tau^*$, where τ_A is the athermal and τ^* the thermal component of the external flow stress. When the temperature increases, more thermal energy is available for the motion of the dislocation, and τ^* is reduced. On the other hand, the amplitude, and thus the energy, of thermal vibrations has a distribution in time, which means that the availability of sufficient energy for the dislocation to overcome a certain obstacle is time dependent. With increasing strain rate, the dislocation may not have time to wait for the thermal activation but the missing energy must be replaced by increasing the external stress, i.e., its thermal component τ^*, which means that the observed flow stress of the material increases [1]. The strain rate effects on the material's flow stress can also be due to various drag effects ('viscous drag'), but they become effective only at higher strain rates ($\sim 10^3$ s^{-1}) than those normally observed in crusher applications.

EXPERIMENTAL TECHNIQUES

As discussed above, the strength and therefore also the plastic deformation of metals depends on strain rate. At low and intermediate strain rates, which usually refer to the range of $\sim 10^{-4}$ - 10^1 s^{-1}, the phenomenon can be studied with conventional hydraulic materials testing machines. With special arrangements strain rates as high as ~200-500 s^{-1} can be achieved in tension. In compression, however, at high strain rates above $\sim 10^2$ s^{-1} special devices are needed, and most commonly this means the use of Hopkinson Split Bar devices, the principle of which is shown in Figure 2.

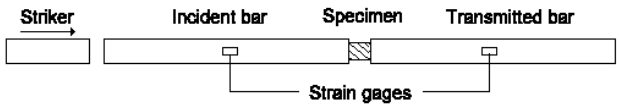

Figure 2. The general principle of a compressive Hopkinson Split Bar -device.

When a striker is shot at the end of the first (incident) pressure bar, a compressive elastic wave with a length twice the length of the striker, is generated. The elastic wave travels at a speed of sound in the bar to the interface between the bar and the specimen, where part of the wave is reflected back as a wave of tension, while part of the original wave goes through the specimen into the second (transmitted) bar. The elastic waves are recorded from the pressure bars with strain gages, and from the three resulting waves (incident, reflected, and transmitted), the strain, stress, and strain rate in the specimen can be calculated using the following equations [2]:

stress in the specimen:
$$\sigma(t) = \frac{A\,E\left[\varepsilon_i(t) + \varepsilon_r(t) + \varepsilon_t(t)\right]}{2A_s} \tag{1}$$

strain in the specimen:
$$\varepsilon(t) = \frac{C_0}{L_s}\int_0^t \left[\varepsilon_t(t) - \varepsilon_i(t) + \varepsilon_r(t)\right] dt \tag{2}$$

strain rate in the specimen: $$\dot{\varepsilon}(t) = \frac{C_0\left[\varepsilon_t(t) - \varepsilon_i(t) + \varepsilon_r(t)\right]}{L_s} \quad (3)$$

In equations 1-3, A is the cross-section of the bars, E is the Young's modulus of the bar material, C_0 is the longitudinal sound velocity in the bars, A_s is the cross-section of the specimen, and L_s is the length of the specimen. A general view of the Hopkinson Split Bar device used in this work is shown in Figure 3.

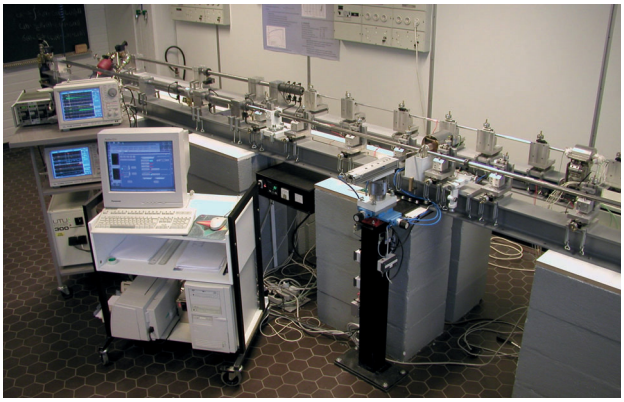

Figure 3. Hopkinson Split Bar device at the Institute of Materials Science, Tampere University of Technology.

MATERIALS

In this work, plastic deformation of copper crusher elements from two different manufacturers (denoted as "A" and "B") was studied as a function of strain rate. The nominal diameter and length of all elements, which where used as test specimens as such, were 5 mm and 7 mm, respectively. The aspect ratio of the specimens was therefore quite large (1.4), which is ideal for the low strain rate tests but not for the Hopkinson tests, where the aspect ratio is normally kept close to 0.5. In the current work, however, this was not expected to cause any problems because the primary task was to study the behavior of the elements rather than to determine the material properties. The chemical compositions of the two materials were practically identical, as shown in Table 1. The grain sizes of the materials, however, differed quite much, which explains the different calibration values of the elements through the common $d^{-½}$ (Hall-Petch) dependence. Microstructures of the materials are shown in Figure 4.

Table 1. Chemical compositions and average grain sizes of the studied materials.

	A (d ~15μm)	B (d ~50μm)
Cu	99.998%	99.998%
C	<0.001%	0.001%
Ag	14 ppm	14 ppm
Al	<10 ppm	<10 ppm
Cd	<5 ppm	<5 ppm
Cr	<10 ppm	<10 ppm
Fe	3 ppm	4 ppm
Mn	<1 ppm	<1 ppm
Ni	<10 ppm	<10 ppm
Si	<20 ppm	<20 ppm
Zn	<10 ppm	<10 ppm
O	26 ppm	29 ppm

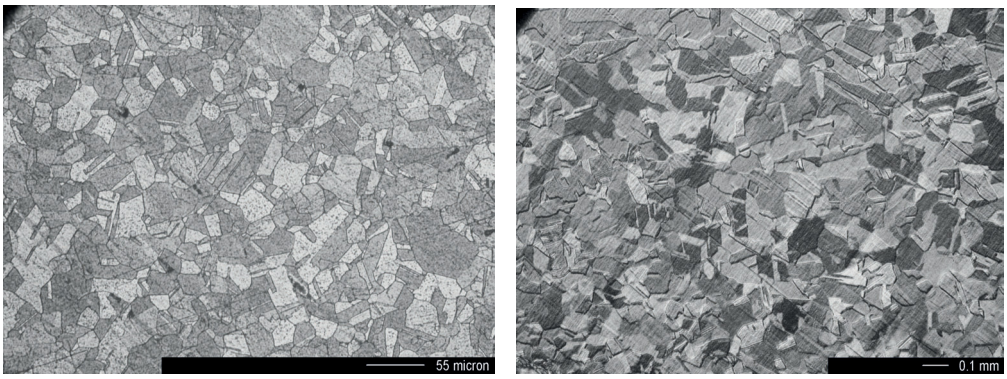

Figure 4. Microstructures of the studied materials, A (left), B (right).

TESTS AND RESULTS

The low and intermediate strain rate compression tests (<5 s^{-1}) were conducted with an Instron 8800 servo-hydraulic materials testing machine between two tungsten carbide hard metal compression plates. In the Hopkinson Split Bar tests the biggest challenge was to obtain low enough strain rates at the same time with high strains. In practice, the strain rate in a HSB test depends on the length of the specimen, length of the loading pulse, and total amount of strain. Because the specimen length could not be varied (i.e., all tests were conducted on original crusher elements), the only possibilities were to lengthen the duration of the loading pulse or to limit the amount of strain in a single experiment. Most of the tests were conducted using an extra long striker of 1000 mm, which gives a pulse duration of about 400 μs (the length of the pulse is 2L, where L is the length of the striker). With this arrangement the strain rate could be dropped to a level of ~800 s^{-1} while the total strain was still the required 40 %. At strain rates below this the required total strain could not be reached in a single test but the specimen had to be deformed several times. By carefully adjusting the amplitude of the incident pulse, multiple loadings during a single test could be avoided without the use of a recovery system (use of a recovery system with a 1000 mm striker would have required the use of a too long incident bar for the current set-up). The lowest strain that could be achieved with this technique was about 80 s^{-1}. The individual stress-strain curves were added end-to-end after confirming the starting strain of each test by measuring it directly from the specimen. An example of the results and data handling of a HSB test is given in Figure 5.

MODELING

The modeling of the effects of strain rate on the deformation behavior of materials can be based on both physical and phenomenological models. One of the most commonly used models is the Johnson-Cook model, where flow stress σ depends on strain, strain rate, and temperature according to the following equation [3]

$$\sigma = \left(\sigma_0 + B\varepsilon^n\right)\left(1 + C\ln\frac{\dot{\varepsilon}}{\dot{\varepsilon}_0}\right)\left(1 - \left[\frac{T - T_r}{T_m - T_r}\right]^m\right) \tag{4}$$

where ε is the strain, $\dot{\varepsilon}$ the strain rate, and $\dot{\varepsilon}_0$ the reference strain rate, which usually has a value of 1.0 s^{-1}.

In the present study, the temperature was kept constant and therefore only the first two terms of equation (4) were included in the modeling. The main drawback of the Johnson-Cook model is that it assumes the effects of strain and strain rate (and temperature) to be independent of each other, which is generally known not to be true. On the other hand, in many cases the model works reasonably well, its parameters are easy to determine from a limited number of experiments, and the model is easy to implement in different finite element computer codes, which explains the widespread popularity of the model. In this case, however, the model could not describe the behavior of the crusher elements well enough, and therefore an alternative approach to modeling had to be taken.

Because the main purpose of this study was to develop a model for the conversion of the change in the crusher element's length to maximum pressure, the model does not have to be a so-called parametric constitutive model. Therefore, the goal can be achieved also by a mere fitting function, which describes accurately enough the dependence of the plastic deformation of the crusher element on the maximum pressure under given circumstances. Candidates for the function that would fit all the

stress strain curves determined at different strain rates were searched by *TableCurve 2D*®, and the best simple function turned out to be the rational function

$$\sigma = \frac{(a + c\varepsilon)}{(1 + b\varepsilon)} \tag{5}$$

whose parameters a, b and c for each stress strain curve of material B are presented in Table 2. Figure 6 shows, that the function describes all the stress strain curves very well.

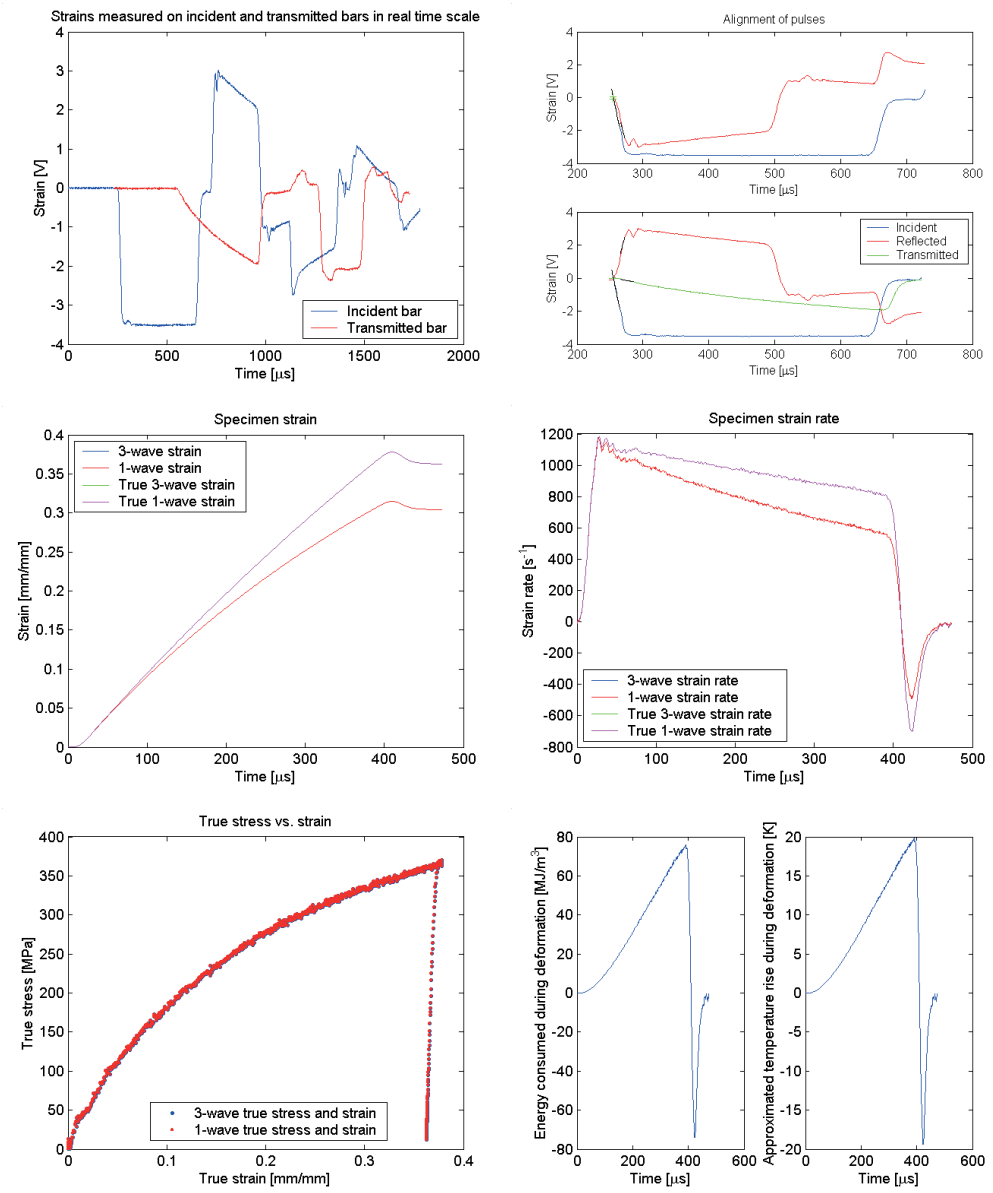

Figure 5. An example of the results and data handling of a Hopkinson Split Bar –test data.

Table 2. Fitting parameters of equation (5) for material B.

$\dot{\varepsilon}$ (s^{-1})	a	b	c
0.0014	23.28798	5.345203	2405.492
0.1126	23.42199	4.784474	2375.701
2.3963	24.84452	4.67641	2423.818
88.3	29.26381	4.315714	2287.817
306	20.64857	3.600842	2222.203
492	24.54853	3.460277	2167.054
519.8	18.22643	3.840796	2302.682
916	24.34579	3.335467	2156.783
928.2	26.66988	3.710483	2310.544

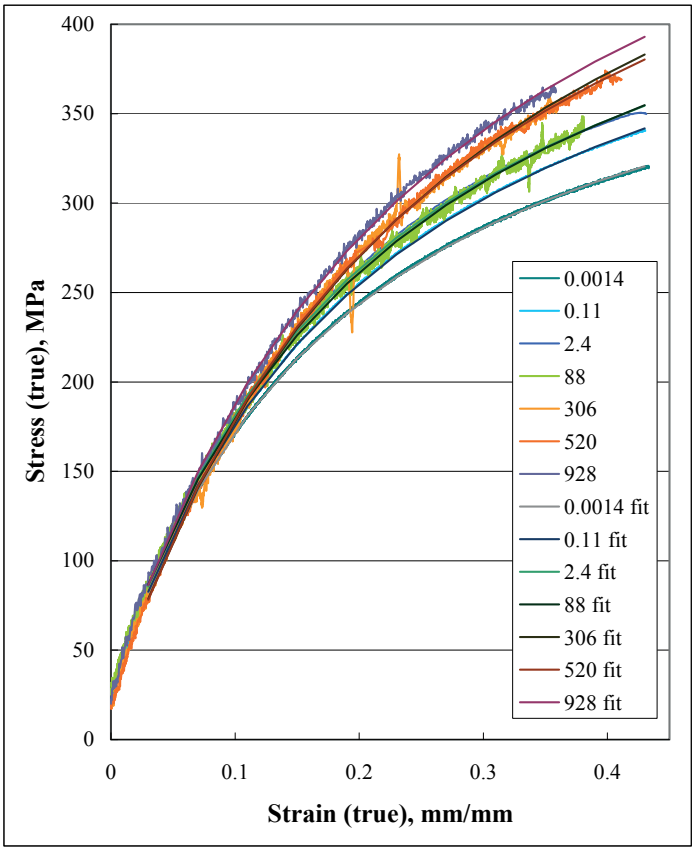

Figure 6. Fitting of equation (5) to the measured stress strain data. Some of the original curves were produced by several consecutive compression tests on the same specimen.

From experience we know that in the strain rate region where dislocation motion is thermally controlled the flow stress depends on strain rate as $\sigma \propto \ln(\dot{\varepsilon})$. On the other hand, thermally activated dislocation motion depends on the obstacle structure on the slip plane, which in the case of pure metals consists mainly of other dislocations. The number and arrangements of these dislocations depend on the amount of preceding strain and on the rate at which this strain was achieved. Therefore, the flow stress depends on strain both directly and through the strain dependent strain rate effect, and the conversion equation can be finally written as

$$\sigma(\varepsilon) = A(\varepsilon) + B(\varepsilon)\ln(\dot{\varepsilon}) \tag{6}$$

Functions A(ε) and B(ε) are determined by first making constant strain sections for the stress strain curves reconstructed using equation (5), from which we can construct σ *vs.* $\ln(\dot{\varepsilon})$-plots at different values of strain, as shown in Figure 7. Then we fit the function $\sigma = A + B\ln(\dot{\varepsilon})$ to each of these curves (which actually are more or less straight lines), and get A and B at different values of strain. Figure 7 shows also this fitting at strains from 3 to 43 %. Finally, we fit equation (5) again to A vs. ε data and a second order polynomial to B vs. ε data to get the final model with six parameters and two variables. An example of the A vs. ε fit for material B is shown in Figure 8, and the final parameter values for both studied materials in Table 3.

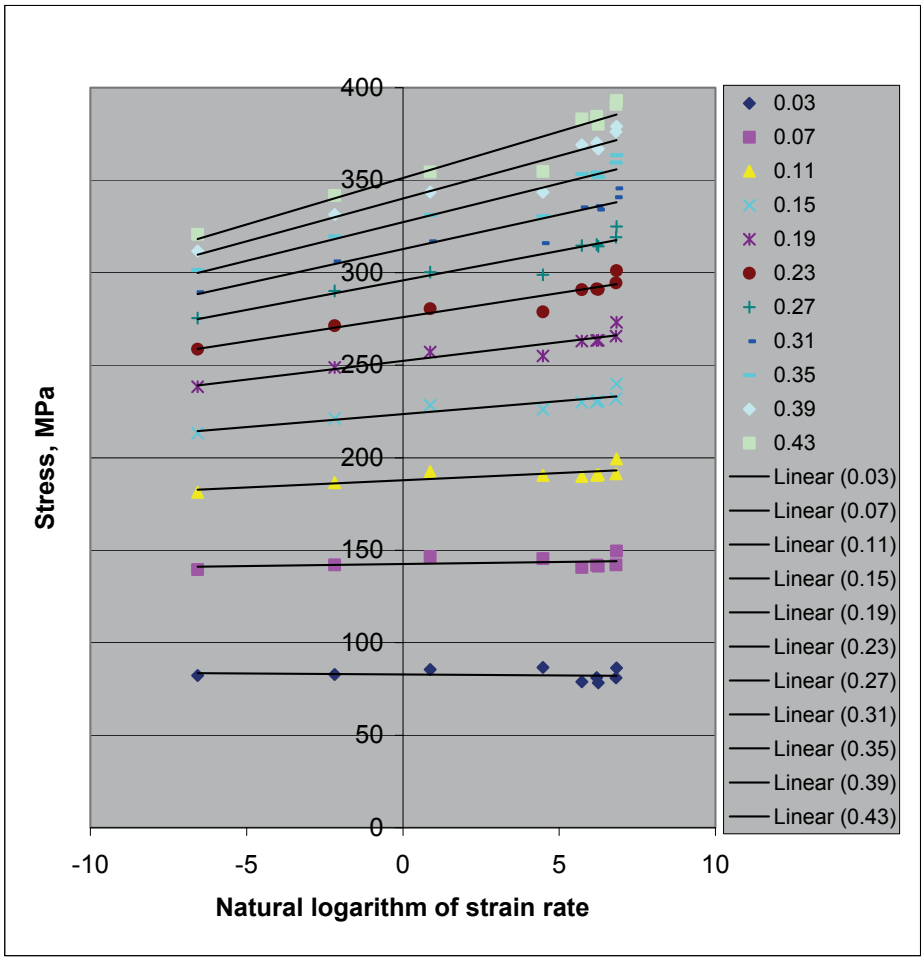

Figure 7. Stress–strain rate plots at constant strain values. The lines are $\sigma = A + B\ln(\dot{\varepsilon})$ fits to the data.

Table 3. Fitting parameters of functions A(ε) and B(ε) for both studied materials.

	$A(\varepsilon)=\frac{(a+c\varepsilon)}{(1+b\varepsilon)}$			B(ε) = $a_0 + a_1x+a_2x^2$		
	a	b	c	a_0	a_1	a_2
Material A	43,940	4,887	2455,959	-0,572	19,997	-11,001
Material B	24,35	4,446288	2321,055	- 0,7338	15,343	-4,1075

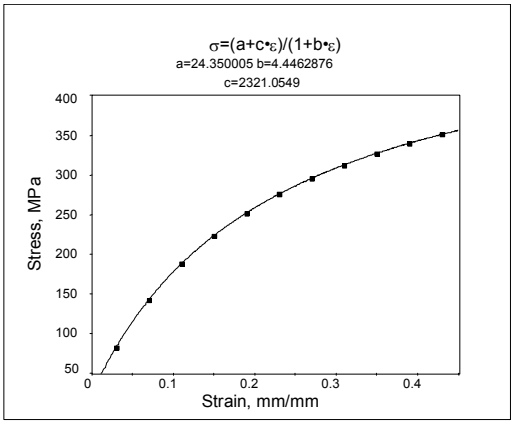

Figure 8. Fit of the rational function σ =(a+cε)/(1+bε) to A vs. ε data for material B.

APPLICATION OF THE RESULTS

The obtained results can be applied basically in two different ways: 1) by using equation (6) as such to convert the measured crusher deformation into maximum gun pressure, or 2) by correcting the original calibration curve, supplied by the crusher element manufacturer, by the actual strain rate of the crusher element. In the second case, equation (6) can be rewritten as

$$\sigma(\varepsilon) = \sigma(\varepsilon)_{cal} + B(\varepsilon)\ln(\dot{\varepsilon}/\dot{\varepsilon}_0) \qquad (7)$$

where $\sigma(\varepsilon)_{cal}$ is the original calibration curve for the crusher element, $\dot{\varepsilon}_0$ is the strain rate at which this calibration curve was determined, and $\dot{\varepsilon}$ is the average strain rate at which the crusher element was deformed during firing.

In practice, equations (6) and (7) are used as follows:

1. measure the final length of the crusher element *l*
2. calculate the strain in the crusher element, $\varepsilon_c = \ln(1+(l_0-l)/l_0)$
3. calculate the average strain rate in the crusher element, $\dot{\varepsilon}_c = \varepsilon_c/\Delta t$, where Δt is the rise time of pressure characteristic for the gun
4. replace values for ε_c, $\dot{\varepsilon}_c$ and $\dot{\varepsilon}_0$ in equation (6) or (7)

The main problem in the described method is the determination of the true strain rate $\dot{\varepsilon}_c$ of the crusher element, because only the final length of the element can be accurately measured. It seems, however, that for all studied guns the rise time Δt of the maximum pressure is characteristic to each gun and quite independent of the maximum pressure value. Therefore, quite reasonable estimates for the strain rate can be obtained simply by dividing the total strain of the crusher element by this characteristic rise time. Considering also that the flow stress depends on strain rate logarithmically, small uncertainties in the rise time do not significantly affect the obtained pressure readings.

COMPARISON OF THE CRUSHER AND PIEZOELECTRIC PRESSURE TRANSDUCER READINGS

Figures 9 and 10 compare the pressure values obtained by piezoelectric pressure transducer measurements, by the manufacturers' calibration curves, and by using equations (6) and (7) for different combinations of guns and ammunition. For both materials, the static calibration values clearly underestimate the pressure, especially at higher pressures. The dynamic calibration table, which was also available for material B, gives reasonably good results over the whole pressure range, which suggests that this table was not compiled for a single strain rate but is probably based on actual firing tests, and therefore already includes the effect of strain rate. The values calculated by equations (6) and (7) seem to be quite close to the piezoelectric pressure transducer values with some exceptions, where most probably some problems occurred in the crusher measurement (e.g., blow by). At low pressures the strain-rate–corrected calibration value (equation 7) clearly overestimates the pressure for material B, but at higher pressures the values are very close to the piezoelectric pressure transducer values. For element material A, equation (7) gives values which are very close to the piezoelectric pressure transducer values over the whole studied pressure range, which shows that the method works well when $\dot{\varepsilon}_0$ is constant and its precise value is known.

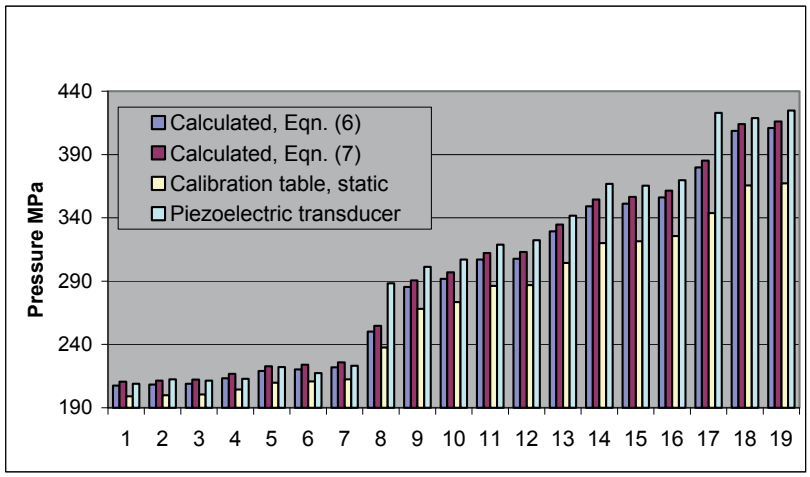

Figure 9. Comparison of pressure values obtained by different methods for material A.

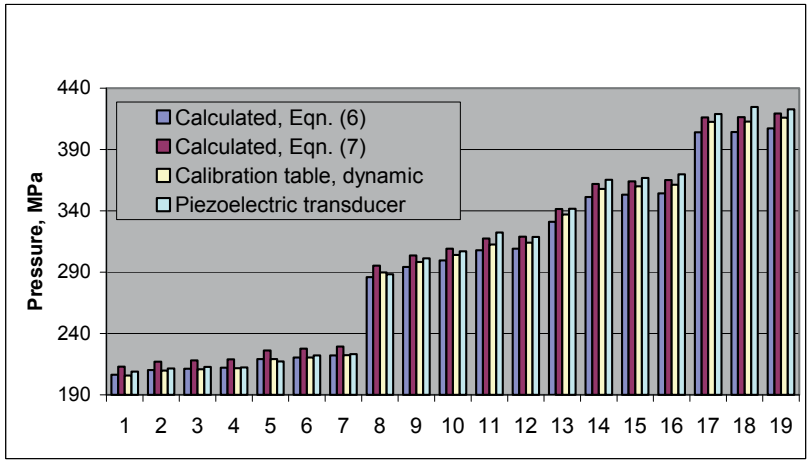

Figure 10. Comparison of pressure values obtained by different methods for material B.

SUMMARY AND CONCLUSIONS

The aim of this study was to improve the accuracy of crusher pressure measurements and to ensure the correctness of the results also at high pressures. The goal was to develop a mathematical model, which converts the measured plastic deformation of the crusher element into maximum pressure by taking into account the true deformation and work hardening behavior of copper as a function of both strain and strain rate.

The stress-strain response of copper was first attempted to model with a Johnson-Cook type equation, but its accuracy turned out to be insufficient. Therefore also other types of mathematical expressions were examined. The developed model is a six-parameter two-variable fitting model of type $\sigma(\varepsilon) = A(\varepsilon) + B(\varepsilon)\ln(\dot{\varepsilon})$, where ε is the plastic deformation of the crusher element and $\dot{\varepsilon}$ the average strain rate in it during firing of the gun. The model can also be used in the form $\sigma(\varepsilon) = \sigma(\varepsilon)_{cal} + B(\varepsilon)\ln(\dot{\varepsilon}/\dot{\varepsilon}_0)$, where $\sigma(\varepsilon)_{cal}$ is the manufacturer's calibration curve for the crusher element and $\dot{\varepsilon}_0$ is the strain rate, at which the calibration curve was determined. Function *A(ε)* is a simple rational function and *B(ε)* a second order polynomial, whose coefficients a, b, c and a_0, a_1, a_2 were determined for two different crusher element materials.

Because for a certain gun type the rise time Δt of the pressure seems to be quite independent of the maximum pressure, the average strain rate can be obtained by dividing the total deformation of the crusher element by this characteristic rise time. Another possible method to determine the rise time of pressure could be a simple strain gage measurement from the outer surface of the gun barrel. Even through the measured strain values could not be converted directly to the internal pressure of the gun, this type of measurement could give the shape of the pressure pulse as a function of time and thus facilitate the accurate determination of the rise time of the pressure pulse.

Comparison of the pressure values calculated from two manufacturers' calibration curves, measured by piezoelectric pressure transducers, and calculated using the developed model equations shows, that the accuracy of the pressure readings can be significantly improved by the developed method, especially when compared with the values obtained from static calibration curves. The best results were obtained by the method where manufacturers' calibration curves were corrected for the strain dependent strain rate effects.

ACKNOWLEDGEMENTS

This work was supported by the Scientific Advisory Board of Defence, Ministry of Defence of Finland, under Grant No 28/Mdd616/02.

REFERENCES

1. Kettunen P.O. and Kuokkala V.-T. "Plastic Deformation and Strain Hardening", Materials Science Foundations, Vol 16-18, Trans Tech Publications, Uetikon-Zurich, 2003.

2. Gray George T. III "Classic Split-Hopkinson Pressure Bar Testing", Mechanical Testing, Vol 8, ASM Handbook, American Society for Metals, 2002.

3. Johnson G.R. and Cook W.H. "A constitutive model and data for metals subjected to large strains, high strain rates, and high temperatures", in "Proc. 7th Int. Symp. on Ballistics", publ. The Hague, The Netherlands, pp. 541-547, 1983.

PUBLICATION II

Influence of rubber parameters on the calculation of nip pressure profile in paper coating

J. Rämö, T. Vuoristo, V-T. Kuokkala, G. Simbierowicz and R. Vanninen

Proc. ECCMR 2005 - Fourth European Conference on Constitutive Models for Rubber, The Royal Institute of Technology, Stockholm, Sweden, June 27-29th, 2005, pp. 415-420, 2005

Influence of rubber parameters on the calculation of nip pressure profile in paper coating

J. Rämö, T. Vuoristo & V-T. Kuokkala
Tampere University of Technology, Tampere, Finland

G. Simbierowicz & R. Vanninen
Metso Paper, Järvenpää, Finland

ABSTRACT: Rubber covered nip rolls have a number of applications in the paper industry. One of them is the coating process, where color or size is applied on one or both sides of the paper web. Finite element modeling can be an accurate and inexpensive tool in the optimization of the coating process, as long as it reflects the real phenomena. Therefore, the choice of optimal material parameters for the model is one of the most important tasks. In this study, a universal material testing machine and a compressive Split Hopkinson Pressure Bar (SHPB) equipment were used to produce material data for OptiSizer test set-up conditions (strain rate 1 s^{-1}, room temperature, ambient moisture) as well as for OptiSizer production conditions (temperature 60 °C, strain rate 1600 s^{-1}, saturated moisture in artificial paper mill water at test temperature). The OptiSizer machine was modeled using the Abaqus software. The nip pressure was calculated for linear elastic and hyperelastic models of the covers and compared with measured data. The model shows good agreement with the measurements in the test sep-up conditions and can therefore be used to simulate the mechanical contact in coating processes in actual production conditions and to optimize the shape and materials of the contacting rolls.

1 PROBLEM IDENTIFICATION

The OptiSizer film coating method is based on simultaneous color or size application on both sides of the paper web in order to improve the printing properties of the paper. The nip pressure between the rolls and the shape of the web surface directly influence the coating quality. Paper's tendency of form "uncoated wrinkles" (Fig. 1) can be diminished by choosing the optimum crowning shape for the rolls as a function of nip load and cover material parameters. This goal can be achieved by modeling and measuring the mechanical contact in the nip in order to obtain a uniform distribution of the nip pressure in machine direction.

In modern paper machines the rate of deformation in the nip has increased to such levels that the effects of strain rate cannot be omitted. Therefore, to determine the cover material parameters for the discussed FE-models, quasi-static compression tests with a universal material testing machine and high strain rate compression tests with a Split Hopkinson Pressure Bar device were conducted.

2 MATERIAL TESTING EQUIPMENT

Increasing strain rate affects the behavior of most materials by increasing the stress needed to produce a certain amount of deformation (Meyers 1994).

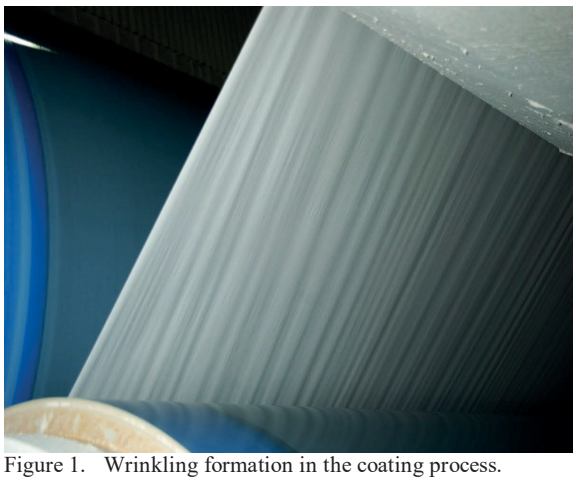

Figure 1. Wrinkling formation in the coating process.

With increasing strain rate, the stress at constant strain (e.g. at 10 %) increases first moderately but then, above a certain material dependent threshold value, a very rapid increase is often observed. In metals this 'upturn' takes typically place at about 10^3 s^{-1}, but in polymeric materials it may happen already at much lower strain rates (Chou et al. 1973, Briscoe & Hutchings 1976).

In polymers, the strain rate sensitivity is related to the viscoelastic nature of deformation, but the actual mechanisms, and especially the reason for the change in the strain rate sensitivity, are not yet fully understood. The large variety of polymeric materials and their composites is also one of the reasons why there is no widely accepted theory that would adequately explain the stress-strain behavior of polymeric materials at high strain rates.

In paper machines, there are big differences between the quasi-static nip pressure measurement conditions and the production conditions, where the effects of strain rate, temperature and moisture can be substantial.

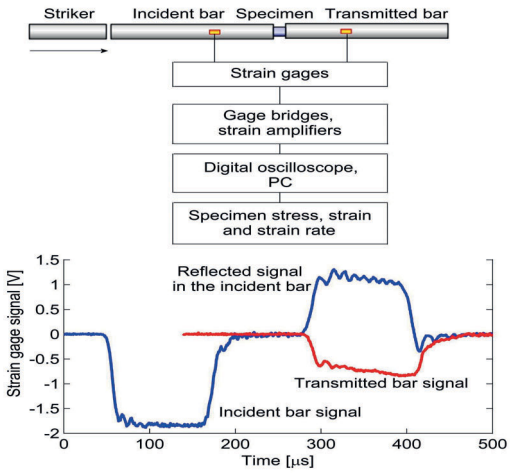

Figure 2. The SHPB technique schematically.

With servo-hydraulic testing machines, tension, compression, and shear tests can be readily conducted up to strain rates of the order of 1 s^{-1}, but above this other techniques must be utilized (Nemat-Nasser 2001). Split Hopkinson Pressure Bar technique is used to measure the stress-strain response of materials at high strain rates, typically in the range of $10^2...10^4$ s^{-1}. The SHPB method is based on the propagation of one-dimensional elastic pressure waves in two slender bars, between which the specimen is placed. A short duration stress pulse is created in the loading bars by shooting a short projectile at the end of one of the bars. The compressive stress wave propagates at the speed of sound in the bar towards the interface between the bar and the specimen, where part of the wave is reflected back as a wave of tension while part of it continues through the specimen into the second bar as a wave of compression.

The three waves are recorded from the loading bars with strain gages (Fig. 2). The stress, strain, and strain rate in the specimen can be calculated from these three waves with appropriate equations. A detailed description of the SHBP technique can be found, for example, in Vuoristo (2004).

3 TESTING AND MODELING OF RUBBER

One of the materials used in coater roll covers is RayFlex 5000, which is a heat, wear, and chemical resistant, fully cross-linked rubber material containing, among other ingredients, active inorganic fillers. In the current tests, the cylindrical compression specimens of 18 mm in diameter had a length of 15 mm in the low strain rate tests with servo-hydraulic testing machines and 5 mm in the high strain rate tests with the SHBP device. The surfaces of the specimens were lubricated with molybdenum disulfide in order to avoid excess barreling of the specimens.

Compression tests show almost linear strain rate dependence in a semi-logarithmic scale up to a strain rate $\dot{\varepsilon}$ = 1 s^{-1}, and still at 1600 s^{-1} no drastic change in the strain rate sensitivity is observed (Fig. 3). Increasing strain increases the effect of strain rate, as shown in Figure 3 by the steepening slope of the plot when strain, for which the stress is measured, increases from 10% to 30%. Increasing temperature decreases the measured stress (Fig. 4), whereas moisture does not have an essential effect on the results because the material absorbs only small amounts of water.

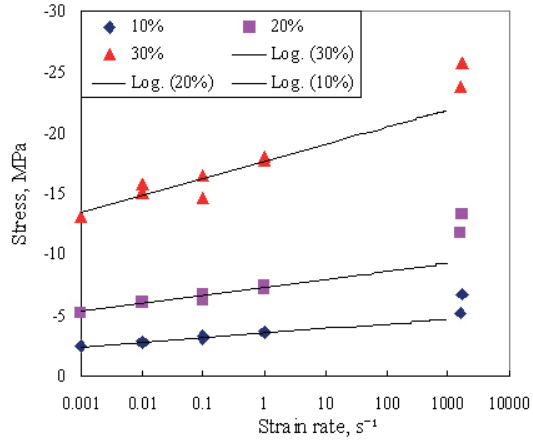

Figure 3. Dependence of stress on strain rate for RayFlex 5000. Percentages represent the amount of strain for which the stress is measured. Measurements were done at 50 °C in ambient moisture.

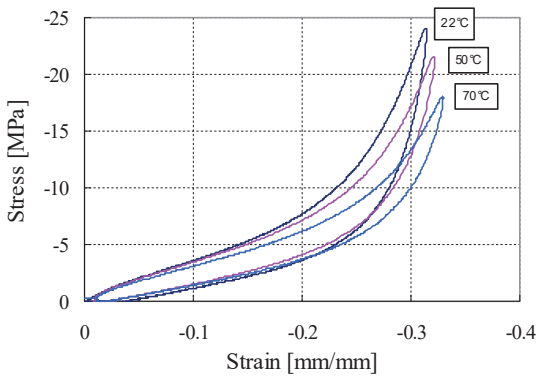

Figure 4. Stress-strain curves measured at 22, 50 and 70 °C at a strain rate of 1 s^{-1} in ambient moisture.

In this paper, the behavior of the coater nip is considered in two different conditions: a) room temperature, strain rate 1 s^{-1}, ambient moisture, and b) 60 °C, strain rate 1600 s^{-1}, saturated moisture in paper machine water at the test temperature. To enable realistic simulations of the nip behavior with Abaqus, experimental data on the behavior of the studied roll cover materials was produced by compression tests at different temperatures. Before actual compression tests to a total deformation of 33%, the samples were mechanically conditioned twice with similar compression cycles. The tests were repeated twice with identical specimens at room temperature, 50 °C, and 70 °C. At each temperature, an arithmetic average of the loading parts of the measured curves was calculated to be used in further simulations with Abaqus. The data at 60 °C is an average of the results obtained at 50 °C and 70 °C (Fig. 5).

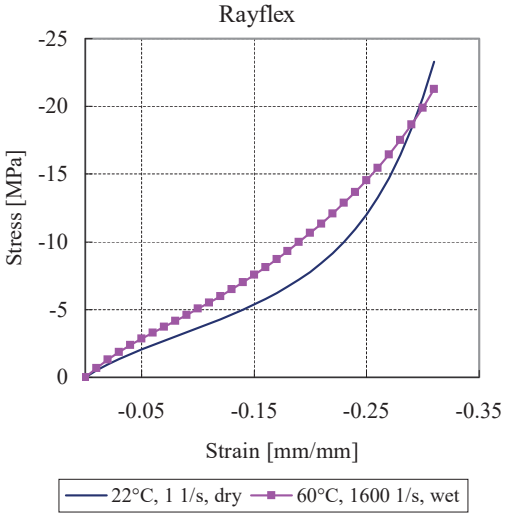

Figure 5. Test data in compression.

The linear elastic materials are described by constant elastic modulus and Poisson's ratio. If only hardness data for the material is available, the elastic modulus can be estimated based on that data. This approach may be used for low stress levels, but it cannot accurately model the behavior of rubbers at larger strains. For the hyperelastic models the stress strain relation is described using a proper strain energy function (Austrell 1997). For only one set of data, e.g. uniaxial compression, Abaqus recommends the use of Marlow form of strain energy potential.

The Marlow model assumes that the strain energy potential is independent of the second deviatoric invariant. The model can be implemented by providing test data that describes the deviatoric behavior and, optionally, the volumetric behavior if compressibility must be taken into account. Abaqus constructs strain energy potential that reproduces the test data as (Abaqus manuals 2004):

$$U = U_{dev}(\bar{I}_1) + U_{vol}(J_{el}) \quad (1)$$

where U is the strain energy per unit reference volume with U_{dev} as its deviatoric and U_{vol} as its volumetric part. The elastic volume ratio $J_{el} = J/J_{th}$, where J is the total volume ratio and J_{th} the thermal volume ratio. Assuming incompressibility and isothermal response of the material, $J_{el} = 1$. $\bar{I}_1$ is the first deviatoric strain invariant defined as:

$$\bar{I}_1 = \bar{\lambda}_1^2 + \bar{\lambda}_2^2 + \bar{\lambda}_3^2 \quad (2)$$

where $\bar{\lambda}_i$ are the deviatoric stretches. Since $\bar{\lambda}_i = J^{-\frac{1}{3}}\lambda_i$ and $J = 1$, we can write Eqn. 2 also as

$$\bar{I}_1 = \lambda_1^2 + \lambda_2^2 + \lambda_3^2 \quad (3)$$

where λ_i are the principal stretches. Because in the current case the material is assumed to be incompressible and isothermal, term U_{vol} in Eqn. 1 vanishes.

4 THE MODEL OF THE CONTACT

To obtain the nip pressure profile in machine and cross machine directions, the contact between the rolls was modeled in Abaqus using a 3D nonlinear static analysis (Fig. 6).

One of the causes for wrinkle formation is the high gradient of nip pressure at the ends of the rolls. By changing the shape of the rolls, one can alter the pressure profile by making use of properly calibrated FE -models. To check the reliability of the models, measurements of the nip pressure were performed using Fuji color forming and developing films. Due to the limitation of the measurement method that requires dry surfaces and low rotation speed, the OptiSizer must be operated at a crawling speed during the measurement, and therefore the measurement conditions differ substantially from the normal operating conditions.

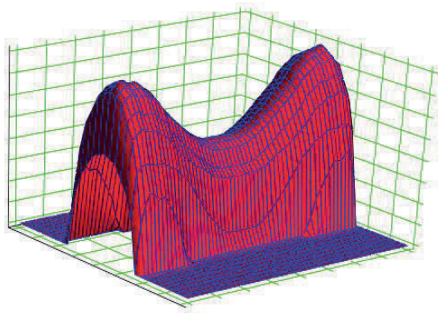

Figure 6. Nip pressure profile.

For lower nip loads there is a reasonable agreement between measured and calculated data when using the elastic model for the cover (i.e. a constant Young's modulus and high Poisson's ratio). The difference increases when the nip load becomes higher (Fig. 7).

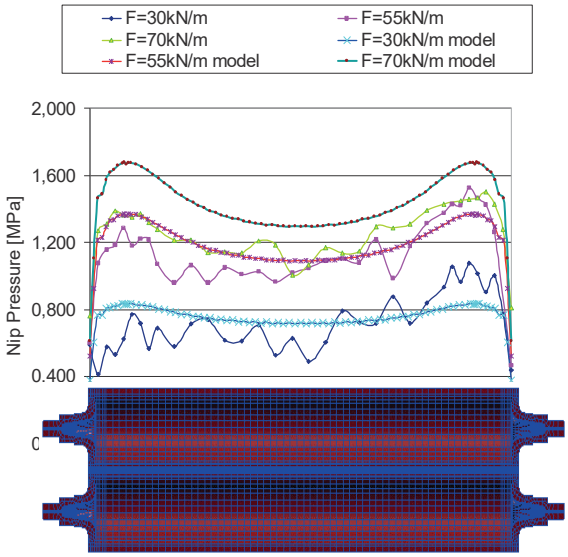

Figure 7. Calibration of the model using the pilot machine. Measurements were performed using a pressure sensitive film.

For a production size paper machine with a roll length of 11 m, a comparison between the measurements, the elastic model, and the hyperelastic models was performed for two different conditions defined above. The results are shown in Figure 8.

In order to decrease the nip pressure gradient in production conditions, the shape of the rolls can be modified by changing the crowning profile (Fig. 9). In this way the width of the nip increases while the maximum pressure in the middle of the nip contact area decreases.

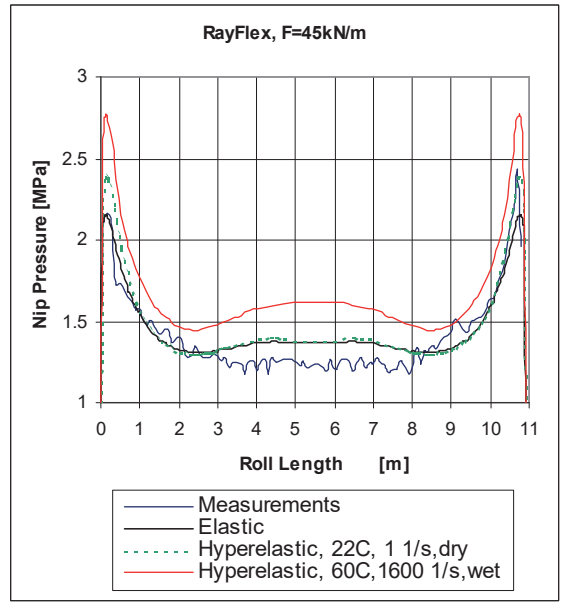

Figure 8. Comparison between the models and the measurements.

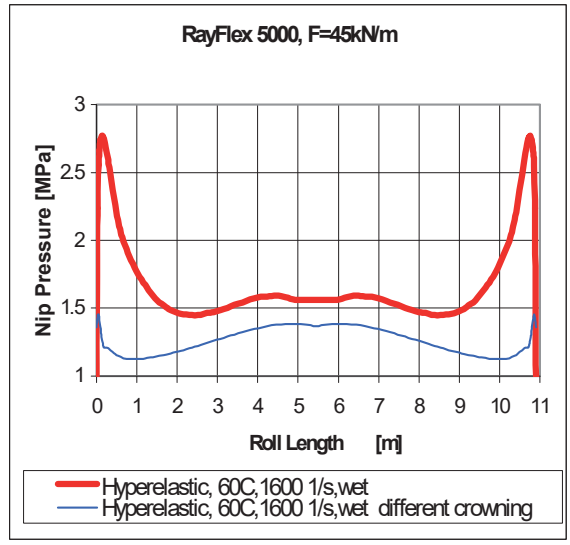

Figure 9. Nip pressure profile as a function of crowning.

The dynamic process was modeled using a steady state transport analysis. In the model, the rotating deformable roll is in contact with paper modeled as a rigid body (Fig. 10). With this simulation, the position of sticking and slipping contact regions can be estimated by comparing the shear stresses and nip pressure that appear in the nip, that is:

$$\tau \leq \mu \cdot p \Rightarrow \text{sticking} \quad (4)$$

$$\tau \geq \mu \cdot p \Rightarrow \text{slipping} \quad (5)$$

where τ is the shear stress, μ is the friction coefficient between paper and the roll cover, and p is the

nip pressure (Fig. 11). The changes in the velocity profile in the nip are shown in Figure 12.

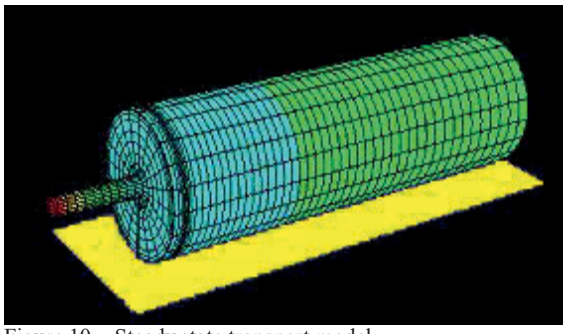

Figure 10. Steady state transport model

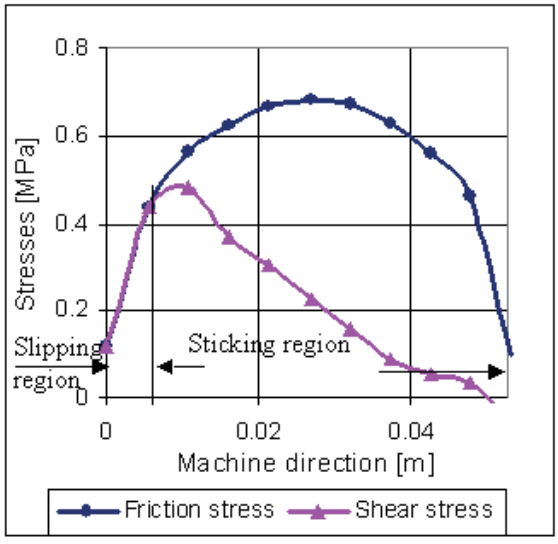

Figure 11. Slipping and sticking regions in the nip.

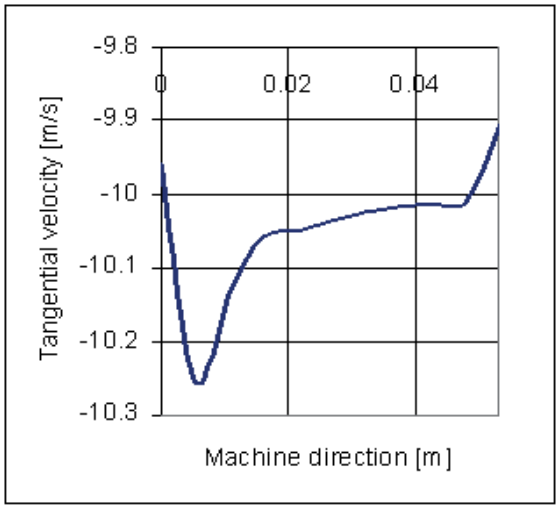

Figure 12. Velocity profile in the nip.

The calibration of the steady state transport model is quite difficult, and therefore the material data used in simulations should be accurate and relevant to the loading conditions. While in the static calculation compression was the predominant mode of loading, in the dynamic calculation shear stresses have a more significant role. For this reason, shear and volumetric tests are needed to improve the accuracy of the model.

5 CONCLUSIONS

The nip pressure distribution and optimum velocity profile can be improved by using an optimum crowning shape. This diminishes the paper's tendency to form wrinkles, increases the coating quality, and extends the lifetime of the rubber covered rolls.

The hyperelastic model of the cover gives better agreement between the calculated and measured conditions for static nip pressure than the elastic one. After calibration, the model can be used for simulating the mechanical contact in paper machine operating conditions and for explaining the changes in the wrinkling amplitude and directions between the start-up and production conditions.

In order to simulate dynamic processes where shear stresses are significant, shear and volumetric tests of the rubbers are needed.

REFERENCES

Abaqus manuals. Version 6.5. 2004.

Austrell P.-E., 1997. *Modeling of elasticity and damping for filled elastomers,* Lund University, Sweden.

Briscoe B. J., Hutchings I. M., 1976. Impact yielding of polyethylene. *Polymer* 17: 1099-1102.

Chou S. C., Robertson K. D., Rainey J. H., 1973. The effect of strain rate and heat developed during deformation on the stress-strain curve of plastics. *Experimental Mechanics* 13: 422-432.

Meyers M. A., 1994. *Dynamic Behavior of Materials,* John Wiley & Sons, Inc., New York.

Nemat-Nasser S., 2001. Introduction to high strain rate testing, In *ASM Handbook Vol. 8: Mechanical Testing and Evaluation*. Materials Park, Ohio.

Vuoristo, T., 2004. Effect of Strain Rate on the Deformation Behavior of Dual Phase Steels and Particle Reinforced Polymer Composites, Doctoral thesis, Tampere University of Technology, Finland.

PUBLICATION III

Strain rate dependent deformation behavior of cold heading steels

T. Vuoristo, V-T. Kuokkala, J. Rämö, J. Partinen and J. Kolsi

Proc. Asia Steel International Conference 2006 (Asia Steel '06), Fukuoka, Japan, 9-11.5.2006, pp. 902-907

Strain rate dependent deformation behavior of cold heading steels

Taina Vuoristo[1], Veli-Tapani Kuokkala[1], Jari Rämö[1], Jarkko Partinen[2*], and Jari Kolsi[2]
[1] Tampere University of Technology, Institute of Materials Science, Tampere, Finland
[2] Ovako Wire, Koverhar, Finland
[2*]Currently at Outokumpu Technology Research Center, Pori, Outokumpu Research Oy, Finland

ABSTRACT

Strain rates in cold heading processes may locally reach very high values, up to several thousands per second. As the flow stress of most materials is known to increase drastically in the high strain rate region, this phenomenon also affects the cold heading process itself. In this study, the effect of strain rate on the cold headability of steel wires was investigated by compression and tensile tests made at a wide strain rate range of $10^{-4}…10^{3}$ s^{-1} using both servohydraulic materials testing machines and the split Hopkinson bar technique (SHB). Special attention was paid to the effects of transient and permanent strain hardening as a function of strain rate. The aim of this study was to develop techniques for the determination of optimal loading amplitudes and loading rates for specific cold heading steels to avoid formation of cracks in the cold headed components. The stress-strain data obtained from the mechanical tests can also be utilized in more accurate FE simulations of the cold heading operations of parts and components.

Keywords:cold heading, strain rate, split Hopkinson bar

1 INTRODUCTION

Cold heading, or upsetting, is a cold forming method commonly applied for making different types of fasteners and other relatively simple mass production parts from round wire at a high speed. In the basic operation of cold heading, the wire is transformed into desired parts by one or two blows with a fast moving punch, which forms a 'head' in the part by plastically deforming the material. Forming of the head can take place either in a die, the punch, or both. The highest production rates can be of the order of ten(s) per second, depending on the complexity of the part and number of blows needed. Traditionally the cold heading materials have been ductile steels or other metal alloys with low work hardening characteristics, but today also higher strength materials are routinely being cold headed.

Cold headability of metal is defined as the capability of a cylindrical piece of metal to be shaped into a head of a bolt, screw, or other cold formed part at a high strain rate without cracking [1]. The strength and strain hardening properties of the material are the key factors that determine the material's cold headability. Strength of practically all materials depends on both temperature and strain rate, decreasing with the former and increasing with the latter. In the cold heading process the local strain rates can reach quite high values, up to about 1000 per second [2]. At such high strain rates the duration of deformation is usually so short that the conditions are essentially adiabatic, which means that the temperature of the headed part can increase substantially.

So far there is no standardized test to determine cold headability of metals, not to mention a test that would give the limits for workability of the material at the same high strain rates as in the real cold heading application. Instead, the current tests are mostly made at quasi-static strain rates, typically using a so-called upset test. In an upset test, a relatively short (L/D-ratio of the specimen typically 1…1.5) is compressed between platens and the change in length that causes cracking is noted. In addition, the hoop and axial strains of the specimen after the test can be determined. The upset test, however, does not simulate the cold heading operation, because: a) the strain rates are much lower than those in actual heading, b) friction conditions between the platens and the specimen affect the material flow differently, and c) visual verification of a crack on a specimen surface is subjective [3]. Also no stress-strain data is recorded during the test and thus information on the strain hardening behavior of the material cannot be obtained. Sometimes also tensile tests are used to evaluate cold headability by determining the yield and tensile strength and ductility of cold heading metals. In tensile tests, however, the stress state differs greatly from the stress state in actual cold heading. Efforts have also been made to increase the rate of testing in compression tests. For example, Ma et al. [1] have developed a drop weight tower (DWT) testing method, which better corresponds to the deformation and also the strain rates that occur in actual cold heading process. The stress-strain relationship during deformation, however, cannot be recorded and the effect of strain hardening cannot be evaluated.

2 STUDIED MATERIAL

The studied steel is a cold heading quality steel used in lower strength grade bolts, screws and other cold-formed fasteners. The steel is aluminium-killed and it is not intended for heat treatments such as quenching. The designation in standard EN 10263 is C17C. The nominal composition and tensile strength of the steel are given in Table 1, and the microstructure in Figure 1. As Figure 1 shows, the microstructure of the steel is ferrite and pearlite with an average ferrite grain size of about 10 µm.

An upset test is made as a part of quality control for all cold heading steel wires at Ovako Wire. In these tests, the formability of the steel is evaluated based on the amount and severity of cracks formed on the surface after the specimen with a length to diameter ratio of 1.5 has been compressed to either 1/3 or to 1/4 of its original length. Figure 2 shows the basis of the evaluation of cold headability, *i.e.*, the upset test samples are classified on a scale from 1 to 5 based on the severity of cracks formed. The studied steel had passed the quality control upset tests with the grade of 1.

Table 1. Nominal composition and tensile strength of the studied steel.

Steel	C [%] Min…max.	Si [%] Max	Mn [%] Min…max.	P [%] Max.	S [%] Max.	Cr [%] Max.	Al [%] Min…max.	R_m [MPa]
C17C	0.16…0.19	0.10	0.70 - 0.90	0.020	0.020	0.07	0.025 - 0.050	500…520

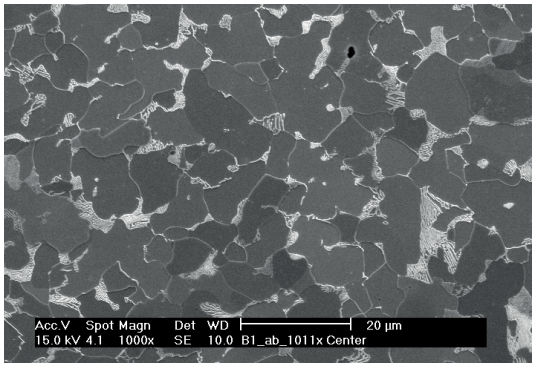

Figure 1. SEM micrograph of the studied steel.

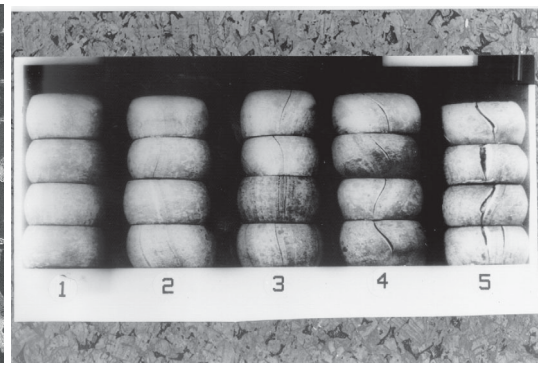

Figure 2. Estimation of cold headability of steel wires based on cracks formed in upset tests.

3 EXPERIMENTAL METHODS

In this research project, the deformation behavior of a cold heading steel was studied at a wide range of strain rates, $10^{-4}…3{\cdot}10^{3}$ s^{-1}, using both servohydraulic materials testing machines and the split Hopkinson bar method. In addition, a preliminary FE-analysis was performed to find the locations of maximum deformation and strain rates during cold heading of wire to a simple bolt shape.

3.1 Quasi-static tests

The compression and tensile tests at quasi-static strain rates ($10^{-4}…10^{-1}$ s^{-1}) were made using an Instron 8800 servohydraulic materials testing machine. In the tensile tests, the specimen strain was measured directly on the specimen using a 25 mm gage length, +/-2.5 mm range dynamic extensometer. In the compression tests, the same extensometer was attached to the compression plates to measure their displacement during compression. Due to the experimental setup, the strain measurement especially in the beginning of a compression test contains some inaccuracies due to which the elastic slopes of the compressive stress-strain curves were too low. Thus, the elastic modulus cannot be accurately determined from these results. However, the stress and plastic strain as well as the yield strength values can be considered reliable and can be used in comparisons with the high strain rate tests.

3.2 Split Hopkinson bar technique – compression at high rates of strain

Split Hopkinson bar (SHB) technique is used to measure the stress-strain response of materials at high strain rates, typically in the range of $10^{2}...10^{4}$ s^{-1}. The SHB method is based on the propagation of one-dimensional elastic pressure

waves in solids. A schematic illustration of the SHB technique, the data acquisition setup, and an example of recorded signals is shown in Figure 3 [4]. When a striker, accelerated typically to a velocity ranging from a few meters up to some tens of meters per second, hits the front end of the incident bar, a compressive stress wave is generated which propagates in the bar at the velocity of sound (about 5100 m/s in steel) until it reaches the interface of the incident bar with the specimen. At the interface, part of the stress wave is reflected back as a pulse of tension, while the remaining part is transmitted through the specimen to the transmitted bar. The generated stress pulses are recorded at strain gage stations 1 and 2 (see Fig. 3). The average stress, strain, and strain rate in the specimen are calculated from the measured strain signals using Equations 1-3 (so-called 1-wave solution).

Average stress in the specimen:
$$\sigma(t) = \frac{A_b\, E\, \varepsilon_t(t)}{A_S} \qquad (1)$$

Average strain in the specimen:
$$\varepsilon(t) = \frac{2\, C_0}{L_s} \int_0^t (\varepsilon_r)\, dt \qquad (2)$$

Average strain rate in the specimen:
$$\dot{\varepsilon} = \frac{2\, C_0\, \varepsilon_r(t)}{L_S} \qquad (3)$$

where A_b is the cross-sectional area of the bars and E and C_0 the Young's modulus and the elastic wave speed of the bar material, respectively. L_s and A_s are the length and the cross-sectional area of the specimen. $\varepsilon_i(t)$, $\varepsilon_r(t)$, and $\varepsilon_t(t)$ are the incident, reflected, and transmitted axial strains measured in the incident and transmitted bars as a function of time.

The test parameters that affect the strain rate and the amount of deformation obtained in a compression test are the striker velocity, striker length and specimen length. The stress, and thus the elastic deformation in the pressure bars depend on the striker length according to equations 4 and 5. Both the amount and rate of strain can be affected by varying the specimen length. The length to diameter ratio (L/D) is normally in the range of 0.2 to 1.0, on one hand to obtain stress equilibrium in the specimen, and on the other hand to minimize inertial and frictional effects. Because the maximum strain and strain rate are both dependent on the same test parameters (striker length, specimen length, striker velocity), the free choice of reachable strain and strain rate in a test is limited. For example, obtaining large deformations (*e.g.*, 40 %) at a relatively low strain rate (in the order of 100…800 s^{-1}) is extremely difficult. Such tests would require the use of a very long striker bar (up to several meters), which would further require the use of long enough incident and transmitted bars in which the long duration pulses could be measured separately without incident and reflected pulses overlapping each other.

$$\sigma = \frac{v_a \rho_a C_{0a}}{2} \qquad (4)$$

$$T = \frac{2 L_a}{C_{0a}} \qquad (5)$$

The split Hopkinson bar apparatus used in this study consists of two pressure bars made of AISI 4340 high strength steel. The diameter of the bars is 22 mm and the length of the incident bar 2800 mm and that of the transmitted bar 1800 mm. In this research project, a challenge was to obtain large amounts of plastic deformation, up to 70 %, by using relatively large specimen length to diameter ratios of 1.5 and 2/3. For this, a striker bar of 800 mm in length was made of the same material as the pressure bars. With this striker bar, loading pulses of approximately 470 microseconds in duration were obtained. The striker bar was accelerated to its final velocity of 10 to 15 m/s by an air gun using loading pressures of 6 to 10 bars. To control the rise time and shape of the loading pulse, a rubber disc of 0.5 mm in thickness and 10 mm in diameter was used as a so-called pulse shaper at the impact end of the incident bar.

3.3 Specimen preparation

The compression test specimens were cut from the delivered steel coil using a precision cutting machine. The diameter of the studied steel wire rod was 5.5. mm. In order to obtain perfectly parallel specimen end faces, 65 mm long pieces of the steel wire were first cast inside of a 12 mm diameter steel tube using cyanoacrylate adhesive. This was done to assure maximum stiffness for the wire during the blade cutting process. For compression tests specimens were cut to nominal lengths of 8.25 and 3.7 mm, *i.e.*, the length to diameter ratio in the tests was either 1.5 or 2/3. For tensile tests, the specimens were cut to 80 mm long pieces and tested as such, *i.e.*, without a smaller diameter gage section. Grids were etched on the surfaces of some compression specimens in order to evaluate the amount and distribution of deformation. An example of a specimen with etched grids is given in Figure 4.

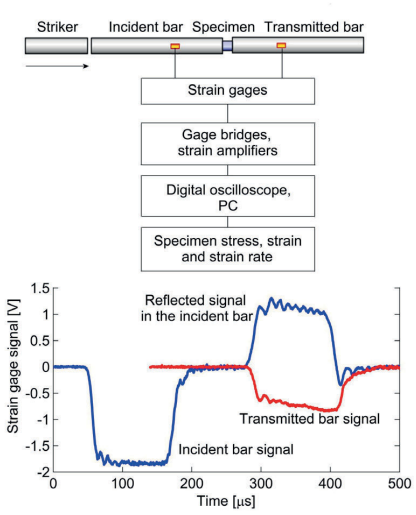

Figure 3. SHB method schematically.

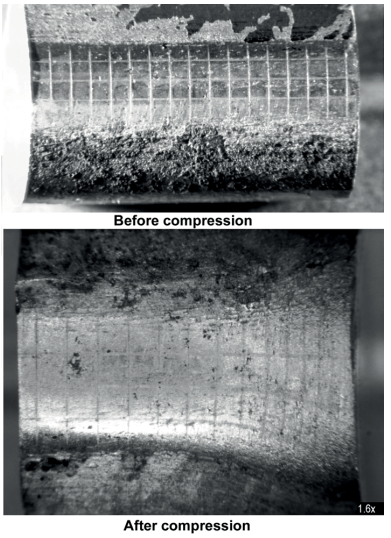

Figure 4. Grids on specimen surface before and after a high strain rate compression test.

4 RESULTS AND DISCUSSION

Figure 5a shows the true stress-strain curves for the entire studied strain rate range for the studied steel wire. The corresponding engineering stress-strain curves are given in Figure 5b. An increase of about 200 MPa in yield strength is observed when the strain rate increases from quasi-static 10^{-1} s^{-1} to the range of 10^{3} s^{-1}. Because the obtainable maximum strains and strain rates are coupled in the high strain rate tests, the highest maximum strains are obtained with highest strain rates. Figure 6a summarizes the results of the compression tests made at a wide range of strain rates giving the flow stresses at different amounts of true plastic strain as a function of strain rate. These results clearly show the transient hardening effect of strain rate.

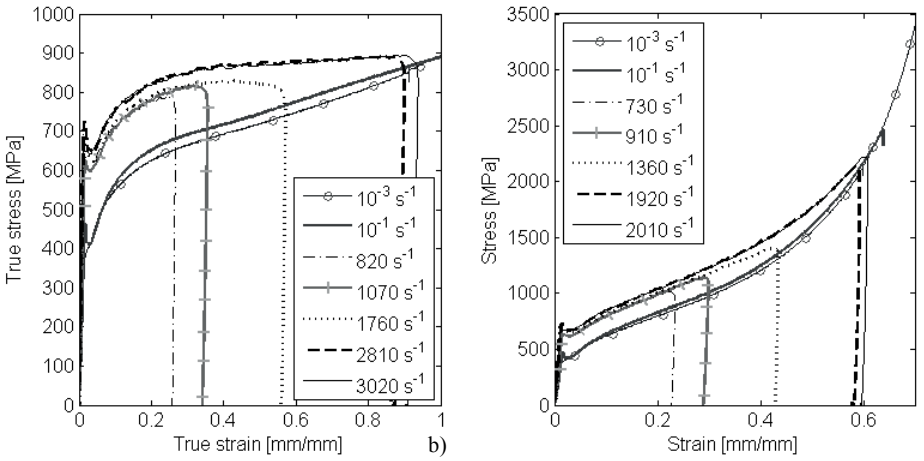

a) b)

Figure 5. True (a) and engineering (b) stress-strain curves at different strain rates.

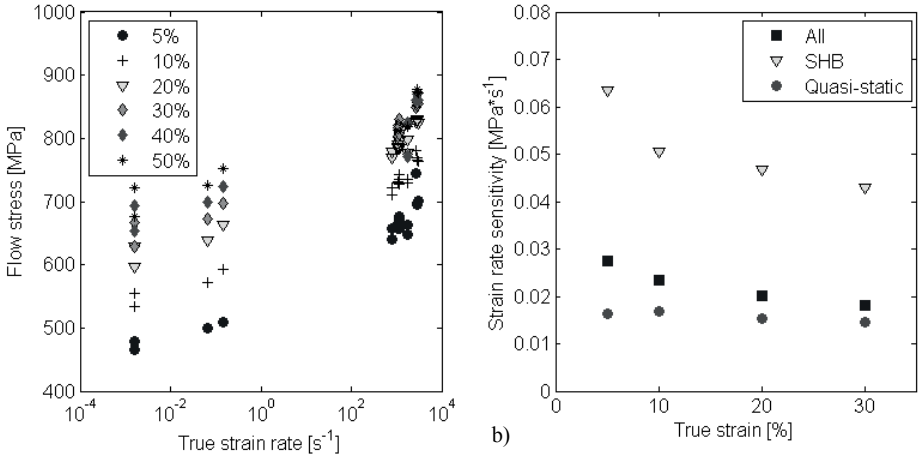

a) b)

Figure 6. True flow stress at constant strains of 5 to 50 % as a function of strain rate (a), and strain rate sensitivity factor $m = \delta \ln R / \delta \ln \dot{\varepsilon}$ at true strains of 5 to 30 %.

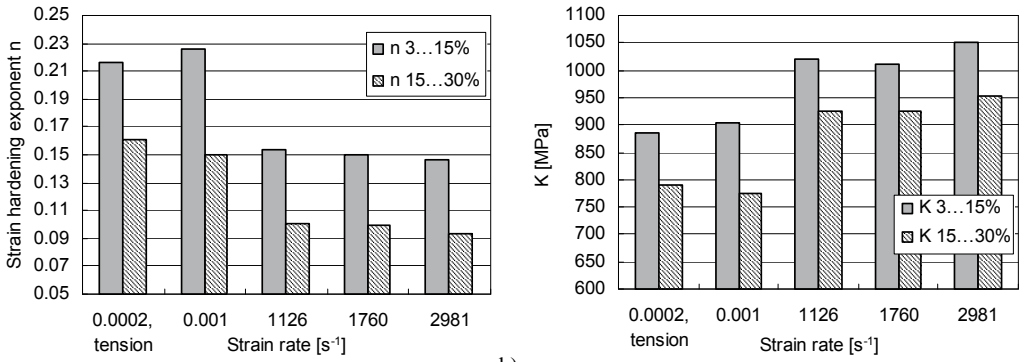

a) b)

Figure 7. The coefficients n and K of the Hollomon equation ($\sigma_T = K\varepsilon_T^n$) as a function of true strain rate.

The transient hardening effect of strain rate is often described by the so-called strain rate sensitivity factor, m, which is the slope of the logarithmic flow stress - strain rate curve. The strain rate sensitivity factor of the studied steel at strains between 5 and 30 % is given in Figure 6b. The strain rate sensitivity of the studied steel was determined separately for both high and quasi-static strain rates and also over the entire strain rate range. As for most materials, also for the studied steel the strain rate sensitivity increases with increasing strain rate, *i.e.*, the strain rate hardening effect is typically stronger at strain rates exceeding 10^2 s^{-1}. Because there is a great difference in the strain rate dependence at quasi-static and high strain rates, the behavior of steels in a high rate cold heading processes cannot be estimated from quasi-static data only, but also high strain rate test results are needed. On the other hand, the strain rate sensitivity of steels typically decreases at higher amounts of plastic strain, as can also be seen in Figure 6b. As this decrease is much more pronounced at high strain rates, the strain hardening behavior at high strain rates evidently differs from that at quasi-static rates.

The strain hardening behavior of metals is often described by the Hollomon equation, $\sigma_T = K\varepsilon_T^n$. Figures 7 a and 7b show the strain hardening coefficient n and the strength factor K of the Hollomon equation determined from the tensile and compression tests for two different strain intervals, *i.e.*, from 3 to 15 % and from 15 to 30 % of true strain. The value of the strain hardening coefficient n clearly decreases as the strain rate increases. Also, the n-value is smaller in the region of higher strains (15…30 %). This indicates that the amount of strain hardening is smaller at higher strain rates as is also seen in the stress-strain curves presented in Figure 5a. One of the reasons for the lower amount of strain hardening at high strain rates can be the adiabatic heating of the specimen. At high rates there isn't enough time for the heat generated during the deformation process to be conducted away, and thus the temperature may locally increase up to 100°C, especially at the high strain levels, which were used in this study. The increase in temperature during the tests was not actually measured

but only evaluated based on the calculations of energy absorption and the assumption that 90 % of that energy is transformed into heat during the deformation process. Figure 7 also shows that the *n*- and *K*-values obtained from the quasi-static tensile tests are slightly higher than the values from compression tests.

A preliminary finite element analysis was made for a simple bolt geometry in order to get an estimate for the amounts and distributions of strain and strain rate in the steel wire during the cold heading process. In this analysis, the wire was compressed at a constant displacement rate in a bolt-shaped die. The duration of the compressive load (= time to cold head one bolt) was set to 0.1 seconds. Figure 8a shows the compression sequence at different times, *i.e.*, just before the load is applied and after 30, 55 and 75 milliseconds. The equivalent strain rates in four selected elements (360, 450, 540 and 673) of the FE-mesh are shown in Figure 8b as a function of time.

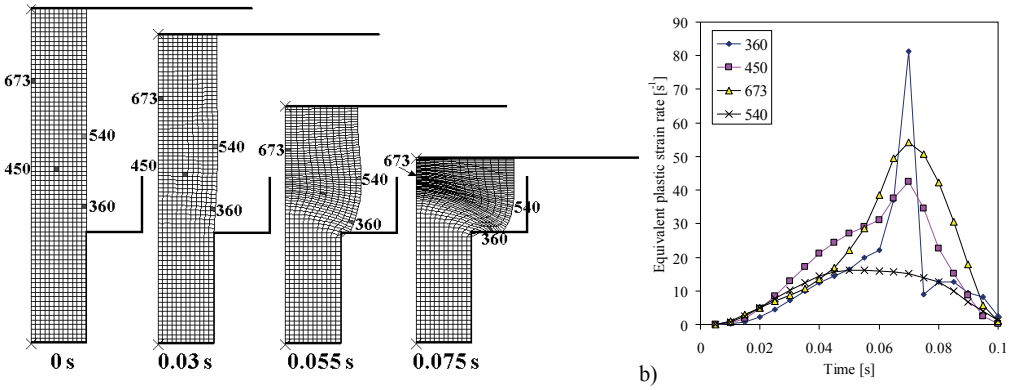

Figure 8. A finite element (FE) analysis of cold heading of a simple bolt (8a). The equivalent strain rate in the elements 360, 450, 540 and 673 are shown in Fig. 8b as a function of time. The thicker black lines represent the punch and the die.

5 CONCLUSIONS

The main conclusions of this study may be summarized as follows:

- The rate of deformation affects the flow stress of steels already at quasi-static strain rates and should therefore be accounted for in the design of cold heading processes.
- Especially at very high strain rates the transient (strain rate) hardening effect is significant and could be utilized in optimizing the cold heading process.
- Strain hardening of the studied cold heading steel decreases and strain rate sensitivity increases with increasing strain rate.
- Strain rate sensitivity of the studied steel decreases with increasing plastic strain. This effect is much more pronounced at high strain rates.
- One of the reasons for the lower amount of strain hardening and higher strain dependence of strain rate sensitivity at high strain rates can be the adiabatic heating of the specimen.
- Split Hopkinson bar (SHB) technique is a powerful method to study the effect of strain rate on the formability of cold heading steels. However, some modifications to the standard techniques must be made to increase the test duration to obtain high enough strains also in the strain rate range of 500…1000 s^{-1}.

REFERENCES

[1] X. Ma, A.O. Humphreys, J. Nemes, M. Hone, N. Nickoletopoulos and J.J. Jonas: "Effect of microstructure on the cold headability of a medium carbon steel," ISIJ International, 44, pp. 905-913, 2004.

[2] G. Brethenoux, E. Bourgain, G. Pierson, M. Jallon and P. Secordel: "Cold forming processes: some examples of predictions and design optimization using numerical simulations", Journal of Materials Processing Technology, 60, 555-562, 1996.

[3] N. Muzak, K. Naidu and C. Osborne: " New methods for assessing cold heading quality," Wire Journal International, 29, pp. 66-72, 1996.

[4] Vuoristo, T.: Effect of Strain Rate on the Deformation Behavior of Dual Phase Steels and Particle Reinforced Polymer Composites, dissertation, Tampere University of Technology Publication 488, 2004.

PUBLICATION IV

A Dynamic Calibration Method for Crusher Gauges Based on Material Testing

H. Nyberg, V.-T. Kuokkala, J. Rämö, A. Järviniemi

Propellants, Explosives, Pyrotechnics, 32, No. 1, 61-67, 2007

Full Paper

A Dynamic Calibration Method for Crusher Gauges Based on Material Testing

Heli Nyberg*

Defence Forces Materiel Command Headquarters, Weapons Systems Division, P. O. Box 69, FI-33541 Tampere (Finland)

Veli-Tapani Kuokkala, Jari Rämö

Tampere University of Technology, Institute of Materials Science, Korkeakoulunkatu 6, P. O. Box 589, FI-33101 Tampere (Finland)

Aulis Järviniemi

Defence Forces Test Firing Centre, Pohjankankaantie 125, FI-38840 Niinisalo (Finland)
DOI: 10.1002/prep.200700008

Abstract

This paper presents a new dynamic calibration method for crusher pressure gauges used in artillery test firings. The calibration method is based on the measurement of the plastic deformation behavior of the crusher elements in the laboratory completely isolated from test firings and measurements by reference pressure transducers. The validity of the calibration model developed is verified by comparison with the pressure records measured in artillery test firings. It was found that the calibration method developed is also suitable for the high load levels and strain rates present in tank firings.

Keywords: Pressure Measurement, Test Firings, Materials Testing, Hopkinson Split Bar

1 Introduction

Both copper crusher and piezo-electric gauges are used to measure the peak chamber pressure during the firing of the round. Crusher gauges, however, are more commonly used because they do not require drilling of the gun barrel [1].

In crusher pressure measurement, the gas pressure is applied via a piston to a copper element contained within the gauge body. The crusher gauge is based on the proportionality of the gun pressure and the amount of plastic deformation of the crusher element. This proportionality, however, is nonlinear because the work hardening behavior of metals is a function of both strain and strain rate [2, 3]. If crushers are calibrated only at one strain rate, which is outside the strain rate range occurring at gun firings, the pressure readings given by these static calibration tables cannot be accurate. When composing dynamic calibration tables, measurements are usually carried out simultaneously by crusher and piezo-electric methods using test firings and/or laboratory pressure chamber tests.

In the literature, only a few reports related to the strain rate dependence of the mechanical behavior of copper crusher elements and composing of the dynamic calibration tables can be found. Johnson and Cook [4] have presented a constitutive model and data for OFHC copper subjected to large strains, high strain rates, and high temperatures. NATO has given a procedure for submission and testing of crusher gauges for NATO approval and a list of NATO approved crusher gauges [5]. To calibrate crusher gauges, Zhu et al. [6] have developed a system based on a drop hammer hydraulic pressure pulse generator and a pressure chamber equipped with reference quartz and strain transducers. Warken and Meineke [7] have presented a dynamic calibration method for crusher gauges based on a pendulum impact machine and damping mechanisms simulating real pressure loads. Lokre et al. [8] have presented a comparison between peak pressures measured using crusher gauges with a static calibration table and the piezo-electric method.

In the test firings organized by the Finnish Defence Forces (FDF) the majority of the crusher pressures have been measured by a certain gauge brand with cylindrical elements. The German manufacturer of this non-NATO approved crusher gauge [5] has provided the FDF with only a static calibration table. In test firings, crusher readings measured with this gauge have been observed to fall behind the piezo-electric readings at pressures higher than about 150 MPa. This has caused some concerns in the FDF and the defense industry regarding the test firing results related to ammunition development and, in particular, to the assessment of Maximum Operating Pressures (MOP) according to STANAG 4110 [9]. Because of the long history of reporting peak pressures for this gauge based on static

* Corresponding author; e-mail: heli.nyberg@mil.fi

calibration tables, it has not been considered reasonable to change the crusher pressure measurement gauge type without a thorough study.

The objective of this study is to develop and verify a dynamic calibration method for crusher gauge elements. It is also our goal to base this dynamic calibration method on experimental stress-strain curves and to isolate it from test firings and chamber peak pressure measurement using reference pressure transducers.

2 Theoretical Background of the Strain Rate Dependence

During firing, the crusher element experiences rapid compression, and the strain rates in the material can be of the order of 100 s^{-1}. Plastic deformation of the material is carried out mainly by the movement of dislocations. Generally there are two kinds of obstacles or barriers that the dislocations meet. Athermal barriers consist of long-range obstacles, such as grain boundaries and dense dislocation walls. Surmounting of an athermal barrier depends on the acting external stress, but temperature or strain rate have no influence on it. Thermal obstacles are short-range barriers caused, for example, by the periodic Peierls force and dislocation intersections with other dislocations, precipitates and solute atoms. Increasing temperature increases the vibrational energy of the atoms, which in turn increases the probability of a dislocation (or an atom) jumping to the next position, hence reducing resistance against plastic deformation. The effect of strain rate depends on the same phenomenon; increasing strain rate reduces the time for the vibrational energy to assist the dislocations, and therefore more external force is needed to continue the plastic deformation.

Figure 1 shows the change in the mechanical and thermal energies with increasing temperature. At 0 K, all energy needed to move the dislocations must come from the external applied stress in the absence of thermal vibrations of atoms. With increasing temperature, the increasing contribution of thermal energy reduces the required mechanical energy and the flow stress, i.e., the stress needed to continue deformation, decreases. Figure 2 shows the contributions of athermal and thermal components to the total flow stress σ as a function of temperature T and strain rate $\dot{\varepsilon}$. Above the critical temperatures T_1 to T_3, depending on the strain rate, the flow stress of the material is determined by athermal obstacles only, because there is already sufficient thermal energy to overcome all thermal barriers.

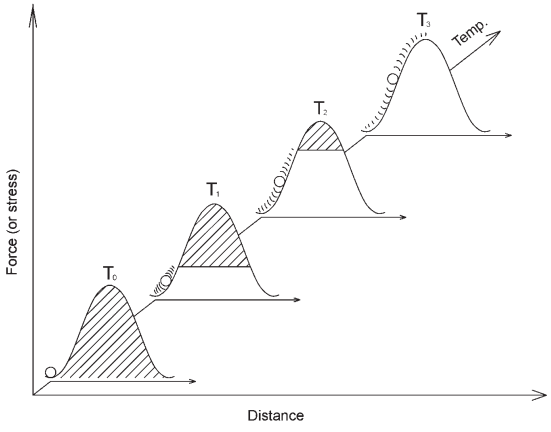

Figure 1. Thermal barrier height at different temperatures. The shaded area represents the required mechanical energy.

3 Experimental

A dynamic calibration table for one lot of cylindrical 5 × 7 mm crusher elements of the crusher gauge brand studied was developed on the basis of laboratory tests, where crusher elements were deformed at different loading rates with a servo-hydraulic materials testing machine and the Hopkinson Split Bar device. The mechanical tests at different strain rates as well as modeling of the results for crusher elements were carried out at the Institute of Materials Science of Tampere University of Technology.

In order to verify the calibration table developed, a statistical comparison of the crusher and piezo-electric peak pressure records was carried out with a rise time analysis of the piezo pressure curves. The pressure records were measured in artillery test firings realized by the Finnish Defence Forces Test Firing Centre during the period 1996 – 2005.

3.1 Crusher Pressure Measurement in Test Firings

Crusher gauges are commonly used for peak chamber pressure measurements because of the ease of use and simple construction [1]. The amount of crusher element deformation is used as a measure of the peak pressure to

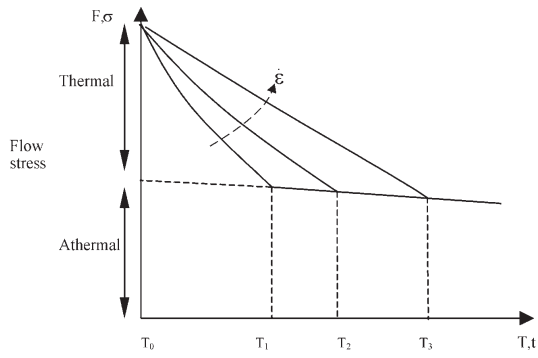

Figure 2. Flow stress versus temperature at different strain rates.

which the gauge was subjected and is interpreted by reference to calibration tables [3, 10].

The crusher peak chamber pressure values for crusher gauges in this study are determined on the basis of static calibration tables delivered by manufacturer for each crusher cylinder lot. The static calibration tables for crusher cylinder lots are determined at 21 °C by applying the load for 30 seconds.

In the test firings related to this study, crusher gauges with 5×7 mm cylindrical elements for 150 – 500 MPa pressure range were used. Crusher gauges are located in the pressure chamber or in the cartridge case as near the breech face as possible, oriented with their sensitive end facing the muzzle, their sensitive axis parallel to the gun axis and, at 10 a.m. and/or 2 p.m. positions on the clock face. The temperature-corrected peak pressure values determined on the basis of the deformation measured from the crusher element and the static calibration table for each crusher element lot are stored in the Test Firing Database.

3.2 Piezo Pressure Measurement in Test Firings

The ability of some crystals to produce electric charges when subjected to pressure is known as the piezo-electric effect [1, 11]. The piezo-electric gauge is the most widely used gauge where full pressure vs. time history is required. In guns, holes are drilled into the barrel in order to mount the piezo-electric transducers. The peak chamber pressure for each round is analyzed based on the measured time-pressure curves.

The piezo pressure measurement instrumentation used in test firings consisted of a Kistler 6215 transducer connected to a Kistler 5011 Charge Amplifier. The output of the amplifier was connected to a National Instruments VXI-MIO-64E-1 Nr. W10046622 A/D converter card. Sampling frequency was typically 100 kHz. The total number of samples was 10 000 – 30 000, including 5 000 samples for pre-triggering. Triggering level was 0.3 V. Recorded waveforms were zeroed just before the start of the pressure signal to remove any offset. The data was smoothed by 20 point moving average, and the resulting maximum of the waveform is quoted as the peak pressure. Piezo-electric transducers are calibrated at least annually at the Finnish Defence Forces Research Centre using AVL B620 DPC Dynamic Calibrator.

If the piezo-electric transducer is located at the cartridge case mouth, there is a systematic difference in the measured crusher and piezo pressure levels because the pressure in the chamber is highest at the breech. This difference is individual for each propelling charge.

3.3 Laboratory Measurements of Crusher Elements

Two materials testing methods were applied in order to determine the mechanical behavior of crusher elements as a function of strain and strain rate. Tests were carried out at room temperature.

Engineering stress σ_E and engineering strain ε_E values are based on fixed reference quantities, i.e., they are calculated by dividing the measured force and displacement by the original dimensions of the specimen. True stress σ_T and true strain ε_T take into account the changes in the cross-sectional area and length of the specimen, describing better the material properties of the sample. For better accuracy, modeling in this study was based on true stress and true strain values.

At low and intermediate strain rates ($0.0014 < \dot{\varepsilon} < 5\ s^{-1}$), the compression tests of the crusher elements were carried out by Instron 8800 servo-hydraulic materials testing machine equipped with hard metal compression platens. The displacement was measured by an inductive LVDT-transducer, and the load by an inertia compensated Instron Dynacell load cell. From the measured load vs. displacement curves, the true stress vs. true plastic strain curves were calculated by Equations (1) and (2).

$$\sigma_T = \frac{F(1+\varepsilon_E)}{A_0} \tag{1}$$

$$\varepsilon_T = \ln(1+\Delta l/l_0) - \sigma_{el}/E = \ln(1+\varepsilon_E) - \varepsilon_{el} \tag{2}$$

A_0 Initial cross-sectional area of the specimen (m^2)
E Young's modulus (Pa)
F Force (N)
l_0 Initial specimen length (m)
ε_{el} Elastic Strain
Δl Compression of the specimen (m)
σ_{el} Elastic stress (Pa)

At high strain rates ($80 – 1000\ s^{-1}$), the compression tests were carried out by the Hopkinson Split Bar (HSB) device. The operating principle of the HSB device is presented in Figure 3.

Shooting a striker to the end of the incident bar generates an elastic stress pulse, which propagates in the bar at the speed of sound, which for steel is about 5100 m/s. Part of this stress pulse is reflected back from the interface between the bar and the specimen, and part of it continues through the specimen to the transmitted bar. Elastic deformation of the bars is measured by strain gauges, as shown in Figure 3. Specimen stress, strain and strain rate can be calculated from the incident, reflected and transmitted pulses using Equations (3) – (5).

$$\sigma_E(t) = \frac{A_b E_b [\varepsilon_i(t) + \varepsilon_r(t) + \varepsilon_t(t)]}{2A_0} \tag{3}$$

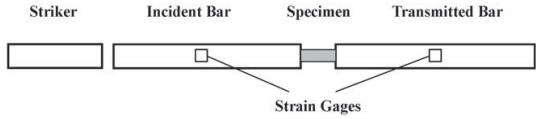

Figure 3. Operating principle of the Hopkinson Split Bar equipment.

$$\varepsilon_E(t) = \frac{C_0}{l_0}\int_0^t [\varepsilon_t(t) - \varepsilon_i(t) + \varepsilon_r(t)]\,dt \quad (4)$$

$$\dot{\varepsilon}_E(t) = \frac{C_0\,[\varepsilon_t(t) - \varepsilon_i(t) + \varepsilon_r(t)]}{l_0} \quad (5)$$

A_b Cross-sectional area of the bars (m^2)
E_b Young's modulus of the pressure bars (Pa)
C_0 Longitudinal sound velocity ($m\ s^{-1}$)
t Time (s)
$\varepsilon_{i,\,r,t}$ Incident, reflected, and transmitted strains
$\dot{\varepsilon}_E$ Engineering strain rate (s^{-1})

4 Results and Discussion

The development and validation of a dynamic calibration model for one 5 × 7 mm element lot of the studied crusher gauge brand is presented in this chapter.

4.1 Chemical Composition and Grain Size of the Crusher Elements

The chemical composition of the studied crusher elements was analyzed in the laboratory of Outokumpu Oy. The material was normal cathode copper with the following chemical composition: Cu 99.998%, C 0.001%, Ag 14 ppm, Al < 10 ppm, Cd < 5 ppm, Cr < 10 ppm, Fe 4 ppm, Mn < 1 ppm, Ni < 10 ppm, Si < 20 ppm, Zn < 10 ppm and O 29 ppm. The average grain size of the crusher element material studied was 15 μm.

4.2 Development of a Dynamic Calibration Model for the Crusher Elements

Since the main purpose of this study was to develop a mathematical model for the conversion of the crusher element deformation to the maximum pressure, the model does not have to be a parametric constitutive model. Therefore, the goal can be also achieved with a fitting function, which describes accurately enough the dependence of the plastic deformation of the crusher element on the maximum pressure under given circumstances. The first step in the model development was to find a function that would fit all the stress strain curves determined at different strain rates. A large number of possible functions were fitted to the data using TableCurve 2D®, and the best simple function turned out to be the rational function

$$\sigma_T = \frac{a + c|\varepsilon_T|}{1 + b|\varepsilon_T|} \quad (6)$$

Parameters a, b and c were determined for each stress vs. strain curve with TableCurve 2D®.

From experience we know that in the strain rate region where dislocation motion is controlled by thermal activation, the flow stress has a logarithmic dependence on strain rate [1, 2]. This means that the plot of flow stress *vs.* logarithm of strain rate at constant strain should give a straight line, and we can write

$$\sigma_T(\varepsilon_T) = A(\varepsilon_T) + B(\varepsilon_T)\,\ln|\dot{\varepsilon}| \quad (7)$$

where A and B are strain dependent constants. Functions $A(\varepsilon)$ and $B(\varepsilon)$ can be determined by first reconstructing the original stress strain curves using Equation (6), and then plotting the σ vs. $\ln|\dot{\varepsilon}|$ points taken from each of the curves at constant values of strain, as shown in Figure 4. Fitting of the function $\sigma = A + B\ln|\dot{\varepsilon}|$ to these points gives A and B at different constant values of strain. Figure 4 also shows this fitting at strains from 3% to 43%. Finally, fitting Equation (6) again to A vs. ε data and a second order polynomial to B vs. ε data gives the final model with six parameters and two variables. The parameter values for $A(\varepsilon_T)$ and $B(\varepsilon_T)$ are presented in Equations (8) and (9) for the crusher elements studied.

$$A(\varepsilon_T) = \frac{43.940 + 2455.959\,|\varepsilon_T|}{1 + 4.887\,|\varepsilon_T|} \quad (8)$$

$$B(\varepsilon_T) = -0.572 + 19.997\,|\varepsilon_T| - 11.001\,|\varepsilon_T|^2 \quad (9)$$

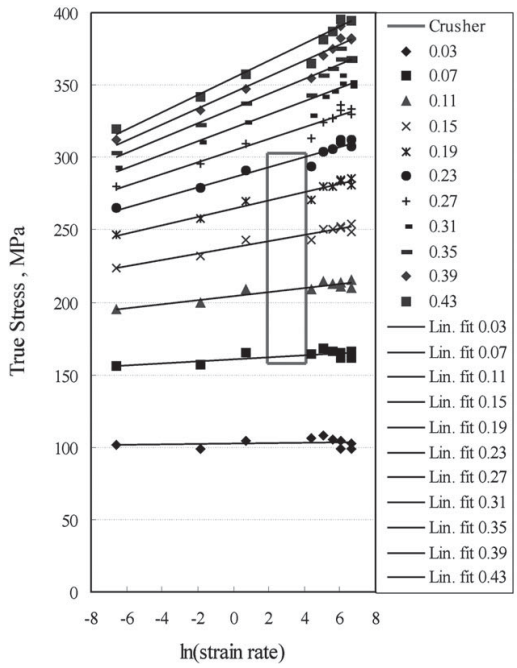

Figure 4. True stress vs. ln $|\dot{\varepsilon}|$ for constant true strain values from 3% to 43%.

4.3 Test Firing Pressure Data Analysis

The peak pressure data for the verification of the dynamic calibration method developed was selected from the Test Firing Database on the basis of the following criteria:

1) The round had been accepted for war materiel or was a corresponding inert round.
2) Records for both piezo-electric and studied crusher gauge (with 5×7 mm element) peak pressures were available.
3) Test firing had taken place in 1996 or later.

The statistical analysis of the pressure records was carried out using MATLAB®. The number of rounds analyzed was 1126. The characteristics of the peak chamber pressure data set and piezo transducer location for each gun are presented in Table 1.

For the 122 mm howitzer and the 152 mm howitzer, the piezo-electric transducer had been located at the cartridge case mouth. The resulting systematic difference between the crusher and piezo-electric peak pressure levels was corrected by adding for each round a specific constant to the piezo-electric pressure records. The magnitude of these constants had been determined in test firings where the barrel had been equipped with a piezo-electric transducer located both at the breech and at the cartridge case mouth.

A rational function of the type given in Equation (6) was fitted to piezo-electric peak pressure vs. crusher pressure data by using the non-linear least-square fitting method. The values obtained from this fit for the three parameters of Equation (6) were as follows: $a = -30.5880$, $b = 0.0013$ and $c = 1.3738$. The piezo-electric peak pressure values for each gun and charge type studied are presented in Figure 5 as a function of the static crusher peak pressure. Figure 5 also shows the curve fitted to the measured data using Equation (6) as well as the modeled stress strain curves for three different strain rates using Equations (7) – (9), which will be discussed in more detail in Section 4.4.

4.4 Verification of the Dynamic Calibration Model

In order to use the calibration model developed, the strain rate in the test firing must be known. Average strain rate is the total strain divided by the rise time of the pressure to its maximum value. The total strain can be readily measured from the crusher element after the firing, but the rise time of the pressure needs to be measured during the firing by some appropriate technique. When the gun pressure is measured both by the crusher gauge and by the piezo-electric transducer, we have all the needed data at hand. This, however, conflicts with the general idea of using crusher gauges, because it should be possible also to use them independently of any other measurements. There are basically two possible ways to solve this problem: a) to find a characteristic rise time of pressure for every combination of gun and charge, or b) to measure the true rise time during every firing by some indirect method, i.e. without making changes in the gun itself.

In this study, a large number of test firings where the pressure was measured with both the piezo-electric and the crusher gauge were analyzed. The piezo-electric pressure curves were collected from the Pressure Database for 8 different rounds. Altogether 303 pressure curves were analyzed. The pressure rise time $t_{90\% - 10\%}$ was defined as the time interval between 10% and 90% from the pressure baseline to the peak pressure [11]. Average strain rate $\dot{\varepsilon}$ was then calculated by dividing the measured total strain with the pressure rise time.

The number of pressure curves analyzed, average pressure rise times, average piezo-electric peak pressures P_h and crusher peak pressures P_{cr}, true strains, and strain rates for each round type are presented in Table 2. According to Table 2, in real artillery firings the strain rate in the copper crusher element ranges from about 7 to 60 s^{-1} for true compressive strains ranging from about 5 to 20 percent. The corresponding pressure values range from about 160 to 380 MPa, as shown in Figure 5. The rectangle included in Figure 4 represents this operation area of studied artillery firings.

Verification of the dynamic calibration model developed was carried out by comparing the test firing piezo-electric peak pressure records with crusher pressure values obtained from Equation (7). For this, dynamic crusher peak pressures were calculated for strain rates 10, 35 and 80 s^{-1}. The calculated curves are presented in Figure 5.

The test firing piezo-electric peak pressure fit (P_h), the difference of P_h and static crusher peak pressures (P_{cr}), and the peak pressure differences between test firing piezo-electric peak pressure fit and the dynamic crusher pressure

Table 1. Characteristics of the peak chamber pressure data set and piezo transducer location for each gun.

Gun	Round type	No. of peak pressure results	Piezo transducer location
122 mm howitzer	122.1	118	Case mouth
130 mm cannon	130.1	205	Breech
	130.2	48	
152 mm howitzer	152.1	44	Case mouth
155 mm cannon	155.1	176	Breech
	155.1	320	
	155.3	110	
155 mm NATO-cannon	155N.1	44	Breech
	155N.2	61	

Table 2. Results of the pressure rise time analysis.

Round	No. of P curves	$t_{90\%-10\%}$ ms	P_h MPa	P_{cr} MPa	ε_T mm/mm	$\dot{\varepsilon}$ s^{-1}	ln $\dot{\varepsilon}$
122.1	12	2.48	291	262	−0.144	58	4.06
130.1	42	5.42	354	308	−0.192	35	3.56
152.1	44	1.83	235	222	−0.110	60	4.10
155.1	69	4.30	338	301	−0.183	43	3.75
155.2	56	4.54	334	299	−0.183	40	3.70
155.3	48	4.51	255	235	−0.121	27	3.34
155N.1	12	5.67	259	240	−0.125	22	3.09
155N.2	20	5.46	198	186	−0.082	15	2.71
155N.3	10	6.78	140	129	−0.045	7	1.90

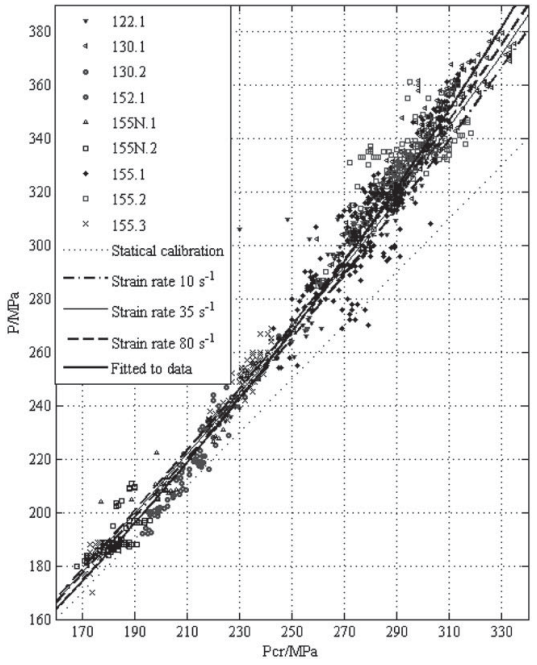

Figure 5. Piezo-electric peak pressures as a function of static crusher peak pressure for each studied gun and charge type, and a curve fitted to that data. Dynamic crusher pressures at strain rates 10, 35 and 80 s^{-1} vs. static crusher pressure are also shown.

model at different strain rates ($dP_{10\,1/s}$, $dP_{35\,1/s}$ and $dP_{80\,1/s}$) are presented in Table 3. From Figure 5 and Table 3, we can see that the difference between the fitted test firing piezo-electric peak pressures and the dynamic crusher model is negative and quite small at low pressures, i.e., the model gives slightly conservative pressure values. At higher pressures, the difference becomes positive, i.e., the model values start to fall behind the piezo-electric pressure values. The difference is smaller when a higher strain rate is used in the model, which is consistent with the fact that a higher maximum pressure also generally leads to a higher strain rate. At P_{cr} 350 MPa, the difference between the model and the piezo-electric values varies between 9 and 18 MPa,

Table 3. Pressure differences.

P_h MPa	$P_h - P_{cr}$ MPa	$dP_{10\,1/s}$ MPa	$dP_{35\,1/s}$ MPa	$dP_{80\,1/s}$ MPa
153	3	−3	−3	−4
207	7	−2	−4	−5
268	16	2	−1	−3
336	36	9	4	2
414	64	18	13	9

which still is much less than 64 MPa, which is the difference between the static crusher and piezo-electric pressure readings.

The total uncertainty of the piezo-electric pressure measurement is about ±3% of the full scale of the transducer. According to the crusher gauge manufacturer, the uncertainty of crusher gauge type used in the test firings is ±5% of the reading for the pressure range presented in the static calibration table. The standard deviation of the piezo-electric peak pressure vs. crusher pressure data, from which the trend of the curve fitted to the measured data using Equation (6) had been subtracted, was 13.8 MPa. As a consequence of the relatively high uncertainty of the pressure measurement, small differences observed in pressure rise times and narrow peak pressure bands for most of the examined rounds it was difficult to distinguish the precise influence of pressure rise time on test firing data (Figure 5).

5 Conclusions

A dynamic calibration model based on laboratory material tests was developed for one 5 × 7 mm cylindrical crusher element lot and verified by comparison to totally independent test firing results. In the laboratory tests with servo-hydraulic testing machines and the Hopkinson Split Bar technique, much wider ranges of stress (or pressure), strain (or compression), and strain rate (or pressure rise rate) could be obtained than in the artillery firings, which facilitates the modeling and improves the validity and accuracy of the model. The only practical difficulty in the application of the model is that it requires knowledge of the true strain rate in the crusher element during pressure build-up. Based on the analysis of a large number of actual test firings, estimates for the effective strain rate for different round types can be obtained which lead to reasonably correct pressure readings. The developed dynamic crusher pressure model was found to give pressure values which are consistent with the pressure records from actual test firings, especially when the general limitations in the measuring accuracy of the piezo-electric and crusher methods are taken into account.

In contrast to the calibration methods for crusher gauges, which are based on modeling of the records of large caliber gun firings and laboratory simulations [5], the material testing method presented in this study is isolated from test firings and piezo-electric pressure measurements and also

takes into account the strain rate in the deforming crusher element.

The calibration model developed in this study is valid only at room temperature. However, testing facilities to extend the model to lower and higher temperatures exist. The calibration method developed is also suitable for the dynamic calibration of crusher elements designed for higher pressure and pressure rise rate levels than those realized in artillery firings, e.g. for use in tank firings.

The method developed in this study allows the FDF in the future to present the crusher pressure records on the basis of both static and dynamic calibration tables. As a result the traceability of the static results heretofore remains and better comparability of the results with piezo-electric peak pressures is gained.

6 References

[1] L. W. Longdon, *Textbook of ballistics and gunnery*, Vol. 2, Part III, Her Majesty's Stationery Office, London **1984**, p. 17.
[2] P. O. Kettunen, V.-T. Kuokkala, *Plastic Deformation and Strain Hardening, Materials Science Foundations*, Vol. 16 – 18, Trans Tech Publications, Uetikon-Zürich **2003**.
[3] M. A. Meyers, *Dynamic Behavior of Materials*, John Wiley & Sons, New York **1994**.
[4] G. R. Johnson, W. H. Cook, A Constitutive Model and Data for Metals Subjected to Large Strains, High Strain Rates, and High Temperatures, *7th International Symposium on Ballistics*, The Hague, The Netherlands, April 19 – 21, **1983**, p. 541.
[5] Pressure Measurement by Crusher Gauges – NATO Approved Tests for Crusher Gauges, *AEP-23,* **2005**, Ed. 2, NATO International Staff.
[6] M.-W. Zhu, C.-M. Wang, G.-L. Liu, R.-J. Liang, Dynamic Calibration of Chamber Pressure Measuring Equipment, *13th International Symposium on Ballistics*, Stockholm, Sweden, June 1 – 3, **1992**, p. 443.
[7] D. Warken, E. Meineke, Copper Crushers: Dynamic Calibration in the Laboratory, *10th International Symposium on Ballistics*, San Diego, USA, October 27 – 29, **1987**, p. 355.
[8] V. L. Lokre, B. J. Abhyankar, S. L. Mankikar, S. S. Gopalani, M. T. Karmarkar, M. V. Vaidya, Comparison of Piezo and Ball Copper Pressure Measurements in Closed Vessel System, *Defence Science Journal* **1977**, *27*, 105.
[9] Definition of Pressure Terms and Their Inter-Relationship for Use in the Design and Proof of Guns (Mortars) and Ammunition, *STANAG 4110*, **1998**, Ed. 3, NATO Military Agency for Standardization.
[10] Pressure Measurement with Crusher Gauges, *STANAG 4113*, **1993**, Ed. 4, NATO Military Agency for Standardization.
[11] Electrical Measurement of Weapon Chamber Pressure, *ITOP 3-2-810,* **1995**, US Army Test and Evaluation Command.

Acknowledgements

This work was partially supported by The Scientific Advisory Board for Defence (MATINE). We thank Mr. Timo Muikku and Mr. Kari-Pekka Niemelä (Defence Forces Materiel Command Headquarters, Finland) for their participation in collection and analyzing the test firing data.

(Received: May 26, 2006; Ms 2006/020)

PUBLICATION V

Influence of Strain Rate and Adiabatic Heating on the Deformation Behavior of Cold Heading Steels

J. Rämö, V-T. Kuokkala and T. Vuoristo

Journal of Materials Processing Technology, pp. 5186-5194, 2009

Journal of Materials Processing Technology 209 (2009) 5186–5194

Contents lists available at ScienceDirect

Journal of Materials Processing Technology

journal homepage: www.elsevier.com/locate/jmatprotec

Influence of strain rate and adiabatic heating on the deformation behavior of cold heading steels

Jari Rämö*, Veli-Tapani Kuokkala, Taina Vuoristo

Tampere University of Technology, Department of Materials Science, P.O. Box 589, 33101 Tampere, Finland

ARTICLE INFO

Article history:
Received 5 April 2008
Received in revised form 1 March 2009
Accepted 7 March 2009

Keywords:
Cold heading
Numerical simulation
Hopkinson split bar

ABSTRACT

In the cold heading process of metals, strain rates in complex parts can vary considerably and locally reach very high values. Therefore, when considering the material's deformation behavior, both the transient hardening at high strain rates as well as softening due to adiabatic heating should be accounted for. In this work, a purely phenomenological model based on experiments performed at strain rates in the range of 10^{-3}–10^{4} s^{-1} at temperatures extending from −150 to 800 °C was devised and used in finite element simulations of the cold heading process. The model separates yielding, including both the upper and lower yield point, from strain hardening, which typically depend on strain rate in a different way due to the adiabatic thermal softening effects at higher strains. The simulation results show good agreement with the high strain rate cold heading results obtained using a direct impact Hopkinson split bar technique.

1. Introduction

Cold heading, or upsetting, is a fast and effective metal forming process to produce large quantities of relatively small-sized products, such as a variety of fasteners for automotive industry. In cold heading, a rolled or drawn metal wire is transformed into desired shapes by one or more blows with a fast moving punch. The wire may be plastically deformed either in a die, the punch, or both. The production rates vary from tens to several hundreds of parts per minute and thus, depending on the magnitude of local plastic deformation, the rate of deformation can become quite high. Typical strain rate values for cold heading found in literature range from 10 to 1000 s^{-1}, but locally the strain rates may be even higher (Brethenoux et al., 1996).

Cold headability, or more generally formability, of a material is usually described as its capability to resist failure during plastic deformation. Mechanical properties required from the wire to be cold headed include high ductility and relatively low initial strength. Cold heading steels are typically low alloy steels with ferritic or ferritic-pearlitic microstructure, but for example dual phase steels with martensite islands in soft ferrite matrix offer another attractive alternative for components requiring high strength without the need for further heat treatments. Voids, inclusions, high carbon content, and poor surface quality decrease the formability of steels, but with proper heat treatments, especially spheroidization, the formability can be greatly improved (Ma et al., 2004). A further variable affecting cold headability is the texture of the wire. There are indications that the stronger the ⟨1 1 0⟩ fiber texture is, the better the formability of the steel wire (Sugondo et al., 1991).

With proper design of the cold heading sequence, relatively complex components can be manufactured. Numerical simulations can be applied in designing the components and the cold heading process, but to do this, the material's true deformation behavior must be known. Due to large deformations and high strain rates, the conditions in the deformed component are close to adiabatic, and thus the temperatures may rise locally by several hundreds of degrees. This means that the deformation resistance of the material must be known not only as a function of strain but also as a function of strain rate and temperature, *i.e.*, in conditions similar to those of practical cold heading applications. To this aim, the strain rate and temperature dependent behavior of cold heading steels was experimentally investigated using the Hopkinson split bar (HSB) technique and servohydraulic materials testing machines. Compression tests to large strains were made in the strain rate range of 10^{-3}–10^{4} s^{-1} at initial testing temperatures ranging from −150 to 800 °C. Temperatures below ambient do not normally occur in the cold heading process, but to map and model the material behavior as completely as possible, also sub-zero temperatures were included in the test program.

It is a challenging task to develop a constitutive model that would realistically describe both the strain rate and temperature dependent behavior of different types of metals over wide ranges of strain. Factors that further complicate the modeling task are, *e.g.*, the complex interdependencies of strain, strain rate, strain hardening rate, and temperature. Despite this, a large variety of models have been presented to describe the strain rate and temperature

* Corresponding author. Tel.: +358 40 8490141; fax: +358 3 31152330.
E-mail address: jari.ramo@tut.fi (J. Rämö).

0924-0136/$ – see front matter © 2009 Elsevier B.V. All rights reserved.
doi:10.1016/j.jmatprotec.2009.03.004

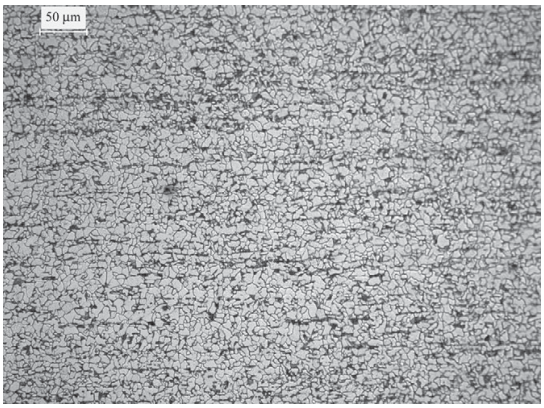

Fig. 1. Optical micrograph revealing the banded microstructure of the studied steel wire. The rolling direction is horizontal.

dependent deformation of metals. Perhaps the most widely used of these is the Johnson–Cook model (Johnson and Cook, 1985), which consists of three multiplicative terms, first of which describes the effect of strain hardening, the second the effect of strain rate hardening, and the third the effect of temperature. Also this model, however, has several limitations. According to the model, for example, the work-hardening rate $d\sigma/d\varepsilon$ increases as the strain rate increases, which is not in accordance with many observations (e.g. Liang and Khan, 1999). Also, the strain rate sensitivity in the Johnson–Cook model is constant throughout the whole strain rate range, which is generally not true for metals. Detailed analyses of the applicability and limitations of the Johnson–Cook model can be found, for example, in (Rule and Jones, 1998). Another frequently used constitutive model is the Zerilli–Armstrong model (Zerilli and Armstrong, 1987), which assumes that the work-hardening rate is independent of temperature and strain rate. Since this assumption also contradicts with general observations, we can conclude that neither the Johnson–Cook nor the Zerilli–Armstrong model describe properly the true strain hardening behavior of most bcc metals.

In this study, an empirical model is developed to describe the elasto-viscoplastic behavior of a particular cold heading steel. The model is further used in the numerical simulation of the cold heading process of a simple component. In this approach, higher order polynomials are fitted to the experimental strain rate and temperature dependent stress–strain data. The model describes all the main features of the deformation behavior, such as the upper and lower yield points, transient and permanent strain hardening, and thermal softening of the studied material. The results of the numerical simulations are compared with force-time data, final shape of the specimen, and microstructural (flow line) images obtained from high rate cold heading experiments conducted with a Hopkinson Split Bar device.

2. Materials

The studied steel is an aluminum-killed low alloy steel that is not intended for heat treatments, such as quenching. The microstructure of the steel contains ferrite and pearlite with an average ferrite grain size of ca. 10 μm, as shown in Fig. 1. The designation of this steel in standard EN 10263 is C17C. The nominal composition and tensile strength of the steel are given in Table 1. The compression test specimens were cut from the delivered steel coil using a precision cutting machine to nominal lengths of 8.25 and 3.7 mm. The nominal diameter of the hot rolled steel wire was 5.5 mm.

Table 1
Nominal composition and tensile strength of the studied steel.

C (%)	Min–max. 0.16–0.19
Si (%)	Max 0.10
Mn (%)	Min–max. 0.70–0.90
P (%)	Max. 0.020
S (%)	Max. 0.020
Cr (%)	Min–max. 0.07
Al (%)	Min–max. 0.025–0.050
R_m (MPa)	500–520

3. Experimental techniques

In this study, the deformation behavior of C17C cold heading steel was experimentally investigated in a wide range of strain rates (10^{-3}–$10^4\ s^{-1}$) and temperatures (−150 to 800 °C). The compression tests at quasi-static strain rates (10^{-3}–$10^{-1}\ s^{-1}$) were made using a 100 kN Instron 8800 servohydraulic materials testing machine. In these tests, a 25 mm gauge length extensometer was attached to the compression plates to measure their relative displacement during compression. The quasi-static tests were made at room temperature only.

The Hopkinson Split Bar technique is used to measure the stress–strain response of materials at high strain rates, typically in the range of 10^2 to $10^4\ s^{-1}$. The HSB method is based on the propagation of one-dimensional elastic pressure waves in slender bars. A detailed description of the technique can be found, *e.g.*, in (Nemat-Nasser, 2000). Because the deformations in cold heading processes are usually quite large, the aim in this work was to obtain large strains also in the HSB tests. In the HSB method, however, the obtainable strain and strain rate are both dependent on the same test parameters (striker length, specimen length, striker velocity), and thus the free choice of strain and strain rate in an experiment is limited. For example, obtaining large deformations (*e.g.*, 80% true strain) at a relatively low strain rate (in the order of 100–800 s^{-1}) is quite difficult. Such tests would require the use of a very long striker bar (up to several meters), which in turn would normally require the use of very long pressure bars so that the long pulses could be measured separately without incident and reflected waves overlapping each other (Vuoristo et al., 2006). Another option would be to make several tests on the same specimen in, *e.g.*, 20% strain steps, but due to adiabatic heating of the specimen, the stress–strain curve consisting of several individual tests would not be continuous as the thermal conditions would change between the tests.

To obtain the high strains at the relatively low strain rates needed in this study, some of the tests were made using an HSB apparatus with a 1500 mm long striker bar. In the tests at higher strain rates, an 800 mm long striker bar was used. With the 1500 mm striker bar, loading pulses of approximately 600 ms in duration were obtained. The striker bar was accelerated to its final velocity of 10–15 m/s with an air gun using loading pressures of 6–10 bars. To control the rise time and shape of the loading pulse, a rubber disc of 0.5 mm in thickness and 10 mm in diameter was used as a pulse shaper at the impact end of the incident bar. Because the length of the incident bar was limited to 1800 mm due to the lack of laboratory space, the incident and reflected signals could not be recorded without overlapping with just one strain gage positioned midway of the length of the bar. Therefore, a wave separation technique was applied with two pairs of strain gages positioned along the incident bar's length at a distance of 50 mm from the impact and specimen ends. The experimental setup allowing the separation of long incident and reflected pulses is presented in Fig. 2. At position SG1, the incident wave that propagates towards the specimen can be recorded in its full length and amplitude, but the reflected wave at position SG2

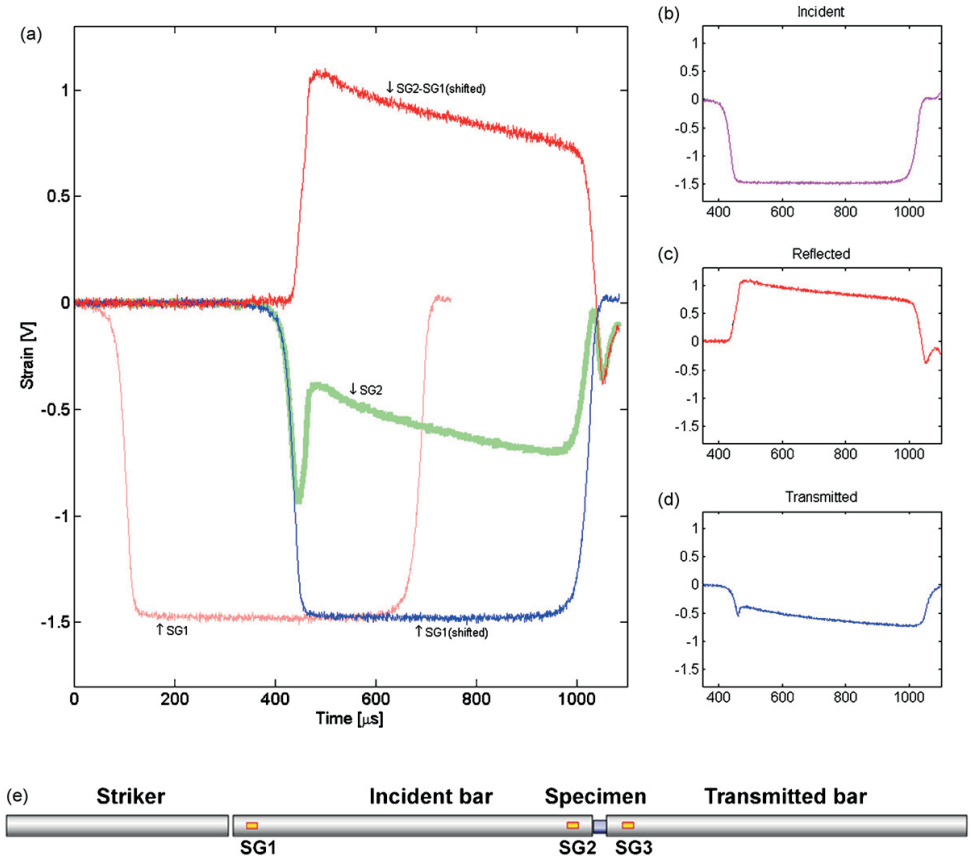

Fig. 2. Experimental HSB setup for extra long loading pulses: (a) the incident bar waves recorded at positions SG1 and SG2, the incident bar wave measured at position SG1 and transferred to the same starting point with the wave measured at position SG2, and the reflected wave obtained by subtraction of the wave measured at position SG2 from the wave measured at position SG1, (b–d) the separated incident, transmitted and reflected waves used in further calculations of the specimen's stress–strain relations, (e) test setup showing the positions of strain gages in the pressure bars.

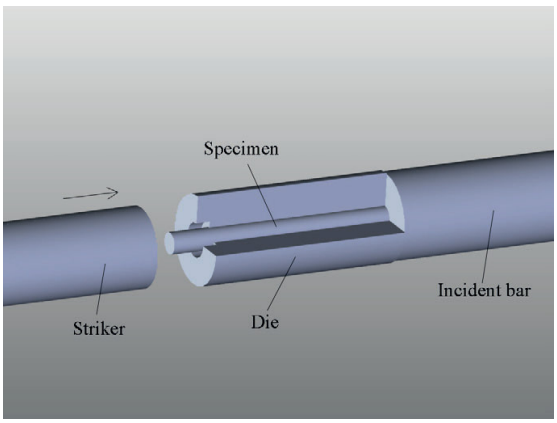

Fig. 3. Experimental setup applied in the cold heading verification tests.

is almost completely overlapped by the tail of the incident wave and thus cannot be directly measured. In addition, at position SG1 the reflected wave overlaps with its own reflection from the impact end of the incident bar. However, since the distance between the strain gages is known, the wave reflected back from the specimen end of the bar can be reconstructed by subtracting the incident wave measured at SG1 from the wave measured at position SG2. The resulting reflected signal as well as the original incident and transmitted signals used in further HSB calculations are shown in Fig. 2b–d.

The use of ordinary servohydraulic testing machines and the Hopkinson Split Bar technique leaves a gap in the strain rate range of ca. 1–200 s^{-1}, which is also rather difficult to cover accurately with any of the other common high strain rate measurement techniques. For example, special high velocity hydraulic testing machines usually cannot be used in compression testing, and also in tensile testing they are plagued with severe oscillations in the load signals. Drop hammers or drop towers, as well the cam plastometers, can produce the above mentioned strain rates, but also their applicability and accuracy are limited, especially with respect to the strain measurement. The practical experience, however, has shown that nothing special usually happens in this strain rate range, and therefore the flow stresses can be quite safely interpolated from the servohydraulic and HSB data. The only problem sometimes encoun-

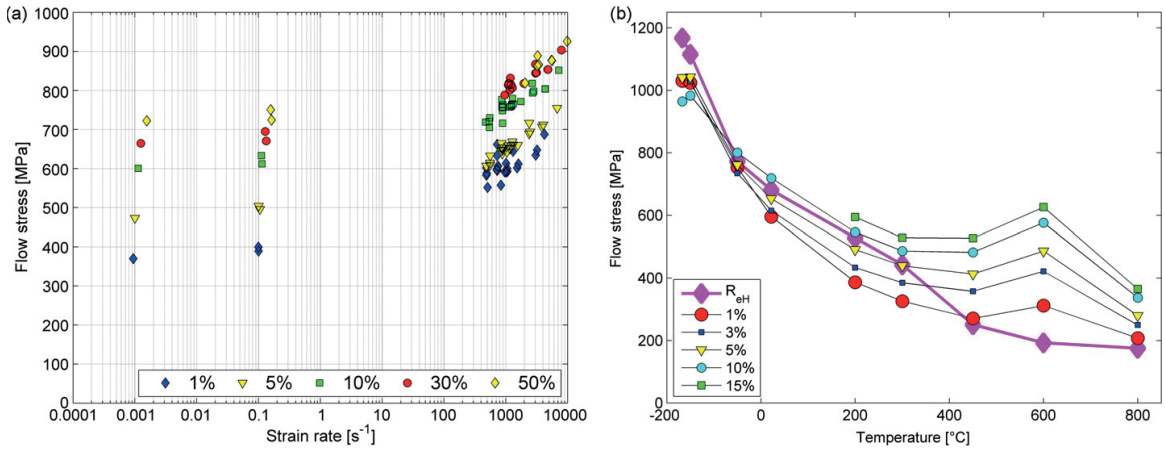

Fig. 4. Results of compression tests for C17C, (a) flow stresses at different constant plastic strains as a function of strain rate at room temperature, (b) flow stresses at different constant plastic strains as a function of temperature at the strain rate of 1100 s^{-1}.

tered is that the onset of the flow stress upturn cannot be exactly determined.

For the high and low temperature HSB tests, a special technique developed at the Department of Materials Science of Tampere University of Technology was used. In this method, fast pneumatically driven mechanical specimen and bar manipulation systems with precise timing are applied. The basic idea in this high/low temperature HSB method is to keep the pressure bars at room temperature

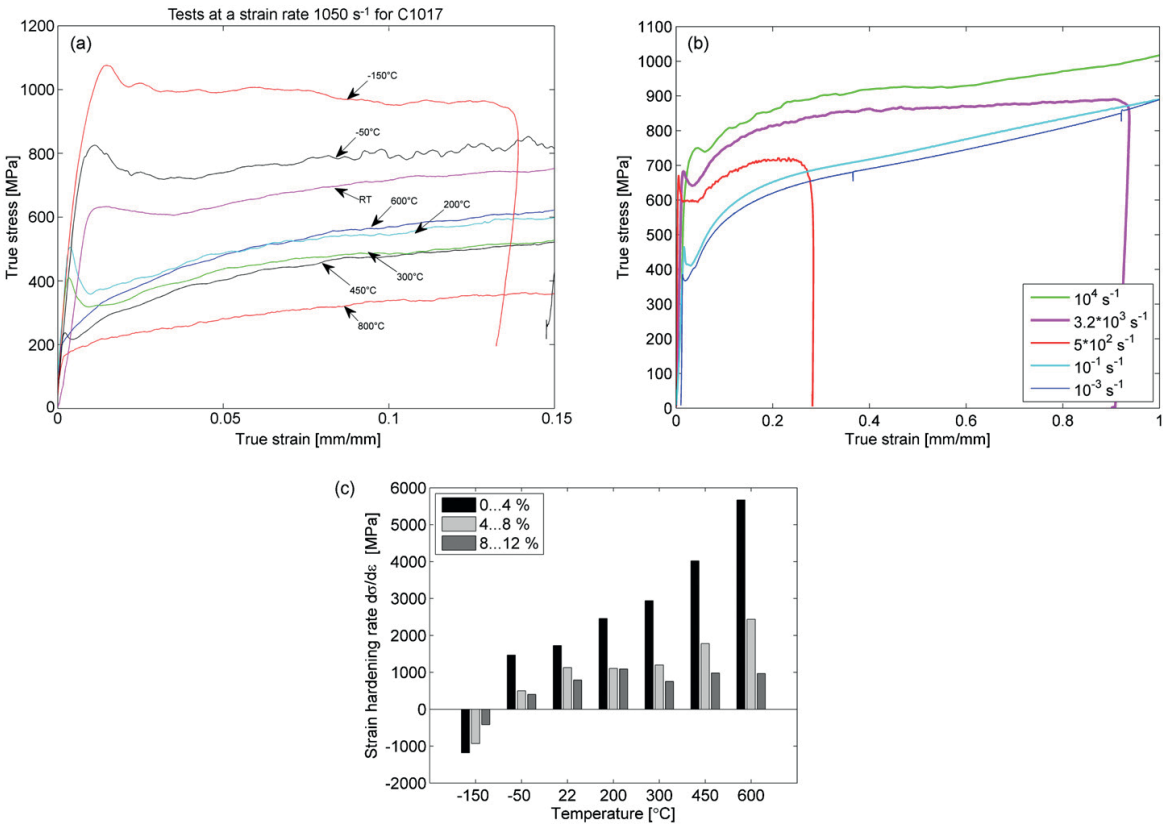

Fig. 5. Stress–strain curves for C17C determined (a) at the strain rate of 1100 s^{-1} at different temperatures, (b) at room temperature at different strain rates, and (c) strain hardening rates at different temperatures determined at 4% plastic strain intervals.

Table 2
Contants in Eqs. (1) and (2).

a_1	a_2	a_3	b	c_1	c_2	c_3	d
−1.5E+07	959695.8	−19069.6	26.36821	−1.13E−06	0.002325	−1.85609	594.1694
e_1	e_2	e_3	e_4	e_5	f_1	f_2	f_3
349.8376	−2162.82	4782.886	−4451.12	2013.256	8.98E−17	−2.65E−12	2.87E−08
f_4	f_5	g_1	g_2	g_3	g_4	h	
−0.00014	0.303457	−2.95E−09	6.38E−07	0.003049	−1.87936	431.5246	

while the specimen is heated in the furnace or cooled in the cooling chamber located beside the bars. The heating system is described in detail and with examples, *e.g.*, in (Apostol et al., 2003). The cooling system uses nitrogen gas, which is cooled in a heat exchanger immersed in liquid nitrogen, to cool the specimen to the desired temperature (Hokka et al., 2006). The temperature range obtained with the combined high/low temperature HSB system is currently 123–1273 K.

A direct impact HSB method was applied for the verification of the results given by the numerical simulations. In this method, a simple cold heading die is positioned at the impact end of the incident bar as shown in Fig. 3. A 55 mm long steel wire with a diameter of 5.5 mm is placed in the die, and a 1500 mm long striker bar is launched at a velocity of 14 m/s. As the striker impacts the steel wire, the wire is plastically deformed into the shape of the die. After the cold heading experiment, the geometry of the cold headed wire can be compared with the deformed shape obtained from the numerical simulations. In addition, the flow of the material revealed by the banded microstructure of the hot rolled steel wire can be compared with the movement of markers in the simulation by preparing cross sectional samples from the cold headed part.

4. Experimental results

Cylindrical specimens cut from the 5.5 mm diameter wire were compressed at quasi-static strain rates using a servohydraulic materials testing machine and at high strain rates using the HSB apparatus. For the quasi-static tests, the length to diameter (L/D) ratio of the specimens was 1.5, but most of the HSB tests were made using specimens with a lower L/D ratio of 0.67. MoS_2 containing lubricant was used between the sample and the bars to reduce friction to a minimum and to prevent barreling of the sample.

The strain rate dependence of the cold heading steel C17C at room temperature is shown in Fig. 4a at various constant plastic strains. The flow stresses increase steadily with increasing strain rate up to about 500 s^{-1}, above which a clear change in the strain rate sensitivity, *i.e.*, the slope of the flow stress *vs.* logarithmic strain rate, is observed. Compression tests were also made at temperatures ranging from −150 to 800 °C at the strain rate of 1100 s^{-1}. Due to the experimental setup, the specimens at high and low temperatures could only be compressed to relatively low strains, *i.e.*, up to about 20% of plastic strain. Fig. 4b shows the flow stress values measured at 1100 s^{-1} as a function of temperature. Up to the temperature of 450 °C, the flow stress values decrease smoothly with increasing temperature, but above this the flow stresses start to increase again. The effect of temperature on the deformation behavior of C17C is also clearly seen in Fig. 5a, which presents the experimental true stress–strain curves at the strain rate of 1100 s^{-1} at different temperatures. Fig. 5c shows the corresponding strain hardening rate values determined at 4% plastic strain intervals, indicating that the strain hardening rate increases with increasing temperature. Fig. 5b shows the room temperature true stress–strain curves at strain rates varying from 10^{-3}–10^{4} s^{-1}, revealing that the strain hardening rate decreases with increasing strain rate.

5. Modeling approach

The objective of this study was to develop a simple yet accurate model that would describe the elasto-viscoplastic behavior of a low alloy steel at different strain rates and temperatures and that could be easily implemented in ABAQUS/Explicit FE-software (Abaqus Version 6.7 Online Documentation, 2007) for simulation of the cold heading process. Since the developed empirical model was desired to describe the material's stress–strain response as precisely as possible, the sharp yield point behavior was also included in the model. Because it is practically impossible to describe both sharp yielding and subsequent strain hardening with a simple function, such as a relatively low-order polynomial, the stress–strain curve was described with two functions, for which the data was fitted separately in appropriate strain regions. In both functions, the variables are strain, strain rate, and temperature. The following equations were found to give a good fit to the experimental data of all conducted compression tests:

Sharp yield point behavior (part 1):

$$\sigma(\varepsilon, \dot{\varepsilon}, T) = \sum_{i=1}^{3} a_i \varepsilon^i + b \ln(\dot{\varepsilon}) + \sum_{j=1}^{3} c_j T^j + d \quad (1)$$

Strain hardening behavior (part 2):

$$\sigma(\varepsilon, \dot{\varepsilon}, T) = \sum_{i=1}^{5} e_i \varepsilon^i + \sum_{j=1}^{5} f_j \dot{\varepsilon}^j + \sum_{k=1}^{4} g_k T^k + h \quad (2)$$

where σ is the true stress, ε the true strain, $\dot{\varepsilon}$ the true strain rate, T the temperature, and a_i, b_j, c_k. . .h are constants. The values for the constants were determined using the *fminsearch* function in MATLAB (Table 2). However, because the current approach is purely numerical, any equations leading to a good match with experimental data could be used instead of those presented in Eqs. (1) and (2).

For fitting, the original measured data, shown for example in Fig. 5a, was sampled so that both parts, *i.e.*, yield point and strain hardening parts, of the stress–strain curves were represented by 20–30 points each. The initial test temperature was measured with a thermocouple just before the start of the test. In the high strain rate experiments ($\dot{\varepsilon} > 100\,s^{-1}$), the temperature rise of the specimen during plastic straining was calculated assuming that 90% of the energy expended in the deformation is converted adiabatically to heat. The quasi-static tests ($\dot{\varepsilon} < 1\,s^{-1}$), however, were assumed to be isothermal. Fig. 6 is a three-dimensional comparison of the experimental data (open circles) and the stress–strain values calculated using Eq. (2) (dots) at different strain rates.

6. Experimental verification of numerical simulations

In order to verify the developed numerical material model, the results of an FE simulation were compared with the results of cold heading experiments using the setup shown in Fig. 3. In this experiment, a button with a diameter of 8.5 mm and thickness of 3.5 mm

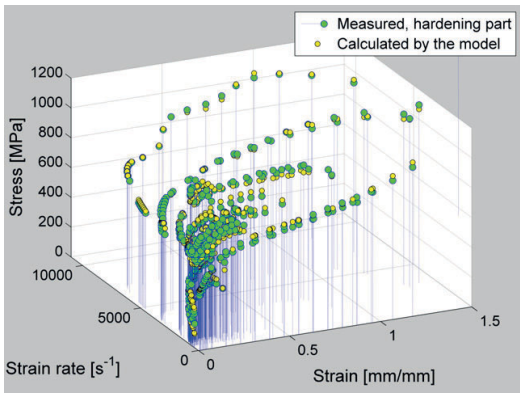

Fig. 6. Comparison of the measured and modeled stress–strain data for C17C at different strain rates.

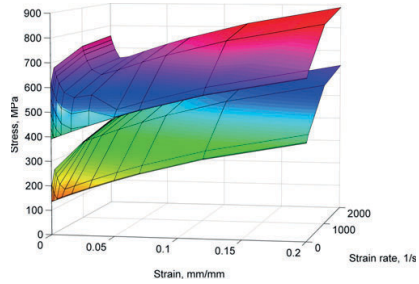

Fig. 8. Material input data at room temperature and at 422 °C.

was cold headed at the end of a steel wire with an original diameter of 5.5 mm. The cold heading die, made of AISI 4340 high strength steel, was placed at the impact end of the incident bar of the HSB device as shown in Fig. 3. The interface between the die and the sample was lubricated with MoS_2 containing grease. The velocity of the 1.5 m long striker bar was 14 m/s, deforming the specimen to its final shape in about 0.8 ms.

The material model presented above was implemented and the high strain rate cold heading experiment was numerically simulated using the FE-software ABAQUS/Explicit. Since both the pressure bars and the cold heading die were axisymmetric, also the model was a 2D axisymmetric model with only half of the geometry. The mesh of the deforming steel wire consisted of about 260 four-node reduced integration axisymmetric quadrilateral continuum elements (CAX4R). Adaptive meshing was used to maintain a high-quality mesh during the large deformation process. The contact friction between the wire, the striker bar and the die was set to 0.19. The friction value was chosen so that the shape of the simulated button end resembled most closely the shape of the actual cold headed test piece. Simulations were also conducted using friction values of 0.14 and 0.24, but 0.19 appeared to yield the best results. The initial striker velocity was set to the same value as in the actual tests, *i.e.*, 14 m/s. The simulation was defined as adiabatic with an inelastic heat fraction of 0.9. Fig. 7 shows the used mesh and equivalent plastic strain distribution in the button-head near the end of the cold heading operation. To describe the material's deformation behavior, flow stress values were calculated using Eqs. (1) and (2) at 17 different strains, ranging from 0–2 mm/mm, at 10 different strain rates, ranging from 10^{-3}–10^{4} s^{-1}, and at 17 different temperatures, varying between 22 and 822 °C. This data was given in tabular form as input data to ABAQUS/Explicit. Fig. 8 shows graphically two isotherms of the input data with the nodes representing the

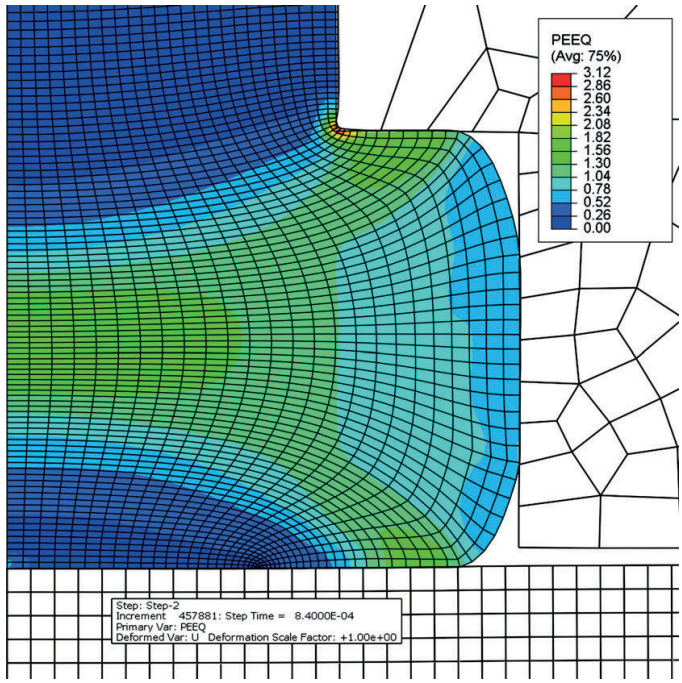

Fig. 7. Element mesh and plastic strain distribution in the cold headed part.

data points. The maximum true strain in the experimental data was about 1.5 mm/mm. During the simulations, however, it turned out that in some locations this value was exceeded. In order to account for this, the material properties were extrapolated to strains up to 2 mm/mm. The errors in the final simulation results caused by this extrapolation were, however, estimated relatively small since it was extensively needed only in very small areas around the inner corner and only at the very end of the simulation. Around the inner corner, the maximum strains, strain rates and temperatures obtained from the simulations were very high (strain ~ 3 mm/mm, temperature 1000 °C, and strain rate 16,000 s^{-1}), but mostly the strain stayed below 1.9 mm/mm, temperature below 600 °C, and strain rate below 9000 s^{-1}.

To compare the results of the simulations with the experiments, the applied force was recorded as a function of time with strain gages bonded on the incident bar at a distance of 50 mm from the interface between the cold heading die and the incident bar, which was also the position from where the forces in the simulations were collected. As Fig. 9 shows, the calculated (solid thin line) and measured forces (gray thick line) correspond to each other quite well. The peak in the curves at around 300 ms is caused by the experimental setup, where the die and the incident pressure bar are two separate components that detach slightly from each other before the forming button starts to fill the die head. The time difference between the peaks appearing in the measured and simulated force curves is explained by the slightly non-circular shape of the hot rolled wire, which leads to a slightly earlier contact between the die channel and the wire in the real experiment compared to the simulation. The origin of the peak in the force-time curve can be verified by making the die and the incident bar one piece in the simulation, which makes the peak disappear. The final thickness of the button was the same both in the simulation and in the experiment, but filling of the die corners was not quite perfect in the cold heading experiment.

The banded structure formed in the wire during hot rolling (see Fig. 1) was used to study the material flow during cold heading. Basically the movement of the so-called tracer particles defined in the ABAQUS simulation should follow the flow lines formed by the bands, but as Fig. 10 shows, the match between the flow lines and the tracer particle arrays is not perfect throughout the cold headed part. There are many possible explanations for these deviations, but in general the deviations indicate that the material flow in a real

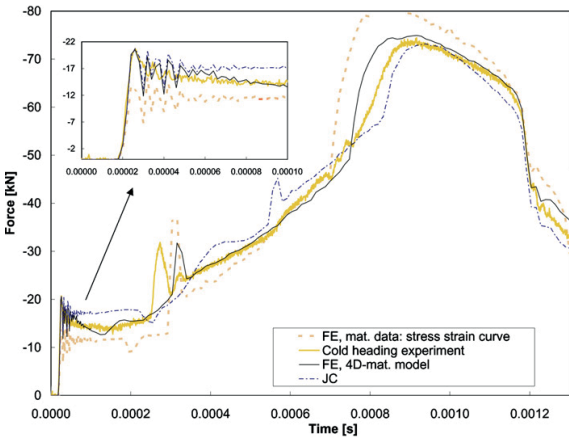

Fig. 9. Force *vs.* time data recorded from the incident bar during the cold heading experiment (thick solid line) and obtained from the FE simulation using material input data calculated with Eqs. (1) and (2) (thin solid line). The dashed line represents the FE simulation using a single room temperature quasi-static stress–strain curve as material input data. The dash-dotted line represents a simulation with the Johnson–Cook model.

case is not perfectly homogeneous and even. Reasons for this can be, for example, inhomogeneous microstructure, unstraightness and ovality of the wire, and non-collinear impact of the striker. Also the use of a simple friction model in the simulation could have lead to slight deviations between the simulated and observed flow of the material. It is also evident that making a perfect material model is in practice impossible because the material will always contain several imperfections and variations in its properties and behavior, i.e., the material itself is never perfect.

The finite element simulation of the cold heading operation discussed above was also done by using a stress–strain curve obtained from a single quasi-static compression test as the material input data, which still is often a common practice because of the lack of adequate dynamic strain rate and temperature dependent data. Fig. 9 shows a comparison between the measured force–time curve and the simulation using both the dynamic model presented by Eqs.

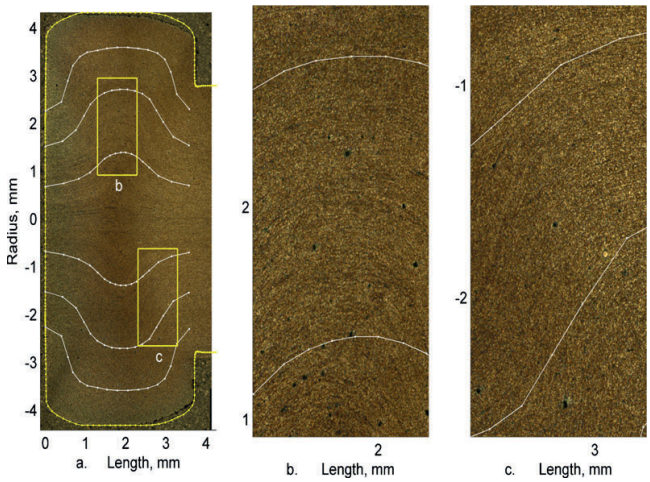

Fig. 10. Comparison between the simulated and observed shapes of the cold headed button, and between the flow lines formed by the initially straight banded structure and the tracer particles in the ABAQUS simulation. Figures b and c are magnifications of areas indicated in Fig. 10a.

(1) and (2) and the simple quasi-static stress–strain data (dashed line). From the figure it is evident that in the beginning of deformation the curve simulated with the quasi-static data underestimates the required force and then, at later stages, overestimates it. The explanation for this is that at small strains the strain rate effect leads to increased demand of force, but at larger strains the adiabatic heating effect outdoes the strain rate effect, resulting in a reduced need of force. This experiment clearly shows that successful modeling of the cold heading process requires accurate stress–strain data also at higher strain rates and temperatures. For comparison, the parameter values for the Johnson–Cook model were also determined from the experiment data. As seen in Fig. 9, the JC model overestimates the required force at low and intermediate strains and slightly underestimates it at high strains. Basically this is because the JC model assumes linear dependence of flow stress on the logarithm of strain rate, despite for example Fig. 4 clearly shows that the strain rate dependence of the studied steel increases considerably in the high strain rate regime.

7. Discussion

To study the dynamic deformation behavior of materials at wide ranges of strain, strain rate, and temperature, novel experimental techniques are needed. For example, the large plastic strains at strain rates lower than $1000\,s^{-1}$ needed in this work would be rather difficult to achieve with standard Hopkinson Split Bar techniques. As $\dot{\varepsilon} \approx \Delta\varepsilon/\Delta t$, basically the only way to do this is to lengthen the pulse duration Δt, which depends linearly on the striker length L as $\Delta t = 2L/C_0$, where C_0 is the propagation velocity of the longitudinal stress wave in the bar material. To prevent the recorded incident and reflected stress waves from overlapping, the location of the strain gage should be at least the length of the striker bar away from both ends of the bar. For long strikers this would require quite long bars, which can cause both practical problems as well as increase the dispersion of the waves traveling long distances between the points of measurement and the specimen. To a certain extent, however, the effects of dispersion can either be corrected for by using numerical correction procedures (Gorham, 1983), or minimized by using proper pulse shaping techniques (Parry et al., 1995). In this work, a rubber disc was used as a pulse shaper at the impact end of the incident bar, and as Fig. 2 shows, the recorded signals do not contain any large amplitude oscillations. This was also verified by making experiments with the same pulse shaping technique but pushing the incident and transmitted bars together without a specimen in-between, in which case the entire incident wave traveled through the incident-transmitted bar interface to the transmitted bar, where it was measured. When the incident wave recorded 50 mm away from the impacted end was compared with the wave recorded at a distance of 50 mm from the specimen end in the transmitted bar, the two waves were practically identical and thus no dispersion correction was needed in the actual tests with a specimen. With the wave separation technique explained in Section 3, plastic deformations up to 35% at strain rates in the order of $500\,s^{-1}$ were obtained using a 1.5 m long striker and only 1.8 m long incident and transmitted bars.

The experimental results clearly show that the deformation behavior of the studied cold heading steel depends strongly on both strain rate and temperature. Not only the yield strength increases with increasing strain rate, but also the transient and permanent strain hardening behaviors are affected by the strain rate as well. The stress–strain curves in Fig. 5b show that the strain hardening rate at higher strain rates, especially when the amount of plastic strain exceeds 20%, is significantly lower than at quasi-static strain rates. This is explained by the adiabatic heating of the specimen at high strain rates, where there is insufficient time for the heat generated during the deformation process to be conducted away. The actual increase of temperature during the tests was not measured, but based on the calculations of energy absorption and the assumption that 90% of that energy is transformed into heat during the deformation process, the average temperature increase in the studied steel can be several hundreds of degrees at the high strain and strain rate levels used in this study. The FE-simulations of the cold heading experiment also showed that the local temperatures in different parts of the deforming component can vary substantially, which further emphasizes the need for accurate data over wide ranges of strain rate and temperature.

The flow stress values obtained from the tests made at different initial temperatures decrease steadily up to the temperature of 450 °C. At 600 °C, however, the strain hardening rate, and thus also the flow stress values, are clearly higher than at the lower temperatures of 300 and 450 °C, as shown in Fig. 5a. This behavior is explained by dynamic strain aging, which again depends on both temperature and strain rate. Generally, dynamic strain aging occurs above a certain temperature when the solute atoms become mobile enough and can diffuse to the dislocations waiting for thermal activation at their short-range obstacles (Nemat-Nasser and Guo, 2005). In addition to increasing the strain hardening rate and the flow stress, dynamic strain aging is often observed to decrease the strain rate sensitivity of the steel, making it even negative in some cases. The temperature at which dynamic strain aging comes into play for the steel studied in this work, however, seems to be above the temperatures observed in cold heading applications.

As discussed in the Introduction, several physically based models have been presented to describe the strain rate and temperature dependent deformation behavior of metals. However, many of them also contain variables and coefficients that lack true physical content, and in that sense even they fall, at least partly, into the category of 'curve fitting models'. The choice between a physically based and a curve fitting model also depends largely on the intended use of the model. If the purpose of the model is only to describe the behavior of a particular material in a finite element simulation of a particular process, a good empirical fitting model will serve the purpose quite well as long as it captures the effects of strain hardening, strain rate hardening, and temperature. This is the case in the current application, where the cold heading process was studied experimentally and through simulations with ABAQUS/Explicit finite element software.

The applicability of the developed empirical model was verified through cold heading experiments performed using a special HSB setup and a simple bolt-like sample geometry. Attempts were also made to measure force–time–displacement relationships in the actual cold heading process, but the measurements in the industrial environment turned out to be extremely difficult to carry out and the obtained data was not considered reliable enough to be used in the comparisons with the simulation results. The force-time curves, cold headed geometry, and flow lines obtained from the HSB cold heading experiments and the simulations showed that a significantly better agreement was obtained with the empirical strain rate and temperature dependent material model than with a single quasi-static stress–strain curve as the material input data or with the Johnson–Cook model. Slight deviations between the simulated and experimental results both in the geometries and in the force data were, however, observed. Temporary detachment of the die from the incident bar causes the peak in the force curve (Fig. 9), appearing about 40 μs earlier in the actual heading than in the simulation. This difference is explained by the non-uniform clearance between the die and the sample in the cold heading experiment, leading to an earlier frictional contact between the die and the wire, which in turn slows down the detachment of the die from the incident bar. Even through the time difference between the peaks is notable, separation of the die and the incident bar is only about

0.13 mm (according to the simulation), and therefore the effect of this on the deformation behavior of the sample is estimated to be very small.

The greatest advantages of the presented empirical model are that (1) it describes accurately the strain rate and temperature dependence of the mechanical response of the studied material, (2) it takes into account the variations in the strain hardening rate as a function of strain rate and temperature, (3) it accounts for the sharp yielding behavior, (4) it takes into account the dynamic strain aging effect at higher temperatures, and (5) basically any mathematical function(s) that fit to the experimental data could be used for modeling of the material behavior. In addition, the number of experiments needed to determine the coefficients of Eqs. (1) and (2) is 10–15, which is a reasonable number and quite easily obtainable in a well-equipped high strain rate testing laboratory.

8. Conclusions

The deformation behavior of C17C cold heading steel was experimentally studied at a wide range of strain rates and temperatures. Higher order polynomial equations accounting for the effects of strain, strain rate, and temperature were fitted to the experimental results. This data was further used as material input data in the FE-simulations of high rate cold heading experiments.

Comparison of the results of the cold heading experiments and the FE simulations made using both the devised dynamic model, simple quasi-static stress–strain data, and the JC model showed that the effects of strain rate and adiabatic heating must be properly taken into account in order to produce reliable simulations.

The banded microstructure of the steel wire was used to study the material flow during the cold heading experiments. The match between the flow lines and FE markers was generally good but not perfect, which underlines the fact that materials or processes seldom behave in an ideal manner, i.e., material properties are almost always inhomogeneous and process conditions cannot be perfectly controlled.

Because the modeling approach used in this study is purely numerical, any equations leading to a good match with experimental data could be used instead of the chosen polynomial functions. In practice, however, determination of the coefficients of simple functions is more straightforward and generally requires less experimental data.

Acknowledgements

The financial support provided by the Finnish Funding Agency for Technology and Innovation (Tekes) and Ovako Wire Oy Ab are gratefully acknowledged.

References

Abaqus Version 6.7 Online Documentation, 2007. Abaqus Inc.
Apostol, M., Vuoristo, T., Kuokkala, V.-T., 2003. High temperature high strain rate testing with a compressive SHPB. J. Phys. IV 110, 459–464.
Brethenoux, G., Bourgain, E., Pierson, G., Jallon, M., Secordel, P., 1996. Cold forming processes: some examples of predictions and design optimization using numerical simulations. J. Mater. Proc. Technol. 60, 555–562.
Gorham, D.A., 1983. A numerical method for the correction of dispersion in pressure bar signals. J. Phys. E. 16, 477–479.
Hokka, M., Kuokkala, V.-T., Curtze, S., Vuoristo, T., Apostol, M., 2006. Characterization of strain rate and temperature dependent mechanical behavior of TWIP steels. J. Phys. IV 134, 1301–1306.
Johnson, G.R., Cook, W.H., 1985. Fracture characteristics of three metals subjected to various strains, strain rates, temperatures and pressures. Eng. Fract. Mech. 21, 31–48.
Liang, R., Khan, A.S., 1999. A critical review of experimental results and constitutive models for BCC and FCC metals over a wide range of strain rates and temperatures. Int. J. Plast. 15, 963–980.
Ma, X., Humphreys, A.O., Nemes, J., Hone, M., Nickoletopoulos, N., Jonas, J.J., 2004. Effect of microstructure on the cold headability of a medium carbon steel. ISIJ Int. 44, 905–913.
Nemat-Nasser S., 2000. Introduction to high strain rate testing, in: ASM Handbook Vol. 8: Mechanical Testing and Evaluation. Materials Park, Ohio, ASM International, pp. 427–512.
Nemat-Nasser, S., Guo, W.-G., 2005. Thermomechanical response of HSLA-65 steel plates: experiments and modeling. Mech. Mater. 37, 379–405.
Parry, D.J., Walker, A.G., Dixon, P.R., 1995. Hopkinson bar pulse smoothing. Meas. Sci. Technol. 6, 443–446.
Rule, W.K., Jones, S.E., 1998. A revised form for the Johnson–Cook strength model. Int. J. Impact Eng. 21, 609–624.
Sugondo, Szpunar, J.A., Gangli, P., 1991. Development of texture in low-carbon steels for cold heading. J. Mater. Proc. Technol. 16, 305–321.
Vuoristo, T., Kuokkala, V.-T., Rämö, J., Partinen, J., Kolsi, J., 2006. Strain rate dependent deformation behavior of cold heading steels. In: Proceedings of Asia Steel International Conference, Fukuoka, Japan, pp. 902–907.
Zerilli, F.J., Armstrong, R.W., 1987. Dislocation-mechanics-based constitutive relations for material dynamics calculations. J. Appl. Phys. 61, 1816–1825.

PUBLICATION VI

High Temperature Dynamic Tension Behavior of Titanium Tested with Two Different Methods

Hueto, F., Hokka, M., Sancho, R., Rämö, J., Östman, K., Galvez, F., & Kuokkala, V-T.

Procedia Engineering, 197, 130-139, 2017

Available online at www.sciencedirect.com

ScienceDirect

Procedia Engineering 197 (2017) 130 – 139

Procedia Engineering

www.elsevier.com/locate/procedia

DYMAT 23rd Technical Meeting

Dynamic Fracture of Ductile Materials

High Temperature Dynamic Tension Behavior of Titanium Tested with Two Different Methods

Francisco Hueto[a,b], Mikko Hokka[a], Rafael Sancho[b*], Jari Rämö[a], Kauko Östman[a], Francisco Gálvez[b], Veli-Tapani Kuokkala[a]

[a]*Tampere University of Technology, POB 589, Tampere, Finland*
[b]*Technical University of Madrid, Department of Materials Science, c/Profesor Aranguren 3, 28040 Madrid, Spain*

Abstract

In this work, the dynamic response of Ti6Al4V alloy at high temperature was studied using the Split Hopkinson Pressure Bar –SHPB- apparatus with two different heating systems. The first device uses direct electric current to heat the sample to the testing temperature in a fraction of a second, whereas the second device uses a furnace to heat the sample and as a consequence, short sections of the bars, in few minutes. Tension tests were carried out at strain rates up to 1500 s^{-1} and at temperatures ranging from room temperature up to 700 °C. The conventional strain gauge measurements from the pressure bars were used to obtain the stress–strain curves and the Johnson-Cook material model was used to fit the results of the tests. High speed photography and digital image correlation were used to quantify the total strain during the test. The plasticity of the titanium alloy clearly increases as the temperature is increased. The maximum strains, obtained from the stress-strain curves, also increase when the temperature is increased from room temperature. DIC results, however, show clear differences in the maximum strain before failure with respect to the values obtained from strain gauges measurements. The maximum strain in the gauge section of the sample prior to failure increases steadily as the testing temperature is increased. At 60 °C, the strains within the gauge section reach values almost 50% just before failure. At 300 °C, the maximum strains are close to 65%, and at 700 °C the maximum strains extend close to 80%.

Peer-review under responsibility of the scientific committee of the International Conference on Dynamic Fracture of Ductile Materials

Keywords: Titanium; high strain rate; high temperature.

Peer-review under responsibility of the scientific committee of the International Conference on Dynamic Fracture of Ductile Materials
doi:10.1016/j.proeng.2017.08.089

1. Introduction

Various industrial and military applications involve dynamic material behavior at high temperatures. Optimal design and development of components requires in-depth understanding of the plastic deformation and failure of materials at these conditions. Nowadays, the most commonly used testing method to study the mechanical behavior of metal alloys at high strain rates is the Split Hopkinson Pressure Bar (SHPB) device. It consists of two long and aligned bars with the specimen sandwiched (compression version) or held (tensile version) between them, and a propulsion device for accelerating a projectile. The striking projectile impacts at the end of one of the bars producing a stress wave which travels along the bars. Strain gauges, amplifiers and oscilloscopes are used to measure the strain wave propagation in the bars and by applying the principles of one-dimensional elastic wave propagation; it is possible to obtain the stress-strain curves of the material, as well as the test strain rate. Moreover, the use of Digital Image Correlation (DIC) technique provides in-depth understanding of the deformation and failure of the specimen by tracking the movement of a surface pattern during testing. Previous research on the dynamic behavior of Ti6Al4V with SHPB devices have been reported [1], including tensile loading [2] and compression loading at high temperatures [3]. However, none has been found involving dynamic tensile loading at high temperatures.

High temperature testing by using the tensile version of the SHPB device is complicated by the fact that the specimen must be firmly fixed to the bars before heating the specimen up to the desired temperature. Because of this, mechanical manipulation of the specimen and the bars is restricted after positioning the specimen. Furthermore, SHPB testing at high temperature presents other difficulties [4]. Due to the length of both bars and the supporting system for keeping bar alignment, it is operationally impossible to heat the entire bar assembly, so a temperature gradient may appear, changing elastic properties of the bars along its length. Consequently, a study of the temperature-gradient effect on the elastic modulus and the longitudinal sound speed should be performed to take into account the corresponding corrections.

High temperature tension tests with the SHPB device can be carried out basically by two ways: heating up the specimen and short sections of the bars to the desired temperature using a furnace [5] [6] [7], or heating up just the sample using, for example, infra-red radiation or direct electric current [8]. Both methods have their advantages, drawbacks, and limitations with respect to the temperature ranges, control of temperature, etc. In fact, no detailed studies have been carried out in the past about the exact effect of the heating method on the obtained final results.

The first method, from now on called furnace method, uses a furnace to slowly heat the sample and inevitably, short sections of the bars, causing some temperature gradient in them. Incident and transmitted bars should be made of a material with a low variation of the elastic properties with temperature to avoid the need for corrections. This method usually implies mechanical clamping since bars are heated up and adhesive degrade its properties at high temperatures. This mechanical clamping could produce disturbances or oscillations in the obtained strain curves.

The second method, which uses direct electric current and called electric method, enables the use of adhesive fixing since the sample is heated up rapidly, so the temperature of the adhesive joint does not increase significantly. Therefore, it would enable to obtain higher quality results. Unfortunately, temperature control of the system becomes difficult since the heating is achieved in less than a second by means of electric current.

There is a third method, which would imply using mechanical devices that brings the room-temperature pressure bars into contact with the heated sample in a fraction of a second before the stress pulse arrives at the end of the incident bar [9] [10]. Regrettably, it is only practical in the case of a compression SHPB test because in tensile SHPB testing the sample needs to be mechanically coupled or adhesively fixed to the pressure bar.

In this paper, the furnace and the electric method are presented and applied to Ti6Al4V alloy.

2. Furnace heating method

The furnace method was employed by using the SHPB tensile system of the Department of Material Science at Technical University of Madrid [5]. In this laboratory, the incident and transmitted bars have 4.05 m and 3.85 m length respectively, 19.3 mm diameter, and they are made of the René 41 alloy, a nickel-based super-alloy with optimal high-temperature properties and low dependence of its elastic properties on temperature. The bars have

screwed ends; consequently it was necessary to design a clamp (see Figure 1.b) to attach the flat specimens to the bars.

Samples, whose geometry is shown in Figure 1.a, were mechanically coupled by two pins, which are introduced by the holes at each side of the samples, fixing the sample to two bolts. Then, the bolts are screwed into the bars. Pins and bolts were also made of René 41 alloy.

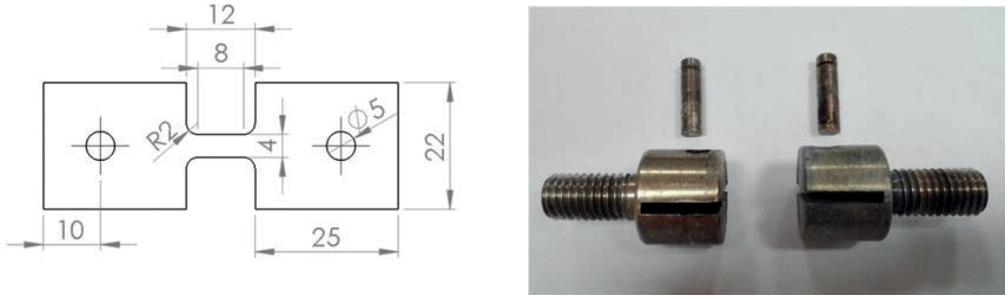

Fig. 1. a. Ti6Al4V samples geometry, Madrid; b. Clamp designed to attach the specimens. All dimensions are in mm.

The furnace, shown in Figure 2, consists of eight resistors and a bar-size opening at each side. It can reach temperatures up to 900 ºC in few minutes. The furnace is supported by a pneumatic system, which enables to remove the furnace to one side of the bars just when the projectile is launched. Therefore, it is possible to visualize and record the tests. Heating rate was set in 30 ºC/min and the heating times were between 5 and 15 minutes. Temperature was acquired by the contact of a thermocouple with the sample.

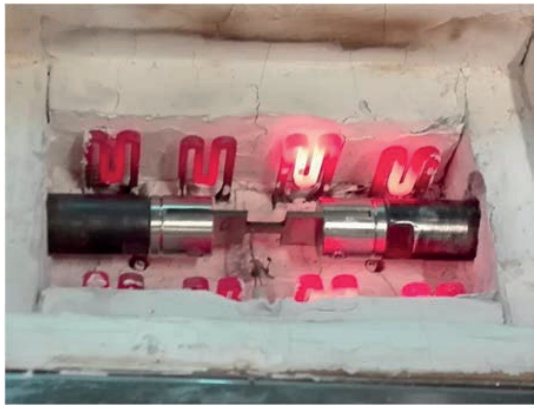

Fig. 2. Resistors system for furnace heating.

Moreover, the system contains two heat-sinks next to the oven and in contact with the bars, where water flows to avoid an excessive heating of the bars and therefore, any damage to the strain gauges.

During testing, the furnace is removed after heating up the sample and while the striker is triggered. Stress waves are registered by strain gauges located at the middle of each bars. The test is recorded by a high-speed camera and DIC technique may be applied if samples have a high-contrast speckle pattern during the test, usually painted with high-temperature resistant paints.

3. Electric heating method

In the tensile Split Hopkinson Bar device designed and built at the Department of Materials Science of Tampere University of Technology [8], each bar has 6.3 m in length and 22 mm in diameter. The incident bar is made of a high strength steel (AISI 4340) and the transmitted bar is made of 2007 aluminum alloy, which allows more accurate measurements of low amplitude strain signals. Samples are fixed to the stress bars by gluing them to slits machined at the end of the bars. The adhesive employed was Loctite 480.

The geometry of the samples is shown in Figure 3 and it is quite similar to the ones used in the previous method. It consists of a gauge section, two glue sections and two electrode sections. The gauge section is the central part of the sample and strains during testing. The glue sections, which let the adhesively attachment between the specimens are bars, are the two large sections at the end of the sample. These sections must be large enough to ensure that the shear strength of the adhesive joint is enough to withstand the applied load. The 10-mm-wide electrode sections, are used to conduct electric current into the sample. Specimens only need these extensions on one side; however, they were machined on both sides for the sake of symmetry.

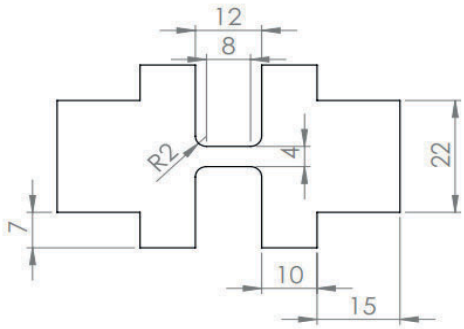

Fig. 3. Ti6Al4V samples geometry, Tampere. All dimensions are in mm.

The heating up system is shown in Figure 4. It consists of four copper electrode pins, with 5 mm diameter, moved by a pneumatic actuator. The pneumatic actuator uses low pressure to move the electrodes up and down and to squeeze these pins to each side of the sample. These four pins, two at each side, are responsible for bringing electric current to heat the sample. Once the heating has finished, the pneumatic actuator retracts away the electrodes, keeping the system far away from the impact. Another reason for taking away the electrodes is that in this way it is possible to use digital image correlation analysis of the sample.

Electric current is provided by a programmable Kempower IMP15 welding transformer, which is controlled by the same computer that controls the SHB device. The transformer uses a low-voltage high-DC-current pulse to heat the sample by Joule's effect. To measure the temperature of the specimen, a thermocouple is previously spot welded to the center point of the gauge section of the specimen and a second high-speed oscilloscope is used to record the temperature. The oscilloscope records the incident loading pulse too. Therefore, the temperature of the specimen can be recorded at the exact moment when the incident loading pulse arrives at the specimen.

Heating times varied between 0.2 and 1 second, enabling to heat only the gauge section (the one with smaller cross-sectional area), while the temperature of the shoulder area, whose cross-sectional area is larger, is not significantly increased and thus, the glue section remains close to room temperature without losing its properties. The electric current and voltage values used for the titanium samples were between 3-5 volts and 300-900 amps. If the maximum current and voltage are kept constant, the maximum temperature of the sample increases almost linearly as a function of the heating time, thus the testing temperature can be estimated before the test by running a series of very short heating experiments. However, when testing different samples the temperatures may vary significantly. It is important to mention that after some heating tests in the same device, the contact between the electrodes and the specimen was lost due to a local melting of titanium. To avoid this problem, a conductive grease was used to improve the conductivity and contribute to better estimations of the temperature.

Although tests were fully computer controlled, there were many things to set up and check before every test, so that we could get accurate timing and control of the different actions. Once the trigger signal is sent, the striker starts moving from resting position until it impacts in the incident bar. Additionally, the electrodes start heating the sample using the DC pulse produced by the transformer. If the heating time is too long and the electrodes are still heating the sample when the wave arrives, the electrodes become damaged. Therefore, electrodes must be taken out before the stress pulse arrives. On the other hand, if the heating time is too short, the specimen may cool down before the stress pulse arrives. Consequently, a heating delay should be set in a way which enables to finish the heating around 50ms before the stress pulse arrives.

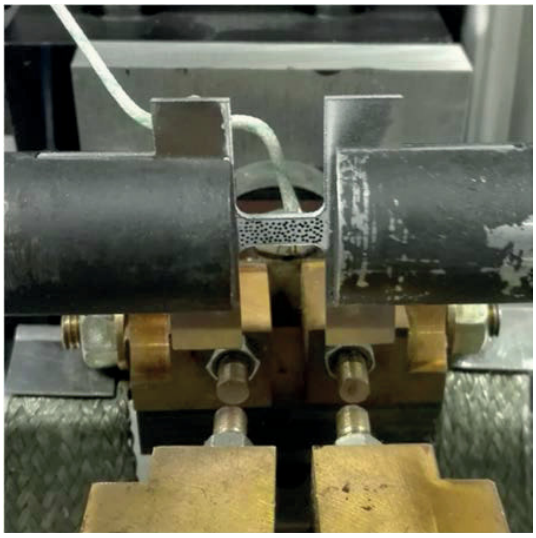

Fig. 4. Four copper electrode system for direct electric heating.

Carrying out this type of test seems much more complex than the previous method, but it is quicker to perform. However, it involves the curing of the adhesive as well as its heating and cleaning with acetone after testing, which limits the use of this method to few daily tests.

4. Results

4.1. True Stress-True Strain Curves

Tensile tests using aforementioned methods were carried out at the same temperature and approximately at the same experimental engineering strain rate (1300 s^{-1}). Using the data from strain gauges, the true stress – true strain curves at 300, 450 and 700 ºC were obtained (see left plot in Figures 5, 6, 7).

It can be appreciated that curves obtained by electric heating and adhesive fixture (EH & GF) have better signal-to-noise ratio. However, the curves obtained by furnace heating and mechanical clamping (FH & MC) show higher oscillations, especially at the beginning, losing information about the yield strength.

To achieve a better comparison of the curves, they were filtered using a low pass and a median filter. Low pass filter was programmed by Fast Fourier Transforms, which gets the 15 dominant frequencies of the signal and compose the wave again. Then, the median filter was applied and finally, low pass filter was used one more time to avoid the stepped behavior of the curve acquired through the median filter.

Filtered curves are shown on the right of Figures 5, 6 and 7. Now, it can be clearly observed that both methods obtain a similar material response. Analogous material properties are obtained except for 450 ºC, where the flow

stress between both methods differs around 100 MPa. This flow stress difference may be due to a different testing temperature during the FH&MC test (a lower value instead of 450º), probably due to a temperature acquisition error. More tests were not able to do because of the lack of samples, so this hypothesis could not be confirmed. However, the three plots show the same work hardening behavior.

During tests at 300 ºC, a third method, which combined mechanical and heat-resistant adhesive fixing during furnace heating (FH & GF), was employed with the goal of reducing the oscillations at the beginning of the curve. The adhesive employed was Henkel Loctite 638. However, the adhesive did not add any significant improvement, probably because the adhesive deteriorated at that temperature.

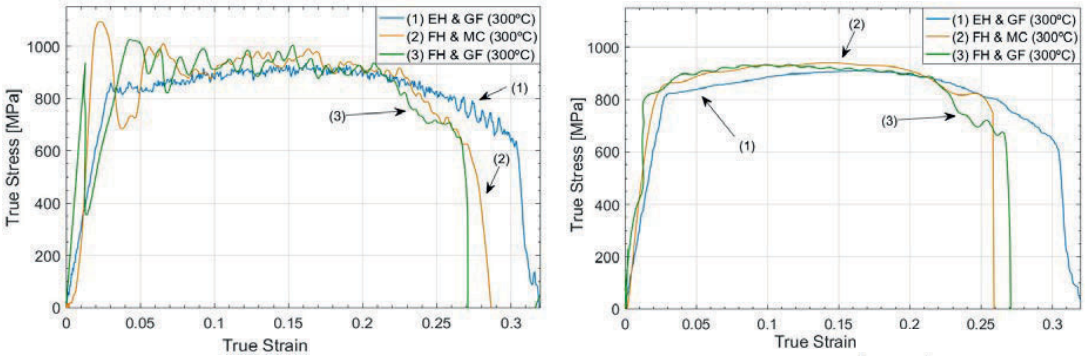

Fig. 5. True Stress – True Strain curves at 300 ºC and 1300 s^{-1} for: electric heating and adhesive fixing (1), furnace heating and mechanical clamping (2) and furnace heating and glue fixing (3) before filtering, left; after filtering, right.

Results from furnace-heating at 450 ºC shown even a higher signal-to-noise ratio than tests at 300 ºC. Higher heating times and temperatures might lead to different thermal expansion between the bar, sample, and pins. Consequently, loosens could appear and lower-quality stress pulses were recorded. The use of adhesive fixing was not feasible at these temperatures in the furnace, but it was by the electric heating method because of the short duration of the heating process (around one second), the room temperature on the glue sections was kept.

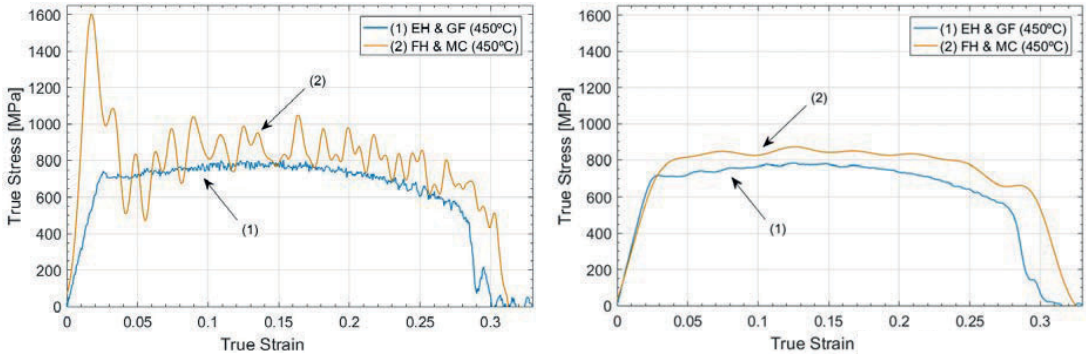

Fig. 6. True Stress – True Strain curves at 450 ºC and 1300 s^{-1} before filtering, left; after filtering, right.

During furnace heating tests at 700 ºC, stress bars were pulled before the withdrawal of the furnace to avoid loosens that may occur during heating. It enabled lower oscillations in the results than 450 ºC tests. The sample spent 15 minutes in the furnace until it heated up to 700 ºC, then the test was carried out. By visual inspection after the test, a thin blue oxide layer could be appreciated on the surface of the sample.

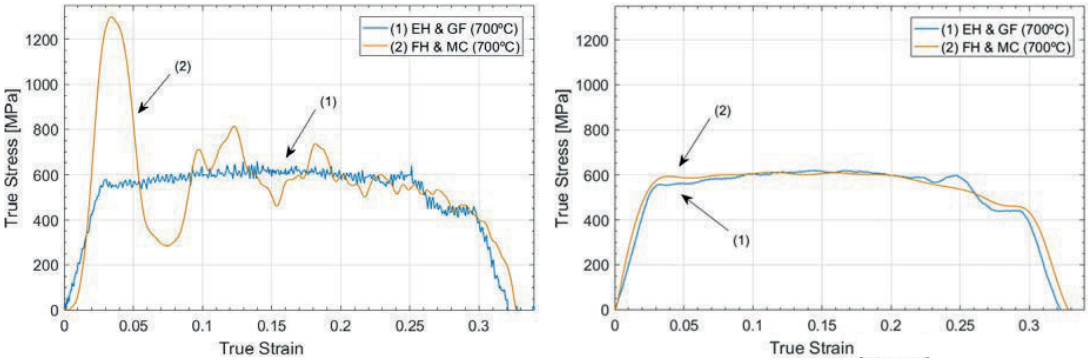

Fig. 7. True Stress – True Strain curves at 700 ºC and 1300 s^{-1} before filtering, left; after filtering, right.

Related to the alloy behavior, previous studies [11] set the yield strength and ultimate tensile strength in tension of Ti6Al4V at room temperature and quasi-static conditions between 900 and 1000 MPa respectively; and around 1200-1300 MPa in dynamic conditions at an engineering strain rate of 1300 s^{-1}, showing that flow stress increases with strain rate.

Concerning the temperature effect, experimental results show that increasing test temperature decreases both, the elastic limit and UTS. By increasing the temperature of the dynamic tests up to 300ºC, the flow stress decreases by 30% and by increasing it up to 700ºC the flow stress decreases by 50%. The high UTS of the alloy at 450ºC (800MPa) may explain the use of Ti6Al4V alloy for high temperature applications. However, its use is limited up to 550 ºC [12], because, as we saw after a few minutes at 700 ºC, an oxide layer appears due to the high interstitials affinity of titanium.

4.2. Adjusted material model

In order to predict the material behavior, a Johnson-Cook material model was adjusted [13] considering the adiabatic softening. At high strain rates, adiabatic heating takes place since it is not possible to dissipate such amount of plastic energy to the surroundings during the short duration of the test, so a temperature increment of the sample occurs. The Johnson-Cook model is defined in equation (1):

$$\sigma = \left(A + B\,{\varepsilon_p}^n\right)(1 + C \ln \dot{\varepsilon}^*)(1 - T^{*m}) \qquad (1)$$

The first, second and third term of previous equation define the influence of the deformation, strain rate and temperature, respectively, in the material behavior. A is the yield strength of the material at quasi-static tests, B and c are parameters that define the evolution of the flow stress as a function of the equivalent plastic strain ε_p , C and m define the strain-rate and temperature sensitivity of the material, respectively.

$\dot{\varepsilon}^*$ and T^* are given by equations (2) and (3):

$$\dot{\varepsilon}^* = \frac{\dot{\varepsilon}}{\dot{\varepsilon}_0} \qquad (2)$$

$$T^* = \frac{\mathrm{T} - \mathrm{T}_{room}}{T_{melt} - T_{room}} \qquad (3)$$

where $\dot{\varepsilon}_0$ is the reference strain rate (quasi-static tests), $\dot{\varepsilon}$ the strain rate of the test, T is the temperature of the specimen, which may increase due to adiabatic heating (see Equation 6) , T_{room} is the room temperature and T_{melt} the temperature at which the material does not show mechanical resistance against deformation.

The parameters employed in the adjustment of the model are shown in Table 1. The adjustment was performed by least-squares fitting and a comparison with the experimental results at three different temperatures is shown in Figure 8. Material model is plotted up to diffuse necking and after this point it is represented with dash lines.

Table 1. Johnson-Cook parameters value.

A	B	n	T_{room}	T_{melt}	m
800 MPa	700 MPa	0.096	25ºC	1400ºC	0.65

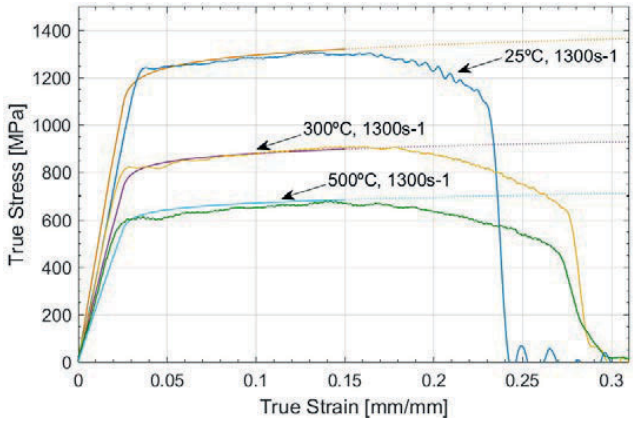

Fig. 8. Comparison between the adjusted Johnson-Cook material model and the experimental results.

The curves include the adiabatic heating, in which the thermal softening is considered. Temperature increments are calculated through the First Law of Thermodynamics and the Taylor Quinney coefficient λ (around 0.9 for metals), showed in equations (4), (5) and (6).

$$dQ = dW_p \tag{4}$$

$$\rho\, C_p\, dT = \sigma\, d\varepsilon \tag{5}$$

$$\Delta T = \frac{\lambda}{\rho\, C_p} \int \sigma\, d\varepsilon \tag{6}$$

4.3. Digital Image Correlation results.

DIC analysis was only possible with direct electric heating method. During the furnace heating, although a heat resistant paint was used, the paint dried excessively, losing its elasticity and causing the appearance of cracks in the paint that affected DIC results.

The observation at slow motion showed (140000 fps were recorded) a bottle neck behavior of the samples before breaking, thus localization occurs in the middle of the samples. Videos were processed, deformation fields were obtained and last frame of every sample was extracted (see Figure 9) to clearly show the strain localization.

A plot of strain over the length of specimen with fixed time in between two curves shows how the specimen has locally deformed with time. This was done by drawing a horizontal line in the center of the samples with the software, and extracting its strain during the different frames. Then, it was possible to see how strain was localized usually at the center of the sample. Curves at 700ºC are shown in figure 9.

Finally, by comparing the last frame of three samples at different temperatures as in Figure 10, it can be observed that the maximum strain in the gauge section of the sample prior to failure increased steadily as the testing temperature was increased. At 60 °C, the strains within the gauge section reached values almost 50% just before failure. At 300 °C, the maximum strains were close to 65%, and at 700 °C the maximum strains extended close to 80%. Therefore, the use of DIC shows a high deformation localization of the samples, and clear increments of the deformation when the temperature is increased.

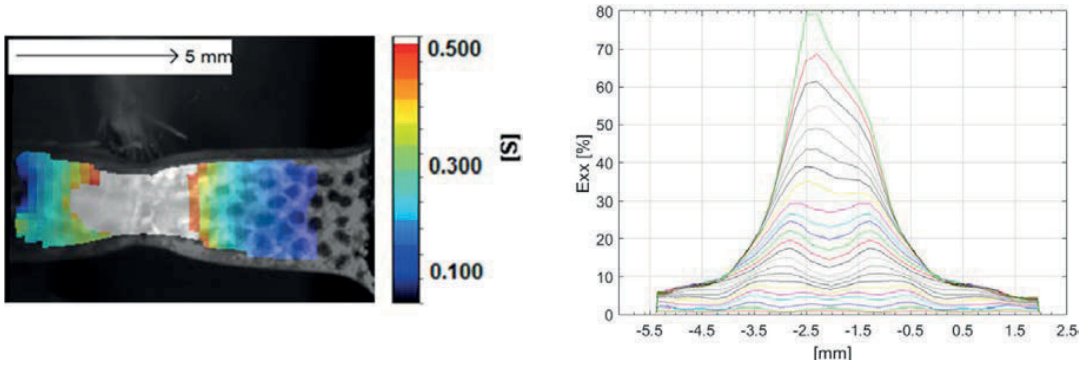

Fig. 9. Last strain field frame before final cracking at 700ºC, left; Strain distribution along the length at 700ºC, right.

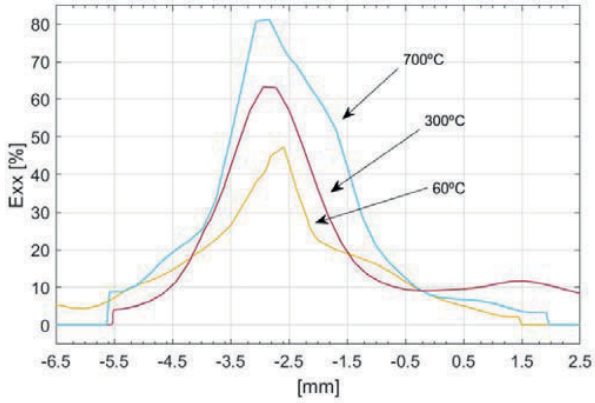

Fig. 10. Comparison of last frame strain distribution along the length of specimens at different temperatures.

5. Conclusions

Dynamic tensile loading at high temperatures on Ti6Al4V have been carried out by two different methods.

The noise on the waves obtained by furnace heating method increased with the test temperature, probably, because of the different thermal expansion between the bars, samples, and pins, which produced loosens in the

mechanical fixture of the samples. However, by using numerical filters it was possible to obtain similar results to those from electrical heating.

Waves obtained by electric heating method and glue fixture showed less oscillations than the ones from furnace method and were less influenced by the heating temperature. Besides, they allowed us to obtain temperatures up to 700 ºC without influencing the adhesive temperature and therefore its properties.

Glue was also employed on the furnace method up to 300 ºC to reduce the oscillations of the results. However, it did not reach the oscillation-free results of the electric heating method.

Temperature prediction resulted complex in electric heating method as it required short heating times and linear approximation. Moreover, it became more difficult due to local heating over the titanium samples-copper electrodes interface. As a solution, conductive aluminum grease was added to the interface.

Fixture and removal of the samples in the electric heating device involved the curing of the adhesive before testing as well as heating and cleaning with acetone after testing to carry on a new test, which limited the number of test to two or three per day.

Finally, the use of DIC showed a high deformation localization of the samples, and clear increments of the deformation when the temperature is increased.

Acknowledgements

The authors would like to express their gratitude to the Comunidad de Madrid (Spain) for their financial support through the project DIMMAT-CM with reference S2013/MIT-2775.

References

[1] Hammer J.T., Yatnalkar R.S., Seidt J.D., Gilat A. (2013) Plastic Deformation of Ti6Al4V Plate over a Wide Range of Loading Conditions. In: Chalivendra V., Song B., Casem D. (eds) Dynamic Behavior of Materials, Volume 1. Conference Proceedings of the Society for Experimental Mechanics Series. Springer, New York, NY.

[2] J. Peirs, P. Verleysen, J. Degrieck, Experimental study of the influence of strain rate on fracture of Ti6Al4V. Procedia Engineering 10:2342-2347. December 2011.

[3] W.-S. Lee, C.-F. Lin, High-temperature deformation behaviour of Ti6Al4V alloy evaluated by high strain-rate compression tests. Journal of Materials Processing Technology. Volume 75, Issues 1–3, 1 March 1998, Pages 127-136.

[4] G. T. Gray III, Split-Hopkinson Bar Testing as a Function of Temperature, Classic Split-Hopkinson Bar Testing, p. 468, Los Alamos National Laboratory, 2000.

[5] F. Gálvez, D. Cendón, A. Enfedaque, V. Sánchez-Gálvez, High Strain Rate and High Temperature Behavior of Metallic Materials for Jet Engine Turbine Containment, Journal de Physique IV, 2006.

[6] W. Huang, X. Zan, X. Nie, M. Gong, Y. Wang, Y. Xia, Experimental study on the dynamic tensile behavior of a poly-crystal pure titanium at elevated temperatures. Materials Science and Engineering: A. Volume 443, Issues 1–2, 15 January 2007, pages 33-41.

[7] X. Chen, Y. Li, C. Shi, T. Suo, The dynamic tensile properties of 2D-C/SiC composites at elevated temperatures. International Journal of Impact Engineering 79, 2015, pages 75-82.

[8] M. Hokka, K. Östman, J. Rämö, V.-T. Kuokkala, High Temperature Tension SHPB Device Based on Direct Electrical Heating, SEM 2014 Annual, A, Conference on Experimental and Applied Mechanics, At Greenville, South Carolina USA.

[9] H. Zhan, Damon Kent, G. Wang, M. S. Dargusch, The dynamic response of a β titanium alloy to high strain rates and elevated temperatures. Materials Science and Engineering: A. Volume 607, 23 June 2014, pages 417-426.

[10] V.-T. Kuokkala, M. Apostol, M. Hokka, High and Low Temperature Techniques in Hopkinson Split Bar Testing. Proceedings of the IMPLAST 2010 Conference, October 12-14 2010, Providence, Rhode Island, USA.

[11] F. Hueto, High Temperature High Strain Rate Testing of Titanium by Direct Electric Heating Tension SHPB device, Master's thesis, Universidad Politécnica de Madrid, 2017.

[12] Smith, William Fortune, Titanium and its alloys, Structure and properties of engineering alloys, McGraw-Hill, 1993.

[13] Johnson, G. R., and Cook, W. H. A constitutive model and data for metals subjected to large strains, high strain rates and high temperatures, Proceedings of the 7th International Symposium on Ballistics, 1983, vol. 21, The Hague, The Netherlands, pp. 541-547.

PUBLICATION VII

Effects of microstructure on the dynamic strain aging in ferritic-pearlitic steels

M. Hokka, J. Rämö, A. Mardoukhi, T. Vuoristo, A. Roth and V.□ T. Kuokkala

Journal of Dynamic behavior of materials (2018)

Effects of microstructure on the dynamic strain aging in ferritic-pearlitic steels

M. Hokka[1], J. Rämö[1], A. Mardoukhi[1], T. Vuoristo[2], A. Roth[3], V.-T. Kuokkala[1]

[1] Tampere University of Technology, Laboratory of Material Science, POB 589, FI-33101, Tampere, Finland

[2]Swerea KIMAB AB, POB 7047, 16407 Kista, Sweden

[3]Schmolz+Bichenbach Group CREAS, POB 70045, 57301 Hagondance Cedex, France

Abstract

Effects of microstructure on the high strain rate high temperature mechanical response and dynamic strain aging of C45 and 27MnCr5 ferritic-pearlitic steels were studied using four different microstructural variants of the standard alloys. The high strain rate high temperature behavior of the steels was studied using a compression Split Hopkinson Pressure Bar device with high temperature testing capabilities. The steels were studied at strain rates up to 4500 s^{-1} and at temperatures from RT to 680 °C. Strong dynamic strain aging was observed for both steels in the studied temperature range. The results also show that the microstructure has a strong effect on the dynamic strain aging sensitivity of the steel. This is especially true at low plastic strains, where the effect of the microstructure is strongest. The effect of microstructure decreases as plastic strain increases. A coarse-grained microstructure showed the strongest dynamic strain aging sensitivity for both steels.

Introduction

Plastic deformation of steels is quite sensitive to both strain rate and temperature. Especially the strength values are known to be affected by both of these factors, which therefore have to be taken into account when selecting materials for dynamic or elevated temperature applications. At low and intermediate strain rates, the mechanical behavior of steels, or metals in general, can be explained by the thermally activated motion of dislocations past the glide obstacles that reside in the crystal lattice. The plastic behavior of a steel alloy is essentially governed by the characteristics of these obstacles, i.e., the microstructure of the material. The nature and density of these obstacles can also change during the plastic deformation, leading to changes in the material's response to external loading. At higher strain rates, various viscous drag effects start to affect the movement of the gliding dislocations, leading to a rather rapid increase in the flow stress when the strain rate approaches 10^3 s^{-1}. On the other hand, strain rate and temperature do not affect too much the strain hardening rate of body centered cubic (BCC) steels, as their main thermally activated glide obstacles are quite independent of the amount of deformation. For pearlitic steels, the most significant thermally activated obstacle for dislocation motion is the lattice friction, which at least in theory does not depend at all on the amount of deformation, and

also on temperature only through the temperature dependence of the shear modulus. Therefore, the stress-strain curves of a BCC metal obtained at different temperatures and/or at different strain rates typically have the same shape, and only the overall level of the flow stress drops or rises depending on how the test temperature or strain rate is changed. Higher temperatures, however, also increase the diffusional flow of small alloy atoms such as carbon and nitrogen, which can cause a sudden increase in the flow stress at certain strain rate – temperature combinations. In addition, at low strain rates jerky or serrated flow can be observed. This is known as the dynamic strain aging (DSA) or the Portevin–Le Chatelier effect [1], which is caused by the alloy atoms that diffuse into the dislocation cores to minimize the lattice strain energy, and temporarily pin or prevent the dislocations from moving further. Further motion of the dislocations requires more work to remove them from the cloud of alloy atoms. At higher strain rates, dynamic strain aging appears as an increase of strength of the material at higher temperatures. This phenomenon has been observed by many scientists for various metals and alloys, including titanium [2-3], niobium [4], vanadium [5], molybdenum [6-7], and stainless steels [8]. For this work, however, the previous work on steels is more interesting. Baird and Jamieson [9] carried out a comprehensive study on the effects of nitrogen and manganese on the high temperature tensile behavior of iron, and noticed both strong solid solution strengthening and dynamic strain aging caused by the alloy atoms. Their work concentrated on the low strain rate region. Gilat and Wu [10] studied the behavior of 1020 steel at various strain rates in shear, and discovered strong dynamic strain aging to occur in the range of 150-550 °C , depending on the strain rate. The effect was very strong at strain rates close to $5*10^{-4}$ s^{-1}, diminishing when the strain rate was increased. Moreover, the maximum dynamic strain aging occurred at higher temperatures when the strain rate was increased. Similar work was carried out by Nemat-Nasser and Guo [11-12], who reported also strong dynamic strain aging at temperatures between 350 °C and 750 °C for the DH-36 and HSLA-65 steels. Similarly, the peak of the dynamic strain aging shifted towards higher temperatures when the strain rate was increased. Shahriary et al. [13] analyzed the stress-strain curves of the 4340 steel obtained at different temperatures, and observed that the ductility of the steel was also affected by the dynamic strain aging. A clear increase in the work hardening exponent and a clear drop in the elongation values was observed in the temperature range of 250-300 °C. The decreased ductility in the temperature range of 250-400 °C is commonly known as blue brittleness, which has been observed by many scientists, for example [14-18]. Blue brittleness is generally attributed to dynamic strain aging.

In general, dynamic strain aging is a diffusional process, and its amount or strength depends on strain rate (time), temperature, density of mobile dislocations, and chemical compositions or more specifically the concentration of participating small atoms [19-20]. However, for steels, the situation is not quite as simple, and it is well known that low carbon steels can be processed and heat treated in numerous different ways to produce steels with the same chemical composition but with significantly different mechanical properties. The local chemical composition, phase composition, amount of precipitates, dislocation density, grain size, and so forth, can vary significantly depending on the thermo-mechanical treatment history. Because of this, also the strength and temperature range where the dynamic strain aging occurs can be affected by the structure of the material. Dynamic strain aging is typically quantified by various models that take into account the effects of strain rate and temperature. Many of the recent models, for example [21-23], are based on some real physical principles and the work done by Follansbee and Kocks [24] or Zerilli and Armstrong [25]. The models are based on the microstructures of the materials

or generalized dislocation dynamics, but they do not include exact information about how the microstructure of the material actually affects the dynamic strain aging. For example, it is quite difficult to estimate what are the effects of ferrite grain size, phase fractions, or the pearlite interlamellar distance on the macroscopic behavior of the steel. Because of this, it is also difficult to estimate how the change in the structure of the material due to, for example, heat treatment will affect the material's response and especially the effect of the dynamic strain aging. In the literature, there are only few examples of studies on how the processing and microstructure of the steel affects the strength of DSA. One example is the work of Chakravartty et al. [26], who studied nickel-manganese steels with different aging treatments and cold worked structures at temperatures up to 250 °C. According to them, the microstructure of the steel has very little effect on the strength of the dynamic strain aging. However, Wagner et al. [27] came to the opposite conclusion for the A48 steel, when they compared the high temperature behavior of the A48 steel with a normalized structure with different quenched multiphase structures. According to their work, the higher martensite content in the steel reduces dynamic strain aging. Their results and conclusions highlight the strong effect of the microstructure on the dynamic strain aging. In this paper, we present results of a systematic study of the effects of the microstructure on the dynamic strain aging in two low carbon steels. Four heat treatments were carried out for both steels to produce samples with different ferritic-perlitic microstructures. The dynamic strain aging and its effects on the material response were characterized at dynamic strain rates at temperatures up to 680 °C. The correlation between the microstructure and the strength of the dynamic strain aging offer new insight for a better understanding of the phenomena affecting the strength and hardening of steels at high temperatures.

Experimental

In this work, the high temperature high strain rate behavior of two standard alloys heat treated to four different microstructures was studied. The chemical compositions of the steels are given in Table 1. Both materials were studied in the standard or Reference (R) microstructural state, which is acquired by austenization annealing followed by isothermal annealing below the austenization temperature. The globular pearlite (GP) structure was obtained by adding an additional annealing cycle to the reference heat treatment, while the Coarse Grain (CG) structure was produced by increasing the austenization temperature of the steels. The fourth microstructure variant was produced by allowing the pearlite bands to grow during slow cooling from the austenization temperature to the subsequent isothermal annealing temperature. This last microstructure variant with pearlite bands (WB) is in the following called the Banded Structure. Figures 1 and 2 show scanning electron microscope images of the tested microstructure variants.

Table 1: Chemical compositions of the studied steels.

Steel	C	Mn	Si	Mo	Cr	P	Fe
C45	0.45	0.78	0.33	0.02	0.12	0.014	Bal.
27MnCr5	0.25	1.19	0.24	0.04	1.06	0.009	Bal.

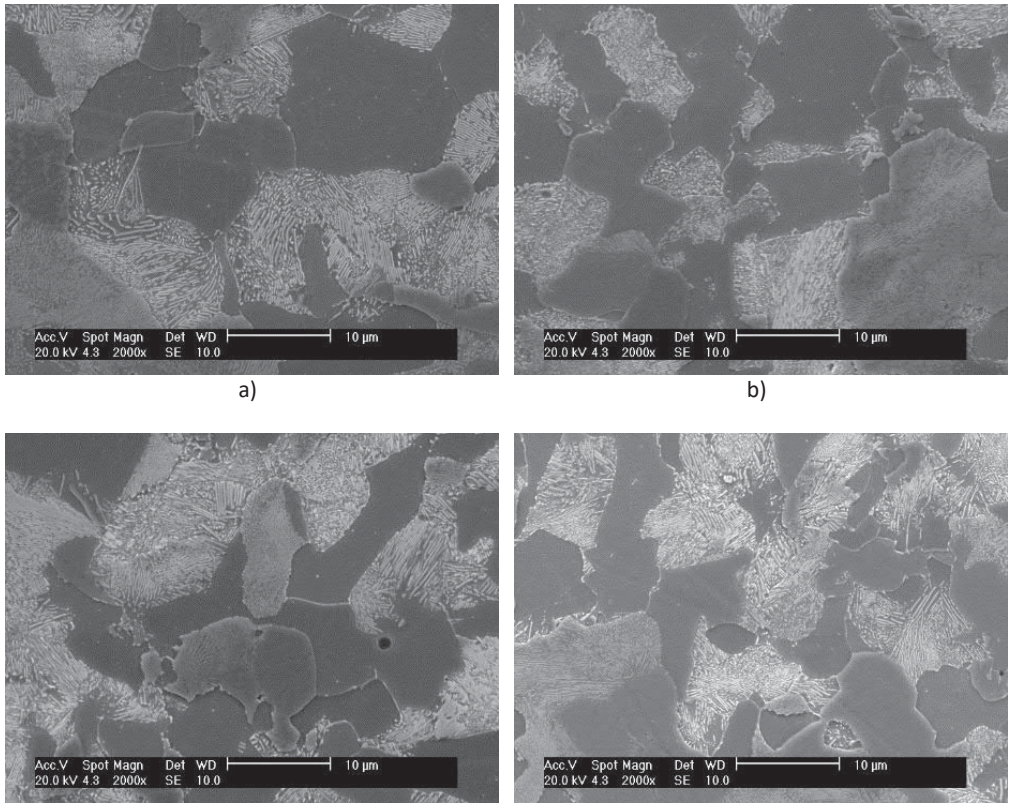

Figure 1: Scanning electron microscope images of the 27MnCr5 steel: a) Reference (R), b) Globular Pearlite (GP), c) Coarse Grained (CG), and d) Banded Structure (WB).

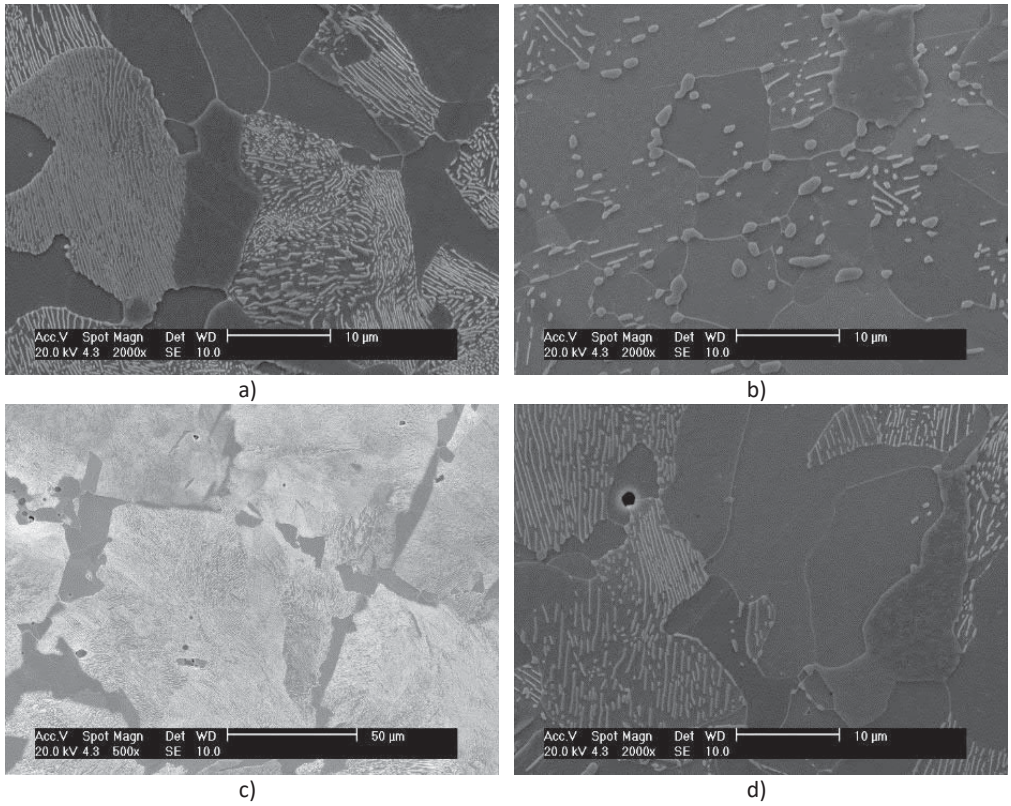

Figure 2: Scanning electron microscope images of the C45 steel: a) Reference (R), b) Globular Pearlite (GP), c) Coarse Grained (CG), and d) Banded Structure (WB). Notice the different magnification in image c).

The microstructures of the studied steels contained different amounts of pearlite, ferrite, and globular pearlite. Also the grain sizes and the distances between the pearlite lamellae were different. Analysis of the microstructures shows that the reference structures for both 27MnCr5 and C45 steels were homogenous ferrite-pearlite structures. Equally, the coarse grained structures of both materials contained large pearlite grains, and the structures were homogenous throughout the specimens. The 27MnCr5 globular pearlite structure had a low globular pearlite content, but for the C45 steel the GP structure contained a very high amount of globular pearlite. The banded structure of the 27MnCr5 steel was close to the reference structure, but the interlamellar spacing of the C45 banded structure was much higher, making it significantly different compared to its reference structure. The phase fractions of the studied steels are shown in Table 2. The phase compositions were obtained using image analysis from 30-40 images, and the standard deviation in the obtained phase fractions was around 8-9%.

Table 2: Phase compositions of the studied steels.

	% ferrite	% lamellar pearlite	% glob. pearlite
27MnCr5 - R	40	54	6
27MnCr5 - CG	52	43	5
27MnCr5 - GP	45	55	0
27MnCr5 - WB	44	56	0
C45 - R	25	56	19
C45 - CG	15	81	4
C45 - GP	10	0	90
C45 - WB	20	64	16

Mechanical testing

The Hopkinson Split Pressure Bar (SHPB) device used for the characterization of the high strain rate behavior of the studied steels comprises 22 mm diameter high strength Maraging steel incident, transmitted, and striker bars. The incident and transmitted pressure bars are aligned along the same horizontal axis by three bearings on four stanchions that can be moved in the Y- and Z-directions. A third pressure bar is placed after the transmitted bar to trap the residual transmitted momentum, i.e., to prevent the transmitted pulse from reflecting back towards the specimen. The momentum trap bar is also made use of in the high temperature set-up to close the gaps between the specimen and the incident and transmitted bars, and to limit the cold contact time of the hot specimen and the cold bars. The length of all three pressure bars was 1200 mm, while the two striker bars used in this work were 200 mm and 300 mm long. A room temperature test is carried out by placing the small cylindrical specimen between the incident and transmitted bars, impacting the striker bar to the free end of the incident bar, and allowing the stress pulse created by the impact to deform the specimen. The stress pulse travels in the incident bar at the speed of sound (~4900 m/s), and once it reaches the bar-sample interface, the pulse moves the end of the incident bar towards the transmitted bar, allowing part of the stress pulse to transmit through the specimen into the transmitted bar. The rest of the incident pulse is reflected back to the incident bar as a tensional stress pulse. These three stress pulses are recorded by strain gages bonded on the surface of the bars at their midpoint. The strain gage signals are amplified using a Kyowa CDV 700A signal conditioner and recorded with a high speed Yokogawa DL 708 digital oscilloscope. Assuming that the stresses over the entire length of the specimen are uniform, i.e., that the specimen is in stress equilibrium, the stress, strain, and strain rate can be calculated using Equations 1-3. In this work, a numerical dispersion correction method adopted from the work of Gorham [28] was used to correct the dispersion of the stress pulses as they propagate in the bars.

Average stress in the specimen:

$$\sigma(t) = \frac{A_b E \varepsilon_t(t)}{A_s} \quad (1)$$

Average strain in the specimen:

$$\varepsilon(t) = \frac{2C_0}{L_s} \int_0^t \varepsilon_r(t) dt \quad (2)$$

Average strain rate in the specimen:

$$\dot{\varepsilon}(t) = \frac{2C_0 \varepsilon_r(t)}{L_s} \quad (3)$$

where A_b, E, and C_0 are the cross sectional area, Young's modulus, and speed of sound of the bar material, L_s and A_s are the length and cross sectional area of the specimen, and ε_r, and ε_t are the dispersion corrected reflected and transmitted stress pulses.

The high temperature testing procedure is presented schematically in Figure 3. In the initial position, the specimen is placed in an insulating ceramic wool ring, and the ring is further placed in a special sample holder arm. This arm can push the specimen into a tube furnace located beside the bars. This way only the sample is heated while the bars remain at room temperature. Before the test, the bars are positioned so that the sample and the sample holder arm can move freely between the bars without touching them. The specimen holder arm pushes the sample into the furnace, where it is heated to the target temperature. The temperature of the specimen is continuously measured with thermocouples inside the furnace. The specimen is kept at the target temperature for approximately 10 minutes to ensure constant and uniform temperature of the sample. Then the pneumatic actuator controlling the specimen holder arm quickly retracts the sample to the centerline of the bars. At this point, the hot sample and the cold bars are not yet in contact with each other. When the sample reaches the centerline, the striker bar is launched at the preset pressure, and the striker bar quickly accelerates towards the incident bar. Just before the impact, a second pneumatic actuator pushes the transmitted bar towards the incident bar, lightly squeezing the sample between the bars. The contact time of the hot sample and the cold bars is measured using optical sensors. The setup limits the time that the hot sample spends outside the furnace before the dynamic loading to less than 200 ms, and more importantly, it limits the contact time of the cold bars and the hot sample to less than 50 ms. Numerical simulations of the heat flow from the specimen to its surrounding, specifically to the bars by conduction, show only a very small temperature drop of the surface of the sample. For a test performed at an initial temperature of 800 °C, the drop in the sample temperature is less than 9 °C in the depth of 150 micrometers from both ends of the cylindrical specimen [29]. A complete technical description of the device, example results, and numerical simulations of the heat transfer during the test can be found in refs. [29-31].

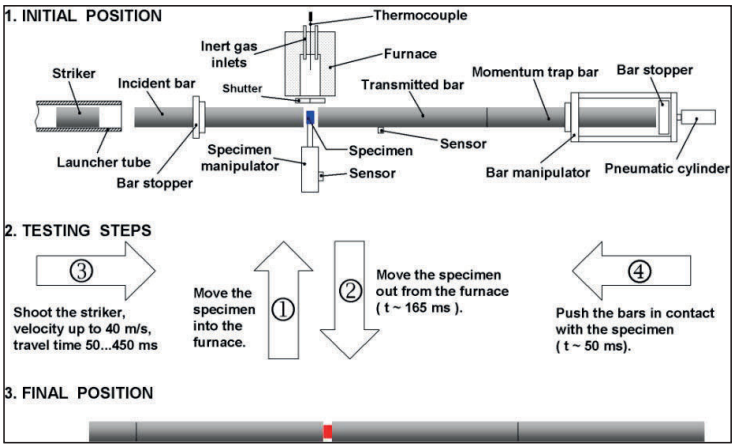

Figure 3: Schematic picture of the high strain rate high temperature compression apparatus and the testing steps associated with carrying out a high temperature test [29].

Results and discussion

Each room temperature compression test was repeated at least three times, whereas the high temperature tests were repeated at least two times. The materials studied in this work are rather homogeneous and the scatter in the tests is low. In the following, only one representative stress-strain curve for each material and testing condition is shown simply to limit the amount to data in the figures for better visual readability.

Figure 4 shows the compression stress-strain curves obtained for the 27MnCr5 steel at different strain rates and temperatures. At room temperature, a sharp yield point is observed at the strain rates of 500 s^{-1} and 2000 s^{-1}, but the yield behavior changes to more continuous when the strain rate is increased to 4500 s^{-1}. When the temperature is increased, the strength decreases and the yield behavior clearly changes to continuous. The room temperature strength after the yield point seems to be rather insensitive to the microstructure of the material, with the exception of the banded structure, which seems to have a slightly higher strength especially at 500 s^{-1} and 4500 s^{-1}. The strain hardening rate of the steel seems also rather insensitive to the microstructure, and the stress-strain curves obtained at a given strain rate and temperature are essentially parallel. Temperature, on the other hand, affects the shape of the stress-strain curve especially at low strains. The material strain hardens strongly at low strains in the high temperature tests, but at higher strains, the strain hardening rate decreases and approaches that observed at room temperature.

Figure 5 shows the stress-strain curves obtained for the C45 steel at the same conditions as discussed above for the 27MnCr5 steel. Moderately sharp or discontinuous yielding is observed for the coarse grained variant (CG), but the variant with the banded structure (WB) shows a very distinct sharp yield point at strain rates 500 s^{-1} and 2000 s^{-1}. However, the yielding behavior changes again to more continuous at the strain rate of 4500 s^{-1}. When comparing the strength of the different variants of the C45 steel, it is

obvious that the microstructure has a much stronger influence on the flow stress than for the 27MnCr5 steel. This was expected since the microstructures of the C45 steel variants differed much more from each other than the variants of the 27MnCr5 steel. The strongest variant of C45 at all strain rates was the one with a coarse-grained structure (CG), followed by the reference structure, the globular perlite, and the banded structure. The strain hardening rate seems again to be less affected by temperature, strain rate, and microstructure than the yielding behavior and the strength values.

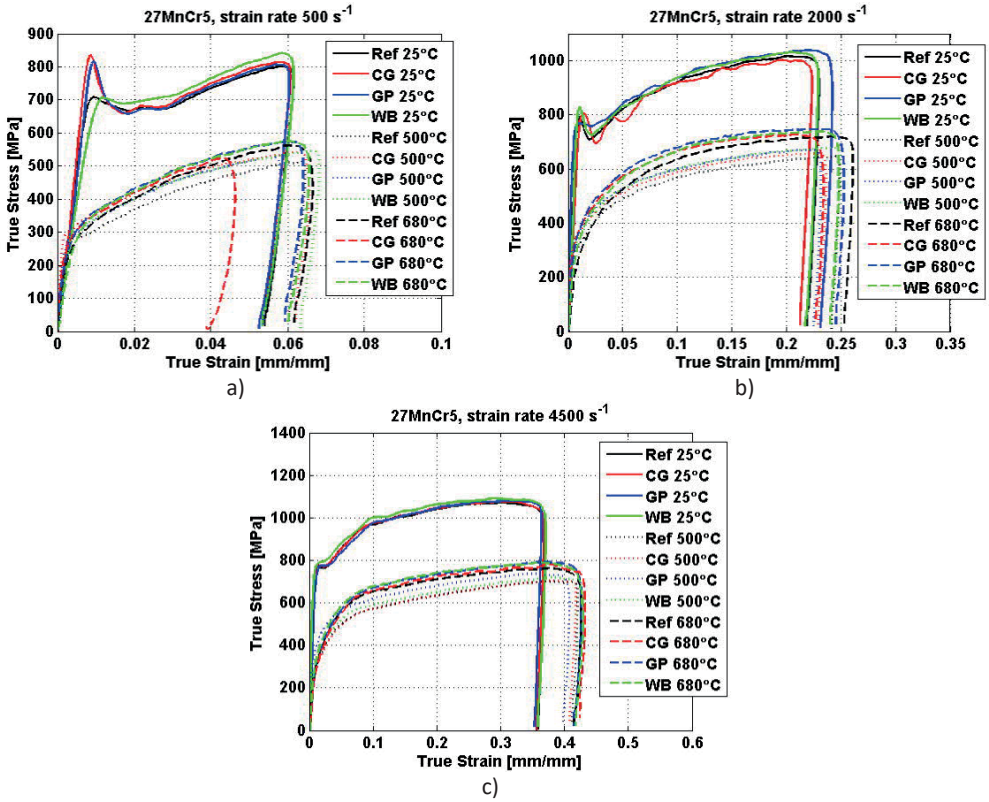

Figure 4: Stress-strain curves at different temperatures for the 27MnCr5 steel at the strain rate of a) 500 s^{-1}, b) 2000 s^{-1}, and 4500 s^{-1}.

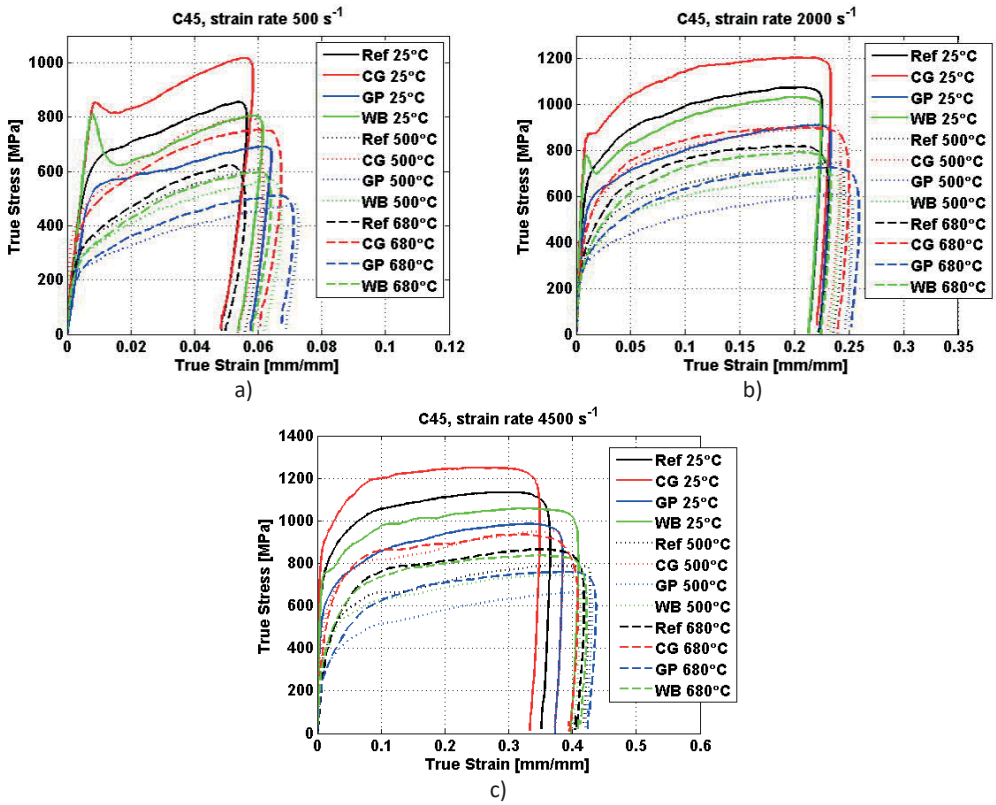

Figure 5: Stress-strain curves at different temperatures for the C45 steel at the strain rate of a) 500 s^{-1}, b) 2000 s^{-1}, and 4500 s^{-1}.

The effects of microstructure and temperature can be better visualized by plotting the flow stress at 5 and 15 percent of plastic strain as a function of temperature at a constant strain rate. Figures 6 and 7 show the flow stress – temperature scatter plots at the strain rate of 4500 s^{-1}, where a strong DSA effect was observed for both materials (for clarity, results for only one strain rate are shown here). For both materials and all variants, the strength decreases significantly as the temperature is increased from room temperature to 400 °C. The minimum strength for all materials is observed at temperatures close to 500 °C. Towards higher temperatures, the flow stresses of both steels increase due to the DSA effect. For 27MnCr5, the flow stress of all variants increases steadily up to the maximum test temperature of 680 °C. The typically observed maximum or peak in the flow stress vs. temperature curve is not observed in the studied temperature range, but the peak might occur at higher temperatures. However, the material structure is not stable at much higher temperatures, and therefore the tests were not continued above 680 °C. For the 27MnCr5 steel, only small differences between the variants can be seen in the rate at which the strength increases due to DSA, and this will be discussed in more details later on. For the C45 steel, on the other hand, the response is slightly different, and again a stronger effect of the microstructure is observed. The maximum of the bell-shaped curve is close to 620 °C and well within the

measurement range for the reference and coarse-grained structures. However, for the globular pearlite and banded structures the maximum would obviously again occur at a higher temperature, which cannot be determined from the current data.

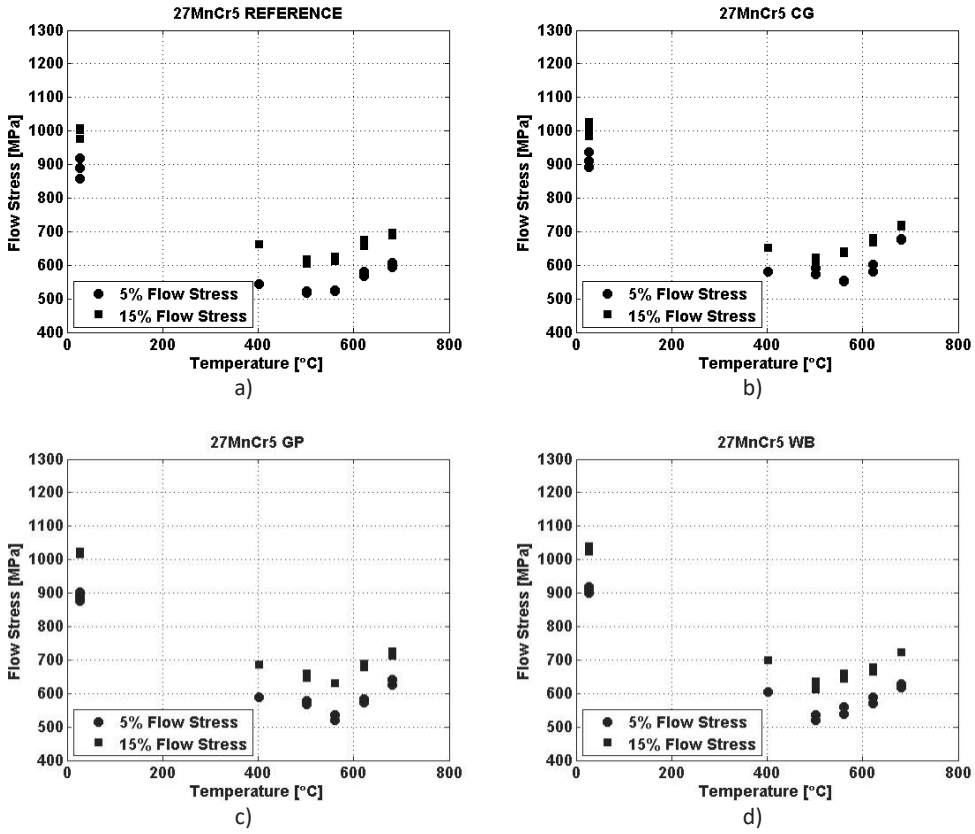

Figure 6: Flow stress at 5% and 15% of plastic strain as a function of temperature at the strain rate of 4500 s^{-1} for the 27MnCr5 steel; a) reference structure, b) coarse-grained structure, c) globular pearlite, and d) banded structure.

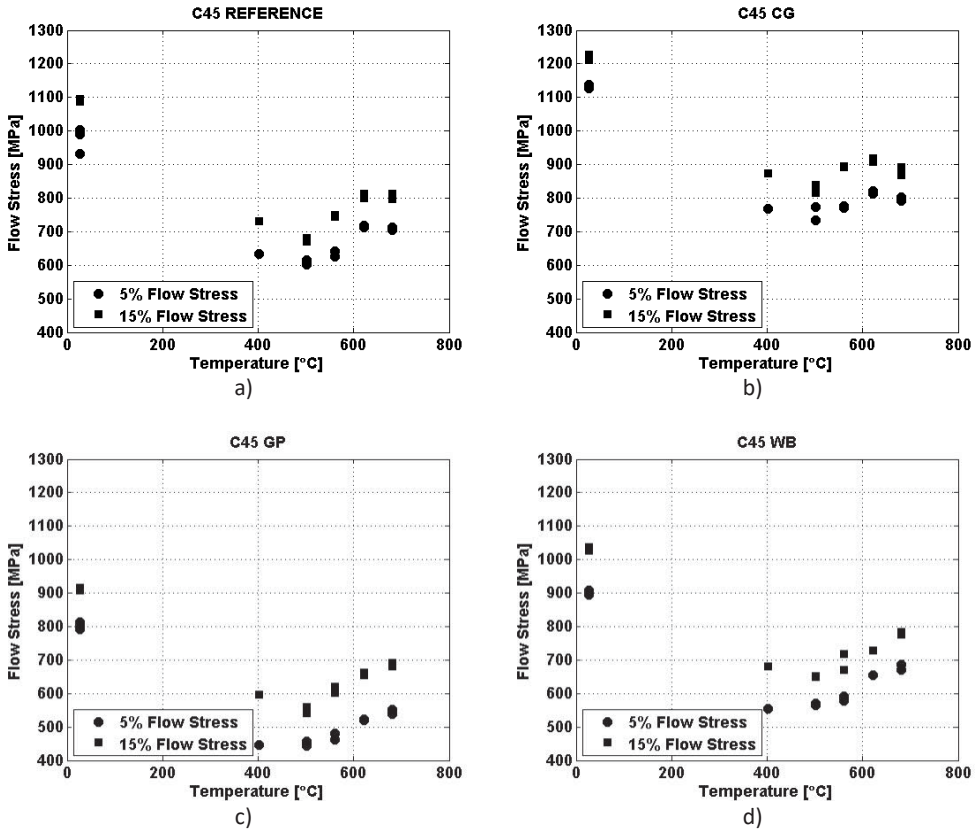

Figure 7: Flow stress at 5% and 15% of plastic strain as a function of temperature at the strain rate of 4500 s^{-1} for the C45 steel.

The strength of the dynamic strain aging effect can be evaluated and quantified using the temperature sensitivity factor η defined in Equation 4, where $\sigma_{\varepsilon,RT}$ and $\sigma_{\varepsilon,T}$ are the flow stresses at a constant plastic strain obtained at room temperature (RT) and at a higher temperature. For RT, the temperature sensitivity factor equals one, but at higher temperatures, it gets values between zero and one. The microstructure's sensitivity to DSA appears as the change (increase or decrease) of the η value, whereas the absolute values of the temperature sensitivity factor also take into account the thermal softening relative to the room temperature strength. Figure 8 shows the temperature sensitivity factor as a function of temperature at a constant strain rate of 4500 s^{-1} for all studied steels. Above 560 °C, the coarse-grained variant shows the highest temperature sensitivity to DSA, followed by the other variants in a somewhat scattered order. The material with the banded structure (WB) and the reference structure show quite low temperature sensitivity values. If the temperature sensitivity values are evaluated at 15 % of plastic strain, the situation changes. The difference between the material variants becomes even smaller, especially at higher temperatures. Strong DSA sensitivity is still observed for all variants. The change in the temperature

sensitivity towards higher temperatures is, however, slower than what was observed at 5% of plastic strain.

$$\eta(\varepsilon, \dot{\varepsilon}, T) = 1 - \frac{\sigma_{\varepsilon,RT} - \sigma_{\varepsilon,T}}{\sigma_{\varepsilon,RT}} \quad (4)$$

For the C45 steel, the effect of microstructure is again stronger than what was observed for the 27MnCr5 steel. At 5% of plastic strain (Figure 8c), the reference and coarse-grained materials show a maximum in the temperature sensitivity factor vs. temperature plot, as expected based on our previous analysis of Figure 6. Overall, the coarse-grained material shows a very high temperature sensitivity factor at all temperatures, and compared to other variants, the values do not change as much as a function of temperature. The globular pearlite and the banded structure have fairly low temperature sensitivity factors compared to the other variants in the lower temperature region, but the temperature sensitivity quickly increases when the temperature is increased. This is especially clear in Figure 8d, where the steels with globular and banded structures show the two lowest temperature sensitivity factor values at 500 °C and the two highest values at 680 °C, indicating a very rapid change in the temperature sensitivity of DSA in this temperature range.

The effect of microstructure on the dynamic strain aging behavior of the studied steels is quite complex. For the 27MnCr5 steel, the microstructure variants are not too different from each other, and therefore the effect of the microstructure on the dynamic strain aging is also smaller. With increasing plastic strain, the differences become even smaller, which implies that the microstructures are developing towards similar DSA conditions, as regards the amount and mobility of glide dislocations and diffusion of the interstitial atoms.

For the C45 steel, the microstructure variants differ considerably more from each other, and therefore also the temperature sensitivities of the variants vary more than with the 27MnCr5 steel. This is very clear especially at low plastic strains. However, also for the C45 steel the differences between the variants become smaller at higher plastic strains, indicating again a change in the microstructure towards more similar DSA conditions. For both steels in the low strain region, the coarse-grained structures with large pearlite grains seem to be most affected by the dynamic strain aging in the tested temperature range. However, the large-grained and the reference structures of the C45 steel also have the maximum DSA effect at lower temperatures than the banded and the globular pearlite structures. Because of this, the strength of the coarse-grained structure already decreases at the highest temperatures, whereas the strength of the banded structure and globular pearlite are still increasing. It is, however, quite clear that the higher austenization temperature and the larger pearlite grain size lead to a higher DSA sensitivity and a lower DSA maximum temperature.

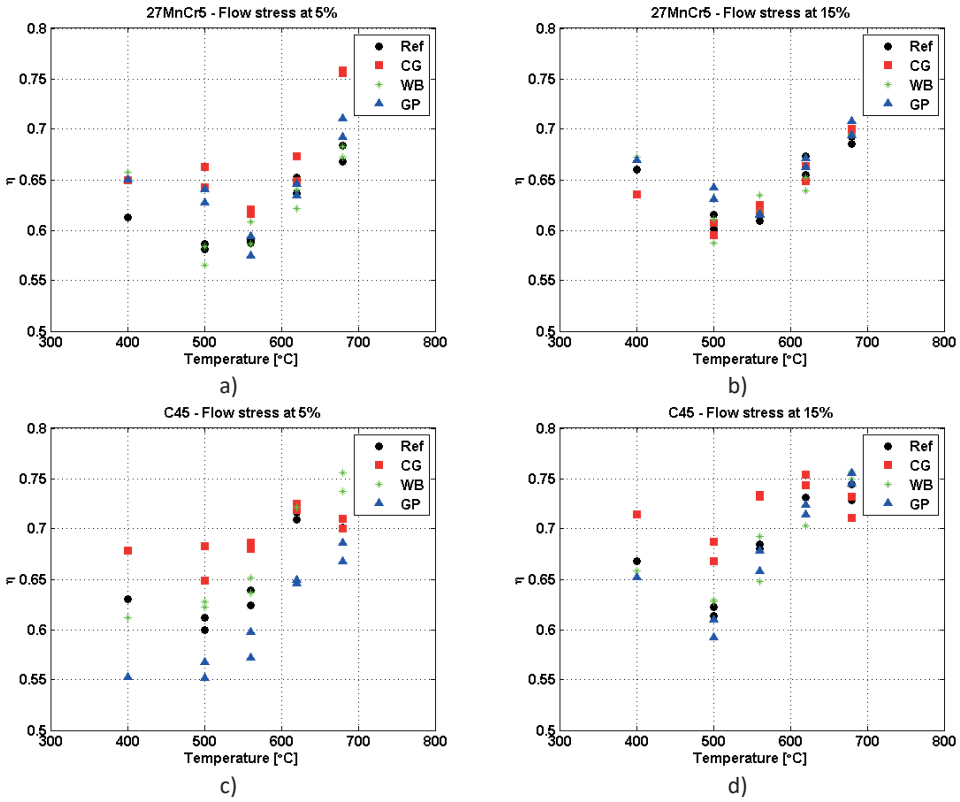

Figure 8: Temperature sensitivity factor η as a function of temperature at the strain rate of 4500 s^{-1} for a) 27MnCr5 at the flow stress of 5%, b) 27MnCr5 at the flow stress of 15%, c) C45 steel at the flow stress of 5%, and d) C45 steel at the flow stress of 15%.

Conclusions

The high strain rate high temperature behavior of two carbon steels was experimentally studied. Four different microstructures were created with heat treatments for both steels. The main emphasis of the work was on the dynamic strain aging at high temperatures and high strain rates and, especially, on how the microstructure of the steel affects its sensitivity to dynamic strain aging and the overall mechanical response at high rates. Based on the experiments, the following conclusions can be made:

- The heat treatment and the following microstructure of the steel have a strong effect on the DSA sensitivity of the steel. For the 27MnCr5 steel, the microstructures of the different variants were rather similar, whereas the microstructures of the C45 steel variants were considerably different from each other. Because of this, the C45 steel variants showed a greater effect of the microstructure on the DSA sensitivity than the 27MnC5 steel.

- The effect of microstructure on DSA was stronger at small plastic strains. This indicates that the microstructures of both alloys and all variants develop towards similar DSA conditions, and therefore, at higher strains, the mobile dislocation densities and the diffusional conditions become basically similar.
- The coarse-grained structure with large pearlite grains, following from a higher austenization temperature, was the most sensitive to dynamic strain aging for both steels. This was especially the case at low plastic strains.
- For the C45 steel, the reference or standard structure and the coarse-grained structure exhibited the maximum DSA effect, or the highest strength, at a lower temperature compared to the other microstructure variants. The other variants did not yet show the maximum increase in the strength due to DSA in the studied temperature range.
- Based on this study, it is very clear that the thermomechanical history and especially the microstructure of the steel have a strong effect on the high strain rate high temperature behavior and dynamic strain aging effect. This should be taken into account when estimating the material behavior in dynamic processes, and especially when numerically modeling the material response at high strain rates and high temperatures.

Acknowledgements

The funding by the European Research Fund for Coal and Steel in the frame of the research project RFSR-CT-2014-00020 (IMMAC) is gratefully acknowledged.

References

1. Portevin A, Le-Chatelier H (1924) Heat treatment of aluminum-copper alloys. Trans. Am. Soc. Steel Treat. 52:457-478.
2. Nemat-Nasser S, Guo W, Cheng J (1999) Mechanical Properties and deformation mechanisms of a commercially pure titanium. Acta Mat. 47:3705-3720.
3. Chen J, Nemat-Nasser S (2000) A model for experimentally observed high strain rate dynamic strain aging in titanium. Acta Mat. 48:3131-3144.
4. Nemat-Nasser S (2000) Flow stress of commercially pure niobium over a broad range of temperatures and strain rates. Mat.Sci.Eng.A. 284:202-210.
5. Nemat-Nasser S, Guo W (2000) High Strain rate response of commercially pure vanadium. Mech.Mat. 32:243-260.
6. Cheng J, Nemat Nasser S, Guo W (2001) A unified constitutive model for strain rate and temperature dependent behavior of molybdenum. Mech.Mat. 33:603-616.
7. Nemat-Nasser S, Guo W, Liu M (1999) Experimentally based micromechanical modeling of dynamic response of molybdenum. Scripta Mat. 40:859-872.

8. Nemat-Nasser S, Guo W, Kihl D (2001) Thermomechanical response of AL-6XN stainless steel over a wide range of strain rates and temperatures. J. Mech.Phys.Sol. 49:1823-1846.
9. Baird J, Jamieson A (1966) Effects of manganese and nitrogen on the tensile properties of iron in the range of 20-600 centigrades. J.Iron.Steel.Inst.
10. Gilat A, Wu X (1997) Plastic deformation of 1020 steel over a wide range of strain rates and temperatures. Int.J.plast. 13:611-632.
11. Nemat-Nasser S, Guo W (1997) Thermomechanical response of DH-36 structural steel overa a wide range of strain rates and temperatures. Mech.Mat. 35:1023-1047.
12. Nemat-Nasser S, Guo W (2005) Thermomechanical response of HSLA-65 steel plates: experiments and modeling. Mech.Mat. 37:379-405.
13. Shahriary M, Koohbor B, Ahadi K, Akrami A, Khakian-qumi M (2012) The effect of dynamic strain aging on room temperature mechanical properties of high martensite dual phase steel. Mat.Sci.Eng.A. 550:325-332.
14. Forni D, Chiaia B, Cadoni E (2016) High strain rate response of S355 at high temperatures. Mat.design. 94:467-478.
15. Wang J, Guo W, Gau W, Su J (2015) The third type of strain aging and the constitutive modeling of a Q245B overa a wide range of temperatures and strain rates. Int.J.Plasticity. 65:85-107.
16. Hong S, Lee S (2004) The tensile and low cycle fatigue behavior of cold worked 316L stainless steel: influence of dynamic strain aging. Int.J.Fatigue. 26:899-910.
17. Samuel K, Ray S, Sasikala G (2006) Dynamic strain aging in prior cold worked 15Cr-Ni titanium modified stainless steel. J.Nuc.Mat. 355:30-37.
18. Kim I, Kang S (1995) Dynamic strain aging in SA508-class 3 pressure vessel steel. Int.J.Press.Vess. 62:123-129.
19. Baird J (1971) Effects of strain aging due to interstitial solutes on the mechanical properties of metals. Met.Rew. 149:1-18.
20. Cuddy L, Leslie W. (1972) Some aspects of serrated yielding in substitutional solid solution of iron. Acta Met. 20:1157-1167.
21. Gao C, Zhang L (2012) Constitutive modeling of plasticity of FCC metals under extremely high strain rates. Int.J.Plasticity 32-33:121-133.
22. Guo W, Gao X (2013) On the constitutive modeling of a structural steel over a wide range of temperatures and strain rates. Mat.Sci.Eng.A. 561:468-476.
23. Lee K, Lee S (2012) Modeling of material behavior at various temperatures of hot isostatically pressed superalloys. Mat.Sci.Eng.A. 541:81-87.
24. Follansbee P, Kocks U (1988) A constitutive description of the deformation of copper based on the use of mechanical threshold stress as an internal state variable. Acta. Met. 36:81-93.
25. Zerilli F, Armstrong R (1987) Dislocation mechanics based constitutive relations for material dynamics calculations. J. App.Phys. 61:1816-1825.
26. Chakravartty J, Wedekar S, Asundi M (1983) Dynamic strain-aging of A203D nuclear structural steel. J.Nuc.Mat. 119:51-58.
27. Wagner D, Moreno J, Priol C (1998) Dynamic strain aging sensitivity of heat affected zones in C-Mn steels. J.Nuc.Mat. 252:527-256.
28. Gorham D. (1983) J.Phys.E. 16:477-479.

29. Apostol M. (2007) Strain rate and temperature dependence of the compression behavior of FCC and BCC metals. Development of experimental techniques and their application to material modeling. PhD thesis. Tampere University of Technology.
30. Leemet T, Hokka M, Shrot A, Baeker M, Kuokkala V-T (2012) Characterization and numerical modeling of the high strain rate mechanical behavior of Ti 15-3 alloy for machining simulations. Mat.Sci.Eng.A. 550:350-357.
31. Hokka M, Leemet T, Shrot A, Baeker M, Kuokkala V-T (2014) Dynamic behavior and high speed machining of ti-6246 and Alloy 625 superalloys: experimental and modeling approaches. Exp.Mech. 54:199:210.